Doctoral Dissertation
博士論文

Elucidating Chemistry and Physics of Planetary System Formation with Millimeter/centimeter Observations

(ミリ波・センチ波観測による惑星系形成の化学・物理の解明)

A Dissertation Submitted for the Degree of Doctor of Philosophy
December 2024
令和6年12月博士（理学）申請

Department of Astronomy, Graduate School of Science,
The University of Tokyo
東京大学大学院理学系研究科天文学専攻

Yoshihide Yamato
大和 義英

Abstract

The envelopes and disks around young low-mass stars contain a substantial amount of the primordial material from which planetary bodies assemble, and thus provide a unique opportunity to study the initial condition and its subsequent evolution during the epoch of star and planet formation. While recent high-resolution interferometric observations with the Atacama Large Millimeter/submillimeter Array (ALMA) have significantly advanced our understanding of the physical and chemical processes associated with the formation of planetary systems, a number of open questions remain on several critical aspects, including when and how planetary systems form, and how the interstellar medium (ISM) is delivered and incorporated into the nascent planets. In addition, longer wavelength observations have recently been recognized as crucial to probe the innermost opaque region of disks and envelopes where the bulk of planet-forming material resides, but observations are limited. This thesis investigates the physical and chemical environments of disk-forming regions and protoplanetary disks using high-resolution interferometric observations with ALMA and the Karl G. Jansky Very Large Array (VLA) across a wide range of wavelengths spanning from (sub-)millimeters to centimeters. The studies presented here aim to elucidate (1) the formation of disk substructures in a young Class I disk to determine when planet formation starts, (2) the nitrogen chemistry in protostellar systems with ammonia (NH_3) molecular line observations at centimeter wavelengths, and (3) the chemistry of complex organic molecules (COMs) in protoplanetary disks. First, I analyze ALMA observations of the Class I protostar L1489 IRS, which reveal a ringed and warped disk structure. The dust continuum observations at 1.3 mm and molecular lines, including ^{13}CO, $C^{18}O$, and SO, show a clear gap-ring substructure and inner disk misalignment. Such features suggest the influence of forming planets and/or dynamic gas infall. This study establishes the idea that disk substructure formation begins during the Class I phase. Second, I present VLA observations of NH_3 and its deuterated isotopologue (NH_2D) toward the Class 0 protostar NGC 1333 IRAS 4A. This study offers the first measurements of the NH_2D/NH_3 ratio, providing insights into the formation conditions of the NH_3 ices and the nitrogen reservoir in the ISM. Our results suggest that ammonia ices form efficiently in the prestellar core phase and undergo chemical reprocessing during the protostellar and protoplanetary disk phases toward the planetary system. In addition, this work demonstrates that NH_3 line observations with the VLA at centimeter wavelengths are useful to decipher the nitrogen chemistry in the ISM and to probe the innermost opaque regions. Third, I study the chemistry of COMs in protoplanetary disks around V883 Ori and MWC 480, both of which are unique laboratories for studying disk ice reservoirs. For the FU Ori-type outbursting star V883 Ori, ALMA Band 3 observations detect several oxygen-bearing COMs and reveal high COM abundance ratios relative to methanol (CH_3OH), similar to cometary compositions. Furthermore, we discover anomalous $^{12}C/^{13}C$ and D/H isotopic ratios of COMs for the first time, indicating some chemical reprocessing in warmer disk environments. For the Herbig Ae star MWC 480, we report the serendipitous detection of dimethyl ether (CH_3OCH_3) but no methanol for the first time in non-transitional disks, suggesting significant chemical reprocessing in the innermost, dense and warm regions. Overall, this thesis presents these important scientific implications for the physical and chemical processes of planetary system formation, but at the same time, provides a crucial guide for future observations with upgraded facilities, such as ALMA's Wideband Sensitivity Upgrade (WSU) and the Next Generation Very Large Array (ngVLA). High-resolution and high-sensitivity observations with these facilities will be pivotal in unveiling a more detailed and complete picture of planetary system formation and the associated astrochemical processes.

Contents

Abstract iii

List of Figures x

List of Tables xiv

Acknowledgments xvii

1 Introduction 1

1.1 Star and Planet Formation 2

1.2 Chemistry in Star- and Planet-forming Regions 6

1.2.1 Formation of Molecules and Its Evolution 6

1.2.2 Isotopic Fractionation 8

1.3 Physical and Chemical Structure of Planet-forming Regions 11

1.3.1 Protostellar Envelopes and Disks 11

1.3.2 Protoplanetary Disk 16

1.3.3 Protostellar Accretion Burst As a Unique Probe of the Disk Ice Reservoir 18

1.4 Interferometric Observations with ALMA and VLA 20

1.4.1 Disk Substructure 20

1.4.2 Chemistry at Envelope/Disk Scales 22

1.5 Thesis Outline 24

2 The Ringed and Warped Structure of the Disk around the Class I Protostar L1489 IRS 27

2.1 Introduction 28

2.2 Observations and Data Reduction 31

2.3 Observational Results 35

2.3.1 1.3 mm Continuum 35

2.3.2 Molecular Lines 37

2.3.3 Radial Intensity Profiles 41

2.4 Analysis 45

2.4.1 Visibility Analysis of the Dust Continuum Emission 45

2.4.2 Velocity Structure Traced by the $C^{18}O$ Emission 49

2.5 Discussion 54

2.5.1 Origin of the Dust Ring 54

2.5.2 Outer Disk Structures 56

2.5.3 Azimuthal Asymmetry 57

2.5.4 Gas Disk Size and Dust Disk Size 60

2.5.5 Origin of the SO Emission: Accretion Shocks and a Warm Inner Disk? 61

2.5.6 Warped Disk Structures 63

2.6 Summary 65

3 The First Interferometric Measurements of NH_2D/NH_3 Ratio in Hot Corinos 71

3.1 Introduction 72

3.2 Observation 75

3.3 Analysis 80

3.3.1 Estimates on the emitting region size 80

3.3.2 Hyperfine fit of NH_3 and NH_2D lines 81

3.4 Results 82
3.5 Discussion 88
3.5.1 NH_3 and NH_2D in the hot corino region 88
3.5.2 Comparison with theoretical models and origin of high NH_2D/NH_3 ratios 91
3.5.3 Comparison with other major species in hot corinos and comet 67P 94
3.5.4 Physical properties of 4A1 and 4A2 cores probed by NH_3 and NH_2D 96
3.6 Summary 97

4 Chemistry of Complex Organic Molecules in the V883 Ori Disk Revealed by ALMA Band 3 Observations 101

4.1 Introduction 102
4.2 Observations 105
4.2.1 ALMA Band 3 Observations 105
4.2.2 Calibration and Imaging 106
4.3 Data Analysis and Result 110
4.3.1 Spectrum Extraction and Line Identification 110
4.3.2 Spatial Distributions 111
4.3.3 Column Density Retrieval 115
4.4 Discussion 119
4.4.1 Comparison of the Spatial Distributions with the Sub-mm Observations 119
4.4.2 The Physical and Chemical Structure of the Innermost Region of the V883 Ori Disk 120
4.4.3 Chemical Abundance Ratios of COMs 123
4.4.4 Isotopic Ratios of COMs 126
4.4.5 Deficiency of Nitrogen-bearing COMs 132
4.4.6 Implications for Sulfur Chemistry 134

4.5 Summary . . . 135

5 Detection of Dimethyl Ether in the Central Region of the MWC 480 Protoplanetary Disk 137

5.1 Introduction . . . 138

5.2 Observations . . . 140

5.3 Detection of Dimethyl Ether . . . 144

5.3.1 Spectra and Spatial Distributions . . . 144

5.3.2 Spectral Analysis . . . 145

5.4 Discussion . . . 146

5.4.1 Chemical Origin of the COM Emission . . . 146

5.4.2 Comparison to Other Disks . . . 149

5.5 Summary and Conclusion . . . 152

6 Conclusion and Outlook 153

6.1 Thesis Summary . . . 153

6.2 Future Prospect . . . 156

A Continuum Maps with Different Robust Parameters 161

B Generation and Selection of Radial Intensity Profiles 163

C Radiative Transfer Model of the L1489 IRS Disk 167

D Hyperfine Models for NH_3 and NH_2D 169

D.1 NH_3 Model . . . 169

D.2 NH_2D Model . . . 171

E Radiative Transfer Modeling 175

F Channel Maps of the COM Emission 181

G JvM effect and Continuum Subtraction 185

H Detected Transitions 189

I Disk-integrated Spectra 197

J LTE Spectral Model 207

K Reconstruction of Radial Intensity Profile 211

L Spectroscopic Data for Molecules 213

L.1 Methanol 213
L.2 Acetaldehyde 214
L.3 Methyl Formate 215
L.4 Dimethyl Ether 216
L.5 Acetone 216
L.6 Ethylene Oxide 216
L.7 Propenal 217
L.8 Propanal 217

M Matched Filter Analysis 219

N Details of Spectral Analysis 221

O Parametric Disk Model 229

P Detection of a New Submillimeter Source 235

References 237

List of Figures

1.1 Star and Planet Formation Processes 4

1.2 P-V Diagram of the CO $J = 2$–1 Emission in the HD 163296 Disk 13

1.3 Schematic of Typical Protoplanetary Disk 17

1.4 ALMA Images of the V883 Ori Disk 20

1.5 Compilation of the eDisk and DSHARP Continuum Images 22

2.1 High-resolution Continuum Images of the Disk around L1489 IRS 38

2.2 Moment Maps of Molecular Lines 42

2.3 Moment Maps of Molecular Lines (Zoomed-in View) 43

2.4 Continuum Radial Intensity Profiles 46

2.5 Molecular Line Radial Intensity Profile 47

2.6 Comparison of Observed Visibility Profile and Model Fit 50

2.7 $C^{18}O$ PV Diagram and Fit by SLAM 53

2.8 Comparison of Radial Intensity Profiles 58

2.9 SO Emission Distribution and PV Diagram 66

2.10 Schematic Figure of the L1489 IRS System 67

3.1 VLA Continuum Image of IRAS 4A 85
3.2 Moment 0 Map Gallery of NH_3 and NH_2D 86
3.3 Hyperfine Fit to Ammonia Spectra and its residual in IRAS 4A1 89
3.4 Hyperfine Fit to Ammonia Spectra and its residual in IRAS 4A2 89

4.1 V883 Ori COMs Moment 0 Gallery 112
4.2 V883 Ori Full Spectra 113
4.3 Line Profiles of COMs in V883 Ori 116
4.4 Reconstructed Radial Intensity Profiles of COMs Lines 116
4.5 Demonstration of Spectral Fit 125
4.6 Comparison of Abundance Ratios of COMs 125
4.7 Measured $^{12}C/^{13}C$ Ratios of COMs 133
4.8 Measured D/H Ratios of COMs 133

5.1 COM Moment 0 Maps and Spectra in the MWC 480 Disk 147
5.2 COM Abundance Comparison among Class II Disks 151

A.1 L1489 IRS Continuum Images with Different Robust Parameters 162

B.1 Comparison of Different Wedges Taken to Generate the Intensity Profiles . 165

C.1 Model Dust Temperature Profile of the L1489 IRS Disk 168

E.1 Gas Density Profile of the IRAS 4A Model 176
E.2 Dust Temperature Profile of the IRAS 4A Model 176
E.3 Comparison of Observed and Modeled Spectra of NH_2D 179

F.1 CH_3OH Channel Map in V883 Ori 182
F.2 CH_3CHO Channel Map in V883 Ori 183
F.3 CH_3OCHO Channel Map in V883 Ori 184

G.1 Spectra After Image-plane Continuum Subtraction 188

I.1 Full Disk-integrated Spectra 1 198
I.2 Full Disk-integrated Spectra 2 199
I.3 Full Disk-integrated Spectra 3 200
I.4 Full Disk-integrated Spectra 4 201
I.5 Aligned Full Disk-integrated Spectra with Fit Model 1 202
I.6 Aligned Full Disk-integrated Spectra with Fit Model 2 203
I.7 Aligned Full Disk-integrated Spectra with Fit Model 3 204
I.8 Aligned Full Disk-integrated Spectra with Fit Model 4 205
I.9 ^{13}C-Methyl Formate Spectra 206

J.1 Line Shape of Aligned Spectra 210

M.1 Matched Filter Responses toward the MWC 480 Disk 220

N.1 Corner Plot of Spectral Fit 228

P.1 Continuum Image of the MWC 480 Disk and Nearby Submillimeter Source 236

List of Tables

1.1 Classification of YSOs Based on Greene et al. (1994) 5

1.2 Sublimation Temperatures of Major Species at Different Gas Densities . . 9

2.1 Properties of the Continuum and Line Images 34

2.2 Best-fit Parameters of the Visibility Fit 52

2.3 Results of the Keplerian Fits to $C^{18}O$ PV Diagram 52

3.1 Observed Transitions and Their Spectroscopic Data 78

3.2 Properties of Image Cubes and Velocity-integrated Intensity Maps of NH_3 and NH_2D 79

3.3 Free Parameters of Hyperfine Fits for 4A1 and 4A2 83

3.4 Results of Fits for 4A1 and 4A2 87

3.5 Molecular D/H Ratios Measured toward the Inner Warm Region of the IRAS4A2 Core and the Comet 67P/C-G 99

4.1 Observational Details 108

4.2 Properties of Image Cubes 109

4.3 Column Density of Molecules 118

4.4 $^{12}C/^{13}C$ Ratios of COMs 129

5.1 Observational Details 143
5.2 Result of the Spectral Analysis 151

D.1 Spectroscopic Data of NH_3 and NH_2D Used in Hyperfine Fits 172

H.1 Detected Transitions for Each Species 190

N.1 Spectroscopic Properties of Major Molecular Lines 224

O.1 Disk Modeling Results 232

Acknowledgments

First and foremost, I would like to express my deepest gratitude to my supervisor, Professor Yuri Aikawa, for her invaluable guidance, continuous support, and patience throughout my doctoral course. This thesis was only possible with her accurate scientific support and personal encouragement. She introduced me to the large collaboration networks, including multiple ALMA Large Programs, provided detailed and thorough comments on the drafts of papers, proposals, and application documents, and provided the opportunity to present my research at many seminars and conferences. I would also like to thank her for regular discussion on the weekly lab meeting, which provided a valuable opportunity to receive feedback from researchers with diverse backgrounds, including theorists, and to learn about the research of other lab members. These experiences greatly improved my knowledge across different aspects of the research field.

I am also deeply indebted to my mentor during the master's course, Gianni Cataldi. He first taught me the basics of radio astronomy and interferometric observations, which are the fundamental basis of the studies presented in this thesis. The collaborative works with him on the MAPS Large Program data resulted in my first publication. I also wanted to thank my close collaborators Kenji Furuya and Shota Notsu. Kenji first introduced me to the collaboration network that enable the VLA study and always helped me shape the potential research direction from a theoretical perspective. Shota provided the ALMA data and generously shared his experiences as a researcher, which greatly helped me in contemplating my future career.

I would also like to thank the examiners of my doctoral thesis, Misato Fukagawa, Motohide Tamura, Fumitaka Nakamura, Shogo Tachibana, and Munetake Momose, for their thorough comments and productive suggestions that help shaping a clear conclusion of this thesis and my potential future research directions.

This thesis was also only possible with the productive collaborations with researchers all over the world. I would like to thank all of my collaborators: John J. Tobin, Jes K. Jørgensen, Nami Sakai, Shingo Hirano, Shoji Mori, Yusuke Aso, Christian Flores, Itziar de Gregorio-Monsalvo, Viviana V. Guzmán, Ilseung Han, Jane Huang, Mihkel Kama,

Miyu Kido, Patrick M. Koch, Woojin Kwon, Charles J. Law, Shih-Ping Lai, Chang Won Lee, Jeong-Eun Lee, Romane Le Gal, Zhi-Yun Li, Zhe-Yu Daniel Lin, Leslie W. Looney, Suchitra Narayanan, Hideko Nomura, Karin I. Öberg, Nagayoshi Ohashi, Yuki Okoda, Magnus V. Persson, Nguyen Thi Phuong, Chunhua Qi, Jinshi Sai, Kazuya Saigo, Alejandro Santamaría-Miranda, Rajeeb Sharma, Shigehisa Takakuwa, Richard Teague, Travis J. Thieme, Kengo Tomida, Merel L. R. van 't Hoff, and Hsi-Wei Yen.

I am grateful to the past and present members of Aikawa lab and Department of Astronomy for discussions at the weekly meeting and daily conversations that made my research life enjoyable. I would especially like to thank Gianni Cataldi, Shoji Mori, Shingo Hirano, German Molpeceres, Taiki Suzuki, Anton Feeney-Johansson, Naoto Harada, Keisuke Hirata, Yuto Komichi, Suguru Takebayashi, and Kazuma Fukutomi. I also thank all the administrative staffs at the department for their kind and helpful assistance on various aspects of my research life. My heartfelt thanks also go to Kaho Morii, Kiyoaki Doi, Tomohiro Yoshida, and others, for insightful discussions and making my research life enjoyable and enriching.

All the studies presented in this thesis are based on the ALMA and VLA data, whose observations and initial calibration were performed by the ALMA and VLA staff. I would like to thank them for their continuous support. This thesis makes use of the following ALMA data: #2019.1.00261.L, #2019.A.00034.S, #2021.1.00357.S and #2021.1.00535.S. I have also been financially supported by a Grant-in-Aid for the Japan Society for the Promotion of Science (JSPS) Fellows (KAKENHI grant No. JP23KJ0636) and IGPEES, WINGS Program of the University of Tokyo.

Last but not least, I would like to thank my family for their support and encouragement over these challenging years, which made this thesis possible. I would also like to thank my partner Kaho, who shared the challenges of pursuing a Ph.D., for all the support throughout my doctoral journey. This thesis was truly only possible with her continuous support and encouragement, which helped me many times when I felt like giving up. I am also thankful for the small joys in life—a good meal, an engaging TV program, inspiring YouTube videos, or the music and performances of talented artists, actors, and idols—which provided me with much-needed relaxation and motivation throughout my research life.

Chapter 1

Introduction

Over the past decades, more than 5,000 exoplanets have been discovered[1], and their physical and chemical properties are found to be diverse in terms of mass, size, orbital shape, temperature, and composition. To understand the origin of this diversity, a detailed study of the physical and chemical properties of protoplanetary disks and disk-forming regions where planets assemble is crucial, since they set the initial condition of exoplanetary system formation and should reflect the outcome of the physical and chemical evolution during these stages.

Observations at radio wavelengths serve as a powerful tool to directly unveil the physics and chemistry occurring in these planet-forming regions. Recent advancement of the interferometers at (sub-)millimeter wavelengths have enabled for high sensitivity observations with high spatial resolutions at ∼10–100 au scales, allowing for a detailed characterization of these regions by disentangling the different physical components around young stars. Moreover, observations at longer wavelength, such as centimeter wavelengths, become recently more vital in probing the inner region close to the central star, which is in general too optically thick to look through the inner midplane of the disk at shorter wavelengths. These multi-wavelength nature are crucial in characterizing the chemical and physical properties across the full range of spatial scales in planet-forming regions.

---

[1] `https://exoplanetarchive.ipac.caltech.edu/`

In recent years, the exploration of our solar system has also made a significant advance with several sample return missions and in situ explorations, including the Hayabusa 2 mission toward the asteroid Ryugu, the OSIRIS-REx mission toward the asteroid Bennu, and the Rosetta mission toward the comet 67P/Churyumov-Gerasimenko. These missions now allow us to directly compare the chemical compositions in these small solar system bodies with the astronomical observations toward planet-forming regions at unprecedented details. In particular, the isotopic ratios of volatile elements, such as D/H, $^{12}\mathrm{C}/^{13}\mathrm{C}$, $^{14}\mathrm{N}/^{15}\mathrm{N}$, and $^{16}\mathrm{O}/^{18}\mathrm{O}$, are key in directly linking the materials in our solar system to the interstellar medium (ISM) and inferring their possible origins. This interdisciplinary approach will also allow us to put our solar system into a broader context of the diverse characteristics of exoplanetary systems (e.g., Tachibana & Sakai 2024).

Overall, the aim of this thesis is to unveil the physical and chemical properties of planet-forming regions using interferometric observations across a wide range of wavelengths from (sub-)millimeter to centimeter. These efforts will eventually contribute to our understanding of the origin of our solar system, and ultimately ourselves.

1.1 Star and Planet Formation

The low- and intermediate-mass star usually refers to the star with a mass of $\lesssim 8\,M_\odot$. These stars are born in molecular clouds by the gravitational collapse[2] (Figure 1.1). The molecular cloud cores are particularly dense regions and their central region is well shielded from the external radiations and thus is cold ($\sim$10 K). Some of such cores are dense enough to gravitationally collapse and eventually form a young stellar object (YSO) at the center, which is initially surrounded by the natal envelope. The typical collapsing timescale is described by the free-fall timescale:

$$t_{\mathrm{ff}} = \left(\frac{3\pi}{32G\rho_0}\right)^{1/2} \simeq 3.4 \times 10^5 \left(\frac{n_{\mathrm{H_2}}}{10^4\,\mathrm{cm^{-3}}}\right)^{-1/2} \mathrm{yr}, \tag{1.1}$$

---

[2] Note that here I treat only single star systems.

where G is gravitational constants and ρ_0 is the initial mass density. Thus, a cloud with a molecular hydrogen density of $10^4\,\mathrm{cm}^{-3}$ typically collapses within $\sim 10^5$–10^6 year.

In the protostellar stage, density and temperature increases inwards due to the heating by the central YSO and the accretion from the surrounding envelopes. Furthermore, circumstellar disks are formed as a natural consequence of the conservation of angular momentum. At this stage, outflows and jets are launched to efficiently remove the angular momentum from the circumstellar disk system. Simultaneously, the material continues to accrete onto the central region, making the disk more massive to be gravitationally unstable. The central protostar also becomes hot enough to start to burn the hydrogen atoms to be a pre-main sequence star. The surrounding envelope typically disperse within a timescale of $\sim 1\,\mathrm{Myr}$. As a consequence, a Keplerian disk and a pre-main sequence star become observable at infrared and optical wavelengths without extinctions by the dense envelope.

Classically, YSOs have been observed in a wide range of wavelength ranging from the optical to the radio. Typical YSOs show more emission from the infrared (IR) wavelength than the optical or near-IR that is expected from the central protostar or pre-main sequence star. This IR 'excess', which is thought to originate from the thermal emission of the dust around the central objects, has been used to empirically classify the YSOs. Lada & Wilking (1984) classified a large sample of observed YSOs into three evolutionary categories; Class I, II, and III, from younger sources to evolved sources. Class I has a large IR excess, while Class II and III have smaller IR excess since the surrounding envelope has already almost dispersed. In Lada (1987), its classification criteria is more quantitatively described by defining the spectral index;

$$\alpha_{\mathrm{IR}} = \frac{\mathrm{d}\log\lambda F_\lambda}{\mathrm{d}\log\lambda}. \tag{1.2}$$

This spectral index has frequently been used in later studies, and usually measured between near- and mid-IR wavelength, e.g., 2 μm and 25 μm.

This classification was extended to the younger end, Class 0, by Andre et al. (1993). Class 0 is the source that does not show any emission in optical or near-IR due to the dense surrounding envelope that highly obscure the central object. Such sources have been identified as the protostellar phase objects from their prominent outflows and infalling signatures toward the center revealed by molecular line observations. This resulted in total five categories of YSOs, and their definitions and properties based on the spectral index are summarized in Table 1.1, following the numerical boundaries of the spectral index presented in Greene et al. (1994).

The relative populations of YSOs are studied by the "*Cores to Disks*" (c2d) legacy survey with the *Spitzer* space telescope (Evans et al. 2009). This large sample survey allowed us to estimate the relative duration of the different YSO phases from their relative populations. While the Class 0 stage is revealed to be brief ($\sim 0.2\,\mathrm{Myr}$; Evans et al. 2009), Class I, II, and III stages have substantial durations of up to several Myrs. These pre-main-sequence star stages are divided into two subcategories based on the stellar mass or spectral types; the lower-mass stars with spectral types of F, G, K, and M refer to as T Tauri stars, while the intermediate-mass stars with spectral types of A and B are so-called Herbig stars.

This thesis focuses on the evolutionary stages from Class 0 to Class II in which a substantial amount of primordial materials remains as envelopes and disks. These stages thus provide a unique opportunity to study the initial condition and its physical and chemical evolution of the planetary system formation in detail.

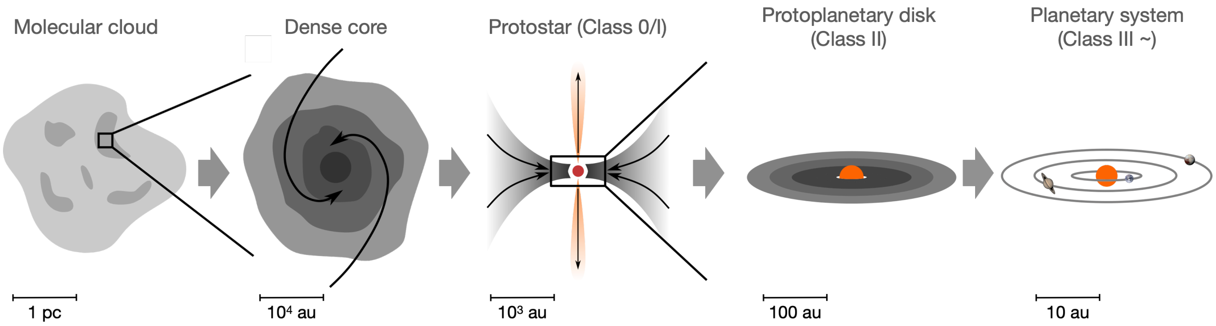

Figure 1.1. Schematic of typical star and planet formation processes.

Table 1.1 Classification of YSOs Based on Greene et al. (1994)

	SED slope	Characteristics
Class 0	undefined	No optical or near-IR emission, molecular outflows
Class I	$\alpha_{\mathrm{IR}} > 0.3$	Strong IR excesses
Flat Spectrum	$-0.3 < \alpha_{\mathrm{IR}} < 0.3$	Almost no gradient in SED slope
Class II	$-1.6 < \alpha_{\mathrm{IR}} < -0.3$	Disk and star system, no envelope
Class III	$\alpha_{\mathrm{IR}} < -1.6$	Optically thin passive disk

1.2 Chemistry in Star- and Planet-forming Regions

While the star- and planet-forming materials are composed of almost molecular hydrogen, a small amount of heavy elements, such as carbon, oxygen, and nitrogen, are also included and are the source of rich chemistry. The cold and dense environment of the molecular cloud cores kick-starts the formation molecules, and the molecular composition evolves with time as star and planet formation proceeds. Indeed, the interstellar detections of more than 200 molecular species (see McGuire 2022) indicate that a high degree of chemical complexity are already present in the ISM. The detected species include highly complex molecules, such as polycyclic aromatic hydrocarbons (PAHs; McGuire et al. 2018; Wenzel et al. 2024) and fullerene (Cami et al. 2010), as well as simple atomic ions. These interstellar molecules will eventually be incorporated into planets formed within protoplanetary disks with a significant chemical evolution during the epoch of star and planet formation. Here I briefly summarize the basic concept of the chemistry in star- and planet-forming regions that is relevant to this thesis.

1.2.1 Formation of Molecules and Its Evolution

While in the diffuse cloud phase heavy elements such as carbon, oxygen, and nitrogen are mainly in the form of atoms or atomic ions, formation of molecules significantly proceeds in the cold and dense molecular cloud due to its well-shielded nature against the ultraviolet (UV) radiation (or high visual extinction A_V). There are two main processes of molecular formation: the gas-phase reaction and grain-surface reaction, both of which play a pivotal role in the interstellar molecular evolution. The ionization by the interstellar cosmic-ray, which is the dominant ionization source in the molecular cloud, initiates the gas-phase chemistry. Ionization of molecular hydrogen ($\mathrm{H_2}$) produces $\mathrm{H_3^+}$ ions, which subsequently forms various molecules by ion-molecule reactions and neutral-neutral reactions. For instance, $\mathrm{HCO^+}$ can form via $\mathrm{H_3^+ + CO \rightarrow HCO^+ + H_2}$. The major destruction pathways of neutral molecules, such as CO, $\mathrm{H_2O}$, and HCN, are the reactions with $\mathrm{He^+}$ and the cosmic-ray-induced photodissociation. In general, the hydrogenation can proceed in the gas-phase only with the reactions with $\mathrm{H_3^+}$, and thus unsaturated molecules, such as carbon-chain molecules, are preferentially formed (e.g., Sakai & Yamamoto 2013).

On the other hand, hydrogenation plays a dominant role in forming molecules on the dust grain surface. For instance, the successive hydrogenation of CO can efficiently form H_2CO and CH_3OH (Hasegawa et al. 1992; Watanabe & Kouchi 2002; Watanabe et al. 2003);

$$\mathrm{CO} \xrightarrow{\mathrm{H}} \mathrm{HCO} \xrightarrow{\mathrm{H}} \mathrm{H_2CO} \xrightarrow{\mathrm{H}} \mathrm{CH_3O} \xrightarrow{\mathrm{H}} \mathrm{CH_3OH}. \tag{1.3}$$

Similarly, CH_4, H_2O and NH_3 are also formed via the hydrogenation of carbon, oxygen, and nitrogen atoms, respectively. The intermediate products of these hydrogenation reactions (i.e., radicals), which are also produced by the photodissociation by the cosmic-ray-induced and/or direct external UV radiation, further contribute to the formation of more complex molecules such as $HCOOCH_3$ and CH_3CHO.

Phase transitions of molecules between the solid and gas phases, namely, adsorption and desorption, also significantly affect the chemistry. For instance, depletion of CO from the gas phase (i.e., adsorption of CO) can enhance the nitrogen chemistry and deuterium chemistry (see Section 1.2.2) because CO is the main gas-phase destroyer of N_2H^+ (and N_2D^+), one of the abundant nitrogen-bearing molecules. The (thermal) desorption temperature (or frequently referred to as sublimation temperature) is defined as the temperature at which the gas-phase and ice-phase abundances of a specific molecule becomes equal. The sublimation temperature of a particular species depends on the binding energy unique to each species and the gas density, and is determined by the balance between adsorption timescale τ_{ads} and desorption timescale τ_{des} (see Furuya & Aikawa 2014),

$$\tau_{\mathrm{ads}} = \frac{1}{\pi a^2 n_{\mathrm{d}} v_{\mathrm{th}}}, \tag{1.4}$$

$$\tau_{\mathrm{des}} = \frac{1}{\nu \exp(-E_{\mathrm{bin}}/T_{\mathrm{d}})}, \tag{1.5}$$

where a is the grain radius, n_{d} is the dust density, v_{th} is the thermal velocity of the gaseous species, and T_{d} is the dust temperature. Table 1.2 lists the latest binding energies (E_{bin}) and pre-exponential factors (ν) of major species taken from Minissale et al. (2022) and the sublimation temperatures of pure ices at different gas densities calculated following the balance between Equations 1.4 and 1.5. Note that the binding energy can depends on the dust surface substrate (e.g., Minissale et al. 2022) and have distributions due to the varying potential energy depths of the adsorption sites (Furuya 2024), which substantially influence the outcome of chemistry.

The time evolution of the molecular abundance has been studied with the computational calculation of large chemical network by solving a set of rate equations for formation/destruction of molecules. As the core collapse timescale (Equation 1.1) is comparable to the typical timescale of major chemical reactions, simulating both physical and chemical evolution simultaneously is key for properly interpreting the observations (e.g., Aikawa et al. 2005). In addition, physical processes such as turbulence are also important for the protoplanetary disk chemistry, including the formation of complex organics (e.g., Furuya & Aikawa 2014; Suzuki et al. 2024), which in turn affect the composition of nascent planets.

The rate constant for each reaction is also important in modeling the chemical evolution. Some specific types of reactions have significant uncertainties in their rate constant, and thus the experimental determination of them is critical. The Kinetic Database for Astrochemistry (KIDA)[3] and the UMIST Database for Astrochemistry[4] are the two major databases that collect literature values for large numbers of reactions.

1.2.2 Isotopic Fractionation

One of the important (and relevant to this thesis) chemical processes is the isotopic fractionation in molecules. Since these fractionation processes occur only at specific physical conditions, isotopic ratios of molecules allow us to probe the formation condition and the thermal history of the molecule. Recently, the measurement of isotopic ratios in various interstellar molecules as well as exoplanets' and brown dwarfs' atmospheres has made a significant advancement owing to the sensitive observations with the Atacama Large Millimeter/submillimeter Array (ALMA) and the James Webb Space Telescope (JWST).

---

[3] `https://kida.astrochem-tools.org/`

[4] `https://umistdatabase.uk/`

Table 1.2 Sublimation Temperatures of Major Species at Different Gas Densities

Species	$E_{\rm bin}$[†] (K)	ν[†] (s^{-1})	$T_{\rm sub}$ (K)[‡]			
			$10^6\,{\rm cm}^{-3}$	$10^8\,{\rm cm}^{-3}$	$10^{10}\,{\rm cm}^{-3}$	$10^{12}\,{\rm cm}^{-3}$
H_2	371	1.98×10^{11}	7.3	8.0	8.9	10.0
H	450	1.54×10^{11}	9.0	9.9	11.0	12.4
N	806	1.17×10^{13}	14.5	14.8	17.4	19.4
N_2	1074	4.51×10^{14}	18.6	19.6	21.4	23.6
O_2	1107	5.98×10^{14}	19.1	20.0	21.9	24.2
CH_4	1232	5.43×10^{13}	21.6	23.6	25.9	28.7
CO	1390	9.14×10^{14}	23.6	25.1	27.4	30.2
O	1751	2.73×10^{13}	31.2	34.1	37.4	41.6
HCN	5344	1.63×10^{17}	82.8	89.2	96.7	105.6
NH_3	5362	1.94×10^{15}	89.6	97.2	106.1	116.8
H_2O	5705	4.96×10^{15}	93.9	101.6	110.8	121.8
CH_3OH	6621	3.18×10^{17}	101.6	109.3	118.4	129.2

[†] Taken from Table 2 in Minissale et al. (2022).

[‡] Sublimation temperature calculated for four typical values of gas densities, 10^6, 10^8, 10^{10}, and $10^{12}\,{\rm cm}^{-3}$, following Furuya & Aikawa (2014, see their Appendix A).

A exhaustive list of recent measurements for major elements are available in Nomura et al. (2023). Here I summarize the basic chemical processes of isotopic fractionation for hydrogen and carbon in star- and planet-forming regions, which is relevant to this thesis.

Hydrogen (Deuterium) Fractionation

Deuterium fractionation is not only a tracer of formation location of molecules (Ceccarelli et al. 2014) but also an evolutionary tracer in the context of star formation (Crapsi et al. 2005). The total elemental deuterium-to-hydrogen (D/H) ratio in the local ISM is 1.5×10^{-5} (Linsky et al. 2006). The fractionation is initiated by the gas-phase exchange reaction of HD with H_3^+;

$$\mathrm{H_3}^+ + \mathrm{HD} \rightleftarrows \mathrm{H_2D^+} + \mathrm{H_2} + 230\ \mathrm{K}. \tag{1.6}$$

The exothermic nature of this reaction suppresses the backward reaction in the low-temperature ($\lesssim 20\,\mathrm{K}$) condition (Millar et al. 1989; Turner 2001) and thus an efficient fractionation occurs. This H_2D^+ reacts with other molecules, such as CO and N_2, to form various deuterated molecules, such as DCO^+ and N_2D^+. The major destroyer of H_2D^+ (and N_2H^+ as well) is CO, and the deuterium fractionation is thus more efficient if CO is depleted (Roberts & Millar 2000).

The gas-phase fractionation is transferred to the grain surface via deuterium atoms that are produced by the electron recombination of protonated ions (H_2D^+, HD_2^+, and D_3^+). The elemental D abundance could be as high as that of H atoms in the region where deuterium fractionation is efficient. The D atoms adsorb onto the dust grains and form deuterated molecules, such as CH_2DOH, HDO, and NH_2D, via hydrogenation. Even multiply-deuterated species are formed in some preferential physical conditions.

Carbon Isotope Fractionation

Carbon has a rare stable isotope ^{13}C. The ^{12}C/^{13}C ratio in the local ISM is ~ 69 (Wilson 1999; Milam et al. 2005). The ^{13}C fractionation can occur via isotope exchange reactions, isotope-selective photodissociation, and potentially gas-ice partitioning. The isotope exchange reaction,

$$^{13}\mathrm{C}^+ + {}^{12}\mathrm{CO} \rightleftarrows {}^{12}\mathrm{C}^+ + {}^{13}\mathrm{CO} + 34\ \mathrm{K}, \tag{1.7}$$

can preferentially incorporate ^{13}C into CO at low temperature ($\lesssim 30\,\mathrm{K}$; Langer et al. 1984). This makes gas-phase CO ^{13}C-rich, while C^+ will be ^{13}C-poor. While the selective photodissociation of ^{13}CO against the self-shielding efficiently works only at low-density regions where UV radiation sufficiently penetrate and makes CO ^{13}C-poor, this ^{13}C-poor CO could be transported to the inner region of the molecular cloud or the midplane of the protoplanetray disks by gas dynamics such as turbulence and vertical mixing (e.g., Furuya & Aikawa 2014). The gas-ice partitioning due to the slightly higher binding energy of ^{13}CO than that of ^{12}CO is proposed as a potential mechanism by Smith et al. (2015), but given that it works only at a narrow temperature regime it is unclear that if this mechanism actually contributes to the ^{13}C fractionation of CO.

1.3 Physical and Chemical Structure of Planet-forming Regions

While the overall structure of the protostellar envelopes and protoplanetrary disks are basically determined as a consequence of the angular momentum conservation during the gravitational collapse, their detailed structures are rather complex, which in turn set the initial condition of planetary system formation and can be the origin of the physical and chemical diversity seen in exoplanetary systems. Here I provide a brief review about the detailed physical structures of protostellar envelopes and protoplanetary disks.

1.3.1 Protostellar Envelopes and Disks

The major physical components in protostellar stages (Class 0/I) are the natal envelope and the rotating disk at the central region. How, when, and where (at which spatial scales) the protostellar disks form has long been the center of the discussions in the study of low-mass star formation. Here, the protostellar disk refers to a flattened, rotationally-supported disk around protostars following the Keplerian rotation;

$$v_{\rm rot} = \sqrt{\frac{GM_\star}{r}}, \tag{1.8}$$

where $M_\star$ is the central stellar mass and r is the radius or distance from the central star. Theoretical studies suggest that the interaction with the magnetic field, including the non-ideal magnetohydrodynamical (MHD) effect, is key in efficiently removing the angular momentum and thus forming the protostellar disk in these early stages (e.g., Machida et al. 2011). It has only recently become possible with the advent of the Atacama Large Millimeter/submillimeter Array (ALMA) that the Keplerian-rotating disks around protostars are directly identified (Tobin et al. 2012; Ohashi et al. 2014; Aso et al. 2015), since high-resolution observations are required to resolve their small physical scales ($\lesssim 100$ au) and disentangle them from the envelope. Typically, spectral lines of CO isotopologues (e.g., $\rm C^{18}O$ $J = 2$–1) are used to study the gas kinematics around the protostars. One of the most plausible ways to identify the disk rotation is the analysis using position-velocity (P-V) diagram, on which the typical spin-up features indicates the rotational motion of the gaseous disk (Figure 1.2). Comparing with models and/or directly fitting a power-law function to the data points extracted from the P-V diagrams allow us to estimate the central stellar mass and disk size, which are critical parameters for disk evolution, as well as identify the Keplerian rotation ($v \propto r^{-0.5}$; Ohashi et al. 2014; Seifried et al. 2016; Aso et al. 2017; Maret et al. 2020; Sai et al. 2020).

Determination of the density structure and thus the mass of the protostellar disks (and envelopes as well) is crucial in inferring the mass reservoir for planet formation. Recent studies suggest that while the mass of Class II disks are insufficient to form a gas giant, Class 0/I disks have more gas reservoir (Manara et al. 2018; Tychoniec et al. 2020). The disk masses are basically determined by the balance between the mass infall from the envelope and the accretion toward the central star and possible planet formation within the disk. The typical mass infall rate from the envelopes is 10^{-6}–$10^{-5}\,M_\odot\,{\rm yr}^{-1}$, while the accretion rate toward the protostars are comparable or slightly smaller (e.g., Beltrán & de Wit 2016; Yen et al. 2017; Tychoniec et al. 2018; Sai et al. 2020), although it could also be episodic (i.e., time-variable; Enoch et al. 2009). The envelope-to-disk mass

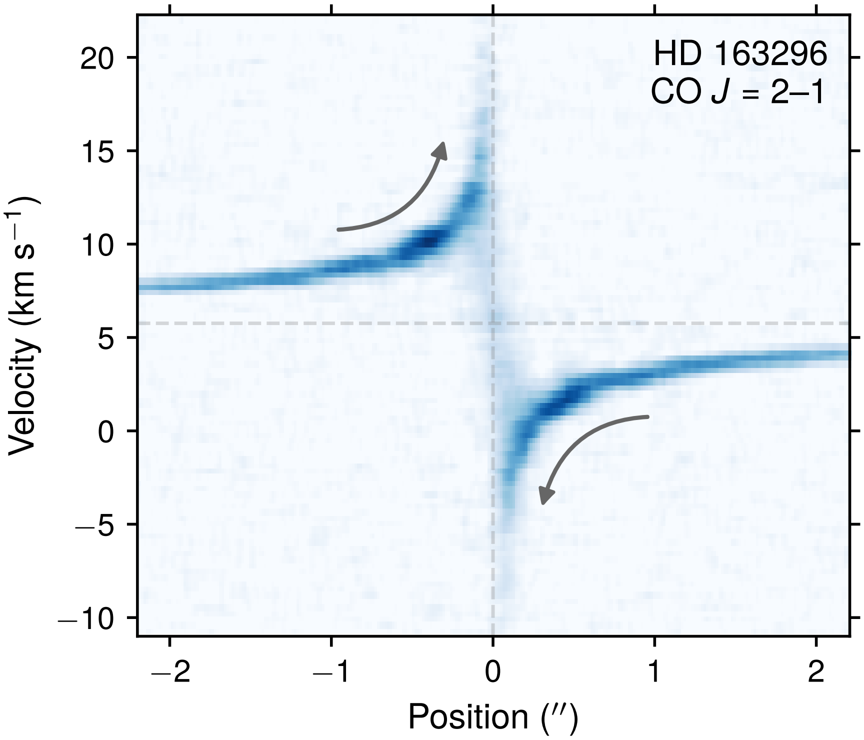

Figure 1.2. P-V diagram of the CO $J = 2$–1 emission in the HD 163296 disk. The spin-up features as guided by the black arrows are evidence of the rotating motion of the gas in an inclined disk. The horizontal gray dashed line marks the systemic velocity of the source ($\approx$ 5.76 km s^{-1}). Data were taken from the publicly-available DSHARP Data Release website (`https://almascience.eso.org/almadata/lp/DSHARP/`) and were originally published in Andrews et al. (2018b).

ratio could also be an evolutionary indicator of sources (Robitaille et al. 2006; Crapsi et al. 2008; Sheehan et al. 2020), since the younger sources are expected to have a more massive envelope and a smaller, less massive disk. Despite these importances, accurately measuring the gas mass is particularly difficult due to several observational limitations. The most frequently used, classical way to estimate the mass from the dust continuum observations are based on the basic radiative transfer theory;

$$M_{\rm dust} = \frac{F_\nu d^2}{\kappa_\nu B_\nu(T_{\rm dust})}, \tag{1.9}$$

where F_ν is the flux density, d is the distance to the source, κ_ν is the dust opacity at the observing frequency ν, and $B_\nu(T)$ is the blackbody radiation at a dust temperature $T_{\rm dust}$. The total gas mass can be obtained by factorizing $M_{\rm dust}$ by a gas-to-dust mass ratio, which is usually assumed to be 100 (Mathis et al. 1977; Bohlin et al. 1978). However, this formulation includes a number of assumptions. First, the Equation (1.9) assumes an optically thin, non-scattering emission, which is not neccesaliry valid for the inner region of the disk where materials are accumulated as suggested at least for more evolved sources (e.g., Zhu 2019). Second, the dust opacity κ_ν depends on the size distributions of the dust grains, which can be varied in the disk where dust growth is expected (e.g., Birnstiel et al. 2018; Koga et al. 2022). Third, this formulation assumes a single dust temperature, while the actual temperature distributions could have radial (and possibly vertical) gradient as discussed below. Multi-wavelength, spatially-resolved observations are likely key in resolving these degeneracies.

Temperature is another critical parameter that regulates various phenomena in protostellar environments, which directly influence several aspects of the disk evolution and planet formation. For instance, temperature determines whether the disk gas can be gravitationally unstable or not (Kratter & Lodato 2016). Gravitational instability is one of the plausible mechanisms for giant planet formation (Boss 1997; Boley 2009) and accretion outburst (Vorobyov 2009). In addition, temperature structure regulates the desorption and freeze-out of molecules. This significantly changes the radial distributions of molecular abundances and elemental abundance ratios (e.g., C/O ratio; Öberg et al. 2011), which in turn affect the composition of forming planets at different disk radii (e.g., Öberg et al. 2011; Ali-Dib 2017; Cridland et al. 2019). The temperature structure of the protostellar disks is, at the first order, determined by the protostellar heating, and a radial temperature gradient is thus naturally expected with a lower temperature at larger radii (i.e., farther from the protostar). The actual temperature distributions, particularly the radius of the desorption front (usually called as snowlines or icelines) of major volatiles like H_2O and CO, are crucial for planet formation studies. The overall conclusion from the recent high-resolution studies is that young disks around protostars are warmer compared to the Class II disks, without CO freeze-out ($\gtrsim 20\,\mathrm{K}$) but not so warm that H_2O and organic molecules sublimate ($\lesssim 100\,\mathrm{K}$; e.g., van 't Hoff et al. 2018b, 2020a,b, see Section 1.2.1). One of the way to anchor the disk temperature structure is to use the chemical tracers. For instance, HCO^+ is expected to be destroyed by the gas-phase H_2O, and is thus a potential tracer of the H_2O snowline (∼100–150 K; van 't Hoff et al. 2018a; Leemker et al.

2021). N_2H^+ is also a CO snowline tracer because N_2H^+ is destroyed by the gas-phase CO and thus a ring-like distribution of N_2H^+ is expected where the inner edge of the ring corresponds to the CO snowline (e.g., Qi et al. 2013).

Outside of the protostellar disks, the natal envelopes still remain in these stages, which are basically described by combination of the infalling and rotating motions (e.g., Ulrich 1976; Cassen & Moosman 1981; Terebey et al. 1984; Sakai et al. 2014; Mori et al. 2024). The boundary between the envelope and disk is called as centrifugal radius or centrifugal barrier, at which drastic changes in chemistry sometimes happens as well (e.g., Sakai et al. 2014; Oya et al. 2016). The centrifugal radius is typically located at a few 10s of au to a few 100s of au radius, depending on the specific physical condition and evolutionary stages.

The density and temperature structure in protostellar envelopes have also long been a subject to study. While they are usually assumed to follow the power-law distributions based on the classic spherically symmetric core collapsing models (Larson 1969; Penston 1969; Shu 1977) and the single-dish observations (e.g., Ward-Thompson et al. 1999; Motte & André 2001), the physical and chemical structures in the inner region of the envelopes ($\lesssim$ a few 100s of au) are rather complex and thus we have to rely on the spatially resolved observations of specific molecular line tracers. For instance, SO and CH_3OH are well-known weak shock tracer (Aota et al. 2015; Miura et al. 2017; van Gelder et al. 2021), and thus they trace the temperature enhancement at e.g., disk-envelope interface or centrifugal radius (e.g., Ohashi et al. 2014; Sakai et al. 2014; Oya et al. 2016). Icy molecules, such as water and complex organic molecules (COMs), are the tracer of the warm ($\gtrsim 100\,\mathrm{K}$) region in the inner (typicaly $\lesssim 100\,\mathrm{au}$) envelope (e.g., Oya et al. 2016, 2018), which are originally recognized as "hot corino" activity based on the single-dish detection of COMs (e.g., Cazaux et al. 2003). The hot corino sources are also a unique laboratory to study the composition and its evolution of the icy molecules because large fractions of ice mantles have sublimated in the inner ($\lesssim 100\,\mathrm{au}$) warm ($\gtrsim 100\,\mathrm{K}$) regions and are subject to the subsequent warm gas-phase chemistry (see review by Jørgensen et al. 2020). Single-dish and interferometric observations have detected highly complex molecules including the pre-biotic ones (Jørgensen et al. 2012), as well as simple, abundant icy molecules such as H_2O and CH_3OH (e.g., Persson et al. 2013). The determination of "what molecular lines traces what physical components" are crucial in unveiling the protostellar environments, and is the main focus of the spatially resolved observational studies with ALMA (Tychoniec et al. 2021).

1.3.2 Protoplanetary Disk

Protoplanetary (Class II) disks are more isolated systems compared to the protostellar systems, and their physical structures, including both radial and vertical structures, are thus relatively well-constrained (Figure 1.3). Protoplanetary disks are composed of gas and dust, whose contributions to the mass budgets are roughly $\sim 99\%$ and $\sim 1\%$, respectively. Dust grains are tends to be more settled down to the midplane, while the gas distributions more spread vertically. The typical size of dust disk is $\sim$ 10–100 au (e.g., Tripathi et al. 2017; Andrews et al. 2018a), while gas disk size, as traced by the CO emission, is usually larger ($\sim$100–500 au; e.g., Ansdell et al. 2018; Long et al. 2018). Similar to the case of protostellar disks, the disk mass estimates suffer from a number of uncertainties, such as dust opacity, CO/H_2 ratio, and dust-to-gas mass ratio (see e.g., Miotello et al. 2023), while recent studies suggest other potentially reliable tracers, such as the HD line emission (Bergin et al. 2013; McClure et al. 2016), combination of CO and N_2H^+ line emission (Trapman et al. 2022), disks' self-gravity (Rosenfeld et al. 2013), and CO line wing broadened by the gas pressure (Yoshida et al. 2022b).

The disk thermal structure predominantly regulates both physics and chemistry within protoplanetary disks, as temperature directly affects various physical phenomena via the sound speed $c_\mathrm{s} = \sqrt{k_\mathrm{B}T/\mu m_\mathrm{H}}$ as well as chemistry by controlling the excitation condition and phase transition (i.e., solid phase to gas phase and vice versa) of molecules. The disk temperature structure shows a radial gradient with decreasing temperature toward the larger radii. Most of the disk region, except for the innermost a few au where the accretion heating could be efficient, is dominated by the stellar irradiation and thus a vertical temperature gradient with decreasing temperature toward the midplane exists as well (i.e., passive disk; Chiang & Goldreich 1997; D'Alessio et al. 1998). Both dust and

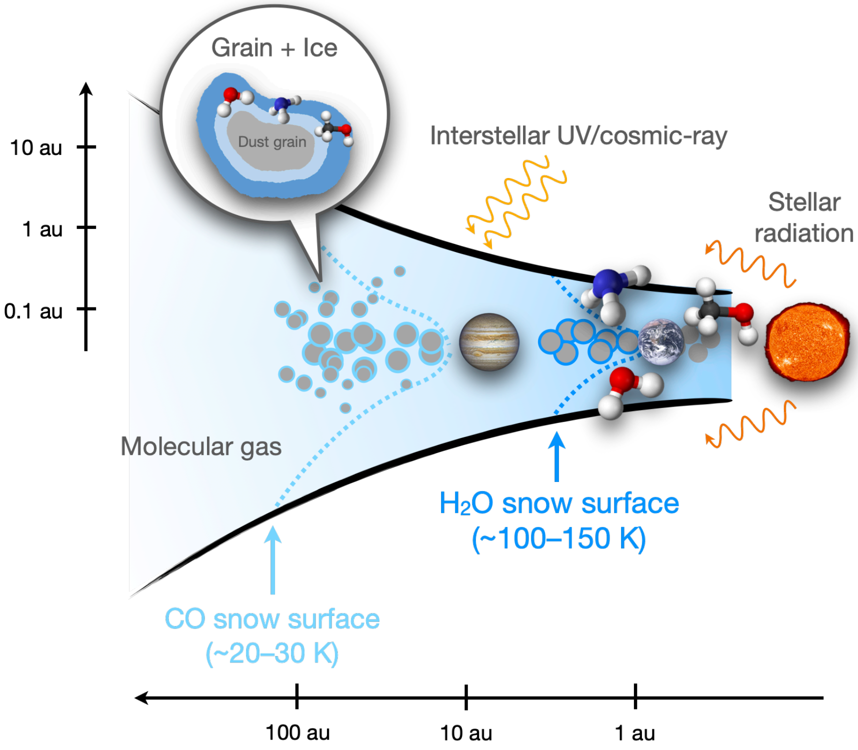

Figure 1.3. Schematic of typical protoplanetary disk structures. The H_2O and CO snow surfaces are marked by the dashed lines. The typical spatial scales along the radial and vertical directions are indicated.

gas temperatures are well coupled in most of the disk region except for the upper disk atmosphere, where density is relatively low and the gas-dust collision not so frequent for thermalization.

The disk thermal structure also sets both radial and vertical chemical structure. The temperature gradient at the disk midplane results in a sequential desorption/freeze-out of different molecules, i.e., a series of snowlines of major volatiles, such as H_2O, CO_2, CO, and N_2 (see Figure 1.3). This sequential phase transition of the major C, N, and O carriers significantly modifies the elemental content of solids and gas (e.g., C/O and N/O ratio; Öberg et al. 2011; Öberg & Wordsworth 2019). In particular, the water snowline divides the disk into two distinct region—the inner dry, terrestrial planet-forming zone and the outer gas-rich, giant planet-forming zone. Inside the water snowline, almost all volatile species, including organic molecules, have sublimated, and are thus in principle observable as molecular line emission, although it is practically challenging to observe inside the water snowline around typical T Tauri and Herbig stars due to its small expected angular size (only a few au or $\lesssim 0\farcs1$ at 100 pc; e.g., Notsu et al. 2016, 2017).

The concept of snowline can be applied to the vertical direction due to the vertical temperature gradient, resulting in an isothermal contour "snow-surface" for each molecular species. The sequential desorption of molecules in vertical direction triggers a rich gas-phase chemistry. In the outer region ($\gtrsim$ a few au), the vertical structure can be divided into three distinct regions, the hot disk atmosphere, the warm molecular layer, and the cold midplane. In the cold midplane ($\lesssim 20\,\mathrm{K}$), a substantial fraction of molecules are frozen-out onto the dust grains, which is the dominant ice reservoir in a disk. The warm molecular layer, as originally proposed by Aikawa et al. (2002), are the site of active gas-phase chemistry to form CO, HCN, H_2CO and so on due to the lukewarm temperature (a few 10s of K) and sufficient density ($\gtrsim 10^6\,\mathrm{cm}^{-3}$), while the hot atmosphere are usually treated as a photodissociation region (PDR; e.g., Hollenbach & Tielens 1999) in which molecules are dissociated by the (inter)stellar radiations and an active photochemistry occurs to produce molecules like C_2H and CN (e.g., Aikawa et al. 2002; Bergin et al. 2016; Teague & Loomis 2020). It is only recently that directly resolving the disk vertical structure with ALMA has become possible by observing edge-on or mid-inclination disks (e.g., Law et al. 2021b; Paneque-Carreño et al. 2023; Law et al. 2023b).

The vertical structure of the innermost region ($\lesssim$ a few au) are not well-constrained. In contrast to the outer region where irradiation dominates, the midplane could be warmer than the disk surface due to the viscous accretion heating. This trend is observed in younger disks around Class 0/I protostars (Takakuwa et al. 2024).

1.3.3 Protostellar Accretion Burst As a Unique Probe of the Disk Ice Reservoir

As mentioned in Section 1.3.2, while protoplanetary disks have a substantial amount of ice reservoirs in the cold disk midplane, it is challenging to probe the bulk ice composition as the major fraction of icy molecules are hidden on the dust mantles. They are released into the gas phase inside the snowline, only at inner a few au in the disk around typical T Tauri stars (e.g., Nomura et al. 2009; Walsh et al. 2014). While the James Webb Space Telescope (JWST) can directly probe the disk ice composition through the infrared absorption spectroscopy (e.g., Sturm et al. 2023), ice band profiles are usually broad and very complex, which hampers accurate estimates of the baseline. Moreover, identification of less abundant species are challenging due to the limited sensitivity and the band overlaps, and ice composition estimates are highly sensitive to the assumption of various ice mixtures.

An alternative way to observe icy molecules is to make use of the protostellar accretion burst. Some fraction of low-mass protostars shows time variation in their luminosities, as revealed by the monitoring observations with e.g., the James Clark Maxwell Telescope (JCMT; e.g., Herczeg et al. 2017). These luminosity variations are likely due to the episodic nature of disk accretion, which is classified into different types of the accretion bursts based on the magnitude and duration timescale (see review by Fischer et al. 2023). Among them, FU Ori outburst shows luminosity increase by orders of magnitude (i.e., $L_{\rm bol} \gtrsim 100\,L_\odot$) and lasts for orders of $\sim$ 100 yr. The disk around the FU Ori-type outbursting stars are ideal target to probe the sublimated icy molecules, such as water and complex organics, because snowlines are shifted outward due to the temporal high luminosity and the sublimation region is thus significantly larger than the typical disks in quiescent phase. Furthermore, the typical outburst timescale is shorter than that of the gas-phase chemical reactions, allowing us to probe the ice composition with minimum gas-phase chemical changes. While several sources of FU Ori-type outbursting stars have been studied at (sub-)millimeter wavelengths (Cieza et al. 2018; Calahan et al. 2024), the most well-studied source is the Class I/II source V883 Ori, which hosts a clear Keplerian-rotating disk (Cieza et al. 2016) and where the water snowline has been imaged for the first time in a protoplanetary disk (Cieza et al. 2016; Tobin et al. 2023). Several COMs have also been detected with rich millimeter spectra similar to the hot corino sources, indicating the ice sublimation (van 't Hoff et al. 2018b; Lee et al. 2019; Jeong et al. 2025).

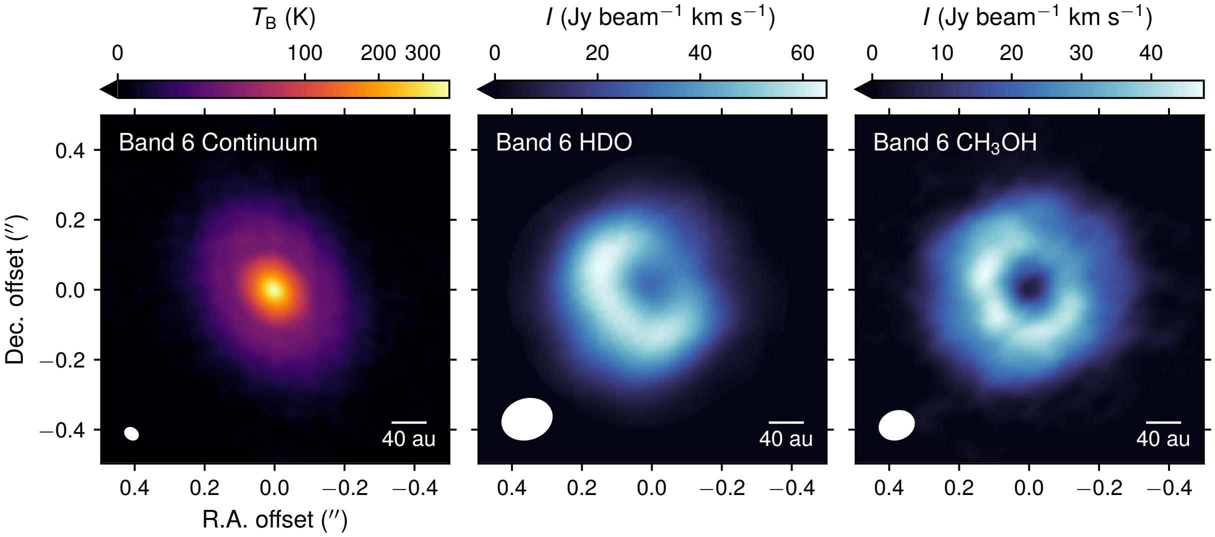

Figure 1.4. Maps of the V883 Ori disk in ALMA Band 6 dust continuum emission (left), HDO line emission (middle), and CH_3OH line emission (right). The ellipse at the lower left corner of each panel show the beam size, while a 40 au scale bar is placed at the lower right corner of each panel. The color scale of the dust continuum image is stretched by the arcsinh function. Data for the dust continuum image are taken from the ALMA Science Archive (project code: 2015.1.00350.S). Data for the HDO and CH_3OH images are originally published in Tobin et al. (2023) and are taken from the Harvard Dataverse repository (`https://doi.org/10.7910/DVN/MDQJEU`).

1.4 Interferometric Observations with ALMA and VLA

1.4.1 Disk Substructure

With a large number of antennas (66) and the long-baseline capabilities up to 16 km, ALMA have afforded unprecedentedly high angular resolution (sub-0.″1 scale) observations with high sensitivity. The high angular resolution observations have enabled us to directly observe the internal small-scale structures of protoplanetary disks, as first demonstrated by its 2014 Long Baseline Campaign that revealed the multi-ringed dust disk around HL Tau (ALMA Partnership et al. 2015). The disk substructure, such as rings, gaps and spirals, in dust continuum are now routinely observed in different star-forming regions (e.g., Long et al. 2018; Cieza et al. 2019; Huang et al. 2024), a large fraction of which are obtained by the Disk Substructures at High Angular Resolution Project (DSHARP)

ALMA Large Program (Andrews et al. 2018b) that anchored the ubiquity and diversity of the disk substructure. Moreover, high-spatial-resolution ($\sim 0\farcs1$) molecular line observations have shown that different molecules in disks also show rich substructures in both radially and vertically (e.g., Law et al. 2021a,b; Paneque-Carreño et al. 2023), as originally revealed by the Molecules with ALMA at Planet-forming Scales (MAPS) ALMA Large Program (Öberg et al. 2021). The MAPS Large Program, which I was also involved in as a co-I, have observed a large set of molecular emission lines with different excitation properties, allowing us to directly reveal the radial and vertical variations of chemistry as well, including the gas elemental composition (e.g., Bosman et al. 2021a), ionization property (Aikawa et al. 2021, incl. Y. Yamato as third author), and isotopic chemistry (Cataldi et al. 2021, incl. Y. Yamato as second author).

The disk substructure studies with high angular resolution observations are now extended to the earlier evolutionary stages, i.e., Class 0/I disks, motivated by the studies suggesting the early planet formation (Manara et al. 2018; Tychoniec et al. 2020). Prior to this thesis, there are only a few observations that report the substructures, such as rings and gaps, in Class 0/I protostellar disks (e.g., Sheehan & Eisner 2017, 2018; Sheehan et al. 2020; Segura-Cox et al. 2020). The Early Planet Formation in Embedded Disks (eDisk) ALMA Large Program, which I was involved in as a co-I, conducted the first-ever large survey on the substructures in 19 Class 0/I disks at $\sim 7\,$au resolution (Ohashi et al. 2023). They found less annular substructures particularly in Class 0 disks in contrast to the more evolved Class II disks, while there are notable asymmetric intensity distributions along the minor axis of the inclined disks—this is interpreted as an outcome of the optically thick emission from the flared dust grains (e.g., Kido et al. 2023; Santamaría-Miranda et al. 2024; Lin et al. 2023; Takakuwa et al. 2024), suggesting that the dust grains in Class 0 disks are not yet settled to the midplane in contrast to the Class II disks in which the dust grains are mostly settled (Villenave et al. 2020, 2022; Doi & Kataoka 2021). Figure 1.5 compares a few examples of the high-resolution dust continuum images of Class 0/I and Class II disks taken in ALMA Band 6 by the eDisk and DSHARP Large Program, highlighting a distinct difference in disk substructure along the evolutionary sequence. However, prior to this thesis, it is unclear when exactly the substructure formation and thus planet formation start due to the lack of detections of substructures in the Class I stage.

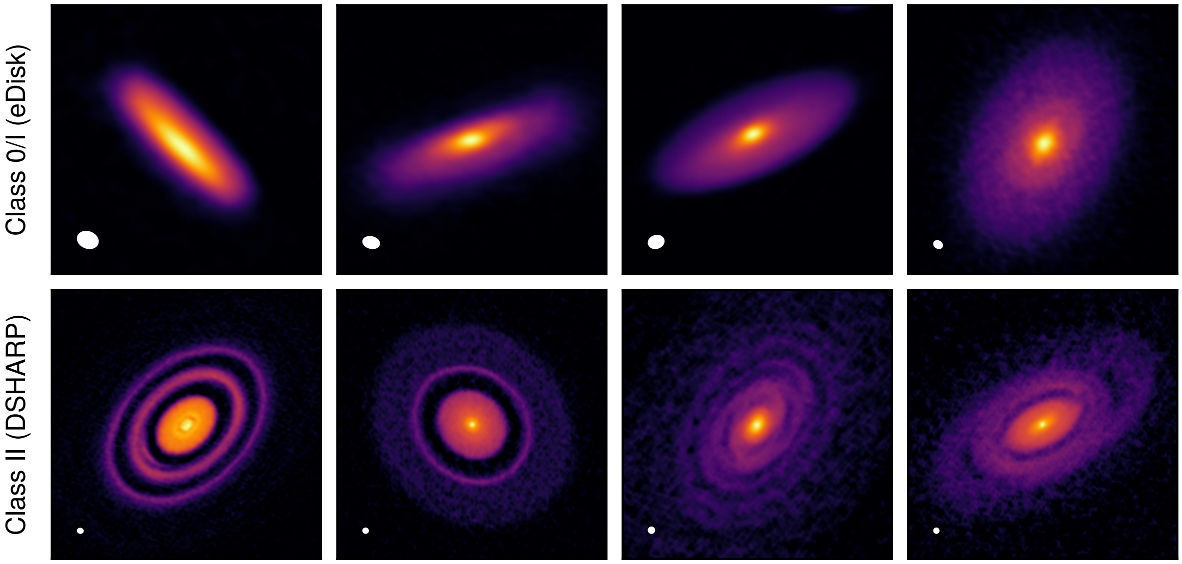

Figure 1.5. Compilation of the dust continuum images of the representative Class 0/I/II disks taken by the eDisk (Class 0/I; top row) and DSHARP (Class II; bottom row) ALMA Large Program, highlighting the less-structured nature of the younger Class 0/I disks compared to the older Class II disks. The beam size of each image (typically $\sim 0\farcs05$) is shown in the lower left corner of each panel. Note that the images are not scaled. Data for the Class 0/I disks (top row) were provided by the eDisk collaboration and originally published in Ohashi et al. (2023). Data for the Class II disks (bottom row) were taken from the publicly-available DSHARP Data Release website (`https://almascience.eso.org/almadata/lp/DSHARP/`) and originally published in Andrews et al. (2018b).

1.4.2 Chemistry at Envelope/Disk Scales

ALMA's high sensitivity, wide instantaneous bandwidth, and high spectral resolving power have also enabled uniform spectral line surveys to study the molecular composition at envelope/disk scales. The ALMA Protostellar Interferometric Line Survey (PILS) is first to conduct such line surveys toward the well-known hot corino source IRAS 16293-2422 at $0\farcs5$ resolution down to 4–5 mJy beam^{-1} with 0.2 km s^{-1} velocity resolution (Jørgensen et al. 2016), which detected a tremendous number (more than 10,000) of spectral lines mainly assigned to COMs and their isotopologues, including pre-biotic molecules such as glycolaldehyde and ethylene glycol (see also Jørgensen et al. 2012). The available large number of transitions for a particular molecular species with different excitation properties allows us to accurately estimate the gas excitation condition, the column density of the molecule, isotopic ratios, and the molecular abundance ratio relative to H_2 gas column density or a specific reference molecule[5] if the amount of H_2 gas is difficult to estimate. Similar line survey studies have been conducted toward outbursting stars, which similarly detected a large number of molecular lines mostly originated from sublimated COMs, such as CH_3OH, CH_3OCHO, and CH_3CHO (e.g., Lee et al. 2019; Jeong et al. 2025; Calahan et al. 2024)

The icy sublimates, including COMs, have recently been detected in a few Class II protoplanetary disks as well. Booth et al. (2021b) reported the detection of CH_3OH emission originated from the sublimation of the inherited ice reservoir in the HD 100546 disk, followed by the detections of COMs, including more complex species such as CH_3OCH_3 and $c{-}H_2COCH_2$, in other a few disks (e.g., van der Marel et al. 2021; Brunken et al. 2022; Booth et al. 2023b, 2024b). Oxygenated species, such as SO, SO_2, NO, and their isotopologues, are also detected (Booth et al. 2021b, 2024a,b). The disks showing these icy sublimates are all transition disks with a large central cavity around Herbig Ae/Be stars, which allows the direct irradiation of the cavity edge that get ices sublimated. However, no detections of icy sublimates have been reported in non-transitional, full disks, and thus the general inner disk chemistry of protoplanetary disks remains poorly understood.

In recent years, in addition to (sub-)millimeter observations with ALMA, the importance of lower frequency observations has begun to be recognized. The (sub-)mm spectral line observations are generally not able to explore the innermost region of the envelopes/disks where the bulk of the material resides due to the highly optically thick dust continuum that obscure the molecular line emission. One of the most prominent example is the V883 Ori disk as shown in Figure 1.4, where a notable inner emission hole is seen in the molecular line maps with a clear spatial coincidence with the bright dust continuum core (Cieza et al. 2016; Tobin et al. 2023). A similar situation happened in a protostel-

---

[5] CH_3OH is one of the parent molecules of other COMs and thus frequently used as a reference.

lar envelope, where López-Sepulcre et al. (2017) identified an absence of molecular line emission at submillimeter with ALMA, while De Simone et al. (2020) detected CH_3OH emission toward the same source at a similar spatial scale with the VLA observations at ~ 23 GHz (or $\sim$1.3 cm). This demonstrates the unique capability of the lower frequency observations to avoid the effect of the optically thick dust continuum emission. Another unique capability of VLA is to observe a number of suitable NH_3 transitions at $\sim$ 23–25 GHz, while there are no observable NH_3 transitions in the ALMA frequency coverage. Due to this, NH_3 observations and thus the nitrogen chemistry in planet-forming regions remain as an unexplored area.

1.5 Thesis Outline

This thesis leverages the interferometric observations at (sub-)millimeter to centimeter wavelengths with ALMA and VLA to unveil the physical and chemical conditions of the disk-forming regions and protoplanetary disks, the parent bodies of planetary system. Specifically, I aim to (1) characterize the physical and chemical structures of a young disk with high spatial resolution observations with ALMA, (2) demonstrate the NH_3 molecular line observations with VLA to study the nitrogen chemistry, and (3) investigate the complex organic chemistry in protoplanetary disks by focusing on disks around an FU Ori-type outbursting star and a warm Herbig Ae star. These studies mainly focus on the icy molecules, which are primary building blocks of planetary bodies. While the composition of gaseous molecules can easily be modified during the epoch of star and planet formation and only a small portion of them is incorporated into planets as the disk gas will eventually dissipate to form planetary systems, icy molecules better imprint the chemical history from the ISM and will determine the initial composition of planets. Through these studies, I therefore aim to provide implications on whether the ISM is inherited to the planetary systems, or its chemical composition is modified during the structural evolution. I also aim to offer a future direction toward a better understanding of the origin of solar system materials and putting them into a broader context of the diverse characteristics of exoplanetary systems.

Chapter 2 presents high-spatial-resolution ALMA observations of the disk around the Class I protostar L1489 IRS as part of the eDisk ALMA Large Program, which observed 19 Class 0/I disks to investigate the disk substructure formation in these early evolutionary phases. L1489 IRS is a well-studied, typical Class I protostar, and thus a ideal source to study the planet formation in Class I phase and anchor when substrcture and thus planet formation start. I use the dust continuum observations at ALMA Band 6 (1.3 mm) as well as a suit of molecular lines to characterize the physical and chemical structure of the disk.

Chapter 3 is one of the first studies that present the NH_3 molecular line observations with VLA at the scales of disk-forming regions. The target source, NGC 1333 IRAS 4A, is a prototypical Class 0 binary system with hot corino chemistry, where interstellar ices have sublimated in the vicinity of the protostars. I detect the molecular line emission of NH_3 and its deuterated isotopologues, NH_2D, and use the NH_2D/NH_3 abundance ratio to examine the D/H ratios of ammonia ices and probe the nitrogen chemistry in the parent star-forming core.

Chapter 4 focuses on the disk around the FU Ori-type outbursting star V883 Ori to study the complex organic chemistry in protoplanetary disks. I use the ALMA observations at Band 3 (~ 3 mm), the lowest frequency band available with ALMA at that time, to investigate whether Band 3 observations can be used to probe the inner molecular gas content that is hidden by the optically thick dust continuum in Band 6/7. I detect several species of COMs, including multiple newly-detected species, demonstrating the sublimation of icy molecules within the disk. A line profile analysis reveals that the molecular line emission in the inner region is still hidden by the continuum even in Band 3, requesting the observations at further longer wavelengths with ALMA Band 1 and/or VLA. I also find high relative abundances and anomalous isotopic ratios of COMs, suggesting an efficient formation of COMs in the disk.

Chapter 5 extends the COM chemistry study to Class II disk in quiescent phase (i.e., non-outbursting star). By focusing on the warm disk around the Herbig Ae star MWC 480, I serendipitously detect dimethyl ether (CH_3OCH_3) and tentatively (CH_3OCHO), while CH_3OH, the most abundant COM in the ISM, are not detected. The CH_3OCH_3 column density ratio relative to CH_3OH is substantially higher than the values in protostars and Class II COM-rich transition disks, implying that the COMs in the full disk may experience substantial chemical reprocessing owing to the strong stellar radiation and/or the high density in the innermost region.

Chapter 2

The Ringed and Warped Structure of the Disk around the Class I Protostar L1489 IRS

This thesis chapter originally appeared in the literature as Yoshihide Yamato, Yuri Aikawa, Nagayoshi Ohashi, John J. Tobin, Jes K. Jørgensen, Shigehisa Takakuwa, Yusuke Aso, Jinshi Sai (Insa Choi), Christian Flores, Itziar de Gregorio-Monsalvo, Shingo Hirano, Ilseung Han, Miyu Kido, Patrick M. Koch, Woojin Kwon, Shih-Ping Lai, Chang Won Lee, Jeong-Eun Lee, Zhi-Yun Li, Zhe-Yu Daniel Lin, Leslie W. Looney, Shoji Mori, Suchitra Narayanan, Nguyen Thi Phuong, Kazuya Saigo, Alejandro Santamaría-Miranda, Rajeeb Sharma, Travis J. Thieme, Kengo Tomida, Merel L. R. van't Hoff, & Hsi-Wei Yen, *The Astrophysical Journal*, 2023, Vol. 951, id. 11. *I led the data reduction, analysis, and discussion, while data acquisition were made by N. Ohashi, the PI of the eDisk Large Program.*

Abstract

Constraining the physical and chemical structure of young embedded disks is crucial to understanding the earliest stages of planet formation. As part of the Early Planet Formation in Embedded Disks Atacama Large Millimeter/submillimeter Array Large Program, we present high spatial resolution ($\sim 0\farcs1$ or $\sim$15 au) observations of the 1.3 mm continuum and ^{13}CO J = 2–1, C^{18}O J = 2–1, and SO $J_N = 6_5$–5_4 molecular lines toward the disk around the Class I protostar L1489 IRS. The continuum emission shows a ring-like structure at 56 au from the central protostar and a tenuous, optically thin emission extending beyond $\sim$300 au. The ^{13}CO emission traces the warm disk surface, while the C^{18}O emission originates from near the disk midplane. The coincidence of the radial emission peak of C^{18}O with the dust ring may indicate a gap-ring structure in the gaseous disk as well. The SO emission shows a highly complex distribution, including a compact, prominent component at $\lesssim$ 30 au, which is likely to originate from thermally sublimated SO molecules. The compact SO emission also shows a velocity gradient along a slightly ($\sim$ 15°) tilted direction with respect to the major axis of the dust disk, which we interpret as an inner warped disk in addition to the warp around $\sim$200 au suggested by previous work. These warped structures may be formed by a planet or companion with an inclined orbit, or by a gradual change in the angular momentum axis during gas infall.

2.1 Introduction

Circumstellar disks are the birthplaces of planets. Constraining the structure of disks is thus essential for understanding the processes of planetary system formation. The physical and chemical structure of Class II disks has been studied in great detail through dust continuum and molecular line observations with the Atacama Large Millimeter/submillimeter Array (ALMA) (e.g., Andrews et al. 2018b; Öberg et al. 2021). These studies have revealed that substructures such as rings and gaps are present in both dust and gas, suggesting that planet formation is ongoing in Class II disks. Furthermore, the presence of formed planets has recently become more apparent through the detection of velocity kinks in channel maps of bright molecular line emission (e.g., Pinte et al. 2018b; Teague et al. 2019), in addition to direct detections of circumplanetary disks within gaps (e.g., Keppler et al. 2018; Benisty et al. 2021; Bae et al. 2022).

The presence of substructures and planets in Class II disks suggests that planet formation could have started in the earlier evolutionary stages. It is thus essential to study what is happening in disks around younger Class 0/I protostars in order to obtain a complete picture of planet formation processes. Recent ALMA observations have revealed substructures in dust continuum emission in a handful of Class 0/I disks (e.g., ALMA Partnership et al. 2015; Sheehan & Eisner 2018; Sheehan et al. 2020; Segura-Cox et al. 2020), suggesting that the first steps toward planet formation may be ocurring while these young disks are still embedded in their natal envelopes. Grain growth has also been suggested in embedded young disks (e.g., Harsono et al. 2018). In addition, recent surveys have shown that the mass of Class II disks is insufficient for giant planets to be formed, while Class 0/I disks are massive enough (e.g., Tychoniec et al. 2021).

Motivated by these previous studies, the Early Planet Formation in Embedded Disks (eDisk) ALMA Large Program (Ohashi et al. 2023) was initiated with the main goal of understanding how early substructures form in the disks around young protostars. The core of eDisk is a high-resolution systematic survey of the dust continuum substructures down to ~ 5 au scales in 19 young embedded sources. In addition to the dust continuum, several molecular lines, mainly CO isotopologue lines, have been observed to probe the gas distributions and kinematics in the embedded disks as well as in the envelopes.

One of the sources of the eDisk sample is the Class I protostar L1489 IRS (or IRAS 04016+2610), located in the Taurus molecular cloud. While several recent studies assume $\sim$140 pc as the distance to L1489 IRS (e.g., Sai et al. 2022; Mercimek et al. 2022) based on the average distance over the Taurus region (141±7 pc; Zucker et al. 2019), Roccatagliata et al. (2020) estimate the distances to six different stellar population groups in the Taurus region using Gaia measurements. One of the groups (Taurus F in the original paper) with an estimated distance of 146 pc includes a nearby source to L1489 IRS (with a separation of $\sim 12'$). Thus, in the present work we assume that the distance to L1489 IRS is 146 pc[1]. Taking into account this distance, as well as the updated photometry from near-infrared to millimeter wavelengths, the bolometric luminosity and bolometric temperature are 3.4 $L_\odot$ and 213 K, respectively (Ohashi et al. 2023), from which L1489 IRS is classified as a Class I source.

L1489 IRS is embedded in a ∼2000 au scale infalling-rotating envelope as revealed by single-dish observations (Hogerheijde & Sandell 2000; Motte & André 2001). A bipolar outflow along the northwest-southeast direction is also identified by infrared and submillimeter line observations (Tamura et al. 1991; Hogerheijde et al. 1998). Brinch et al. (2007) first detected a rotation signature at ∼200–300 au scale using $\sim 1''$ resolution HCO$^+$ line observations with the Submillimeter Array (SMA), which was interpreted as a Keplerian disk. ALMA observations of ^{12}CO and C^{18}O ($J = 2$–1) lines confirmed the presence of a Keplerian disk with a radius of ∼600–700 au and a central stellar mass of 1.6 $M_\odot$ (Yen et al. 2014). Yen et al. (2014) also detected a streamer-like infalling flow feeding the material to the central protostellar disk with the C^{18}O $J = 2$–1 emission. Higher-resolution ($\sim 0\farcs3$) C^{18}O line observations with ALMA revealed that the disk is warped at the boundary ($r \sim 200$ au) between the inner and outer disks (Sai et al. 2020). Dust continuum images obtained with ALMA (Yen et al. 2014; Sai et al. 2020) and the Combined Array for Research in Millimeter-wave Astronomy (carma; Sheehan & Eisner 2017) also show a disk-like structure elongated along the northeast-southwest direction. Furthermore, Ohashi et al. (2022a) tentatively detect a ring-like structure at $r \sim 90$ au in the 1.3 mm dust continuum emission, which may be a hint of dust growth, or even planet formation.

In this chapter, we present high spatial resolution ($\sim 0\farcs1$) observations of dust continuum and molecular lines toward the embedded disk around L1489 IRS as part of the eDisk ALMA Large Program. This chapter is structured as follows. We describe the observational details in Section 2.2, and the observational results (image maps and radial profiles) in Section 2.3. Section 2.4 presents the analysis of the dust continuum and CO

---

[1] We note that there is an independent estimate of the distance toward a neighboring molecular cloud L1498 of 129 pc (Zucker et al. 2020), which is significantly different from 146 pc adopted here.

isotopologue line data to constrain the physical structures of the disk. The results are discussed in 2.5, and finally summarized in Section 2.6.

2.2 Observations and Data Reduction

L1489 IRS was observed as part of the eDisk Large Program (project code: 2019.1.00261.L, PI: N. Ohashi) and a dedicated Director's Discretionary Time (DDT) program (project code: 2019.A.00034.S, PI: J. J. Tobin). Details of the observations and data reduction procedures are provided in Ohashi et al. (2023). Here we summarize the key aspects specific to L1489 IRS. Our observations were made in a total of five executions, two of which used extended antenna configurations (C43-8) from the Large Program, and the other three used compact antenna configurations (C43-5) from the DDT program. The two executions with extended antenna configurations were conducted in 2021 August, while the three executions with compact antenna configurations in the DDT program were conducted in 2021 December and 2022 July.

The eDisk program is designed to observe the dust continuum at 1.3 mm (or 225 GHz), as well as several molecular lines. The targeted molecular lines are listed in Table 2 of Ohashi et al. (2023). In this specific first-look paper on L1489 IRS, we focused on three molecular lines: ^{13}CO $J = 2$–1, C^{18}O $J = 2$–1, and SO $J_N = 6_5$–5_4. In addition to these lines, several other lines (^{12}CO, DCN, H_2CO, and c-C_3H_2) are also detected, while SiO and CH_3OH lines are not detected (see Table 2 in Ohashi et al. (2023) for the complete list of the targeted transitions).

The initial calibration was performed by the ALMA observatory using the standard ALMA calibration pipeline version 2021.2.0.128. We then carried out self-calibration using Common Astronomy Software Applications (CASA) version 6.2.1 (CASA Team et al. 2022). Prior to self-calibration, we imaged the continuum data of each execution block separately. We then found an emission peak on each image and aligned the peaks to a common phase center using the CASA task `fixvis` and `fixplanets`. For the aligned visibilities, we applied an amplitude rescaling by inspecting the azimuthally averaged visibilities (amplitude profile against baseline length) from different executions to correct for possible flux calibration uncertainties (see Ohashi et al. 2023).

We then performed four iterations of phase-only self-calibration and then two iterations of phase and amplitude self-calibration on the compact configuration continuum data. The data were then combined with the extended configuration data and self-calibrated together. For the combined data, we performed two iterations of phase-only self-calibration and no phase+amplitude self-calibration. The self-calibration solutions were then applied to the line data. Finally, the line data were continuum-subtracted using the CASA task `uvcontsub` in the visibility domain.

For the continuum data, we CLEANed down to 2× the RMS noise level using different Briggs robust parameters as shown in Appendix A. The `auto-multithresh` algorithm implemented in CASA was used to generate the CLEAN masks. We adopted the image with `robust` = 1.0 as the representative image considering the balance between spatial resolution and sensitivity. The resulting beam size and RMS noise level of the continuum image are $0''.105 \times 0''.078$ (PA = 12°) and $14\,\mu\mathrm{Jy\,beam^{-1}}$, respectively (Table 2.1). We note that the beam size of the representative image is a factor of ≈2 larger than the typical spatial resolution of other eDisk continuum images ($\approx 0''.05$); because the continuum emission of the L1489 IRS disk is faint, we need to trade off spatial resolution for better sensitivity. Additionally, to clearly show the extended, faint emission, we made another continuum image with `robust` = 2.0 and `uvtaper` = $1000\,\mathrm{k}\lambda$, which has a beam size and RMS noise level are $0''.221 \times 0''.179$ (PA = 11°) and $18\,\mu\mathrm{Jy\,beam^{-1}}$, respectively (Table 2.1). For the line data, we CLEANed down to 3× the RMS noise level with `robust` = 1.0 (and `uvtaper` = $2000\,\mathrm{k}\lambda$ as the default imaging parameter of eDisk line images, see Ohashi et al. 2023) for all lines presented in this paper. As in the case of continuum imaging, the `auto-multithresh` algorithm implemented in CASA was used to generate the CLEAN masks. The typical beam size and RMS noise level of the line images are $0''.1$ and 2 $\mathrm{mJy\,beam^{-1}}$ at a velocity channel width of 0.2 $\mathrm{km\,s^{-1}}$, respectively. We assume an absolute flux calibration uncertainty of 10%. The maximum recoverable scale is $\sim 2''.4$ [2]. The detailed properties of the continuum image and line image cubes, as well as the

---

[2] Based on the Equation 7.7 in https://almascience.nao.ac.jp/documents-and-tools/cycle8/

corresponding spectroscopic data, are reported in Table 2.1[3].

We note that there is an additional uncertainty in the intensity scale of the CLEANed images due to the "JvM effect" (Jorsater & van Moorsel 1995; Czekala et al. 2021): the inconsistency of intensity units between the CLEANed model image and the residual image makes the intensity in the resulting CLEANed image incorrect (see Figure 3 in Czekala et al. 2021 for a comprehensive illustration). Czekala et al. (2021) introduced a method to correct for this effect ("JvM correction"). However, while the JvM correction recovers the correct intensity scales in the restored images, correcting the data in this way artificially manipulates the noise level by rescaling the residual image and may exaggerate the signal-to-noise ratio (S/N) (Casassus & Cárcamo 2022). The modification of S/N could lead to the misinterpretation of the structure and extent of emission. Since we mainly focus on the morphology of the emission, we adopt the images without JvM correction. We exceptionally use the JvM-corrected image when we estimate the dust mass based on the flux density of the continuum emission in Section 2.3.1. Another exception is Section 2.4.1, where we compare the flux density estimated from the visibility analysis with that measured on the image plane, since the visibility analysis is not affected by the JvM effect.

`alma-technical-handbook`.

[3] The self-calibration and imaging scripts for this source are available at `https://github.com/jjtobin/edisk`.

Table 2.1 Properties of the Continuum and Line Images

	Frequency [GHz]	E_{up}[†‡] [K]	Spectral Resolution [km s^{-1}]	Channel Width [km s^{-1}]	Robust	Beam Size (PA)	RMS [mJy beam^{-1}]
continuum	225	—	—	—	1.0	$0\farcs105\times0\farcs078$ (12°)	0.014
continuum (tapered)	225	—	—	—	2.0	$0\farcs221\times0\farcs179$ (11°)	0.018
^{13}CO $J = 2$–1	220.3986842[‡]	15.9	0.17	0.20	1.0	$0\farcs13\times0\farcs11$ (8.9°)	2.4
C^{18}O $J = 2$–1	219.5603541[‡]	15.8	0.17	0.20	1.0	$0\farcs13\times0\farcs10$ (13°)	1.7
SO $J_N = 6_5$–5_4	219.9494420[‡]	35	0.17	0.20	1.0	$0\farcs13\times0\farcs10$ (15°)	2.1

[†] Upper state energy of the transition.

[‡] Taken from the Cologne Database for Molecular Spectroscopy (cdms; Müller et al. 2001, 2005; Endres et al. 2016).

2.3 Observational Results

2.3.1 1.3 mm Continuum

Figure 2.1 shows the 1.3 mm dust continuum images of the L1489 IRS disk. The left panel of Figure 2.1 shows the large-scale view of the continuum emission with `robust` = 2.0 and `uvtaper` = $1000\,\mathrm{k}\lambda$, while the middle and right panels show the zoom-in view with `robust` = 1.0. A disk-like structure elongated along the northeast to the southwest direction is detected, which is consistent with previous observations (Yen et al. 2014; van 't Hoff et al. 2020a; Sai et al. 2020; Tychoniec et al. 2021). In the outermost region, non-axisymmetric, faint tails are also detected as indicated by the white dashed arcs in the left panel of Figure 2.1. These tails are also seen in the continuum image in Tychoniec et al. (2021) and are consistent with the molecular line emission tracing the warped outer disk as well as the accretion flows (Sai et al. 2020; Yen et al. 2014; van 't Hoff et al. 2020a).

The zoom-in view of the continuum image (middle panel of Figure 2.1) shows a central compact source at $\lesssim 0\farcs1$, which is unresolved at the current angular resolution. The peak intensity is 5.4 mJy beam^{-1}, which corresponds to a brightness temperature of 21 K using the full Planck function. This component is spatially unresolved even in the higher resolution maps imaged with smaller robust parameters (Appendix A), indicating that this component is quite compact ($\lesssim 0\farcs04$).

Interestingly, an emission enhancement (i.e., a ring-like structure) is identified at a radius of $\sim 0\farcs4$ from the central protostellar position is identified (middle panel of Figure 2.1). The locations of the ring and the adjunct gap are marked by the white solid and dashed arcs, respectively, in the middle panel of Figure 2.1. A non-axisymmetric brightness distribution (i.e., substructure in the azimuthal direction) at the ring is also observed. The right panel of Figure 2.1 shows the continuum image with an adjusted color scaling to clearly show the asymmetry. The western side of the ring is slightly brighter than its eastern counterpart. We will examine the properties of this ring-like structure in more detail in Section 2.4.1 and discuss its origin in Section 2.5.

To quantify the overall emission properties, we performed a two-component (i.e., central compact component and extended tenuous component) 2D Gaussian fit on the untapered continuum image using the `imfit` task in CASA. We note that due to the ring-like structure, the 2D Gaussian fit yields residuals at a level of $\approx 8\sigma$ at the ring location. The position of the emission peak of the central compact component derived by the fit is $\alpha(\mathrm{ICRS}) = 04^{\mathrm{h}}04^{\mathrm{m}}43.080^{\mathrm{s}}$, $\delta(\mathrm{ICRS}) = +26^{\mathrm{d}}18^{\mathrm{m}}56.12^{\mathrm{s}}$. This is used as the position of the central protostar in the following analysis. The deconvolved sizes of the compact and extended components are $0\farcs037 \times 0\farcs024$ (PA = 180°, $\sim$5.4 au $\times$ $\sim$3.7 au) and $3\farcs9 \times 1\farcs3$ (PA = 66°, $\sim$570 au $\times$ $\sim$190 au), respectively. The deconvolved size of the extended component is consistent with the previous observations (Yen et al. 2014; Sai et al. 2020). The inclination angle of the outer, extended disk is estimated from the deconvolved size to be $\sim$71° (0° for the face-on configuration) assuming a geometrically thin disk. The derived inclination angle is similar to the value measured by previous observations (73°; Sai et al. 2020). The total flux density originating from both components is 91 ± 9 mJy. The flux calibration uncertainty of 10% is added in quadrature. The measured flux density is $\sim$53% larger than that measured by Sai et al. (2020) ($\sim$ 59 mJy), which has been found to be due to the JvM effect (Jorsater & van Moorsel 1995; Czekala et al. 2021, see also Section 2.2). Applying the JvM correction (Czekala et al. 2021) resulted in a JvM ϵ (the ratio of the CLEAN beam volume to the dirty beam volume) of ~ 0.26 and a similar flux density ($\sim$50 mJy) to that derived by Sai et al. (2020).

Assuming that the continuum emission at 225 GHz is purely from the thermal dust emission and optically thin, the total dust mass can be estimated by

$$M_{\mathrm{dust}} = \frac{F_\nu d^2}{\kappa_\nu B_\nu(T)}, \tag{2.1}$$

where F_ν is the flux density, $d = 146\,\mathrm{pc}$ is the distance to the source, κ_ν is the dust mass opacity, and $B_\nu(T)$ is the Planck function of the blackbody radiation at the temperature of T. We adopted the flux density of 50 mJy from the JvM-corrected image, and the dust mass opacity of $\kappa_\nu = 2.3\ \mathrm{cm}^2\,\mathrm{g}^{-1}$ based on Beckwith et al. (1990) with an assumption of the dust-to-gas mass ratio of 0.01. Adopting dust temperatures of $T = 20\,\mathrm{K}$, a typical value used in Class II surveys (e.g., Andrews & Williams 2005; Ansdell et al. 2016; Tobin et al. 2020), and $T = 58\,\mathrm{K}$ based on the prescription in Tobin et al. (2020),

$$T = 43 \left(\frac{L_{\mathrm{bol}}}{1\,L_{\odot}} \right)^{1/4} \mathrm{K}, \tag{2.2}$$

with the bolometric luminosity of $L_{\mathrm{bol}} = 3.4\,L_{\odot}$ (Ohashi et al. 2023), we obtain disk dust masses of $31\,M_{\oplus}$ and $8.9\,M_{\oplus}$, respectively. We note that these estimates are lower limits given that the emission at the central compact component may be optically thick.

2.3.2 Molecular Lines

Figures 2.2 and 2.3 show the molecular line maps of the velocity-integrated intensity (or "zeroth moment"), velocity centroid, and peak brightness temperature with large-scale and zoom-in views, respectively. All the maps are generated using `bettermoments` (Teague & Foreman-Mackey 2018). For the velocity-integrated intensity maps, we integrate only the emission above 2σ. For the velocity centroid maps and peak brightness temperature maps, we use the quadratic method implemented in `bettermoments` rather than traditional first/eighth moments.

^{13}CO

The maps of the ^{13}CO $J = 2$–1 emission are shown in Figures 2.2 and 2.3 (top rows). The emission is detected above 3σ in a velocity range from -0.2 km s^{-1} to 15.6 km s^{-1}, where the systemic velocity is 7.38 km s^{-1} as derived by the velocity structure analysis (Section 2.4.2). The velocity-integrated intensity map with a large-scale view (top-left panel of Figure 2.2) shows an elongated morphology along the major axis of the dust disk at $r \lesssim 1\overset{''}{.}5$, and the velocity centroid map (top-middle panel of Figure 2.2) shows a rotation signature of the disk. In the outer region ($r \gtrsim 1\overset{''}{.}5$), the ^{13}CO emission shows an extended structure, suggesting that the ^{13}CO emission traces the envelope component. Sai et al. (2020) also observed the same transition and found a similar emission morphology (see Appendix C in their work).

The velocity-integrated intensity map with a zoom-in view (top-left panel of Figure 2.3) shows a bright, double-peaked ^{13}CO emission at a spatial scale of $r \lesssim 0\overset{''}{.}5$. Interest-

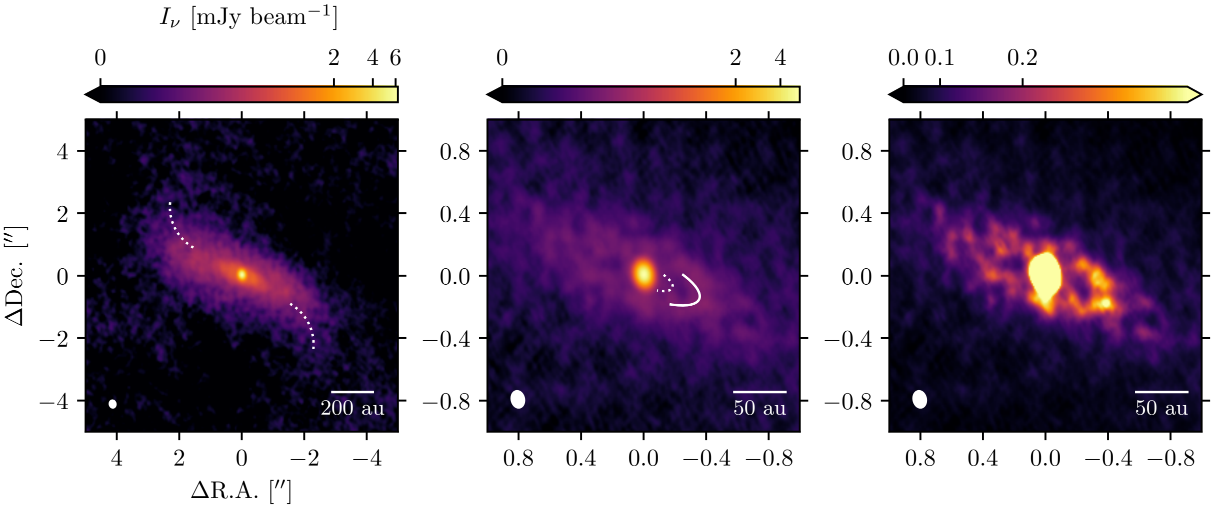

Figure 2.1. 1.3 mm continuum images of the disk around L1489 IRS. Left: Large-scale view of the disk with `robust` = 2.0 and `uvtaper` = 1000 kλ. A non-axisymmetric feature appears in the outermost region as guided by the white dashed arcs. Center: Zoom-in view of the disk with `robust` = 1.0. The locations of the ring and gap are indicated by white solid and dashed lines, respectively. The gap location is identified visually, while the ring location is based on the visibility analysis described in Section 2.4.1. For the left and center panels, the color scaling is stretched by arcsinh function to accentuate features with low surface brightness. Right: Same as the center panel, but with a limited color range stretched by sinh function to accentuate the non-axisymmetric feature at the ring. For each panel, the color scaling is saturated at 0.0, the beam size is represented by the white ellipse at the lower left, and the white scale bars are in the lower right.

ingly, the peaks of the ^{13}CO emission are slightly shifted southward from the disk major axis. This would be evidence that the ^{13}CO emission is originating from the surface of the inclined disk. The brighter emission on the southern side indicates that the southern side is the far side of the disk, from which the emission of the warm disk surface reaches the observer directly (e.g., Ruíz-Rodríguez et al. 2017; Lee et al. 2017; Villenave et al. 2020; Takakuwa et al. 2024). This configuration of the disk is consistent with the outflow directions, where the red- and blue-shifted robes are located in the northern and southern sides, respectively (Yen et al. 2014).

The top-right panels of Figure 2.2 and 2.3 show the peak brightness temperature maps. The peak brightness temperature reaches $\gtrsim 60$ K at $r \lesssim 0\farcs5$, again suggesting that the ^{13}CO emission traces the disk surface where the temperature is higher than the midplane due to the heating by the protostar or the accretion shock. The map also shows the higher brightness temperature on the southwestern (or redshifted) side, which may indicate a non-axisymmetric temperature structure of the disk. The brighter molecular line emission on the southwestern (or redshifted) side of the disk has also been previously observed in C^{17}O and H$_2$CO emission (van 't Hoff et al. 2020a).

C^{18}O

The maps of the C^{18}O $J = 2$–1 emission are shown in Figures 2.2 and 2.3 (middle rows). The emission is detected above 3σ in a velocity range from 0.8 km s^{-1} to 12.8 km s^{-1}. The velocity-integrated intensity map (middle-left panel of Figure 2.3) shows a lack of the C^{18}O emission in the innermost region ($r \lesssim 0\farcs2$). In the intermediate region ($0\farcs2 \lesssim r \lesssim 1\farcs5$), an elongated disk-like emission exists. While the C^{18}O emission shows the double-peaked morphology at $r \approx 0\farcs5$ similar to that of ^{13}CO, no significant shifts of the peaks from the major axis of the disk are seen, in contrast to the velocity-integrated intensity map of ^{13}CO (the top-left panel of Figure 2.3). This indicates that the C^{18}O emission mainly traces the gas near the disk midplane. Also, the radii of the C^{18}O peaks are slightly larger than those of the ^{13}CO peaks, which is more clearly presented in the radial intensity profiles in Section 2.3.3.

In the outer region ($1\farcs5 \lesssim r \lesssim 4''$), a warped structure is seen, where the redshifted part is curved toward southwest and the blueshifted part toward northeast (Figure 2.2). This feature was first found by Sai et al. (2020), where they interpreted it as a misaligned Keplerian disk based on the velocity structure analysis. Furthermore, an extended redshifted emission is present in the outermost region ($r \gtrsim 4''$) of the southwestern (redshifted) side (see the middle-left panel of Figure 2.2), consistent with the infalling accretion flow observed in Yen et al. (2014). The blushifted conuterpart of this component is also seen as a slight extension to the north on the northeastern side.

The centroid velocity map (central panel of Figure 2.3) shows the highest velocity ($\pm$3–5 $\mathrm{km\,s^{-1}}$ with respect to the systemic velocity) along the major axis of the disk, suggesting that the high-velocity component of the $C^{18}O$ emission traces the gas in the rotating disk. A similar velocity structure was observed by Sai et al. (2020). In the innermost region ($\lesssim 0\farcs2$), the map lacks the highest velocity component, which is due to the absence of the disk emission (possibly caused by the actual gas absence and/or the continuum over-subtraction; see Section 2.5.1), as seen in the velocity-integrated intensity map (middle-left panel of Figure 2.3).

The peak brightness temperature map (the middle-right panel of Figure 2.3) also suggests that the $C^{18}O$ emission originates from the disk midplane, as the peak emission components are located close to the disk major axis. Similar to the velocity-integrated intensity map (the middle-left panel of Figure 2.3), the peak brightness temperature also shows a central dip at $r \lesssim 0\farcs4$ and a ring-like structure with a radial peak at $r \sim 0\farcs4$. In addition, the southwestern (or redshifted) side of the disk is slightly brighter than the northeastern side, consistent with the distributions of the ^{13}CO peak brightness temperature structure.

SO

The maps of the SO ($J_N = 6_5$–5_4) emission are shown in Figure 2.2 and 2.3 (bottom rows). The emission is detected above 3σ over a wide velocity range from -3.8 $\mathrm{km\,s^{-1}}$ to $19.2\,\mathrm{km\,s^{-1}}$. Overall, the morphology of the SO emission is different from that of ^{13}CO and

$C^{18}O$. The velocity-integrated intensity map with the zoom-in view (bottom-left panel of Figure 2.3) exhibits a prominent compact emission in the innermost region ($r \lesssim 0\farcs2$) and the diffuse extended emission in the outer disk, while the diffuse SO emission lacks the high-velocity component at $r \approx 0\farcs2$–$1''$ seen in ^{13}CO and $C^{18}O$ (see the middle column of Figure 2.3). The central compact emission is marginally spatially resolved and shows an elongated structure along the east-west direction. Interestingly, this emission component shows a velocity gradient along the elongation direction over the extremely high velocities of ±10–12 km s^{-1} with respect to the systemic velocity (bottom-middle panel of Figure 2.3). The origin of this emission is discussed in detail in Section 2.5.5. The outer diffuse emission shows a complex structure where the emission is mainly distributed along the major axis of the disk as well as in the regions relocated from the axis (bottom-left panel of Figure 2.2). It also shows the velocity gradient along a direction similar to the major axis of the disk, partially tracing the rotating disk (bottom-middle panel of Figure 2.2). In addition, an SO emission clump is detected on the southwestern side of the disk ($r \approx 6''$), consistent with previous observations (Yen et al. 2014).

The peak brightness temperature map of the SO emission (the bottom-right panels of Figures 2.2 and 2.3) is highly intriguing. The multiple local enhancements of the peak brightness temperature are identified in the outer region. They may indicate the local enhancement of the gas temperature due to the accretion shock. On the other hand, the central compact emission shows lower peak brightness temperatures. This will be discussed in more detail in Section 2.5.5.

2.3.3 Radial Intensity Profiles

Figures 2.4 and 2.5 show the radial intensity profiles of the continuum and molecular lines, respectively. The methodology used to generate these radial profiles is described in detail in Appendix B. Briefly, we averaged the emission over certain radial bins within the limited wedge of ±45° with respect to the disk major axis. In addition to the profiles averaged over both sides of the disk, we calculated the profiles extracted from each southwestern (redshifted) side and northeastern (blueshifted) side of the disk to show the azimuthal

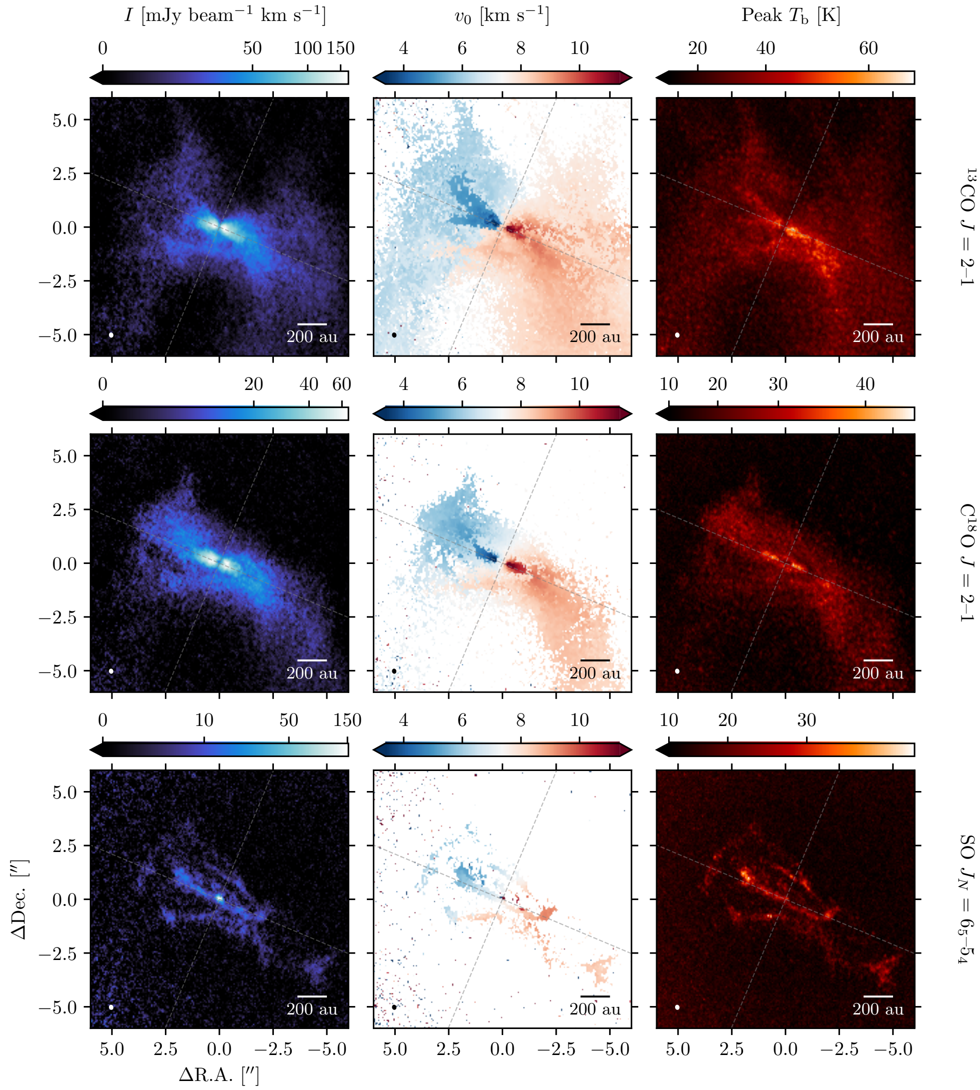

Figure 2.2. Velocity-integrated intensity maps (left column), velocity centroid maps (center column), and peak brightness temperature maps (right column) of ^{13}CO $J = 2$–1 (top row), C^{18}O $J = 2$–1 (center row), and SO $J_N = 6_5$–5_4 (bottom row). The velocity centroid and peak brightness temperature maps are generated by the quadratic method implemented in `bettermoments`. For the velocity-integrated intensity maps, only emission larger than 2σ has been integrated. The color scaling is stretched by arcsinh function and saturated at 0.0. For the peak brightness temperature maps, the conversion from intensity to brightness temperature has been done using the full Planck function. The color scaling is stretched by sinh function and saturated at 10 K for visual clarity. For all panels, the synthesized beam is shown in the bottom left, while the scale bar in the bottom right indicates 200 au. The gray dashed lines indicate the direction of the major and minor axis of the dust disk (PA = 67° as derived by the visibility analysis described in Section 2.4.1).

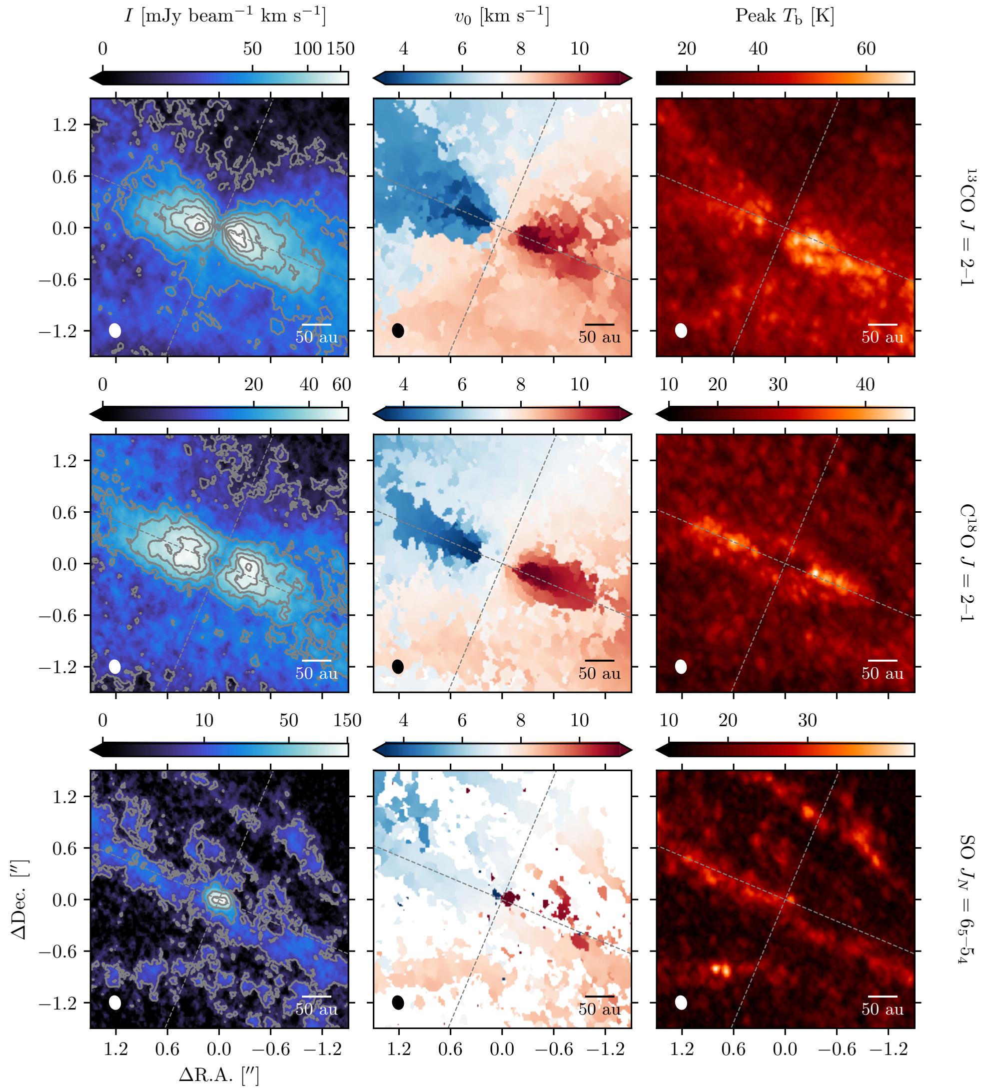

Figure 2.3. Same as Figure 2.2, but with zoom-in views. The contours in the velocity-integrated intensity maps (left column) are [10, 30, 50, 70, 90, 110, 130]σ ($\sigma = 1.2$ mJy beam^{-1} km s^{-1}), [10, 30, 50, 70, 90, 110]σ ($\sigma = 0.57$ mJy beam^{-1} km s^{-1}), and [10, 30, 100, 200]σ ($\sigma = 0.61$ mJy beam^{-1} km s^{-1}) for ^{13}CO, C^{18}O, and SO, respectively.

variations. The radial and azimuthal substructures for the continuum and each line emission are described below. A more detailed comparison of the radial profiles will be made in Section 2.5.

Continuum — Figure 2.4 shows that the continuum emission consists of the centrally peaked compact component and the tenuous extended disk emission. In addition to these components, a gap-ring pair is identified at $\sim 0\farcs2$ (or 30 au) and $\sim 0\farcs4$ (or 60 au) radii from the disk center. The profile extracted from the southwestern side is brighter at the ring position than that extracted from the northeastern side by 0.08 mJy beam^{-1} (i.e., $\approx 10\sigma$ significance), which can be seen more clearly in the inset panel of the left panel of Figure 2.4. In the radial profile of the `robust` = 2.0 tapered image (the right panel of Figure 2.4), two shoulder-like structures are tentatively identified at $\approx 1\farcs5$ (or 220 au) and $\approx 2\farcs3$ (or 340 au). The profiles also show slight variations between the southwestern side and the northeastern side at those shoulder-like substructures. The northeastern side is brighter than the southwestern side.

^{13}CO $J = 2$–1 — The radial intensity profile extracted from both sides peaks at $\sim 0\farcs2$ (or 30 au) radii. Additionally, a subtle shoulder is identified at $\sim 1\farcs3$ (or 190 au) radii. This feature is also seen in the profiles extracted from the southwestern and northeastern sides of the disk, although the feature in the northeastern side is subtle. Overall, the southwestern side is brighter than the northeastern side, while the difference is more significant in the outer radii ($\gtrsim 0\farcs8$).

C^{18}O $J = 2$–1 — The peak of the C^{18}O intensity profile is slightly shifted outward ($\approx 0\farcs4$ or 60 au) compared to the peak of ^{13}CO. From this peak, the C^{18}O profile shows a steep decline until $r \approx 1\farcs4$ (or 200 au). At $r \approx 2\farcs2$, the C^{18}O intensity profile from the southwestern side shows a slight enhancement, which is brighter than the emission on the northeastern side. While the C^{18}O profiles show the difference between the southwestern and northeastern sides of the disk in the outer region ($r \gtrsim 1\farcs5$ or 220 au), the profiles are consistent in the inner disk ($r \lesssim 1\farcs5$).

SO $J_N = 6_5$–5_4 — The SO emission is centrally peaked at $r \lesssim 0\farcs2$, although the innermost bin shows a slight central depression (the inset of the right panel of Figure

2.5). The extent of the central compact component is up to ≈$0''.2$. In addition to the central compact component, there is a tenuous diffuse emission as also seen in the maps (Figure 2.2). There is no major variation between the southwestern and northeastern sides, although the 2D emission distributions are complex (Figure 2.2).

2.4 Analysis

We performed two simple modeling approaches to the observed continuum and line emission: (1) an analytical model fit to the observed continuum emission in the visibility domain to characterize the radial substructures and geometry of the dusty disk (Section 2.4.1) and (2) a rotation curve fit to the position-velocity (PV) diagram of the $C^{18}O$ emission to investigate the nature of the disk rotation (Section 2.4.2).

2.4.1 Visibility Analysis of the Dust Continuum Emission

To precisely characterize the dust disk geometry and morphology, we conduct an analytic model fit to the observed dust continuum data in the visibility domain. Visibility analysis has two advantages against the image analysis. First, the uncertainties associated with imaging can be avoided. Second, visibility can probe the structures on scales smaller than the beam size of the image, although the smallest scale that can be probed is limited by the maximum baseline length. We only consider the axisymmetric component and the innermost dust ring, given that the non-axisymmetric components and outer shoulder-like structures are rather faint. We use a Gaussian ring model with an intensity distribution given by

$$I_{\nu,\mathrm{r}}(r) = I_{\nu,\mathrm{r}} \exp\left(-\frac{(r - r_{0,\mathrm{r}})^2}{2w_\mathrm{r}^2}\right), \tag{2.3}$$

where $I_{\nu,\mathrm{r}}$ is the peak intensity of the ring component, $r_{0,\mathrm{r}}$ is the radius of the ring center, and w_r is the width of the ring. The radial coordinate r is the disk coordinate deprojected with the position angle (PA) and the inclination angle (i). The central compact component is given by

$$I_{\nu,\mathrm{c}}(r) = I_{\nu,\mathrm{c}} \exp\left(-\frac{r^2}{2w_\mathrm{c}^2}\right). \tag{2.4}$$

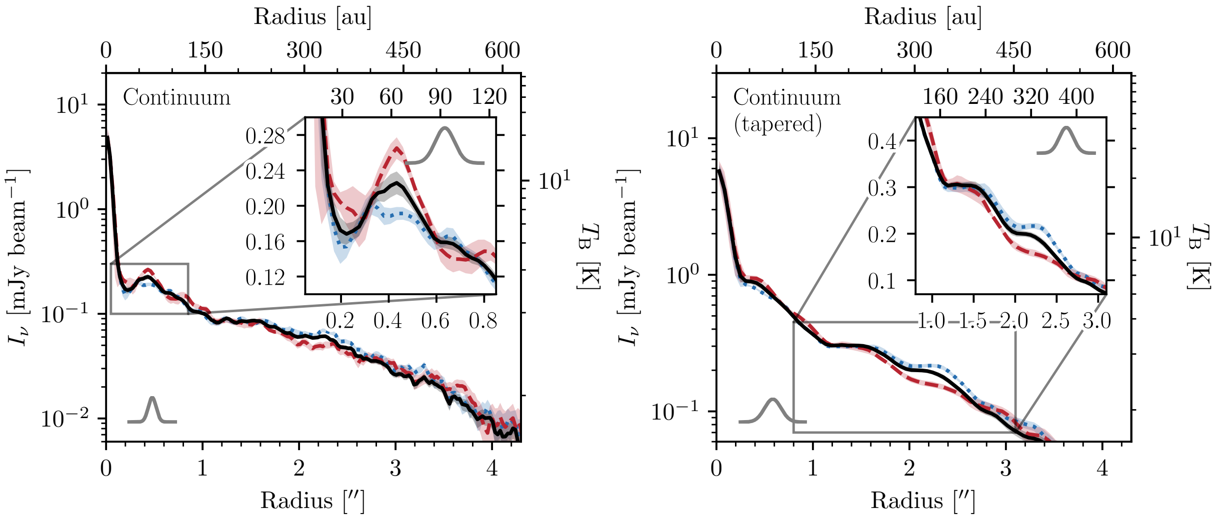

Figure 2.4. Deprojected, azimuthally averaged radial intensity profiles of the 1.3 mm continuum. The left panel presents the radial profile of the image with `robust` = 1.0, while the right panel shows the radial profile of the `robust` = 2.0 tapered image. The dashed red and dotted blue lines represent the profiles extracted from the southwestern (redshifted) side and the northeastern (blueshifted) side of the disk, respectively. The solid black line shows the profile averaged over both sides of the disk. Those profiles are computed by averaging over ±45° wedges with respect to the disk major axis (PA = 67°). The shaded regions indicate 1σ scatter at each radial bin (see Appendix B). In the inset of each panel, the zoom-in views of the innermost ring (left panel) and outer shoulders (right panel) are shown, respectively. The Gaussian profile in the lower left corner of each panel and the upper right corner of the inset indicates the width of the major axis of the synthesized beam. The right vertical axis indicates the brightness temperature, converted from the intensity using the full Planck function.

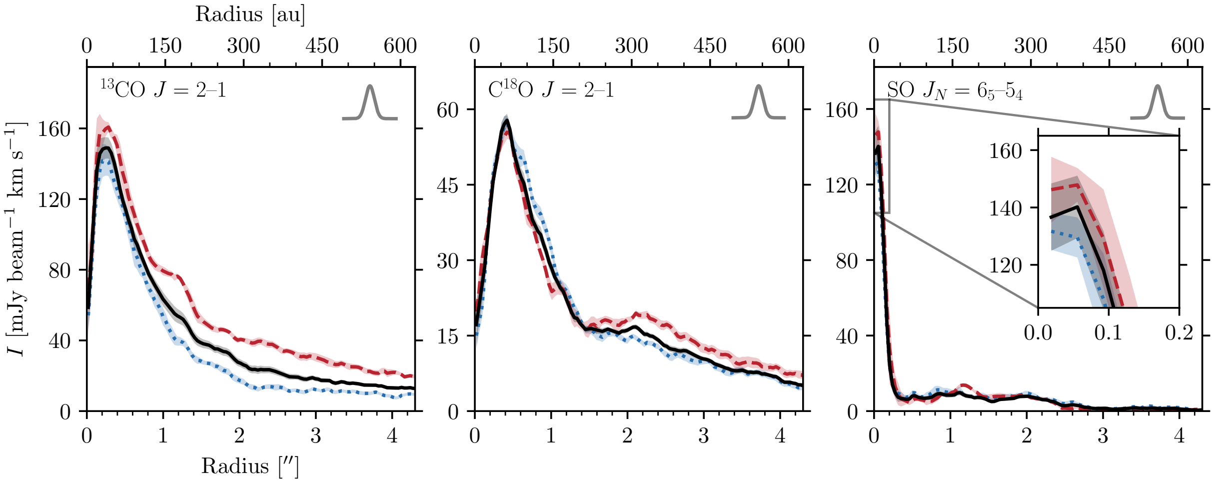

Figure 2.5. Deprojected, azimuthally averaged radial intensity profiles of ^{13}CO J = 2–1 (left), C^{18}O J = 2–1 (middle), and SO $J_N = 6_5$–5_4 (right). While the dashed red and dotted blue lines represent the profiles extracted from the southwestern (redshifted) side and the northeastern (blueshifted) side of the disk, respectively, the solid black line shows the profile extracted from both sides of the disk. Those profiles are computed by averaging over ±45° wedges with respect to the disk major axis (PA = 67°). The shaded regions indicate 1σ scatter at each radial bin (see Appendix B). The Gaussian profile in the upper right corner of each panel indicates the width of the major axis of the synthesized beam. The inset of the right panel shows the slight cetral depression of the SO emission.

We add the extended disk component as a Gaussian and it is similarly given by

$$I_{\nu,\mathrm{e}}(r) = I_{\nu,\mathrm{e}} \exp\left(-\frac{r^2}{2w_\mathrm{e}^2}\right). \tag{2.5}$$

The full model is then given by the sum of all the components,

$$I_\nu(r) = I_{\nu,\mathrm{r}}(r) + I_{\nu,\mathrm{c}}(r) + I_{\nu,\mathrm{e}}(r). \tag{2.6}$$

We directly fit this model to the observed visibilities. We used the flux density ($F_{\nu,*}$) instead of the peak intensity ($I_{\nu,*}$) for the parameters in practice. First, the model image is generated in the image plane, and then Fourier-transformed by the `GALARIO` code (Tazzari et al. 2018) onto the observed sampling of the (u, v)-plane. We also consider the disk center offset from the phase center of the observations, resulting in additional parameters of (x_0, y_0). In total, we consider 11 parameters $\hat{\theta} = \{F_{\nu,\mathrm{r}}, w_\mathrm{r}, r_{0,\mathrm{r}}, F_{\nu,\mathrm{c}}, w_\mathrm{c}, F_{\nu,\mathrm{e}}, w_\mathrm{e}, \mathrm{PA}, i, x_0, y_0\}$, and search the parameter space with the Markov Chain Monte Carlo (MCMC) method using the `emcee` package (Foreman-Mackey et al. 2013). The parameter space is sampled by 200 walkers with 1000 steps, and the initial 700 steps are discarded as burn-in.

Table 2.2 summarizes the resultant parameters of the fit. We find a PA of 67° and an inclination of 72°, both of which are consistent with the 2D Gaussian fit on the image plane (see Section 2.3). The ring radius is estimated to be $0\farcs38$ (or 56 au), which is consistent with the peak of the radial intensity profile (Figure 2.4). The ring width is $0\farcs24$ (or 35 au). The size of the central compact component is derived to be $0\farcs0073$ (or 1 au), which is smaller than the deconvolved size derived by the 2D Gaussian fit on the image plane (see Section 2.3). This indicates that the central component is indeed very compact and not spatially resolved at the current resolution. The size of the extended component ($1\farcs58$ in the standard deviation of Gaussian, or $3\farcs72$ in FWHM) is comparable to that derived by the 2D Gaussian fit. The total flux density (summed up all the components) of 52 mJy is similar to the value derived from the JvM-corrected image (which is expected to recover the correct flux scale; see Section 2.3).

The comparison of the best-fit model (i.e., the model that maximizes the likelihood) with the observed visibilities (deprojected and azimuthally averaged) is shown in Figure 2.6. Overall, the observed visibilities are reproduced well by the model. Importantly, a dip at ∼200 kλ (the inset of Figure 2.6) clearly indicates the presence of a ring-like structure. In the shortest-baseline bin, a slight discrepancy between the observations and the model in both real and imaginary parts exists, although it is within the uncertainty. The discrepancy in the real part indicates that additional emission component(s) in the largest spatial scale (which can be traced by the present observations) may be required to better reproduce the observations. The discrepancy in the imaginary part in the shortest-baseline bin suggests that the additional component(s) would be non-axisymmetric with respect to the phase center. The potential presence of a large-scale, non-axisymmetric structure is consistent with the faint tails in the outermost region seen in the dust continuum image (the left panel of Figure 2.1), which are not included in the current model.

2.4.2 Velocity Structure Traced by the $C^{18}O$ Emission

To investigate the velocity structure of the disk and infer the dynamical stellar mass, we use the $C^{18}O$ emission since the emission morphology suggests that it traces the rotating gas near the midplane (see the middle-left panel of Figure 2.3). Sai et al. (2020) found a large Keplerian disk extended to $r \sim 600$ au with a warped structure at $r \sim 200$ au by conducting the power-law fitting to the data points derived from the position-velocity (PV) diagram of $C^{18}O$ $J = 2$–1, and estimated the central stellar mass of $1.64 \pm 0.12\,M_\odot$ (see also Yen et al. 2014). We here independently verify the Keplerian rotation of the disk and estimate the central stellar mass using the Spectral Line Analysis/Modeling (`SLAM`) code (Aso & Sai 2023). We follow the methodology described in Ohashi et al. (2023). First, the $C^{18}O$ PV diagram along the major axis of the dusty disk (PA $= 67°$ as derived by the visibility analysis; see Section 2.4.1) is generated and shown in Figure 2.7. The representative data point pairs (r, v) are extracted from the diagram, to which a power-law function ($v \propto r^{-p}$) is subsequently fitted. To extract the representative data points, we identified a peak velocity channel for each pixel of the positional axis and subsequently fitted a Gaussian to the adjacent two channels (i.e., in total three channels). This is referred to as the ridge method (e.g., Yen et al. 2013; Lee et al. 2018; Sai et al. 2020, see also Aso & Machida 2020). As a complementary method, we extracted the points where the emission reaches 5σ for each pixel of the positional axis, which is referred to

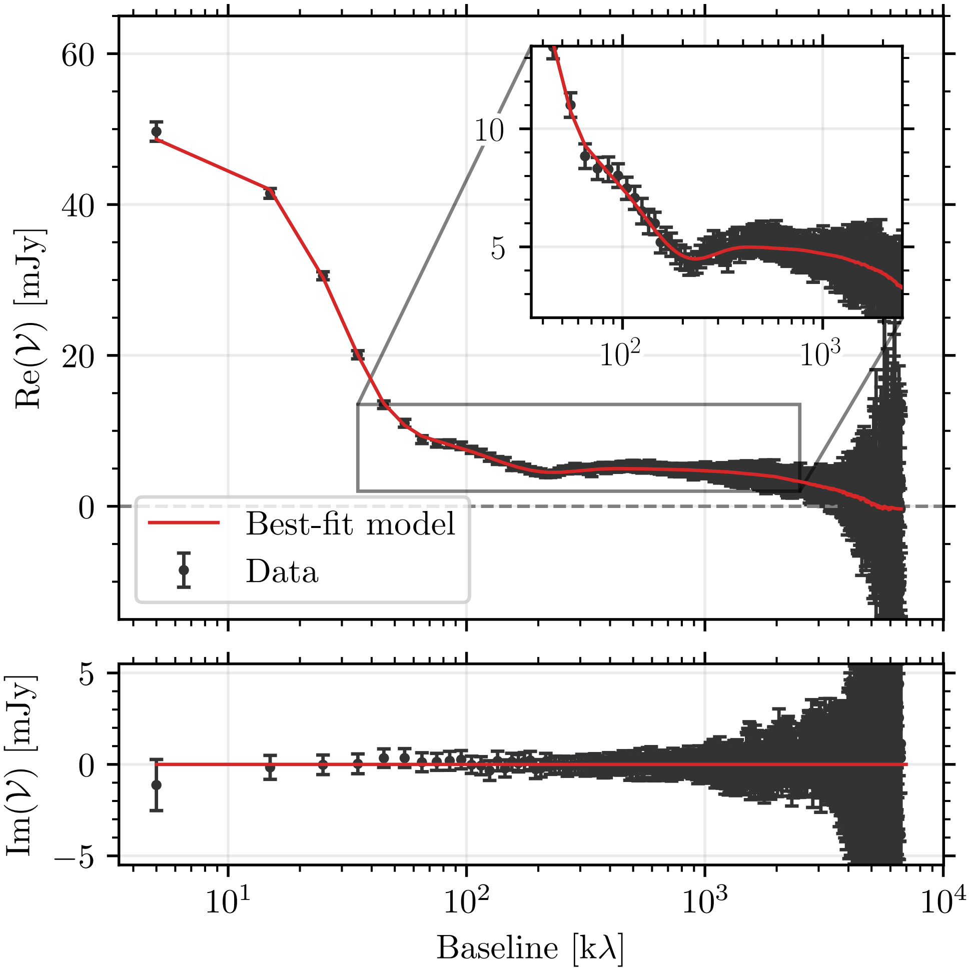

Figure 2.6. Comparison of the deprojected, azimuthally averaged observed visibilities (black) and the best-fit model (red). The upper and lower panels show the real and imaginary parts, respectively. The zoom-in view of the long-baseline regime is shown in the inset in the upper panel.

as the edge method (e.g., Seifried et al. 2016; Alves et al. 2017, see also Aso & Machida 2020). The two methods result in different estimates of the central stellar mass: the ridge method can underestimate it and the edge method can overestimate, depending on the spatial resolution (Maret et al. 2020). The difference between the central stellar masses derived from these methods is thus adopted as a systematic uncertainty. In addition, we only used $r = \pm 0\farcs3$–$1\farcs0$ region to avoid the effects of spatial resolution as described in Appendix of Aso et al. (2015) and substructures (i.e., the central depression and the warped structure at $r \gtrsim 200\,\mathrm{au}$). The extracted representative data points are shown by red and blue points in Figure 2.7. We verified that these data points follow Keplerian rotation by conducting a power-law fit to them with SLAM. The best-fit power-law index p are $0.480^{+0.008}_{-0.008}$ and $0.495^{+0.008}_{-0.008}$ for the ridge and edge methods, respectively; the index $p \approx 0.5$ is consistent with Keplerian rotation. To infer the central stellar mass, we fit the Keplerian rotation model to these data points:

$$v_{\mathrm{los}} = \pm\sqrt{\frac{GM_\star}{r}}\sin(i) + v_{\mathrm{sys}}, \tag{2.7}$$

where v_{los} is the line-of-sight component of the rotation velocity, G is the gravitational constant, $M_\star$ is the central stellar mass, r is the radius, i is the disk inclination angle, and v_{sys} is the systemic velocity. The free parameters are $M_\star$ and v_{sys}. The disk inclination angle is fixed to 72° as derived from the visibility analysis described in Section 2.4.1. To search the parameter space, the MCMC algorithm implemented in the `emcee` package (Foreman-Mackey et al. 2013) is adopted. We ran 1000 steps with 200 walkers and discarded the initial 500 steps as burn-in. The convergence was tested by auto-correlation analysis. The best-fit values (median of the posterior distributions) and uncertainties (16th and 84th percentiles) are reported in Table 2.3 for both ridge and edge methods.

While the derived systemic velocities are consistent between the two methods, the best-fit stellar masses are significantly different (Table 2.3). The value from the edge method is larger than that from the other method, which is natural as the edge method tends to trace a higher velocity than the ridge method at each pixel. Thus, the derived stellar mass including the systematic uncertainty is 1.5–$1.9\,M_\odot$. This is consistent with the previous estimates of $1.64 \pm 0.12\,M_\odot$ by Sai et al. (2020), where they used the ridge method and the data points from the outer warped disk as well.

Table 2.2 Best-fit Parameters of the Visibility Fit

Parameter	Unit	Description	Value†
$F_{\nu,\mathrm{c}}$	mJy	Flux density of the central compact component	$5.05^{+0.04}_{-0.04}$
w_c	$''$	Size of the central compact component	$0.00722^{+0.00024}_{-0.00024}$
$F_{\nu,\mathrm{r}}$	mJy	Flux density of the ring component	$5.39^{+0.22}_{-0.22}$
w_r	$''$	Width of the ring	$0.238^{+0.016}_{-0.016}$
$r_{0,\mathrm{r}}$	$''$	Radius of the ring location	$0.384^{+0.018}_{-0.019}$
$F_{\nu,\mathrm{e}}$	mJy	Flux density of the extended component	$41.4^{+0.4}_{-0.4}$
w_e	$''$	Size of the extended component	$1.58^{+0.02}_{-0.02}$
PA	$^\circ$	Position angle of the disk measured from north to east	$67.0^{+0.3}_{-0.3}$
i	$^\circ$	Inclination angle of the disk (0° for face-on)	$72.0^{+0.2}_{-0.3}$
x_0	$''$	Source offset from the phase center along Right Ascension	$0.00881^{+0.00010}_{-0.00010}$
y_0	$''$	Source offset from the phase center along Declination	$0.00101^{+0.00015}_{-0.00016}$

†The uncertainties correspond to the 16th and 84th percentiles of the posterior distributions.

Table 2.3 Results of the Keplerian Fits to C^{18}O PV Diagram

Method	$M_\star$ $[M_\odot]$	v_sys [km s^{-1}]
ridge	$1.498^{+0.008}_{-0.008}$	$7.372^{+0.009}_{-0.009}$
edge	$1.911^{+0.010}_{-0.009}$	$7.377^{+0.010}_{-0.010}$

Note. — The uncertainties correspond to the 16th and 84th percentiles of the posterior distributions.

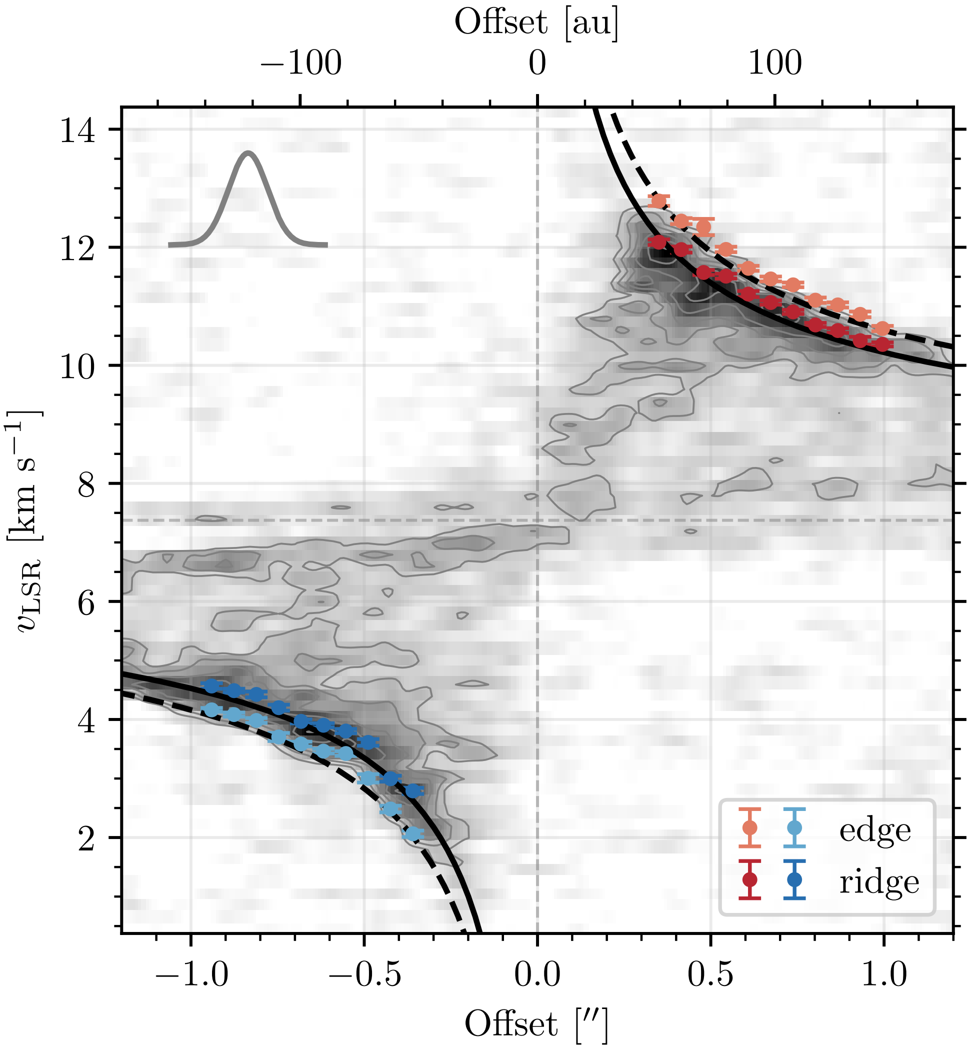

Figure 2.7. PV diagram of the C^{18}O J = 2–1 emission along the disk major axis (PA= 67°). The contours are drawn from 5σ to 15σ in steps of 2σ, where σ = 1.7 mJy beam^{-1}. The derived data points from the PV diagram by SLAM are indicated by red/blue circles (ridge method) and orange/light blue circles (edge method). The black solid and dashed lines represent the rotation curve with the best-fit parameters listed in Table 2.3 for data points derived from the ridge and edge methods, respectively. The systemic velocity derived from both fits (averaged the best-fit values; 7.375 km s^{-1}) is indicated by the horizontal grey dashed line. The Gaussian profile in the upper left corner indicates the size of the major axis of the synthesized beam.

2.5 Discussion

2.5.1 Origin of the Dust Ring

As described in Section 2.3, our observations have detected several radial substructures in both dust continuum and molecular line emission. Various mechanisms have been suggested as the origin of ring/gap structures in protoplanetary disks: e.g., planet-disk interaction (e.g., Zhang et al. 2018), modification of dust grain properties at the snowlines of volatiles (Zhang et al. 2015; Okuzumi et al. 2016), disk winds (e.g., Takahashi & Muto 2018), and dust growth (Ohashi et al. 2021).

If the dust ring at $\sim$56 au is carved by a planet, gas will also show a ring-gap structure at a similar radius. To explore the gas and dust structures around the dust ring, we compare the radial profiles of the dust continuum and line emission in the innermost region in Figure 2.8 (left panel). Interestingly, the dust ring and the radial peak of $C^{18}O$ intensity profile coincide with each other. Because the $C^{18}O$ emission is likely to trace the region near the midplane based on the emission morphology on the velocity-integrated emission map (Figure 2.3), this coincidence may indicate the presence of a ring-like structure in both dust and gas. In the adjacent dust gap (at $\approx$30 au), the ^{13}CO emission is bright, which is likely due to its optically thick emission at the disk surface as indicated by the morphology on the velocity-integrated intensity map (Figure 2.3). While the dust and $C^{18}O$ intensity profiles at $r \gtrsim 30$ au show similar behavior, the $C^{18}O$ intensity profile monotonically decreases inwards at $r \lesssim 30$ au, where the dust intensity profile shows a rapid increase. The ^{13}CO intensity profile also shows a rapid decrease at $r \lesssim 20$ au. These are likely due to the continuum over-subtraction (e.g., Weaver et al. 2018), which makes it difficult to infer the presence/absence of the gas gap, while the coincidence of the dust ring and the radial peak of the $C^{18}O$ emission is likely real.

If we assume that the gas disk has a gap with the same depth as the dust gap and that it is carved by a formed planet, the mass of the planet M_p can be estimated using

$$M_\mathrm{p} = 5 \times 10^{-4} \left(\frac{1}{\Sigma_\mathrm{p}/\Sigma_0} - 1 \right)^{1/2} \left(\frac{h_\mathrm{p}}{0.1} \right)^{5/2} \left(\frac{\alpha}{10^{-3}} \right)^{1/2} M_\star, \tag{2.8}$$

where $\Sigma_\mathrm{p}/\Sigma_0$ is the surface density contrast (i.e., gap depth), h_p is the disk aspect ratio (i.e., the ratio of the scale height to the disk radius), α is the turbulence parameter, and $M_\star$ is the central stellar mass (Kanagawa et al. 2015). If we adopt the contrast of 0.64 as measured on the dust intensity profile (Figure 2.4; assuming the emission is optically thin) as $\Sigma_\mathrm{p}/\Sigma_0$, and assume $h_\mathrm{p} = 0.05$–0.1, $\alpha = 10^{-4}$–10^{-2}, and the central stellar mass of 1.5–1.9 $M_\odot$ as derived in Section 2.4.2, the mass of the planet (if present) would be $\sim$0.033–2.4 M_J.

Another possible mechanism to explain the innermost ring/gap structures in the dust emission is the dust growth front, which is recently proposed by Ohashi et al. (2021). They calculated the time evolution of the dust size distribution and surface density profile considering the grain growth via coagulation and radial drift of dust grains and found that a ring-like structure in the surface density profile is formed at the dust growth front (or pebble production line; Lambrechts & Johansen 2014). Outside the dust growth front, the dust particles have not grown and remain in their initial states (μm size), while inside the growth front they have grown to mm size or larger and radially drifted, resulting in a local maximum of the surface density profile (i.e., ring-like structure) at the growth front. The expected radial location of the ring matched well the observed dust ring locations in young protostellar disks (Ohashi et al. 2021, 2022a), suggesting that the dust growth front mechanism could be a possible explanation for the origin of dust rings particularly in young disks. Ohashi et al. (2021) constructed an equation that predicts the radial location of the ring formed by this mechanism based on the radiative transfer modeling. The important parameters that control the location of the dust ring (R_c) are the disk age (t_disk), stellar mass ($M_\star$), and dust-to-gas mass ratio (ζ_d):

$$R_\mathrm{c} = 56 \left(\frac{M_\star}{M_\odot}\right)^{1/3} \left(\frac{\zeta_\mathrm{d}}{0.01}\right)^{2/3} \left(\frac{t_\mathrm{disk}}{0.1\,\mathrm{Myr}}\right)^{2/3} \mathrm{au}. \tag{2.9}$$

If we adopt the stellar mass of 1.5–1.9 $M_\odot$ as derived in Section 2.4.2, $\zeta_\mathrm{d} = 0.01$, and $t_\mathrm{disk} = (3$–$8)\ \times 10^4\,\mathrm{yr}$ (Sai et al. 2022), the expected location of the dust ring is 28–59 au. The ring location of 56 au found by the present observations is consistent with this expectation. Ohashi et al. (2022a) also tentatively detected the ring-like structure at $\sim$90 au in the L1489 IRS disk; the difference with our result is likely due to their coarser spatial resolution. If the dust ring is produced by the dust growth front mechanism, dust grains in the inner $\lesssim$60 au has already grown to millimeter size or even larger (Ohashi et al. 2021). To confirm that grain growth indeed has taken place, higher resolution, multi-band observations are needed to measure the spectral indices across the dust ring.

The observed ring/gap structure may also be formed by the inner misaligned disk. We will discuss this possibility in Section 2.5.6.

2.5.2 Outer Disk Structures

In addition to the dust ring at 56 au, we identified two shoulder-like structures in the outer disk in the dust continuum radial profile (Figure 2.4). The comparison of the radial intensity profiles of the dust continuum and line emission in the outer region is shown in the right panel of Figure 2.8. The inner shoulder at ~220 au coincides with the CO snowline location based on the radiative transfer modeling by Sai et al. (2020). The rapid inward increase of the $C^{18}O$ profiles at the shoulder also indicates the sublimation of CO molecules. Similar behaviors of CO line intensity profiles have been observed in Class II disks as well (e.g., Zhang et al. 2021). While the coincidence between the dust shoulder and the CO snowline may imply the change of the dust property to form the substructure, it is also possible that the rapid increase of the radial profiles of the CO isotopologues could simply be due to the gas density enhancement. We also note that the shoulder radius of $\sim$ 200 au coincides with the warped structure as revealed by the $C^{18}O$ emission (Section 2.3.2; see also Sai et al. 2020)

The outer shoulder at ~340 au is located in the outer warped disk. At the same location, the $C^{18}O$ emission, which traces near the disk midplane, exhibits a subtle emission enhancement. Similar enhancements of the line emission have been observed in $C^{18}O$ $J = 2–1$ by Sai et al. (2020) and $C^{17}O$ $J = 2–1$ by van 't Hoff et al. (2020a). This may imply that CO depletion is much less significant outside ~340 au, which we call the secondary CO snow line. As the disk column density decreases with radius, photodesorption due to penetrating UV radiation could keep CO in the gas phase outside a certain radius. A similar re-enhancement of the line emission at an outer radius is also observed in several disks (Dutrey et al. 2017; Flores et al. 2021; Lin et al. 2023). In Class II disks, similar secondary CO snow lines have also been suggested by the double emission rings of DCO^+, which is expected to trace the gas-phase CO (Öberg et al. 2015; Cataldi et al. 2021).

2.5.3 Azimuthal Asymmetry

In addition to the radial substructures, the dust continuum and molecular line emission also show azimuthal asymmetries (Section 2.3). As for the dust continuum, the southwestern side of the disk is brighter than the northeastern side in the dust ring (see the right panel of Figure 2.1). Non-axisymmetric dust emissions have been observed in a handful of disks of both Class 0/I and Class II (e.g., van der Marel et al. 2013; Sheehan et al. 2020), at least part of which is considered to be non-axisymmetric dust traps, e.g., vortices. In the L1489 IRS disk, the ring at $\sim 56\,\mathrm{au}$ may thus have the dust trap (i.e., gas pressure maximum) on the southwestern side. Alternatively, the azimuthal variance of the temperature can also lead to the asymmetry of the dust emission, which could be caused by an inner misaligned disk (see Section 2.5.6).

The L1489 IRS disk shows the asymmetry of the dust continuum emission along the major axis (see the left panel of Figure 2.1). This is in contrast to several other eDisk sources which exhibit asymmetries along the disk minor axis (see Ohashi et al. 2023 for a gallery of the continuum images). The latter is evidence that the dust grains are flared but not settled to the disk midplane; brighter emissions from the far side of the disk and fainter emissions from the near side of the disk are observed as a natural consequence of an flared optically thick disk with a radial temperature gradient (decreasing temperature as a function of radius; Ohashi et al. 2022b; Lin et al. 2023).

The lack of brightness asymmetry along the disk minor axis in the L1489 IRS disk could be due to its optically thin emission. In the case of the optically thin emission, the entire columns are seen at both near and far sides, resulting in a symmetric emission distribution along the minor axis. The low brightness temperature of the dust emission in the outer disk ($\lesssim 4\,\mathrm{K}$, see Figure 2.4) indeed suggests that the dust emission is likely optically thin except for that originating from the spatially-unresolved innermost region ($\lesssim 0\farcs1$).

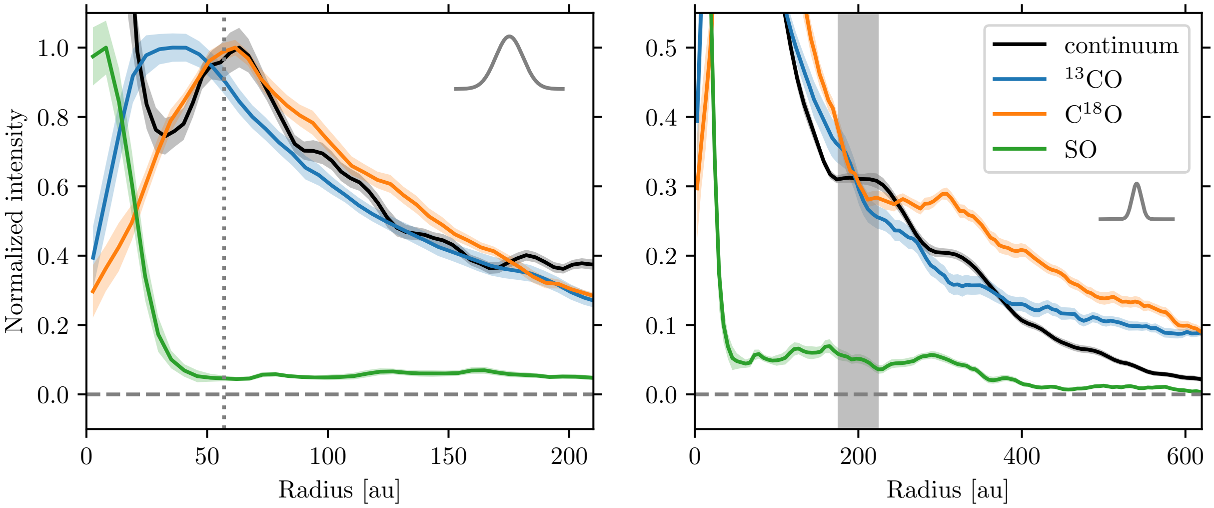

Figure 2.8. Comparison of radial intensity profiles of continuum, ^{13}CO, C^{18}O, and SO. While the left panel shows the profiles in the innermost region, the right panel presents the outer region. The profiles of line emission are normalized by the radial peaks, while the continuum profile is normalized by the intensity at the peak of the ring. The horizontal dashed line represents the zero-intensity levels. In the left panel, the vertical dotted line indicates the position of the innermost dust ring, while the vertical grey-shaded region in the right panel marks the position of the CO snowline inferred by Sai et al. (2020).

It is also possible that the dust in the L1489 IRS disk is settled to the midplane, which causes the lack of asymmetry along the minor axis of the disk. In contrast to young Class 0/I disks, observations of Class II disks indicate that the large dust grains are settled well to the midplane (e.g., Kwon et al. 2011; Pinte et al. 2016; Villenave et al. 2020, 2022). This suggests that the dust settling occurs during the evolution from the Class I phase to the Class II phase. It has also been speculated that L1489 IRS is in the later evolutionary stage of the Class I phase based on its relatively small disk mass compared to other Class I disks (Sai et al. 2020). Therefore, L1489 IRS may be in transition between the Class I and Class II phases, where the dust settling has started. A similar lack of asymmetry along the minor axis is also observed in the disk around V883 Ori, which is in transition from the Class I phase to the Class II phase (Cieza et al. 2016; Lee et al. 2019).

In addition to the dust continuum emission, the molecular line emissions also show azimuthal asymmetries (Figure 2.2 and 2.3). The slight shift of the emission peaks from the disk major axis to the southern side of the disk on the ^{13}CO velocity-integrated emission map (Figure 2.3) is clear evidence that ^{13}CO emission traces a significantly higher layer above the disk midplane (so-called “emission surface”)[4]. The direction of the shift indicates that the southern side is the far side of the disk, which is consistent with the outflow configuration where the southern lobe is blueshifted (Yen et al. 2014). Similar molecular line structures elevated from the midplane have been observed in a number of disks (e.g., Law et al. 2021b, 2022; Lin et al. 2023). Furthermore, the ^{13}CO and C^{18}O emissions show higher brightness temperatures on the southwestern side of the inner ($r \lesssim 0\farcs5$) disk (Figure 2.3). These asymmetries, as well as the non-axisymmetric brightness distribution of the dust continuum emission, may be explained by the warped disk structure (see Section 2.5.6).

---

[4] We note that we tried to estimate the emission surface of ^{13}CO using the `disksurf` package (Pinte et al. 2018a; Teague et al. 2021), but no reasonable estimates were obtained due to the contamination from the envelope emission.

2.5.4 Gas Disk Size and Dust Disk Size

Disk size is a key to undestanding disk evolution processes. Submm/mm Observations of Class II disks have revealed that the extent of the bright ^{12}CO line emission is generally larger than that of the dust continuum emission (e.g., Andrews et al. 2012; de Gregorio-Monsalvo et al. 2013; Ansdell et al. 2018; Long et al. 2022). This difference has been interpreted as a consequence of grain growth and radial drift, although the difference could also be explained by the larger optical depth of the ^{12}CO line emission than that of the dust continuum emission (e.g., Panić et al. 2009; Facchini et al. 2017; Trapman et al. 2019).

For the L1489 IRS disk, while the dust disk radius derived from the visibility analysis is ∼230 au, the gas disk radius was estimated to be ∼600 au from the rotation curve analysis of the C^{18}O emission (Sai et al. 2020). This factor of ∼2–3 difference in the size of the gas and dust disks is consistent with the averaged ratio of the gas disk radii to the dust disk radii in samples of Class II disks (Ansdell et al. 2018; Long et al. 2022), suggesting that the dust growth and radial drift have already been occurred in the L1489 IRS disk. This is also consistent with the ring-like structure of the dust emission (see Section 2.5.1) and suggests that the L1489 IRS could be in transition between the Class I phase to the Class II phase (see also Section 2.5.3).

However, it may be also possible that the difference in the radii of the gas and dust disks is due to the difference in the optical depths of the gas and dust emission (Panić et al. 2009; Facchini et al. 2017). The brightness temperature of the dust continuum emission in the outer region of the L1489 IRS disk (∼ a few K; see Figure 2.4) is lower than that of the C^{18}O emission (∼ a few tens of K; see Figure 2.2). This may indicate the difference in the optical depths, although it is also possible that the dust emission and the C^{18}O emission trace the different vertical layers of the disk that should have different temperatures.

2.5.5 Origin of the SO Emission: Accretion Shocks and a Warm Inner Disk?

As described in Section 2.3.2, the nature of the SO emission is highly complex. Outside the radius of ∼30 au ($r \gtrsim 0\farcs2$), diffuse SO emission has been observed (Figure 2.2). The non-uniform diffuse SO emission suggests the localized enhancement of the SO column density rather than a smooth distribution of SO within the disk. In addition, the localized enhancements of the SO brightness temperature (Figure 2.2) indicate the elevated gas temperature. In particular, the SO brightness temperature enhancement is prominent at $r \sim 300$ au on the disk major axis, and this radius roughly coincides with the landing point of the accretion flow observed in the $C^{18}O$ emission. Yen et al. (2014) reproduced the observed accretion flow with parabolic trajectories assuming a landing point (or centrifugal radius) of ∼300 au. It is thus likely that the origin of the diffuse SO emission is an accretion shock onto the protostellar disk caused by the infalling material. At the interface between the infalling material and the protostellar disk, slow shocks can occur; SO molecules are released into the gas phase due to the aerodynamic heating of dust grains in the post shock gas and/or formed from other desorbed molecules (e.g., Aota et al. 2015; van Gelder et al. 2021). In the Class 0 protostar L1527 IRS, the ring-like distributions of the SO emission have been interpreted as an indication of accretion shocks at the interface between the envelope and disk (Ohashi et al. 2014; Sakai et al. 2014, 2017, but see also van't Hoff et al. 2023). SO emissions originating from the accretion shock of the late-stage infalling streamer are also observed in Class I/II disks, DG Tau and HL Tau, as well (Garufi et al. 2022). Alternatively, the outer diffuse SO emission may originate from non-thermally desorbed SO molecules (e.g. photodesorption). However, the non-uniform distribution of the SO emission would be better explained by accretion shock.

In the innermost region ($r \lesssim 0\farcs2$), on the other hand, a compact, prominent SO emission exists (Figure 2.3). This emission component is distinct from the outer diffuse emission in terms of the spatial distribution and the brightness, suggesting a separate origin. The comparison of the radial intensity profiles (Figure 2.8) clearly shows that the SO emission is distributed in inner regions ($\lesssim 30$ au) compared to ^{13}CO and $C^{18}O$. Given the usual temperature structure of the disk (i.e., the higher temperature at a smaller radius), the compact SO emission traces the higher temperature region than that traced by CO isotopologue lines. Sai et al. (2020) calculated the temperature structure of the L1489 IRS disk by radiative transfer modeling. The midplane dust temperature at the SO emitting radii ($\lesssim 30$ au) is $\gtrsim 40$ K (see Appendix C), which is comparable to or higher than the sublimation temperature of SO (~ 50 k; e.g., Sakai et al. 2014; Aota et al. 2015; Miura et al. 2017), and the disk surface would be even warmer. The compact SO emission thus likely originates from the thermal sublimation of SO or its precursor (e.g., H_2S) at the warm inner region. The bright emission also requires abundant SO gas, which could be naturally explained by thermal sublimation. Although the relatively low peak brightness temperatures of SO in the innermost region (see Figure 2.3) seemingly contradicts this interpretation, the brightness temperatures at the innermost region may be reduced due to the beam dilution effect. Additionally, the SO emission in the innermost region could be optically thin, resulting in lower peak brightness temperature than the actual gas temperature.

While a bright, compact SO emission is detected in the innermost region, a CH_3OH transition with an upper state energy of 45 K, which is observed in the same spectral setup, is not detected. In the Class II disks around IRS 48 and HD 100546, SO emission and bright emission from complex organic molecules including CH_3OH have been detected co-spatially (Booth et al. 2021a,b, 2023a; Brunken et al. 2022), indicating a hot-corino-like chemistry in the warm ($\gtrsim 100$ K) region. The detection of SO and the non-detection of CH_3OH in the L1489 IRS disk may indicate that the temperature is not high enough for CH_3OH ice to thermally sublimate: while the sublimation temperature of SO is ~ 50 K (e.g., Sakai et al. 2014; Aota et al. 2015; Miura et al. 2017), a higher temperature ($\sim$ 100 K) is required for CH_3OH ice to sublimate. Alternatively, the emitting region size of CH_3OH molecules may be smaller than that of SO and the CH_3OH emission is thus beam-diluted and/or absorbed by the bright continuum emission. Higher angular resolution observations at lower frequencies, where the dust continuum emission is expected to be more optically thin, would be a key to revealing the chemistry in the innermost region of the L1489 IRS disk.

2.5.6 Warped Disk Structures

We also found that the compact SO emission shows a velocity gradient along a slightly different direction from the disk traced by ^{13}CO and C^{18}O. The left panel of Figure 2.9 shows the velocity-integrated intensity map of the high-velocity component ($\pm$8–12 km s^{-1} with respect to $v_{\rm sys}$) of the redshifted and blueshifted SO emission. The position angle of the velocity gradient ($\approx 82^\circ$) is slightly ($\approx 15^\circ$) tilted with respect to the position angle (67°) of the disk traced by ^{13}CO, C^{18}O, and dust continuum. The PV diagram of the SO emission along the position angle of 82° (the right panel of Figure 2.9) indicates that the highest-velocity component of the SO emission is fairly consistent with the Keplerian velocity derived from the C^{18}O analysis (see Section 2.4.2), suggesting that the compact SO emission originates from the innermost rotating disk.

The slight tilt of the velocity gradient direction is highly intriguing. While the non-axisymmetric emission distributions in the upper layers of the disk may result in such an appearance, the most straightforward interpretation is that the disk is warped; the rotation axis of the innermost SO disk is slightly ($\approx 15^\circ$) misaligned with respect to that of the outer disk, while the misalignment may be underestimated due to the projection effect. Observations of protostellar/protoplanetary disks have shown that many of those have misaligned or warped structures: e.g., the L1527 IRS disk (Sakai et al. 2018) and the GW Ori disk (Bi et al. 2020; Kraus et al. 2020). In the L1489 IRS disk, a warped structure at the outer radius ~ 200 au is also found by Sai et al. (2020).

With this innermost tilted disk, the observed features in both dust and molecular line emission may be explained consistently. The dust gap and the potential gas gap suggested by the C^{18}O emission at ≈ 30 au (see Section 2.5.1) can be the boundary between the outer disk and the innermost disk (e.g., Nealon et al. 2018). Furthermore, a tilted disk can cast a shadow on the outer disk and make an azimuthal variation in the temperature of the outer disk via irradiation (Figure 2.10). As a consequence, azimuthal brightness asymmetries in dust continuum and molecular line emission are expected (e.g., Facchini et al. 2018; Young et al. 2021). Indeed, our observations show a slightly weaker dust continuum emission on the northeastern side of the disk (Figure 2.1), which is consistent with the expectation from the misalignment direction of the innermost SO disk and the configuration of the outer disk; i.e., the northeastern side is shadowed considering that the southern side is the far side of the disk (see Figure 2.10). The ^{13}CO and C^{18}O emissions also show lower brightness temperatures on the northeastern side (Figure 2.3; see also Section 2.5.3).

We discuss the possible origins of the disk warp at $\sim$30 au based on the present observations and theoretical studies. Numerical simulations suggest that warped disks can be formed by the interaction with an embedded planet (e.g, Nealon et al. 2018; Zhu 2019). If the orbital plane of the planet is inclined with respect to the outer disk, the inner disk can warp from the outer disk. If we assume that the observed gap is opened by a planet with an inclined orbit, the expected planet mass from the gap depth (Section 2.5.1) is slightly modified. Zhu (2019) revised Equation 2.8 considering the inclination of the planet orbit (see also Kanagawa et al. 2015). Based on Equation (12) and (13) in Zhu (2019), the expected planet mass would be a factor of $\sim$ 1.4–2 larger than the estimate in Section 2.5.1, i.e., ~ 0.042–$4.7\,M_{\rm J}$, assuming orbital inclinations of 15–90° and a typical disk aspect ratio of $h/r \sim 0.05$–0.1.

Theoretical works have shown that the warped disk structure can also be formed by an inclined binary (e.g., Nixon et al. 2013; Facchini et al. 2018). Nixon et al. (2013) suggests that the binary torque can tear the disk and break it into two, inner and outer, disks with a misalignment. Numerical simulations of a circumbinary disk also showed that the circumbinary disk is broken into misaligned outer and inner disks (Facchini et al. 2018). The binarity of L1489 IRS has been discussed in previous studies, although there is still no direct evidence that L1489 IRS is a binary. Sai et al. (2020) derived an upper limit on the separation of the binary ($a \lesssim 30$ au) based on a scattered-light image obtained with the Hubble Space Telescope (Padgett et al. 1999). Although our higher resolution observations of the dust emission in mm wavelength do not spatially resolve the central compact emission either, we can provide a tighter constraint on the upper limit of the binary separation. Considering that the spatial resolution of the `robust` $= -2$ image is $\approx 0\farcs04$ or ≈ 7 au and that the emission is spatially unresolved, i.e., a point source (see Appendix A), the separation would be $\lesssim 7$ au.

Can such a close, inclined binary form the gap at $\sim 30\,\mathrm{au}$ observed in the dust (and potentially $C^{18}O$) emission? Nixon et al. (2013) simulated the binary system with a misaligned orbit with respect to its circumbinary disk and derived a formula to estimate the disk-breaking radius. Assuming the bending-wave regime ($h/r \gg \alpha$ where α is the viscosity parameter), the possible maximum disk-breaking (or gap) radius would be $\lesssim 2a \approx 14\,\mathrm{au}$. Here we assume an inclination angle of the binary orbit with respect to the disk of 45°, an equal-mass binary, and a typical disk aspect ratio of $h/r \sim 0.1$, which maximizes the disk-breaking radius. While this expected maximum gap radius of $\approx 14\,\mathrm{au}$ seemingly does not explain the observed gap radius of $\sim 30\,\mathrm{au}$, the latter may be overestimated due to the beam smearing effect: the dust ring width is spatially resolved while the central compact component is unresolved (see Table 2.2), and the actual gap radius (i.e., the local minima of the radial profile) could thus be smaller. Therefore, it may be possible to form the observed gap by the inner inclined binary.

Warped structures are also formed by the change of the angular momentum in the envelope and the disk during the accretion process. Hydrodynamical simulations show that the temporal variation of the angular momentum axis direction during the gas infall indeed results in a warped disk system (Sai et al. 2020). The outer warped structure at $\sim 200\,\mathrm{au}$ observed in $C^{18}O$ is likely to be formed by this mechanism rather than a binary (Sai et al. 2020). Similarly, a misalignment of the magnetic field and the angular momentum axis of the core results in a warped disk (Matsumoto et al. 2017; Hirano & Machida 2019; Hirano et al. 2020). The warped structure of the L1489 IRS disk with tilts at ~ 30 au and ~ 200 au suggests the gradual change of the angular momentum axis of the infalling material.

2.6 Summary

We have observed the disk around the Class I protostar L1489 IRS in the 1.3 mm continuum and ^{13}CO $J = 2$–1, $C^{18}O$ $J = 2$–1, and SO $J_N = 6_5$–5_4 lines at spatial resolutions of $\sim 0\overset{''}{.}1$, as part of the eDisk ALMA Large Program. Our findings are summarized as follows:

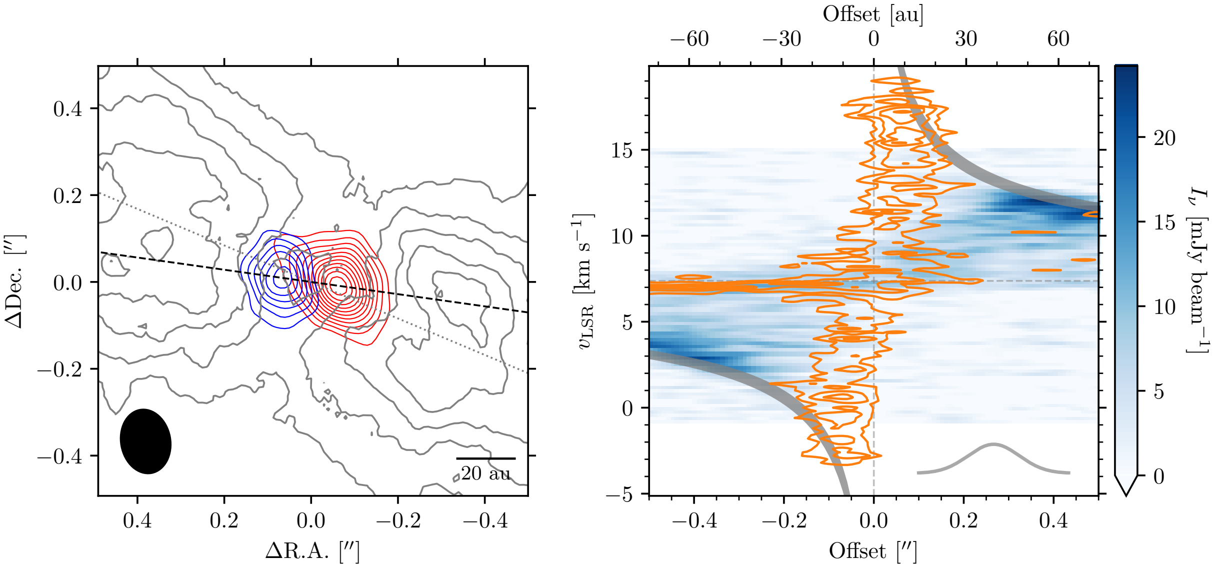

Figure 2.9. Left: Velocity-integrated intensity map (red and blue contours for red- and blue-shifted emission respectively) of the SO emission for the highest velocity component ($\pm$8–12 km s^{-1} with respect to $v_{\rm sys}$), overlayed on the C^{18}O velocity-integrated intensity map (grey contours; same as the middle-left panel of Figure 2.3). The contours of the SO emission start from 5σ followed by 2σ steps, where $\sigma = 1.9\,{\rm mJy\,beam^{-1}\,km\,s^{-1}}$. The contours of the C^{18}O emission indicate [20, 30, 40, 50, 60, 70]σ, where $\sigma = 1.0\,{\rm mJy\,beam^{-1}\,km\,s^{-1}}$. While the grey dotted line marks the dust disk PA of 67°estimated by visibility analysis (see Section 2.4.1), the black dashed line indicates a slightly tilted PA of 82°, which approximately intercepts the peak location of the red- and blue-shifted SO emission lobes. The beam is shown in the lower left. The scale bar in the lower-right indicates 20 au scale. Right: PV diagrams of the C^{18}O emission (color) along a position angle of 67° and the SO emission (orange contour) along a position angle of 82°. The contours indicate [3, 5, 7, 9]σ, where $\sigma = 2.1\,{\rm mJy\,beam^{-1}}$. The gray-shaded curves indicate the Keplerian velocity assuming the stellar mass derived from the PV diagram fits (Section 2.4.2). The shaded region indicates the uncertainty owing to the range of the stellar mass (1.5–1.9 $M_\odot$). The Gaussian profile in the lower right indicates the beam size along the offset axis.

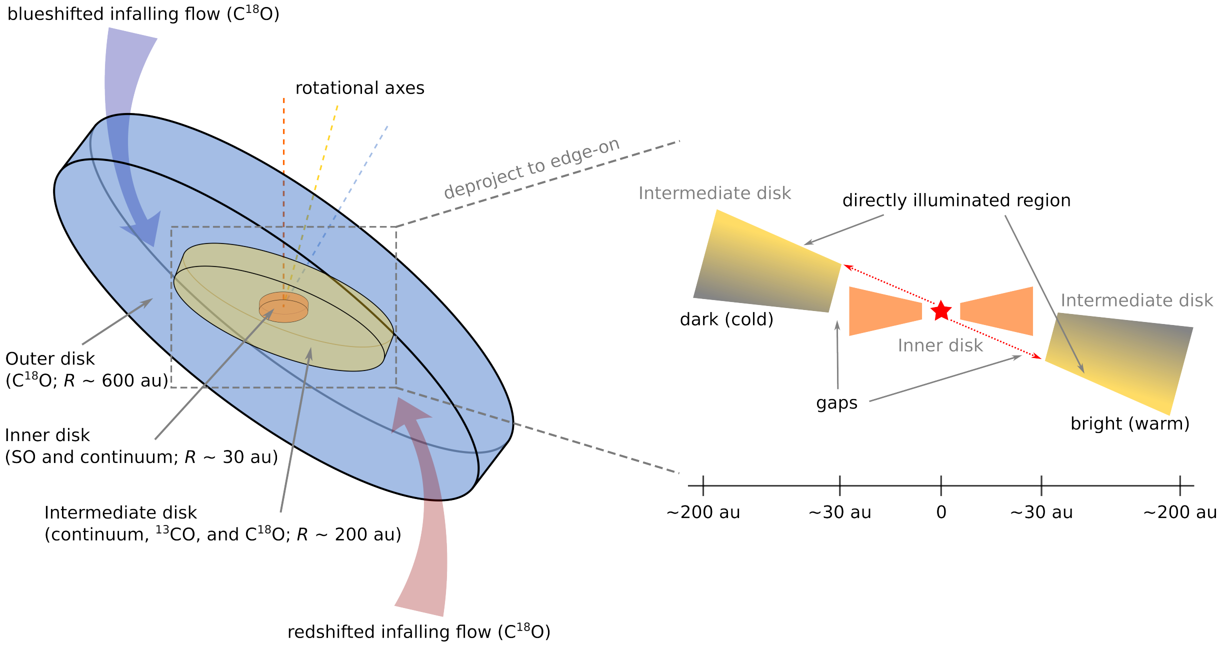

Figure 2.10. Schematic illustration of the L1489 IRS system. The observing configuration of the warped disk is shown in the left figure, while the right figure shows the edge-on view of the inner and intermediate disks. In the right figure, the observer is in front of the screen, but slightly on the southern side (downside), and thus the brightness asymmetry (i.e., the western side is brighter than the eastern side) is observed.

1. In the 1.3 mm continuum emission, we detected a disk-like elongated structure with a non-axisymmetric, faint tails in the outermost region ($r \gtrsim 2''$ or ~ 300 au) and a ring-like structure at $r \sim 0.''4$ (or ~ 56 au). The dust continuum ring also shows azimuthal asymmetry, where the southwestern side is brighter than the northeastern side. We also detected a centrally peaked compact emission which is not spatially resolved. Furthermore, two tentative shoulder-like substructures at $\sim 1.''5$ (or $\sim$220 au) and $\sim 2.''3$ (or $\sim$340 au) are also identified in the radial intensity profile of the tapered continuum image.

2. The high-velocity components of the ^{13}CO and C^{18}O emissions trace the protostellar disk. While ^{13}CO originates from the disk surface as suggested by the shift of the emission peak along the disk minor axis, C^{18}O traces the region near the midplane. The ^{13}CO and C^{18}O emissions also show (slightly) higher brightness temperatures on the southwestern side of the disk. In the outer region ($\gtrsim 1.''5$), ^{13}CO shows an extended structure, suggesting that it traces the envelope. C^{18}O traces the warped disk structure as well as the streamer-like accretion flow in the outer region, which is consistent with the previous studies (Yen et al. 2014; Sai et al. 2020).

3. The SO emission distribution shows a highly complex structure. While a compact, prominent emission appears in the innermost region ($\lesssim 0.''2$), emission in the outer region is diffuse and non-uniform. The central compact component exhibits a velocity gradient over the extremely high velocities ($\pm$10–12 km s^{-1} with respect to the systemic velocity). In the outer region, multiple localized enhancements of the peak brightness temperature are identified.

4. We performed an analytical fit to the dust continuum emission in the visibility domain, from which we confirm that the observed visibility can be explained by a simple model that consists of two Gaussian components (central compact one and outer extended one) and one Gaussian ring at $r = 0.''39$ (or 56 au). We also precisely characterized the properties of each component and dust disk geometry through the fit. While the central component is quite compact ($\sim$ 1 au), the size of the outer component is $\sim$540 au. The disk inclination and position angles are also constrained to be 72° and 67°, respectively.

5. We estimated the central stellar mass by the analysis of the $C^{18}O$ PV diagram. The estimated central stellar mass of 1.5–1.9 $M_\odot$ is consistent with the previous studies (Yen et al. 2014; Sai et al. 2020).

6. We discuss the possible origin of the observed substructures. The coincidence between the dust ring and the peak of the $C^{18}O$ radial intensity profile suggests that the gas disk also has a ring/gap structure. If we assume that the gas gap is carved by a formed planet, the planet mass would be $\sim 0.6\,M_{\rm Jup}$. Alternatively, the grain growth may be responsible for the observed dust ring, as the ring radius is consistent with the prediction of the dust coagulation model.

7. The non-uniform distributions and localized brightness temperature increases of the SO emission suggest that the origin of the outer diffuse SO emission is likely to be an accretion shock caused by the infalling material. On the other hand, we suggest that the central compact component originates from the thermal sublimation of SO and/or its precursor molecules at the warm inner disk. Indeed, the disk model of L1489 IRS shows a midplane dust temperature of $\gtrsim 40\,$K at the SO emitting radii, which is comparable to the sublimation temperature of SO ($\sim$50 K).

8. We also find that the velocity structure of the compact SO emission is consistent with the Keplerian rotation and that its velocity gradient direction is slightly ($\approx 15^\circ$) misaligned with respect to that of the disk traced by ^{13}CO and $C^{18}O$. We propose that the inner disk is tilted, i.e., the rotation axis of the inner disk traced by SO is misaligned with respect to the outer disk traced by ^{13}CO and $C^{18}O$. The disk misalignment can make shadowed region in the outer disk, which explains the observed azimuthal asymmetry in the brightness of the dust and molecular line emission. We discuss the possible origins of the misalignment, planet or binary with an inclined orbit, or the temporal variation of the angular momentum axis direction during the gas infall.

9. Combined with the previous studies, the L1489 disk has a warped structure with tilts at ~30 au and ~200 au (Figure 2.10). While the tilt at ~30 au can be explained by a planet or binary with an inclined orbit, the temporal variation of the angular

momentum axis direction during the gas infall could explain the whole warped structure.

Chapter 3

The First Interferometric Measurements of NH_2D/NH_3 Ratio in Hot Corinos

This thesis chapter originally appeared in the literature as
Yoshihide Yamato, Kenji Furuya, Yuri Aikawa, Magnus V. Persson, John J. Tobin, Jes K. Jørgensen, & Mihkel Kama, *The Astrophysical Journal*, 2022, Vol. 941, id. 75. *I led the data reduction, analysis, and discussion, while data acquisition are made by M. V. Persson.*

Abstract

The nitrogen chemical evolution during star and planet formation is still not fully understood. Ammonia (NH_3) is a key specie in the understanding of the molecular evolution in star-forming clouds and nitrogen isotope fractionation. In this paper, we present high spatial resolution observations of multiple emission lines of NH_3 toward the protobinary system NGC1333 IRAS4A with Karl G. Jansky Very Large Array (VLA). We spatially resolved the binary (hereafter 4A1 and 4A2) and detected compact emission of NH_3 transi-

tions with high excitation energies ($\gtrsim$100 K) from the vicinity of the protostars, indicating the NH_3 ice has sublimated at the inner hot region. The NH_3 column density is estimated to be $\sim 10^{17}$–10^{18} cm^{-2}. We also detected two NH_2D transitions, allowing us to constrain the deuterium fractionation of ammonia. The NH_2D/NH_3 ratios are as high as ∼0.3–1 in both 4A1 and 4A2. From the comparisons with the astrochemical models in the literature, the high NH_2D/NH_3 ratios suggest that the formation of NH_3 ices mainly started in the prestellar phase after the formation of bulk water ice finished, and that the primary nitrogen reservoir in the star-forming cloud could be atomic nitrogen (or N atoms) rather than nitrogen-bearing species such as N_2 and NH_3. The implications on the physical properties of IRAS4A cores are discussed as well.

3.1 Introduction

Nitrogen is the fifth most abundant element in the interstellar medium (ISM) with an abundance of $\sim 6 \times 10^{-5}$ with respect to hydrogen (Przybilla et al. 2008). Determining the main nitrogen reservoirs in molecular clouds is a fundamental problem in astrochemistry. The nitrogen budget in molecular clouds also affects the formation of nitrogen-bearing complex organics molecules and chemistry in planet-forming disks (e.g., Schwarz & Bergin 2014).

In molecular clouds, the main nitrogen reservoirs in the gas phase are expected to be molecular nitrogen (N_2), which are formed in the gas-phase (e.g., van Dishoeck et al. 1993; Furuya et al. 2018) (see also Öberg & Bergin 2021). While in the central region of the clouds, N_2 is self-shielded against the interstellar UV photons and thus abundant, a substantial amount of atomic nitrogen (or N atoms) could also be present in the outer regions where the density is relatively low. N and N_2 freeze-out onto the surface of dust grains in the molecular clouds, and subsequently form other nitrogen-bearing molecules such as ammonia (NH_3) via a sequence of hydrogenation (Jonusas et al. 2020; Hidaka et al. 2011; Fedoseev et al. 2015). Nitrogen-bearing molecules are also formed via gas-phase reactions (e.g., Le Gal et al. 2014), and can successively deplete onto the dust grain mantles (e.g., Caselli et al. 2022; Pineda et al. 2022). However, the partition of elemental nitrogen into these species is still not well constrained (Öberg & Bergin 2021).

Observationally constraining the main nitrogen reservoirs is generally difficult. Neither N_2 nor atomic N in the gas-phase can be observed due to the lack of low energy transitions that can be excited at the low temperature in molecular clouds. Instead, Maret et al. (2006) used the N_2H^+ emission line in molecular cloud cores to constrain the N_2 abundance in the gas phase. N_2H^+ is primary formed by $N_2 + H_3^+$, and thus its abundance reflects the abundance of gaseous N_2. Based on the relatively weak N_2H^+ emission, they suggested that N_2 is not the main nitrogen reservoir, and instead atomic N in the gas phase would be. This is also consistent with the low N_2 abundance in comets. Rubin et al. (2015) made the in situ measurement of N_2 in the comet 67P/Churyumov-Gerasimenko, revealing that the N_2/CO ratio is depleted by a factor of ∼25 compared with the case where all protosolar C and N are in CO and N_2. Icy nitrogen-bearing species in molecular clouds have been observed in infrared. While the NH_3 ice absorption bands at $3\,\mu$m band have long been debated, its $9.1\,\mu$m band was clearly detected by Lacy et al. (1998, see also Gibb et al. 2000). Observations with the *Spitzer* Space Telescope revealed that ∼10 % of overall nitrogen is locked up in ices, mainly as NH_3 (e.g., Bottinelli et al. 2010; Öberg et al. 2011) (see also Boogert et al. 2015). Still, this relatively low NH_3 abundances imply that N_2 and N can be the main nitrogen reservoir in molecular clouds. Alternatively, there are also possibilities that a substantial amount of NH_3 is converted into ammonium salts, and they can constitute a significant portion of the nitrogen reservoir as observed in the comet 67P (Altwegg et al. 2020a). In summary, observational constraints on the main nitrogen reservoir in molecular clouds and how they vary with the evolution from clouds to comets are still lacking.

The molecular D/H ratios of ice can probe the formation history of molecules. As deuterium fractionation is more efficient in the dense, cold environment (e.g., molecular cloud cores; Millar et al. 1989), information about the formation stage of molecules is imprinted into molecular D/H ratios. Recently, Furuya & Persson (2018) proposed a new approach to constrain the main nitrogen reservoir in molecular clouds using D/H ratios of NH_3 ice, i.e., NH_2D/NH_3[1]. They performed gas-ice astrochemical simulations

---

[1] Strictly speaking, D/H ratio of NH_3 is 1/3 of NH_2D/NH_3, since the chance for ammonia during its

to investingate the evolution of nitrogen-bearing species from the formation of molecular clouds, dense prestellar core, and then to the protostellar stage. They showed that if most nitrogen is already locked up in NH_3 ice in the molecular cloud stage, the NH_2D/NH_3 in bulk ice mantle and thus the ratio in the sublimates in the central warm region of the protostellar envelopes (typically $\lesssim$100 au and $\gtrsim$100 K; so-called "hot corino") are as low as $\sim 4 \times 10^{-3}$ similar to or slightly higher than the HDO/H_2O ratio. If N atoms are the dominant nitrogen reservoir in the molecular cloud and NH_3 ice formation starts only in the prestellar stage, on the other hand, the NH_2D/NH_3 ratio in the protostellar stage could be a few percent or even higher (e.g., Furuya & Persson 2018; Aikawa et al. 2012). The NH_2D/NH_3 ratio in the hot corinos, where ices sublimate, tells us when the NH_3 ice is mainly formed.

The deuteration of NH_3 in the cold outer envelope of Class 0 protostars has been measured by single-dish observations. The NH_2D/NH_3 ratios in the gas-phase are derived to be as high as a few to a few tens of percent (e.g., Shah & Wootten 2001; Hatchell 2003). Even doubly- and triply-deuterated ammonia (NHD_2 and ND_3) have been detected (e.g., Loinard et al. 2001; van der Tak et al. 2002). On the other hand, deuteration of NH_3 in the hot corino has not been measured so far, as high resolution and sensitivity observations by interferometers are needed.

One of the few sources where NH_3 emission has been detected in the hot corino is NGC1333 IRAS4A (hereafter IRAS4A), a deeply embedded low-mass Class 0 protobinary system located at a distance of ~300 pc (Ortiz-León et al. 2018; Zucker et al. 2020). IRAS4A harbors two protostars IRAS4A1 and IRAS4A2 (hereafter 4A1 and 4A2, Lay et al. 1995; Looney et al. 2000). The $(J, K) = (2, 2)$ and $(3, 3)$ inversion transitions of NH_3 at 24 GHz have been observed the Karl G. Jansky Very Large Array (VLA) toward 4A1 and 4A2 by Choi et al. (2007, 2010, 2011). Both 4A1 and 4A2 show compact emission of those transitions, indicative of the NH_3 ice sublimation. Most recently, De Simone et al. (2022) also observed $(J, K) = (3, 3)$ to (7,7) inversion transitions of NH_3 with the VLA,

---

formation to have D is three times higher than e.g. C_2H. But we use the term D/H ratio for the ratio of monodeuterated to normal isotopologues in the text for brevity. We consider this statistical issue when we compare the D/H ratio among molecules in Section 3.5.3.

revealing abundant warm NH_3 gas sublimated from ice in the hot corino.

In this chapter, we report the first detection of singly-deuterated ammonia (NH_2D) emission in the hot corinos of 4A1 and 4A2, using interferometric observations at centimeter wavelengths with the VLA. In Section 3.2, our observations and data reduction are described. We analyzed the NH_3 and NH_2D emission line profiles to constrain the NH_2D/NH_3 ratios in the central region of 4A1 and 4A2 as described in Section 3.3. In Section 3.4, constraints on the column densities of NH_3 and NH_2D, excitation temperatures, and NH_2D/NH_3 ratios are shown. We discuss the implications from the derived NH_2D/NH_3 ratios and constraints on the formation stage of NH_3 molecules in Section 3.5. Finally, we summarize our results in Section 3.6.

3.2 Observation

The IRAS4A system was observed with VLA during the Semester 2018B (PI: Magnus V. Persson, project code: 18B-125). Two tracks of observations were performed in C-configuration using K-band receivers (18–26.5 GHz) on 2018 November 26 and 2019 January 19, both centered on 4A2 ($\alpha(\mathrm{J2000}) = 03^{\mathrm{h}}29^{\mathrm{m}}10\overset{\mathrm{s}}{.}440$, $\delta(\mathrm{J2000}) = +031^{\circ}13'32\overset{\prime\prime}{.}160$). The phase, flux, and bandpass calibrators are J0336+3218, 0542+498 (3C147), and J3019+4130, respectively. The absolute flux calibration uncertainty is 10-15% for K-band[2].

The observed data were split into 23 spectral windows, 10 of which were dedicated to continuum observations and 13 of which are used to observe the line emission. The spectral resolution and bandwidth of the line spectral windows are 7.812 kHz ($\sim$0.1 km s^{-1}) and 4 MHz ($\sim$50 km s^{-1}), respectively. The spectral setup targeted several NH_3 and NH_2D transitions listed in Table 3.1 using seven out of 13 line spectral windows. Other spectral windows targeted $^{15}NH_3$ transitions and H_2O maser emission, which are not presented in this paper. We note that our correlator setup covers all the hyperfine satellites for NH_3 (1,1) transition, while only the inner satellites are covered for NH_3 (3,3) and NH_2D

---

[2] `https://science.nrao.edu/facilities/vla/docs/manuals/oss/performance/fdscale`

$3_{1,3}$–$3_{0,3}$ and $4_{1,4}$–$4_{0,4}$ transitions. For NH_3 (4,4) and (5,5) transitions, the correlator setup do not cover the hyperfine satellites and only main lines are covered.

The data were calibrated using the VLA pipeline in Common Astronomy Software Applications (casa) 5.4.1 (CASA Team et al. 2022). Bad data were identified from an initial pipeline run. These data were flagged and the pipeline was re-run. To protect the spectral lines from RFI flagging and down weighting, we manually specified continuum regions in a `cont.dat` file for the spectral line windows. In order to identify the line-free channels in the spectral windows with many lines (e.g., NH_3 (1,1) hyperfines), we first Fourier-transformed the visibilities of line spectral windows without any continuum subtraction. The line-free channels are manually selected by carefully inspecting the image cubes. Afterwards, continuum subtraction is done in the *uv* plane using `uvcontsub` task for all line spectral windows specifying the line-free channels selected in the image plane.

The visibilities in all continuum spectral windows and line-free channels in line spectral windows are averaged to ~4 MHz channel widths, and deconvolved down to 3 × root mean square (RMS) noise level of the dirty image using the multi-scale CLEAN algorithm implemented in `tclean` task with scales of [0,10,30] pixels (with a pixel scale of $0''.1$) and a Briggs parameter of 0.5. To determine the CLEAN components, we used the *automasking* feature implemented in `tclean` task with the parameters of *sidelobethreshold* = 2.0, *noisethreshold* = 4.25, and *lownoisethreshold* = 1.5. We manually checked that all the emission components are masked by carefully inspecting the resulting image.

Figure 3.1 presents the 22.3 GHz (~1.3 cm) continuum image. The resulting beam size and RMS noise level of the continuum image were $0''.99 \times 0''.75$ (P.A. = 82°) and 7.4 μJy beam^{-1}, respectively. The RMS noise level was measured in the emission-free region. The continuum peak positions are estimated by the 2D Gaussian fitting to be $\alpha(\mathrm{J2000}) = 03^{\mathrm{h}}29^{\mathrm{m}}10^{\mathrm{s}}.540$, $\delta(\mathrm{J2000}) = +031^{\circ}13'30''.893$ for 4A1 and $\alpha(\mathrm{J2000}) = 03^{\mathrm{h}}29^{\mathrm{m}}10^{\mathrm{s}}.442$, $\delta(\mathrm{J2000}) = +031^{\circ}13'32''.011$ for 4A2, which are consistent with those derived by De Simone et al. (2020). The peak intensities of 2.2 ± 0.3 mJy beam^{-1} and 0.42 ± 0.06 mJy beam^{-1} for 4A1 and 4A2, respectively. The flux calibration uncertainty was added in quadrature. These values are consistent with those derived by De Simone et al. (2020) within uncertainty.

The visibilities in line spectral windows are imaged using the multi-scale CLEAN algorithm with scales of [0, 10, 30] pixels, a Briggs parameter of 2.0, $1.0\,\mathrm{km\,s^{-1}}$ velocity channel widths, and the same *automasking* parameters as the continuum imaging. The properties of images such as beam sizes and RMS noise levels (σ_{RMS}) are listed in Table 3.2.

Figure 3.2 shows the gallery of velocity-integrated emission maps for all NH_3 and NH_2D lines, generated using `bettermoments` (Teague & Foreman-Mackey 2018). The image cubes are integrated over the velocity ranges listed in Table 3.2 encompassing all detected hyperfine components. The velocity ranges for integration are adjusted for each transition to include only the emission by visually inspecting the image cubes. The noise levels σ for these maps are calculated by `bettermoments` as $\sigma = \sigma_{\mathrm{RMS}} \times \sqrt{N} \times dv$, where N is the number of integrated channels and dv is the channel width ($1.0\,\mathrm{km\,s^{-1}}$). These values are reported in each panel of Figure 3.2. We clearly see the detection of all NH_3 lines toward both 4A1 and 4A2 at S/Ns of ∼10–20, while NH_2D lines are detected toward 4A1 with S/N of ∼5 and only tentatively detected toward 4A2 with S/Ns of ∼3–5. These S/N values are reported in Table 3.2 as well.

Table 3.1 Observed Transitions and Their Spectroscopic Data

Specie	Transition	ν_0 [GHz]	$\log_{10} A_{\mathrm{ul}}$ [s^{-1}]	g_{u}	E_{u} [K]
NH_3	(1,1)	23.6944955	−6.78260	6.0	23.26484
	(2,2)	23.7226333	−6.65631	10.0	64.44806
	(3,3)	23.8701292	−6.59744	28.0	123.53904
	(4,4)	24.1394163	−6.55545	18.0	200.52091
	(5,5)	24.5329887	−6.51738	22.0	295.37076
NH_2D	$3_{1,3}$–$3_{0,3}$	18.807888	−7.42815	63.0	93.91931
	$4_{1,4}$–$4_{0,4}$	25.023792	−7.01363	27.0	152.25741

Note. — The spectroscopic data are retrieved from the Jet Propulsion Laboratory (JPL) Catalogue (Pickett et al. 1998) and Cologne Database for Molecular Spectroscopy (cdms, Müller et al. 2005) via the Splatalogue interface. The original data are presented in Yu et al. (2010) for NH_3 and De Lucia & Helminger (1975); Cohen & Pickett (1982); Fusina et al. (1988) for NH_2D.

Table 3.2 Properties of Image Cubes and Velocity-integrated Intensity Maps of NH_3 and NH_2D

Specie	Transition	RMS [mJy beam^{-1}]	Synthesized Beam (P.A.)	Integration Range[†] [km s^{-1}]	S/N[‡]	
					4A1	4A2
NH_3	$(1,1)$	0.69	$1\farcs35 \times 0\farcs99$ (75°)	[−14, −11], [−3, 1], [4, 9], [12, 16], [23, 29]	12	16
NH_3	$(2,2)$	0.62	$1\farcs32 \times 0\farcs98$ (75°)	[−13, −8], [4, 10], [21, 26]	9.2	13
NH_3	$(3,3)$	0.60	$1\farcs31 \times 0\farcs98$ (75°)	[−16, −11], [3, 11], [25, 30]	10	18
NH_3	$(4,4)$	0.55	$1\farcs25 \times 0\farcs95$ (77°)	[3, 10]	11	13
NH_3	$(5,5)$	0.60	$1\farcs27 \times 1\farcs02$ (73°)	[3, 10]	9.0	14
NH_2D	$3_{1,3}$–$3_{0,3}$	0.59	$1\farcs52 \times 1\farcs23$ (81°)	[4, 10]	5.5	3.1
NH_2D	$4_{1,4}$–$4_{0,4}$	0.58	$1\farcs26 \times 0\farcs92$ (74°)	[4, 10]	5.2	4.9

† Integration ranges for velocity-integrated emission maps.

‡ Peak signal-to-noise ratios on the velocity-integrated emission maps.

3.3 Analysis

In order to estimate the column densities of NH_3 and NH_2D, first we extracted the spectra for all lines from a single pixel toward the continuum peak position estimated in Section 3.2 for each source. The extracted spectra are presented in Figure 3.3 and 3.4 for 4A1 and 4A2. For the following analysis, NH_3 (1,1) and (2,2) transitions are excluded; given their relatively low excitation energies, the extended emission may contaminate the emission from the central hot region.

3.3.1 Estimates on the emitting region size

To estimate the emitting region size, we inspected the visibility profiles in (u, v) plane (amplitude–baseline length plot) for each transition. However, all of the transitions show almost flat profiles, indicating that it is difficult to infer the emitting region size even from visibility data. Instead, we estimated the emitting region size of NH_3 using our data and the data presented in Choi et al. (2010, 2011). Choi et al. (2010, 2011) observed NH_3 (3,3) transitions toward the IRAS4A system with a circular beam of $0\farcs3 \times 0\farcs3$, which is higher spatial resolution than our data. The difference in the beam sizes between the data in Choi et al. (2010, 2011) and our data allows us to evaluate the beam dilution and accurately estimate the emitting region size, assuming that the both observations trace the region with the same physical condition and that the lines are optically thick. We will confirm that the main component of NH_3 (3,3) is highly optically thick ($\tau \gtrsim 10$) in the following section.

We fitted a Gaussian to the spectra presented in Figure 4 in Choi et al. (2011) and Figure 1 in Choi et al. (2010) for IRAS4A1 and IRAS4A2, resulting in the peak brightness temperatures of 44.4 ± 2.3 K and 73.2 ± 2.5 K, respectively. We also fitted a Gaussian to the NH_3 (3,3) main component of our data to obtain the peak brightness temperature. The observed peak brightness temperatures can be modeled as $T_{\rm int} \times f$, where $T_{\rm int}$ is the intrinsic temperature and f is the beam filling factor given as

$$f = \frac{\theta_\mathrm{s}}{\sqrt{\theta_\mathrm{s}^2 + \theta_\mathrm{maj}^2}} \frac{\theta_\mathrm{s}}{\sqrt{\theta_\mathrm{s}^2 + \theta_\mathrm{min}^2}}, \tag{3.1}$$

where θ_s is the emitting region size, and θ_maj and θ_min are the size of the beam major and minor axes, respectively. Here we assume that the emission distribution of the source is a symmetric 2D Gaussian with a FWHM of θ_s. Assuming that T_int is the same between the data, the relation between the observed peak brightness temperature ratio and θ_s can be inferred. We constructed the likelihood function of the observed brightness temperature ratio and θ_s. To sample the posterior distribution, we employed the Markov Chain Monte Carlo (MCMC) method implemented in `emcee` python package (Foreman-Mackey et al. 2013). We used an uniform prior in the interval [$0.''01$,$0.''6$] for θ_s and run the 200 walkers for 600 steps, including initial 100 steps discarded as burn in. We found $\theta_\mathrm{s} = 0.''25^{+0.05}_{-0.06}$ and $0.''30^{+0.03}_{-0.03}$ for 4A1 and 4A2, respectively, where the estimated values are the median of the posterior distributions and uncertainties are the 16th and 84th percentile. These estimates are used in the subsequent analyses. The estimated emitting region is close to the beam size of Choi et al. (2010), in which the deconvolved sizes of the sources are derived to be $0.''44 \times 0.''25$ for 4A1 and $0.''55 \times 0.''30$ for 4A2. These values are slightly larger than our estimates, most probably because they averaged the images of (2,2) and (3,3), while our estimates are based on the (3,3) transition only.

3.3.2 Hyperfine fit of NH_3 and NH_2D lines

We fitted the observed spectra with a synthetic model considering hyperfine splitting (Rosolowsky et al. 2008). The details of the model used in the present work are described in Appendix D. Among the observed NH_3 and NH_2D transitions, both ortho (NH_3 (3,3) and NH_2D (3,3)) and para (NH_3 (4,4), (5,5), and NH_2D (4,4)) transitions are included, which in principle allows us to estimate the ortho-to-para ratio of NH_3 and NH_2D. In our model, we assume local thermo-dynamical equilibrium (LTE) so that the observed spectra can be fitted by a common excitation temperature for NH_3 and NH_2D transitions under the assumption that they originate from the same gas. The LTE assumption should be valid for targeted sources because the H_2 density in the vicinity of the protostar ($\lesssim$100 au) should be $\gtrsim 10^6\,\mathrm{cm}^{-3}$ (e.g. Persson et al. 2016; De Simone et al. 2020), which is far higher than the critical densities of NH_3 transitions ($\sim 10^3\,\mathrm{cm}^{-3}$; e.g., Shirley 2015).

First, we fitted these models to the NH_3 and NH_2D line profiles simultaneously; the ortho-to-para ratios of NH_3 and NH_2D are fixed to one and three, respectively, which are the statistical values expected in the warm ($\gtrsim$100 K) environments. This resulted in 14 free parameters (Table 3.3): velocity dispersions (ΔV) and systemic velocities (v_{sys}) for all five transitions, the logarithms of column densities of NH_3 and NH_2D ($\log_{10} N(\mathrm{NH_3})$ and $\log_{10} N(\mathrm{NH_2D})$), and the common excitation temperature (T_{ex}) and emitting region size (θ_{s}) among all five transitions. We also ran a fit with the ortho-to-para ratio of NH_3 as a free parameter to check if the assumptions of statistical equilibrium affects derived parameters. We sampled the posterior distributions with MCMC method implemented in `emcee` Python package. We used uniform priors for all parameters except for the emitting region size. We used tight Gaussian priors for emitting region sizes based on the estimates in previous subsections. We run 200 walkers for 5000 steps, including the initial 2500 steps discarded as burn in. During the fit, we initially generated model spectra with much higher velocity samplings and then resampled down to the ones in the actual data ($1.0\,\mathrm{km\,s^{-1}}$).

3.4 Results

The observed spectra overlaid by the model spectra generated from posterior samples, as well as the residual spectra after subtracting the model spectra are presented in Figure 3.3 and 3.4. The results of the fits are summarized in Table 3.4.

For 4A1, high excitation temperatures are derived in both fits with ortho-to-para ratio fixed and varied (98^{+8}_{-7} K and 110^{+10}_{-10} K, respectively). The total optical depth (including the hyperfine) of each NH_3 transition is greater than unity, while the hyperfine satellites of the NH_3 (3,3) transition provide the constraints on the column density of NH_3. In the fits with free ortho-to-para ratio, the NH_3 column density is more uncertain and the NH_3 ortho-to-para ratio is not well constrained. Since a statistical NH_3 ortho-to-para

Table 3.3 Free Parameters of Hyperfine Fits for 4A1 and 4A2

Parameter	Prior for 4A1 fit^{a}	Prior for 4A2 fit^{a}
ΔV [$\mathrm{km\,s^{-1}}$]†	U, [0.1, 10]	U, [0.1, 10]
v_{sys} [$\mathrm{km\,s^{-1}}$]†	U, [4, 10]	U, [4, 10]
$\log_{10} N(\mathrm{NH_3})$ [$\mathrm{cm^{-2}}$]	U, [14, 21]	U, [14, 21]
$\log_{10} N(\mathrm{NH_2D})$ [$\mathrm{cm^{-2}}$]	U, [14, 21]	U, [14, 21]
T_{ex} [K]	U, [50, 350]	U, [50, 350]
θ_{s} [$''$]	G, [0.25, 0.06]	G, [0.30, 0.03]
o/p‡	U [0.01, 100]	U [0.01, 100]

[a] The prior distributions of the parameter. The type of prior (uniform or Gaussian) and its parameters are listed. "U" represents an uniform prior, followed by the lower and upper bound of the uniform prior. "G" represents a Gaussian prior, followed by the center and standard deviation of the Gaussian prior.

† The priors are common for all transitions, while treated as individual parameters for each transition.

‡ The ortho-to-para ratio of $\mathrm{NH_3}$. Used for fits with free ortho-to-para ratio only.

ratio of unity is expected in the hot region, we employ the fit with the fixed ortho-to-para ratio as the fiducial result. The NH_2D column densities result in similar values ($\sim 7 \times 10^{17}\,\mathrm{cm^{-2}}$) in both fits. Particularly, the undetected hyperfine satellites of NH_2D ($4_{1,4}$–$4_{0,4}$) at $\sim -16\,\mathrm{km\,s^{-1}}$ and $\sim$26 $\mathrm{km\,s^{-1}}$ (see Figure 3.3) are helpful to constrain the column density. The line widths of NH_3 (4,4) and (5,5) transitions are broader than those of NH_3 (3,3) and NH_2D transitions (Table 3.4). This may indicate that these higher transitions of NH_3 preferentially trace inner regions with higher infall velocity than (3,3) transition of NH_3 and NH_2D transitions. We will discuss this issue in more detail in Section 3.5 Finally, both fits yield high NH_2D/NH_3 column density ratios of $0.96^{+0.76}_{-0.39}$ and $0.28^{+0.59}_{-0.23}$, consistent within the uncertainties.

For 4A2, the fit with a fixed ortho-to-para ratio yields a lower excitation temperature (87^{+13}_{-10} K) than that with a free ortho-to-para ratio (160^{+30}_{-20} K). In the former, the peak brightness temperature of the main component of NH_3 (3,3) transition is significantly underestimated (Figure 3.4) and thus the lower excitation temperature is not reasonable. In contrast, the spectra are better reproduced in the fit with a free ortho-to-para ratio, which suggests that the higher excitation temperature is more reasonable. However, the obtained ortho-to-para ratio of NH_3 in the fit ($4.5^{+1.5}_{-1.3}$) is significantly higher than the statistical ratio of unity. This does not seem to be realistic since the ortho-to-para ratio of NH_3 should be unity in the hot region as indicated by the derived excitation temperature. Nevertheless, the column density estimates in the two fits agreed within the uncertainties. We thus adopt the NH_3 column density derived from the fits with free ortho-to-para ratio as our fiducial value. The NH_2D column density is also well constrained, although the line widths are not well constrained due to the lower S/N. The widths of NH_3 lines are typically $\sim$2–5 $\mathrm{km\,s^{-1}}$, and broader for higher excitation transitions (Table 3.4). This could again imply that the emitting region is smaller (i.e., inner region with higher velocity) for higher transitions. Finally, the fiducial fit yield a NH_2D/NH_3 ratio of $0.48^{+0.17}_{-0.13}$, consistent with that derived in the fit with fixed ortho-to-para ratio within the uncertainties.

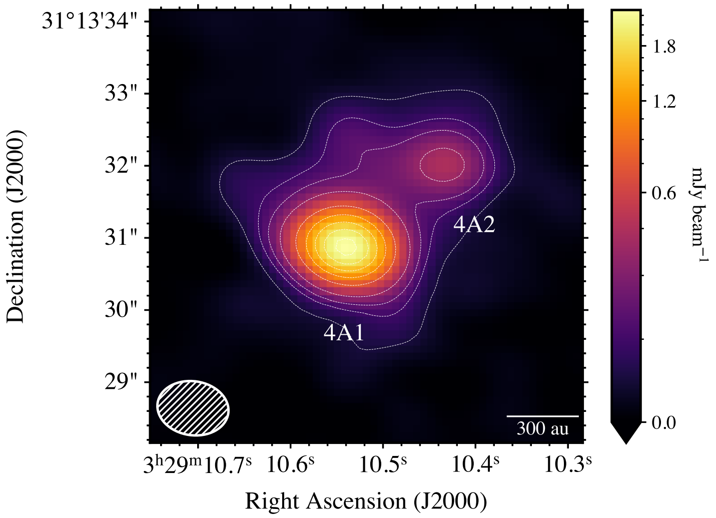

Figure 3.1. The 22.3 GHz continuum emission maps toward IRAS 4A and IRAS 4B. The contours (white dashed lines) correspond to [10, 20, 30, 50, 100, 150, 200, 250, 300] $\times\, \sigma_{\mathrm{RMS}}$, where $\sigma_{\mathrm{RMS}} = 7.4\,\mu\mathrm{Jy\,beam}^{-1}$ for both maps. The beam sizes of $0\farcs99 \times 0\farcs75$ (P.A. = 82°) and scale bars of 300 au are shown at lower left and right. We note that the color scales employ arcsinh stretches, with the lower end saturating at 0.0.

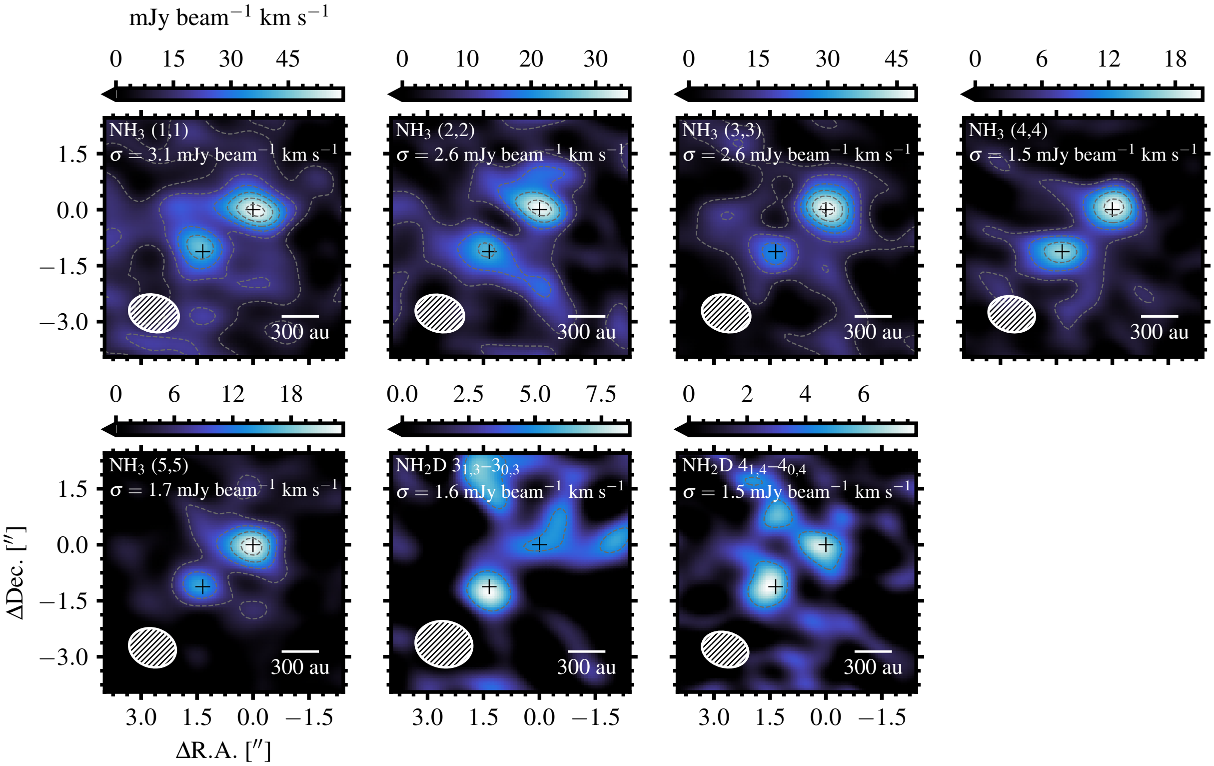

Figure 3.2. Gallery of velocity-integrated intensity maps of NH$_3$ and NH$_2$D transitions. Transitions are indicated at the upper left in each panel. The continuum emission peaks for 4A1 and 4A2 are indicated by black crosses in each panel. The grey dashed contours start from 3σ, followed by steps of 3σ. The beam size and scale bar of 300 au are shown in lower right and left in each panel, respectively. We note that the color scale is saturated at the lower end of 0.0.

Table 3.4 Results of Fits for 4A1 and 4A2

o/p†	θ_s [″]	T_{ex} [K]	ΔV_{FWHM} [km s^{-1}]					N(NH$_3$) [cm^{-2}]	N(NH$_2$D) [cm^{-2}]	NH$_2$D/NH$_3$	Fiducial
			NH$_3$ (3,3)	NH$_3$ (4,4)	NH$_3$ (5,5)	NH$_2$D $3_{1,3}$–$3_{0,3}$	NH$_2$D $4_{1,4}$–$4_{0,4}$				
					IRAS 4A1						
1 (fixed)	$0.25^{+0.06}_{-0.06}$	98^{+8}_{-7}	$1.9^{+0.3}_{-0.2}$	$3.9^{+0.7}_{-0.6}$	$3.5^{+0.9}_{-0.7}$	$1.8^{+0.8}_{-0.5}$	$1.6^{+1.1}_{-0.8}$	$8.1^{+4.0}_{-2.5} \times 10^{17}$	$7.3^{+5.4}_{-1.9} \times 10^{17}$	$0.96^{+0.76}_{-0.39}$	✓
11^{+40}_{-8}	$0.25^{+0.06}_{-0.06}$	110^{+10}_{-10}	$1.3^{+0.3}_{-0.2}$	$4.7^{+1.0}_{-0.8}$	$4.3^{+1.0}_{-0.8}$	$1.9^{+0.8}_{-0.5}$	$1.6^{+1.1}_{-0.8}$	$2.8^{+11.0}_{-2.0} \times 10^{18}$	$6.9^{+3.8}_{-1.6} \times 10^{17}$	$0.28^{+0.59}_{-0.23}$	
					IRAS 4A2						
1 (fixed)	$0.33^{+0.02}_{-0.03}$	87^{+13}_{-10}	$2.2^{+0.2}_{-0.2}$	$2.2^{+0.3}_{-0.2}$	$4.1^{+0.7}_{-0.7}$	$0.9^{+2.0}_{-0.5}$	$5.1^{+2.0}_{-1.6}$	$7.9^{+2.5}_{-1.6} \times 10^{17}$	$3.1^{+1.2}_{-1.0} \times 10^{17}$	$0.38^{+0.17}_{-0.13}$	
$4.5^{+1.5}_{-1.3}$	$0.26^{+0.02}_{-0.02}$	160^{+30}_{-20}	$2.0^{+0.2}_{-0.2}$	$3.0^{+0.6}_{-0.5}$	$4.7^{+0.6}_{-0.6}$	$2.0^{+5.2}_{-1.3}$	$5.1^{+2.0}_{-1.5}$	$1.0^{+0.3}_{-0.2} \times 10^{18}$	$4.9^{+1.9}_{-1.4} \times 10^{17}$	$0.48^{+0.17}_{-0.13}$	✓

† The ortho-to-para ratio of NH$_3$

3.5 Discussion

3.5.1 NH_3 and NH_2D in the hot corino region

We have detected the high excitation transitions of NH_3 (4,4) and (5,5) toward both 4A1 and 4A2 in addition to the (2,2) and (3,3) lines, which were previously detected by Choi et al. (2007, 2010). The excitation temperatures derived in the hyperfine fits (∼100 K for 4A1 and ∼150 K for 4A2) are comparable to or higher than the typical NH_3 sublimation temperature of 100–140 K depending on the gas density and composition of ice mixture (Hama & Watanabe 2013; Furuya & Aikawa 2014; Minissale et al. 2022). Since the gas and dust temperatures are expected to be well coupled in the high density region, the high excitation temperatures indicate that the observed emission traces the NH_3 ice sublimation zone in the vicinity of the protostars. This conclusion is also supported by the compact emitting regions ($\sim 0\overset{''}{.}25$ or ∼75 au) and the high column density of NH_3 ($\sim 10^{17}$–$10^{18}\,\mathrm{cm^{-2}}$). Taquet et al. (2013) derived the column density of sublimated H_2O to be (3–5) $\times 10^{19}$ $\mathrm{cm^{-2}}$ towards IRAS 4A, assuming the emitting region size of $\sim 0\overset{''}{.}4$. The NH_3/H_2O abundance ratio of 10^{-2}–10^{-1} is consistent with the composition of interstellar ices observed towards low-mass protostars (Öberg et al. 2011). In addition to NH_3, we have detected the high excitation transitions of NH_2D. The observed line profiles are reasonably reproduced by the same emitting region sizes and excitation temperature as those of NH_3, suggesting that the observed emission traces NH_2D sublimated from ices. The NH_2D column densities are also high, resulting in high NH_2D/NH_3 ratios of ∼0.5–1 toward both 4A1 and 4A2.

The high NH_2D/NH_3 ratios, higher than expected from Furuya & Persson (2018), motivate careful discussions and confirmation. Firstly, the NH_3 column densities may be underestimated, as the NH_3 lines are optically thick. Particularly, our spectral windows do not cover the hyperfine satellites of NH_3 (4,4) and (5,5) transitions that can be optically thin ($\tau < 1$). De Simone et al. (2022) observed the higher excitation lines up to $(J, K) = (7, 7)$ covering all of the hyperfine satellites, which allows them to accurately estimate the column density of NH_3 with non-LTE LVG analysis. While our estimates of NH_3 column density in 4A2 ($\sim 1 \times 10^{18}\,\mathrm{cm^{-2}}$) is consistent with the estimates by De Simone

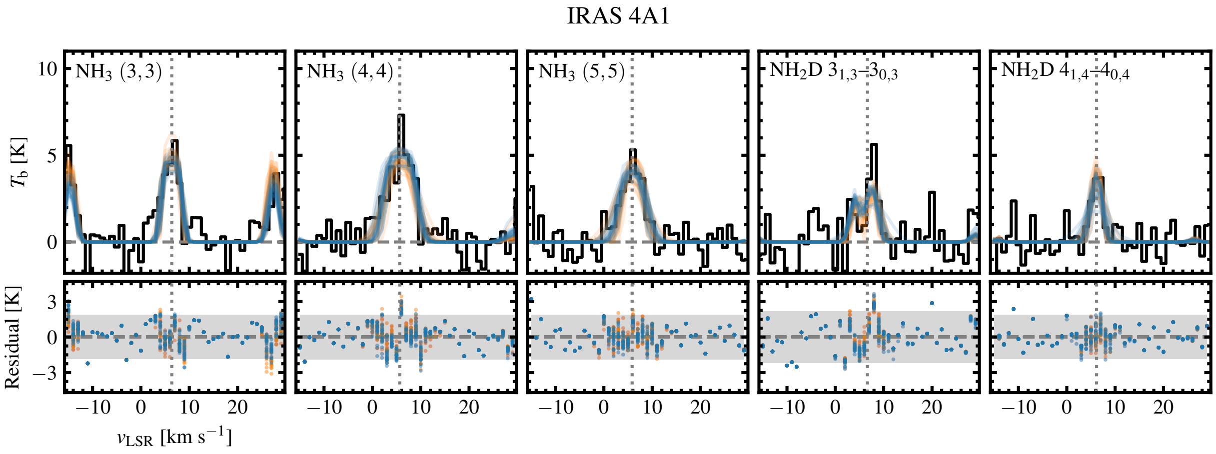

Figure 3.3. (top) Observed spectra of NH$_3$ (3,3), NH$_3$ (4,4), NH$_3$ (5,5), NH$_2$D $3_{1,3}$–$3_{0,3}$, and NH$_2$D $4_{1,4}$–$4_{1,4}$ (black) extracted toward the continuum peaks of 4A1. The model spectra generated by 20 randomly selected parameter samples from the MCMC chains of the fits with fixed (blue) and free (orange) ortho-to-para ratios of NH$_3$ are overlaid. (bottom) Residual of observations and fitted model with fixed (blue) and free (orange) ortho-to-para ratio of NH$_3$. Each data point correspond to the randomly selected models from MCMC chains. The grey-shaded regions indicate $2\sigma_{\rm RMS}$ range. For both top and bottom panels, while the zero flux levels are indicated by grey dashed horizontal lines, the vertical dotted line indicate the systemic velocity.

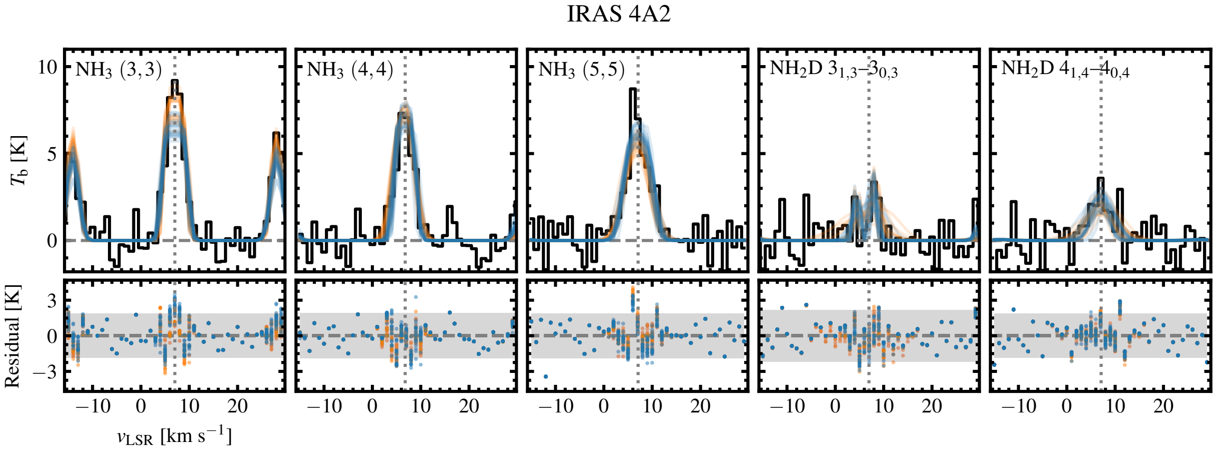

Figure 3.4. Same as Figure 3.3, but for 4A2.

et al. (2022, (0.6–3) × $10^{18}\,\mathrm{cm}^{-2}$ with a best-fit of 2 × $10^{18}\,\mathrm{cm}^{-2}$), our estimate for 4A1 (∼8 × $10^{17}\,\mathrm{cm}^{-2}$) is lower by a factor of a few than the estimates by De Simone et al. (2022, (1–5) × $10^{18}\,\mathrm{cm}^{-2}$ with a best-fit of 2 × $10^{18}\,\mathrm{cm}^{-2}$). In their work, the optically thin (7,7) transition allowed them to constrain the column density. Our analysis may indeed underestimate the NH_3 column density, particularly in 4A1. It is also possible that the column density of para-NH_3 that was constrained from NH_3 (4,4) and (5,5) is underestimated due to the lack of hyperfines; this might cause the peculiar ortho-to-para ratio in one of the fits. NH_2D/NH_3 best-fit ratios are still higher than the model prediction, 0.4 for 4A1 and 0.3 for 4A2, if we adopt the best-fit NH_3 column densities derived by De Simone et al. (2022).

Another possible caveat is that the kinetic gas motion could deviate the line profile from a simple Gaussian, which also could alter the estimation of column density and NH_2D/NH_3 ratios. The gas infall motion of the envelope can result in the blue-skewed or inverse P-Cygni profile, which has already been observed toward IRAS4A system (e.g. CH_3OH and H_2O lines, Di Francesco et al. 2001; Kristensen et al. 2012; Mottram et al. 2013; Sahu et al. 2019). Indeed, the observed spectra of NH_3 (3,3) and (4,4) toward 4A1 in Figure 3.3 show subtle deviations from Gaussian with rapid intensity decreases at the redshifted wings, which may trace the infall motion of the envelope, although it could also be due to the noise. The disk rotation could affect the line profile as well. The Keplerian rotation of the circumstellar disk with a significant inclination will result in a double-peaked profile. Although more sophisticated modeling that include these physical structures is desirable to more accurately evaluate the deuteration of NH_3, our results of high deuteration would not change qualitatively as no clear evidence of infall or rotation is detected at the current spatial/spectral resolution and sensitivity.

Finally, we note that the line widths are different among the observed transitions (Table 3.4). Particularly, the line widths of NH_3 (4,4) and (5,5) are broad compared to the other transitions[3], which may indicate that these transitions trace the more inner regions where the gas infall velocities are larger. If free-fall ($v \propto r^{-0.5}$) is assumed as the

---

[3] Although NH_2D $4_{1,4}$–$4_{0,4}$ toward 4A2 is also broad, we do not consider this as a robust result due to the relatively low S/N of the line.

gas kinetics, the difference in line widths between NH_3 (4,4) and (5,5) (~4 km s^{-1}) and the other transitions (~2 km s^{-1}) indicates the 4 times smaller radius of the emitting region for the former. We thus conducted the fit described in Section 3.3 using only NH_3 (3,3) and NH_2D transitions, all of which show a similar line width. Assuming an ortho-to-para ratio of NH_3 of unity, the column densities of NH_3 and NH_2D, and thus NH_2D/NH_3 ratios are consistent with those of fiducial fits in Table 3.4 within uncertainties. Therefore, the high NH_2D/NH_3 ratio should be trustworthy at the spatial scales traced by NH_3 (3,3) and NH_2D transitions (i.e., $\sim 0\farcs25$ or ~75 au).

Yet it is possible that the distributions of NH_3 (traced by (4,4) and (5,5)) and NH_2D are different at smaller spatial scales. Namely, the narrower line widths of NH_2D may imply that the line emission originates from more outer region than (4, 4) and (5, 5) NH_3 lines, e.g., a ring-like distribution of NH_2D. The NH_2D/NH_3 ratio derived in $\sim 0\farcs25$ scale then would be lower limit for the ring regions and upper limit for the inner region with higher velocity, while we need higher spatial and/or spectral resolution to confirm such radial distribution. The ring region of very high NH_2D/NH_3 ratio could be due to sublimation of multi-layered ice mantle (see Section 3.5.2)

3.5.2 Comparison with theoretical models and origin of high NH_2D/NH_3 ratios

Shah & Wootten (2001) detected NH_2D rotation-inversion transitions at 86 GHz and 110 GHz with the NRAO 12 m telescope. They derived NH_2D/NH_3 ratios of ~0.07 at ~24000 au scale in the circumbinary envelope of IRAS4A system. Hatchell (2003) also observed the 86 GHz transitions with the IRAM 30 m telescope to obtain NH_2D/NH_3 ratio of ~0.25 at ~7000 au scale. These values are consistent with predictions of theoretical models (e.g. Aikawa et al. 2012; Taquet et al. 2014; Furuya & Persson 2018). In those models, the molecular D/H ratios in the cold outer envelope (typically at radii outside a few hundreds of au) are controlled by the exothermic exchange reactions in the gas-phase. For example, NH_3 can be formed from NH, which is a product of dissociative recombination of N_2H^+; NH reacts with H_3^+ to form NH_2^+, which is converted to NH_4^+

via sequential reactions of H_2. NH_3 is formed by the dissociative recombination of NH_4^+. In dense cold regions, H_3^+ is highly deuterated due to the exchange reaction and CO depletion, and its high D/H ratio propagates to N_2H^+ and thus to NH_3 (e.g. Aikawa et al. 2005). If N atom is abundant in the cold region, NH_3 can be formed more efficiently via hydrogenation of N atoms on grain surfaces than via gas-phase reactions. They are also deuterated by abundant D atoms, which are formed by dissociative recombination of H_2D^+. NH_3 and NH_2D formed on cold grain surfaces, however, remain in the ice phase, and desorbed only inefficiently via non-thermal desorption at low temperatures (Hama & Watanabe 2013; Martín-Doménech et al. 2014; Tinacci et al. 2022).

In the central region (typically $\lesssim$100 au), on the other hand, temperature increases to $\gtrsim$100 K. Volatiles such as NH_3 start to sublimate from the grain surface and their gas-phase abundances rapidly increase. In this region, the molecular D/H ratios reflect those of sublimated ice (e.g, Furuya & Persson 2018). While the sublimated molecules are subject to gas-phase reactions, the typical destruction timescale via gas-phase reactions is $\sim$ several 10^4 yr (e.g. Nomura & Millar 2004). Even if we consider the enhanced ionization by X-rays (Notsu et al. 2021), the infall timescale would be shorter than chemical timescale in the compact hot corino region ($\lesssim$ 100 au). The high excitation temperature ($\gtrsim$ 100 K) and high column densities of NH_3 and NH_2D are indeed consistent with the ice sublimation. The derived NH_2D/NH_3 ratios ($\sim$0.5–1 from our analysis, or $\sim$0.3–0.4 adopting the NH_3 column density of De Simone et al. (2022)) are, however, significantly higher than predicted in Furuya & Persson (2018), i.e. a few % even in their N atom rich model.

Since our NH_2D/NH_3 ratios are similar to the ratio obtained in the outer envelope ($\sim$ 0.25) by Hatchell (2003), one may wonder if our observations partially trace the emission of NH_2D from the cold or intermediate temperature regions. While the estimated emitting region sizes, which can be used as a proxy of the sublimation region of NH_3, are $\sim$0.″25 or $\sim$75 au, the spatial resolution of our observations are much lower, i.e. $\sim$1″or $\sim$300 au. In addition, even intermediate temperatures (e.g., $\sim$50 K) could excite observed NH_3 and NH_2D transitions with the energy levels of 90–150 K from the ground state. We thus conducted a non-LTE radiative transfer simulation of a free-falling envelope model and compared the simulated spectra with the observed spectra (see Appendix E for details). We confirmed that the observed NH_2D emission is dominated by the emission from the hot corinos.

The very high NH_2D/NH_3 ratio and the possible ring-like distribution of NH_2D could be due to multi-layered structure of ice mantle. Taquet et al. (2014), who calculated gas-grain chemistry of a star-forming core as in Furuya & Persson (2018), explicitly showed the fractional abundances of icy molecules in each monolayer of ice mantle. While NH_2D/NH_3 is $\lesssim 10^{-2}$ in deep layers which are formed in the early times, the ratio is ~ 0.3 in the surface layers of ice when the dense prestellar core is about to collapse. As the ice-coated grains enter the central warm region of the core, the highly deuterated ice on the grain surface will be the first to sublimate.

Even though NH_2D may be distributed in a ring region, our observation suggests that N atom is the major nitrogen reservoir in molecular clouds. The NH_3 column density estimated from the (3, 3) transition, which has a similar line width as that of NH_2D, is similar to the column density derived from the combination with higher transitions (see Section 3.5.2). The ammonia formed in the cold prestellar stage with a high D/H ratio is thus at least comparable in amount to that in the innermost regions. Since icy ammonia is more efficiently formed via hydrogenation of N atoms on the grain surfaces than in the gas-phase, atomic nitrogen should be abundant and remains as the main nitrogen reservoir in prestellar core stage, where enhanced deuteration is possible. In the model of Taquet et al. (2014), which predicts relatively abundant NH_3 ice and very high NH_2D/NH_3 in the surface of ice mantle, nitrogen is assumed to be all atomic in their initial condition.

Furuya & Persson (2018) showed that the $[NHD_2/NH_2D]/[NH_2D/NH_3]$ ratio could better trace the primary nitrogen reservoir than the NH_2D/NH_3 ratio alone. If the atomic nitrogen is largely converted into the molecular form such as N_2 and NH_3 in the early stage of molecular clouds, most of ammonia ices should have formed by then, which results in relatively low NH_2D/NH_3 ratio. NHD_2 is yet formed mainly in the later prestellar stage, since it requires more deuterium atoms, and the NHD_2/NH_2D ratio will be higher than NH_2D/NH_3, i.e., $[NHD_2/NH_2D]/[NH_2D/NH_3] > 1$. On the other hand, if atomic nitrogen remains the dominant nitrogen reservoir in the prestellar phase, which is likely the case for IRAS4A, all the deuterated isotopologues will be formed in the prestellar phase, and $[NHD_2/NH_2D]/[NH_2D/NH_3]$ will be the statistical ratio ($\sim$1/3). Thus, observations of doubly-deuterated NH_3 emission are desirable to confirm our conclusion.

3.5.3 Comparison with other major species in hot corinos and comet 67P

The first measurement of NH_2D/NH_3 ratios achieved in this work enables us to compare the molecular D/H ratios among molecules in hot corinos. Comparison with cometary D/H ratios is also important, since the molecules in hot corinos could be incorporated to protoplanetary disks and then to planetary material. The D/H ratios of major species such as water and methanol in the inner warm regions of protostellar cores have extensively been studied toward several sources including IRAS4A (e.g., Persson et al. 2014; Jensen et al. 2019; Taquet et al. 2019). Recent in situ measurements on the comet 67P/Churyumov-Gerasimenko (hereafter 67P) by Rosetta project (Altwegg et al. 2019) has revealed the molecular D/H ratios in major volatiles. The observed molecular D/H ratios toward IRAS4A and comet 67P are summarized in Table 3.5. We note that the D/H ratios of water and methanol toward IRAS4A are available only toward 4A2 because the deuterated as well as normal isotopologues have not been detected in emission toward 4A1 in (sub-)millimeter wavelengths probably due to the absorption by the highly optically thick dust. We note that the following comparison stands even if we adopt the NH_3 column density derived in De Simone et al. (2022), which results in NH_2D/NH_3 $\sim$0.3.

Among water, methanol, and ammonia, water shows the lowest D/H ratios of $\sim 10^{-4}$ toward IRAS4A (Persson et al. 2014, see also Jensen et al. 2019). This has been interpreted as evidence that the water ices are mainly formed in the early molecular cloud phase (Furuya et al. 2016). We note that in the comparison of the D/H ratio among molecules, we need to take into account the number of hydrogen in the normal isotopologue; e.g., the chance for NH_3 to get one hydrogen replaced by deuterium is 3/2 times higher than for H_2O. The HDO/H_2O ratio is still significantly low compared with the deuteration fraction of CH_3OH and NH_3.

In contrast to water, methanol shows higher D/H ratios of $\sim 10^{-2}$ toward IRAS4A (Taquet et al. 2019), suggesting the formation of methanol ices in the cold prestellar core phase. Higher D/H ratios of methanol than water are also seen in other protostellar cores such as IRAS2A and IRAS 16293-2422 (Persson et al. 2014; Taquet et al. 2019; Jørgensen et al. 2018; Manigand et al. 2020). The D/H ratio of ammonia measured toward IRAS4A in this work ($\gtrsim 10^{-1}$) is higher than that of methanol. We note that the D/H ratio of NH_3 is still higher than that of methanol, even if we consider the statistical correction and uncertainties associated with the observations. The lower limit of NH_2D/NH_3 ratio is ~ 0.3 in 4A2 if we consider the uncertainty discussed in Section 3.5.1. This is higher than the upper limit of the (CH_2DOH + CH_3OD)/CH_3OH ratio by a factor of ~ 6 (Table 3.5). With the statistical correction, the D/H ratio of NH_3 is higher than that of CH_3OH by a factor of ~ 9. This indicates that the ammonia ices are mostly formed in the later stage of prestellar cores, possibly even later than the formation of methanol ices, where the deuteration is more efficient. Observations of ammonia deuteration towards other hot corinos are desirable to confirm that the high D/H ratio and late formation of ammonia ices are general.

The D/H ratios of water and methanol in the comet 67P shows a similar trend to those in IRAS4A (i.e., water D/H is lower than methanol, Altwegg et al. 2017, 2019; Drozdovskaya et al. 2019), suggesting the inheritance of the volatiles in the star-forming core to the planetary materials. The correlation in COMs abundances between the hot corinos and the comets also supports the inheritance (Drozdovskaya et al. 2019; Bianchi et al. 2019). On the other hand, the D/H ratio of ammonia in the comet 67P is lower than methanol, which is different from the relation in the IRAS4A. It suggests some chemical reprocessing for ammonia ices, or nitrogen as a whole, during the accretion onto the protostellar disk or subsequent protoplanetary disk stage. In the coma of comet 67P, Altwegg et al. (2020a) recently detected a substantial amount of ammonium salts, which implies the chemical processes of ammonia. Alternatively, 67P inherits the low D/H component of ammonia, which is probed as high-velocity component in our observation, while the high D/H component is fully released to the gas-phase as discussed in Section 3.5.1. Indeed, Furuya et al. (2017) showed that stellar UV radiation can selectively remove the high D/H component from the surface of the ice via photodesorption, and the D/H ratios of water can be lower in the protoplanetary disk than those in protostellar envelopes. The same mechanism may work for ammonia as well.

3.5.4 Physical properties of 4A1 and 4A2 cores probed by NH_3 and NH_2D

Although the detailed modeling of the line profiles are difficult due to the relatively low S/N and poor velocity resolutions, several implications about the physical and chemical structures of the 4A1 and 4A2 cores including their similarities and differences can be obtained based on the results of our hyperfine fits.

The derived excitation temperatures are significantly different between 4A1 and 4A2; i.e. the excitation temperature in 4A2 ($\sim$150 K) is higher than that in 4A1 ($\sim$100 K). This difference is also clearly indicated by the higher peak brightness temperature in 4A2 (Figure 3.4). Since the excitation is expected to be thermalized, i.e., satisfies the LTE condition, the excitation temperatures can be directly used as a proxy of kinetic temperature. A similar trend has already been suggested by De Simone et al. (2020); they have detected the optically thick CH_3OH emission to estimate the kinetic temperature of 100 K and 160 K for 4A1 and 4A2, respectively. The emitting region sizes of CH_3OH in De Simone et al. (2020) ($0\overset{''}{.}20$–$0\overset{''}{.}30$) are similar to the NH_3 emitting region sizes derived in the present work, suggesting that both CH_3OH and NH_3 trace the region with the similar temperatures (see also De Simone et al. 2022). This is reasonable given that the sublimation temperature of CH_3OH and NH_3 are expected to be similar (100–140 K depending on the gas densities and major composition of ice; e.g., Furuya & Aikawa 2014; Hama & Watanabe 2013; Minissale et al. 2022). The lower temperature of 4A1 may reflect either higher column density of the dust or lower stellar and accretion luminosities.

The difference in the NH_2D/NH_3 ratios between 4A1 and 4A2 may in fact reflect the difference in the temperature. As discussed in the previous subsections, ices on the grain surface are expected to consist of two layers; the bulk mantle with lower deuteration formed in the molecular cloud stage and the surface component with higher deuteration synthesized in the dense core stage (e.g., Taquet et al. 2013; Furuya et al. 2016; Furuya

& Persson 2018). Thus, the higher NH_2D/NH_3 with a lower temperature in 4A1 may indicate that only the NH_3 ices in the surface layer have sublimated.

3.6 Summary

We have observed NH_3 and NH_2D high excitation transitions at $\sim 1''$resolution toward the protobinary NGC1333 IRAS4A with the VLA to measure the NH_2D/NH_3 ratio in the warm gas around the protostars, where ammonia ices have sublimated. Our main findings are summarized as follows:

1. We have detected the NH_3 (1,1) to (5,5) inversion transitions with S/N of $\gtrsim$10 toward both of the sources, 4A1 and 4A2. We have also detected NH_2D $3_{1,3}$–$3_{0,3}$ and $4_{1,4}$–$4_{0,4}$ rotation transitions with S/N of $\sim$5 toward 4A1, while they have been marginally detected with S/N of $\sim$3–5 toward 4A2.

2. We have estimated the excitation temperature and column density of NH_3 and NH_2D, and NH_2D/NH_3 column density ratios from the spectral line fitting. We found high NH_3 and NH_2D column densities of $\sim 10^{17}$–10^{18} cm^{-2} with high excitation temperatures ($\gtrsim$100 K) for both 4A1 and 4A2, indicating that the NH_3 and NH_2D lines originate from the inner warm regions. The NH_2D/NH_3 ratios are remarkably high, $\sim$0.5–1. The ratio is $\gtrsim$0.3, even if we take into account the slightly higher NH_3 column density derived by De Simone et al. (2022).

3. The high NH_2D/NH_3 ratios indicate the efficient formation of ammonia ices in the prestellar core stage, which in turn suggests that the primary nitrogen reservoir in molecular clouds is atomic nitrogen rather than nitrogen-bearing molecules such as N_2 and NH_3.

4. In IRAS4A1, the line widths of NH_2D are similar to that of NH_3 (3, 3) transition, but are narrower than those of NH_3 higher transitions. It may indicate a ring-like distribution of NH_2D. The ring-like distribution of NH_2D and very high NH_2D/NH_3 ratio could be due to sublimation of multi-layered ice mantle. The highly deuterated

NH_3 ice is formed in the outermost layer of the ice mantle in the late stage of prestellar core and is the first to be sublimated when the grains fall onto the central warm regions.

5. The obtained D/H ratios of ammonia ices have been compared with those of other major volatiles in the IRAS4A core and the comet 67P. The higher D/H ratios of ammonia than those of water and methanol in IRAS4A indicate that ammonia ices are formed in the later stage of the prestellar core phase, where the deuteration is particularly efficient. The higher NH_2D/NH_3 ratio in IRAS4A than that in the comet 67P may suggest that chemical reprocessing during the accretion onto the protostellar disk and subsequent protosplanetary disk phase. Alternative explanation is sublimation of highly deuterated layer of ice mantle in IRAS4A.

Table 3.5 Molecular D/H Ratios Measured toward the Inner Warm Region of the IRAS4A2 Core and the Comet 67P/C-G

Source	HDO/H_2O	$(CH_2DOH + CH_3OD)/CH_3OH$	NH_2D/NH_3	References
IRAS4A	$5.4 \pm 1.5 \times 10^{-4}$	$(1.5–4.7) \times 10^{-2}$	$4.8^{+1.7}_{-1.3} \times 10^{-1}$	1,2,3,4
67P/C-G	$1.05 \pm 0.14 \times 10^{-3}$	$5.6 \pm 1.2 \times 10^{-2}$	$\sim 1 \times 10^{-3}$	5,6,7

References. (1) Persson et al. (2014); (2) Jensen et al. (2019); (3) Taquet et al. (2019); (4) this work; (5) Altwegg et al. (2017); (6) Drozdovskaya et al. (2021); (7) Altwegg et al. (2019).

Note. — The values in IRAS4A2 are shown as the representatives of the IRAS4A system.

Chapter 4

Chemistry of Complex Organic Molecules in the V883 Ori Disk Revealed by ALMA Band 3 Observations

This thesis chapter originally appeared in the literature as
Yoshihide Yamato, Shota Notsu, Yuri Aikawa, Yuki Okoda, Hideko Nomura, & Nami Sakai, *The Astronomical Journal*, 2024, Vol. 167, id. 66. *I led the data reduction, analysis, and discussion, while data acquisition were made by S. Notsu.*

Abstract

Complex organic molecules (COMs) in protoplanetary disks are key to understanding the origin of volatiles in comets in our solar system, yet the chemistry of COMs in protoplanetary disks remains poorly understood. Here we present Atacama Large Millimeter/submillimeter Array (ALMA) Band 3 observations of the disk around the young out-

bursting star V883 Ori, where the COMs sublimate from ices and are thus observable thanks to the warm condition of the disk. We have robustly identified ten oxygen-bearing COMs including ^{13}C-isotopologues in the disk-integrated spectra. The radial distributions of the COM emission, revealed by the detailed analyses of the line profiles, show the inner emission cavity, similar to the previous observations in Band 6 and Band 7. We found that the COMs abundance ratios with respect to methanol are significantly higher than those in the warm protostellar envelopes of IRAS 16293-2422 and similar to the ratios in the solar system comet 67P/Churyumov-Gerasimenko, suggesting the efficient (re-)formation of COMs in protoplanetary disks. We also constrained the ^{12}C/^{13}C and D/H ratios of COMs in protoplanetary disks for the first time. The ^{12}C/^{13}C ratios of acetaldehyde, methyl formate, and dimethyl ether are consistently lower (~ 20–30) than the canonical ratio in the interstellar medium (~ 69), indicating the efficient ^{13}C-fractionation of CO. The D/H ratios of methyl formate are slightly lower than the values in IRAS 16293-2422, possibly pointing to the destruction and reformation of COMs in disks. We also discuss the implications for nitrogen and sulfur chemistry in protoplanetary disks.

4.1 Introduction

Our Solar System formed from its protoplanetary disk, or the proto-solar disk, a byproduct of the Sun's formation via the gravitational collapse of the parent molecular cloud. Observations have found many volatile ices in solar system comets, which should contain information about the chemical composition of the solar nebula, suggesting that the proto-solar disk was rich in volatiles such as water and organics. Organic molecules are of particular interest because they could be the precursors of the prebiotic molecules that may have given rise to life on Earth. (Ceccarelli et al. 2023).

The origin of the cometary water and organics has been extensively discussed but remains controversial. The most commonly discussed possibility is that the cometary ices are, at least in part, inherited from the interstellar medium (ISM) through the formation of the Solar System. For example, the higher D_2O/HDO ratio than the HDO/H_2O ratio in both the warm inner envelopes of protostars (Coutens et al. 2014; Jensen et al. 2021) and a solar system comet (Altwegg et al. 2017) strongly suggests the inheritance of water from the ISM rather than the chemical reset (e.g., destruction and reformation). Organic molecules have also been detected in both protostellar envelopes and solar system comets (e.g., Jørgensen et al. 2016; Rubin et al. 2019). In the warm inner envelopes heated by the central protostar, organic molecules are thermally desorbed from the grain surfaces at a typical sublimation temperature of $\sim 100\,\mathrm{K}$, allowing us to observe them in the gas phase. Among these molecules, carbon-bearing molecules with six or more atoms are empirically referred to as complex organic molecules (COMs). The composition of COMs in protostellar envelopes is compared with that in comets, from which the possible inheritance of COMs from the prestellar and protostellar phases is discussed (e.g., Drozdovskaya et al. 2019).

Observations of COMs in protoplanetary disks are rather sparse compared to those in protostellar envelopes, since COMs are mainly locked into ices due to the colder nature (<100 K) of typical disks around T Tauri stars. Relatively simple organic molecules such as CH_3OH, CH_3CN, and HCOOH, which are non-thermally desorbed and/or formed via the gas-phase chemistry in the outer cold region, are detected in a handful of disks (Walsh et al. 2016; Öberg et al. 2015; Bergner et al. 2018; Loomis et al. 2018a; Ilee et al. 2021; Favre et al. 2018), but these observations do not directly trace the bulk composition of COMs hidden in the ice mantles. Recently, high-sensitivity observations with Atacama Large Millimeter/submillimeter Array (ALMA) have just begun to detect the emission of thermally desorbed COMs in warm disks around Herbig Ae/Be stars (van der Marel et al. 2021; Booth et al. 2021b; Brunken et al. 2022; Booth et al. 2023b), but the detections are still limited to a few numbers of disks and molecular species. Since protoplanetary disks could be potential sites for the chemical reset from the ISM (e.g., Walsh et al. 2014; Furuya & Aikawa 2014; Eistrup et al. 2016), constraining the composition and distribution of COMs in disks is crucial to fully understand the chemical evolution during star and planet formation.

Recent observations of the disk around the young outbursting star, V883 Ori, have opened a new window to COMs in protoplanetary disks. V883 Ori is a low-mass ($M_\star = 1.3\,M_\odot$; Cieza et al. 2016) FU Orionis type object located in the L1641 cluster in the Orion molecular clouds ($d \approx 400\,\mathrm{pc}$; Strom & Strom 1993) with a well-developed Keplerian-rotating disk (Cieza et al. 2016), which shows a large-amplitude outburst in the optical ($\Delta m_\mathrm{V} > 4\,\mathrm{mag}$) with an increased luminosity of $\sim 200\,L_\odot$ (Furlan et al. 2016). This high luminosity warms the disk and shifts the sublimation front (or snowline) of water and COMs (Tobin et al. 2023), allowing for observing thermally desorbed molecules in the disk. In addition, because the duration of the outburst ($\sim 10^2\,\mathrm{yr}$) is shorter than the timescale of the typical gas-phase chemical reaction (several $10^4\,\mathrm{yr}$; e.g., Nomura et al. 2009), it is possible to observe the fresh sublimates without significant gas-phase chemical changes and probe the composition of disk ices almost directly. van 't Hoff et al. (2018b) detected CH_3OH emission for the first time in this disk with high-resolution ($\sim 0\farcs14$) ALMA Band 7 observations, followed by the additional detection of several COMs such as CH_3OCHO, CH_3CHO, and CH_3CN in ALMA Band 7 at $\sim 0\farcs1$ resolution (Lee et al. 2019). These COM emissions all show the velocity structure consistent with the Keplerian rotation traced by the $C^{18}O$ emission (Cieza et al. 2016; van 't Hoff et al. 2018b), proving that the COM emission originates from the rotationally supported disk. The COM emission spreads over 40–120 au radii with an inner emission cavity ($\lesssim 40\,\mathrm{au}$ radius), similar to the spatial distribution of the water emission (Tobin et al. 2023). Lee et al. (2019) compared the abundances of a few COMs with respect to CH_3OH, the simplest COM, with those in the warm envelopes of the Class 0 protostar IRAS 16293-2422 B (hereafter IRAS 16293B; e.g., Jørgensen et al. 2016) and the solar system comet 67P/Churyumov-Gerasimenko (hereafter 67P/C-G; e.g., Altwegg et al. 2019). They found that the abundances of COMs in the V883 Ori disk are generally higher than those in IRAS 16293B (except for CH_3CN) and similar to those in 67P/C-G, suggesting potential chemical evolution in protoplanetary disks.

However, there are several limitations to these observations. First, in ALMA Band 7, i.e., the sub-mm wavelengths, the intense dust continuum emission obscures the molecular line emission in the innermost region ($\lesssim 40\,\mathrm{au}$ radius), resulting in an apparent inner cavity in the molecular line emission (van 't Hoff et al. 2018b; Lee et al. 2019; Tobin et al. 2023). This necessitates observations at longer wavelengths, where the dust continuum emission is generally expected to be fainter, to investigate the chemical composition there, i.e., the comet- and terrestrial-planet-forming zone. Second, the limited number of unambiguously detected species (Lee et al. 2019) makes it difficult to derive a general and concrete picture of chemical evolution in protoplanetary disks. Third, previous observations did not measure the isotopic ratios (e.g., ^{12}C/^{13}C and D/H) of COMs (except for the D/H ratio of CH_3OH; Lee et al. 2019), the most sensitive chemical fingerprint for tracing the formation conditions and thermal history.

In this chapter, we present the new observations of COMs toward the V883 Ori disk in ALMA Band 3. Observational and imaging details are described in Section 4.2, followed by a detailed analysis of the disk-integrated spectra in Section 4.3 where we report the first (tentative) detection of several species including ^{13}C- and D-isotopologues. We discuss the implications of the present observations for the physical and chemical structure of the V883 Ori disk, as well as for the chemical composition and isotopic chemistry of COMs in protoplanetary disks in Section 4.4. We finally summarize the present work in Section 4.5.

4.2 Observations

4.2.1 ALMA Band 3 Observations

V883 Ori was observed in Band 3 during ALMA Cycle 8 (project code: 2021.1.00357.S, PI: S. Notsu). The observations were carried out in a total of four executions, one with a compact antenna configuration and the other three with an extended antenna configuration. The observation dates, number of antennas, on-source integration time, precipitable water vapor (PWV), baseline coverage, angular resolution, maximum recoverable scales (MRS), and calibrator information are listed in Table 4.1.

The correlator setup included eleven spectral windows (SPWs) in Frequency Division Mode (FDM), one of which was dedicated to continuum acquisition with a wide bandwidth of 937.5 MHz for an accurate determination of the continuum level. The frequency resolution of the continuum SPW was 0.488 MHz, resulting in a velocity resolution of ∼1.5 km s^{-1}. The continuum SPW included many spectral lines of COMs. Other ten SPWs targeted specific spectral lines with narrower bandwidths of 58.59 MHz or 117.19 MHz, which also covered many COMs lines. The frequency resolution of these SPWs was 0.141 MHz, resulting in a velocity resolution of ∼0.4–0.5 km s^{-1}. The detailed properties of the SPWs are summarized in Table 4.2. We note that two SPWs (8 and 9) were partially overlapped, and only the wider SPW 9 is used for analysis.

4.2.2 Calibration and Imaging

Initial calibrations were performed by the ALMA staff using the standard ALMA calibration pipeline version 2021.2.0.128. Subsequent self-calibration and imaging were performed using the Common Astronomy Software Applications (casa; CASA Team et al. 2022) version 6.2.1.7. The pipeline-calibrated data were first imaged without any deconvolution (i.e., dirty imaging) or continuum subtraction to accurately specify the line-free channels by visually inspecting the dirty image cubes. These line-free channels are averaged to obtain the continuum visibilities. The continuum emission peak on the image from each execution block was aligned to a common direction, $\alpha(\mathrm{ICRS}) = 05^{\mathrm{h}}38^{\mathrm{m}}18\overset{\mathrm{s}}{.}101$, $\delta(\mathrm{ICRS}) = -07^{\mathrm{d}}02^{\mathrm{m}}26\overset{\mathrm{s}}{.}00$, which was used as the disk center in the following analysis. Self-calibration was then performed using the continuum visibilities with the `gaincal` and `applycal` tasks. A round of each phase-only and amplitude self-calibration was first performed on the data with a compact antenna configuration. The extended antenna configuration data were then concatenated and self-calibrated together. Two rounds of phase-only self-calibration and one round of amplitude self-calibration were performed on the combined data. The solutions were then applied to the spectral line visibilities.

The combined dust continuum image at 3.3 mm (or 92 GHz) was made using the `tclean` task with the Briggs weighting (`robust` = 0.5) and is shown in Figure 4.1. The beam size and the RMS noise level were $0\overset{''}{.}39 \times 0\overset{''}{.}27$ (P.A. = −74°) and 27 μJy beam^{-1}, respectively. We performed a Gaussian fit to the continuum image using the `imfit` task and obtained a deconvolved size of $0\overset{''}{.}23 \times 0\overset{''}{.}21$ (P.A. = 106°), indicating that the dust continuum disk is marginally spatially resolved. The brightness temperature at the disk center was ∼ 65 K, which was lower than that of the higher-resolution Band 6 image

(Cieza et al. 2016) mainly due to the beam dilution effect.

As for the line image cubes, each of the SPWs was imaged using the `tclean` task (Högbom 1974) with Briggs weighting (`robust` = 0.5). The `tclean` task was run in parallel using `mpicasa` implementation. As a specific weighting scheme, `briggsbwtaper` was used with independent weight densities for each channel (i.e., `perchanweightdensity = True`) to achieve more uniform sensitivity across channels. For each SPW, a common restoring beam across all channels was used. A few channels at the edge of the SPW were removed during the imaging process due to the large deviation in beam size caused by a slight difference in the frequency coverage between the data with compact and extended antenna configurations[1]. All SPWs were cleaned down to $3 \times$ RMS with the native channel widths. An automatic masking algorithm with `automultithresh` was also used to generate the CLEAN mask. The typical beam size and the RMS noise level were $\sim 0\farcs3$–$0\farcs4$ and 0.6–1 mJy beam^{-1}, respectively. The beam sizes were comparable to the emitting region sizes of COM emission in Band 6 and Band 7 (Lee et al. 2019; Tobin et al. 2023). The RMS noise level was measured on the images without primary beam correction. The beam sizes and RMS noise levels for each SPW are listed in Table 4.2. We adopt a 10% uncertainty as an absolute flux calibration accuracy[2]. Finally, the continuum component is subtracted from these image cubes using the `imcontsub` task to produce the spectral-line-only image cubes. The continuum subtraction on the image plane instead of the visibility plane (e.g., with the `uvcontsub` task) mitigates as much as possible the Jorsater & van Moorsel (JvM) effect (Jorsater & van Moorsel 1995; Czekala et al. 2021) on the line emission, which is critical for the flux scale (see Appendix G). Throughout this paper, we use the image cubes that were continuum-subtracted on the image plane, unless otherwise noted.

---

[1] See `https://casadocs.readthedocs.io/en/stable/notebooks/memo-series.html#Correcting-bad-common-beam`.

[2] See Chapter 10.2.6 of ALMA Cycle 8 2021 Technical Handbook (`https://almascience.nao.ac.jp/documents-and-tools/cycle8/alma-technical-handbook`)

Table 4.1 Observational Details

Date	# of Ant.	On-source Int. (min)	PWV (mm)	Baseline (m)	Ang. Res. (″)	MRS (″)	Bandpass/Amplitude Cal.	Phase Cal.
2021 Nov. 21	44	43	2.2	41–3396	0.3	5.2	J0423-0120	J0541-0541
2021 Nov. 21	44	43	2.0	41–3396	0.3	5.2	J0538-4405	J0541-0541
2021 Nov. 22	43	43	3.8	41–3396	0.3	4.7	J0423-0120	J0541-0541
2022 Jan. 20	41	47	3.6	14–740	1.5	17.4	J0423-0120	J0541-0541

Table 4.2 Properties of Image Cubes

SPW	Cent. Freq. (GHz)	# of Chan.	Bandwidth (MHz)	Channel Width		Vel. Res. ($\mathrm{km\,s^{-1}}$)	Beam Size (P.A.)	RMS ($\mathrm{mJy\,beam^{-1}}$)
				(MHz)	($\mathrm{km\,s^{-1}}$)			
0	85.160960	478	58.229	0.122	0.43	0.51	$0\farcs42\times0\farcs31$ ($-75°$)	1.1
1	85.530202	478	58.229	0.122	0.43	0.50	$0\farcs42\times0\farcs31$ ($-75°$)	1.0
2	85.851713	478	58.229	0.122	0.43	0.50	$0\farcs42\times0\farcs31$ ($-75°$)	0.99
3	85.924957	478	58.229	0.122	0.43	0.50	$0\farcs41\times0\farcs31$ ($-75°$)	0.99
4	86.669481	478	58.229	0.122	0.42	0.50	$0\farcs41\times0\farcs31$ ($-75°$)	0.94
5	86.752980	958	116.824	0.122	0.42	0.50	$0\farcs41\times0\farcs31$ ($-75°$)	0.94
6	87.327244	478	58.229	0.122	0.42	0.49	$0\farcs41\times0\farcs31$ ($-75°$)	0.98
7	96.490854	478	58.229	0.122	0.38	0.45	$0\farcs37\times0\farcs28$ ($-75°$)	1.0
8	96.743210	478	58.229	0.122	0.38	0.45	$0\farcs37\times0\farcs27$ ($-75°$)	0.99
9	96.754197	958	116.824	0.122	0.38	0.45	$0\farcs37\times0\farcs27$ ($-75°$)	0.99
10	97.979676	3839	937.036	0.244	0.75	1.5	$0\farcs36\times0\farcs26$ ($-73°$)	0.59

4.3 Data Analysis and Result

4.3.1 Spectrum Extraction and Line Identification

Figure 4.2 shows the spectra integrated over $1''\!.2$ aperture and corrected for the line broadening due to the Keplerian rotation of the disk. The original disk-integrated spectra are shown in Figures I.1–I.4 in Appendix I. More zoom-in spectra with the Keplerian rotation correction are also shown in Figures I.5–I.8 in Appendix I. To obtain the spectra corrected for the Keplerian line broadening, we use the `integrated_spectrum()` function implemented in the Python package `gofish` (Teague 2019). This method first deprojects the disk and then aligns the Dopper-shifted spectra at each position within the disk to a common velocity (the systemic velocity of the source) to recover the single peak spectra for each transition, facilitating the identification of the blended transitions. In this procedure, we assume a position angle (32°) and inclination angle (38.3°) of the disk, a central stellar mass of $1.29\,M_\odot$, and a distance of 400 pc, based on previous works (Cieza et al. 2016; Tobin et al. 2023). We also assume that the emission originates from the midplane of the disk, and do not consider the vertical extent of the emission. The uncertainties of the spectra are calculated per channel basis within the `integrated_spectrum()` function taking into account the spectral decorrelation (Yen et al. 2016).

As shown in Figure 4.2, numerous spectral features are detected in the disk-integrated spectra. Since many of the COM transitions exist in narrow frequency ranges and overlap between different molecular species, visual identification of the lines is challenging. Alternatively, we fitted a synthetic spectrum to the observed spectra to identify each of these features. The details of the synthetic spectral model are described in Appendix J. Briefly, the model used a common emitting region size, a common excitation temperature, and a common line width under the local thermodynamic equilibrium (LTE) conditions. We varied the emitting region size, excitation temperature, line width, and the column density of each species to fit the observed spectra, and test if they could be reproduced with the model. To construct the model, the spectroscopic data of the molecular lines are taken from the Jet Propulsion Spectroscopy (jpl; Pickett et al. 1998) and the Cologne Database for Molecular Spectroscopy (CDMS; Müller et al. 2001, 2005; Endres et al.

2016), as detailed in Appendix L. Only the transitions with an Einstein A coefficient for spontaneous emission of $\geq 10^{-8}\,\mathrm{s}^{-1}$ and an upper state energy of $\leq 1000\,\mathrm{K}$, which are detectable under the physical condition of the V883 Ori disk, are considered in the model.

Following Jørgensen et al. (2020), we set two criteria for the identification of molecular species. First, the synthetic spectrum of multiple (more than one) transitions of a given species accounts for the observed spectra including at least one detected transitions that is not blended with transitions of other species. Second, no undetected transitions are over-predicted by the synthetic spectrum. Species that fulfill the second criterion but with no unblended transitions detected are considered as tentative identifications. Based on these criteria, we robustly identified 10 species and their isotopologues: CH_3OH, CH_3CHO, CH_3OCHO, CH_3OCH_3, c-C_2H_4O, CH_3COCH_3, t-C_2H_3CHO, s-C_2H_5CHO, $^{13}CH_3OCHO$, and $CH_3O^{13}CHO$. We also tentatively identified 6 species and isotopologues: $CH_3^{13}CHO$, $^{13}CH_3OCH_3$, CH_2DOH, CH_2DCHO, CH_3CDO, and C_2H_3CN. In addition, one transition of each sulfur-bearing molecule (OCS and SO_2) was detected. The detected transitions are listed in Table H.1 in Appendix H. In addition to the disk-integrated spectra for the full frequency range in Figures I.1–I.8, we also present the zoom-in spectra of $^{13}CH_3OCHO$ and $CH_3O^{13}CHO$ in Figure I.9 in Appendix I for the purpose of visually clarity to confirm the detection of these species.

4.3.2 Spatial Distributions

Velocity-integrated Intensity Maps

Figure 4.1 shows the velocity-integrated intensity map (zeroth moment map) of the selected transitions without significant blending with other species. These maps are created using `bettermoments` (Teague & Foreman-Mackey 2018) by integrating over the velocity range of ± 3.5 km s^{-1} with respect to the source systemic velocity ($v_{\mathrm{sys}} = 4.25$ km s^{-1}; Tobin et al. 2023) without any masking. For CH_3OCH_3 and CH_3COCH_3, multiple blended transitions of each species are integrated together. For these molecules, the integration range is the combination of the default integration range (± 3.5 km s^{-1}) for the multiple blended transitions. The molecular line emission is all confined to the disk region ($\sim 0\farcs3$

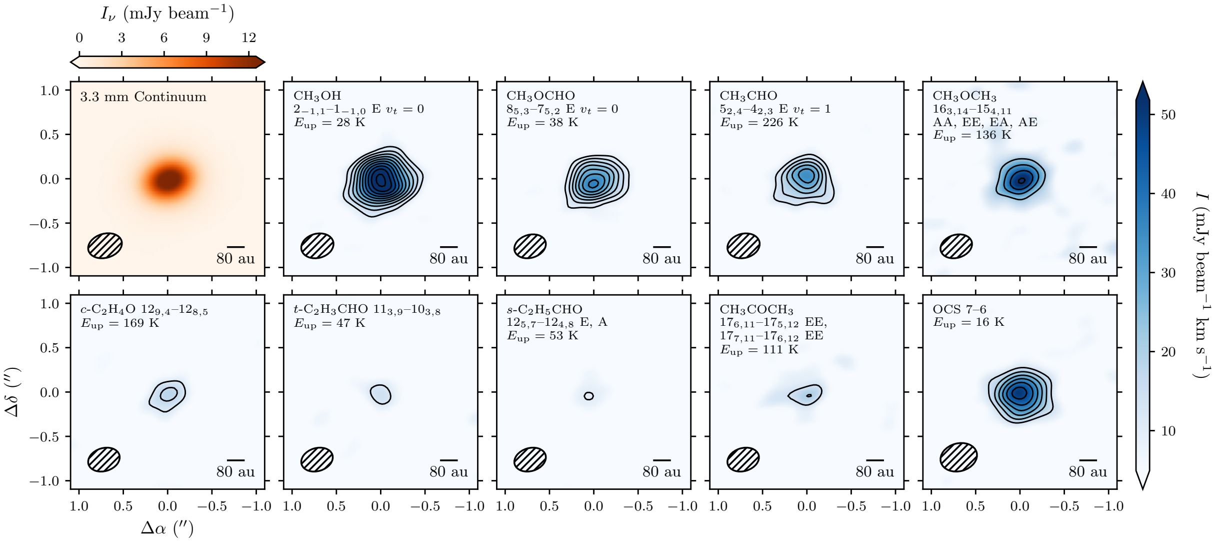

Figure 4.1. The 3.3 mm dust continuum image (left top) and the velocity-integrated intensity maps of the molecular line emission (others) in the V883 Ori disk. The velocity range for integration are ±3.5 km s^{-1} with respect to the source systemic velocity $v_{\rm sys}$ = 4.25 km s^{-1} (Tobin et al. 2023) including CH_3OCH_3 and CH_3COCH_3, where multiple blended transitions are integrated together. The molecular species, transitions, and upper state energy levels are indicated in the upper-left corner of each panel. The black contours start from 5σ with steps of 2.5σ, where σ are the noise level of each map measured on the emission-free region, spanning σ = 1.8–4.4 mJy beam^{-1} km s^{-1} depending on the maps. The synthesized beam and a scale bar of 80 au are shown in the lower left and right corner of each panel, respectively.

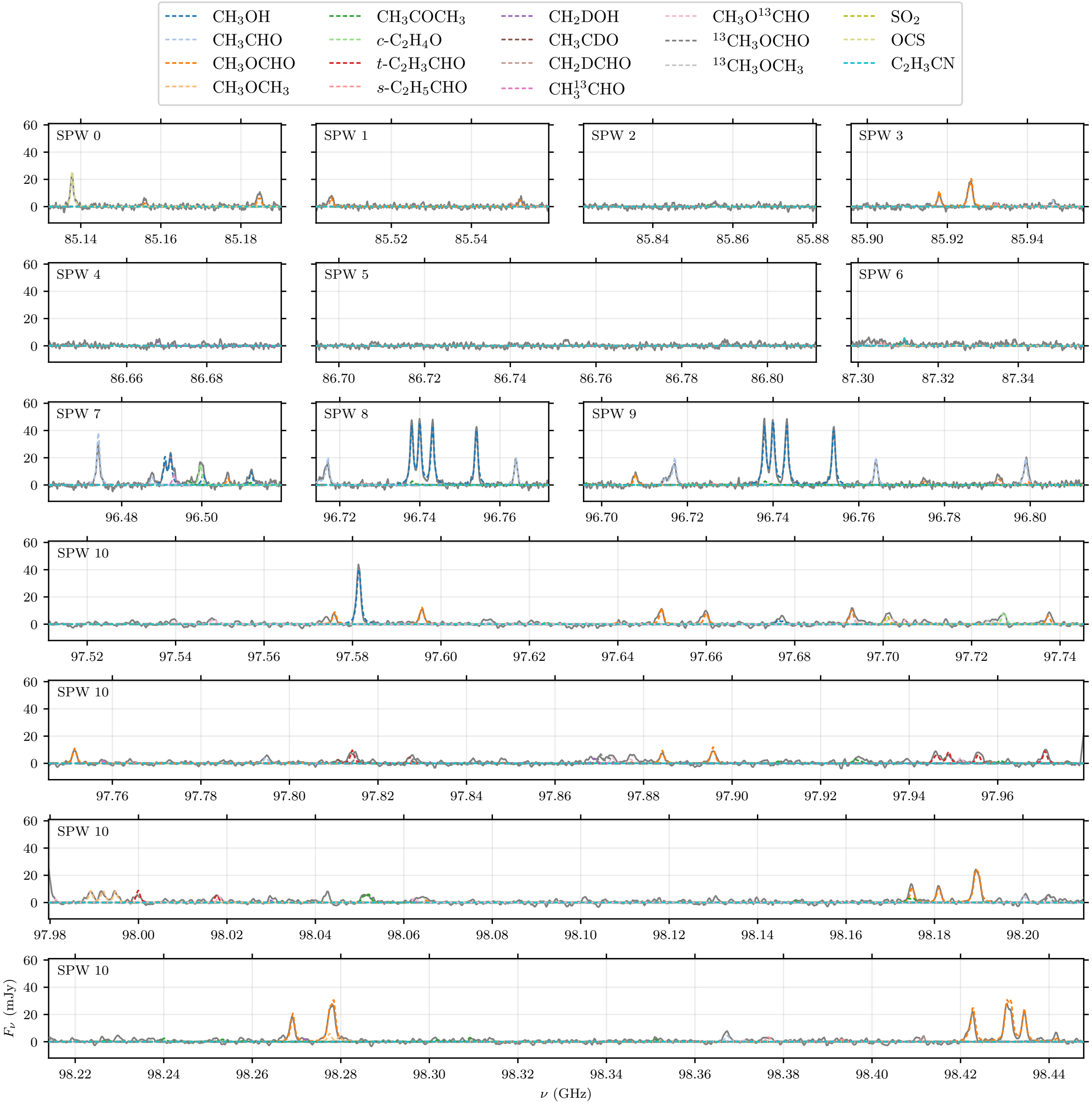

Figure 4.2. Spectra corrected for Keplerian rotation toward the V883 Ori disk (gray). The model spectra for each species are shown in colored lines.

or ~ 120 au radius) and is marginally spatially resolved. While the spatial extent of the emission is consistent with previous ALMA observations in Band 6 and Band 7 (van 't Hoff et al. 2018b; Lee et al. 2019; Tobin et al. 2023) considering the difference in the beam size, the central emission cavities seen in the Band 6/7 data are not detected in these maps at the current spatial resolution of $\sim 0\farcs3$.

Line Profile Analysis

As the disk emission is only marginally spatially resolved, it is difficult to directly infer the distribution of the emission in the inner region, particularly the emission cavity seen in the sub-mm line observations in Bands 6 and 7 (van 't Hoff et al. 2018b; Lee et al. 2019; Tobin et al. 2023). Alternatively, we can indirectly probe the emission in the inner region, which is not spatially resolved in the velocity-integrated intensity maps (Figure 4.1), from the line profile by assuming gas kinematics. For the line emission of gas in a Keplerian-rotating disk, the high-velocity components with respect to the systemic velocity, or the line wings, purely contain information about the emission from the inner region. More specifically, the maximum velocity of Keplerian rotation as a function of disk radius ($v_{\rm max}(r)$) can be written as

$$v_{\rm max}(r) = \sqrt{\frac{GM_\star}{r}} \sin i, \tag{4.1}$$

where G is the gravitational constant, $M_\star$ is the central stellar mass, and i is the inclination of the disk. The V883 Ori disk has been revealed to be a Keplerian-rotating disk by the higher-resolution observations in Bands 6 and 7 (Cieza et al. 2016; Lee et al. 2019). To confirm this in the present Band 3 data, we examined the line profiles of three bright transitions of $\rm CH_3OH$, $\rm CH_3CHO$, and $\rm CH_3OCHO$ (Figure 4.3). These line profiles are all double-peaked, consistent with the Keplerian rotation. We then compared these profiles with the maximum velocity of Keplerian rotation at certain radii (Equation 4.1) in Figure 4.3. As seen in the line wings of each line profile, no significant emission is detected in the velocity channels corresponding to $\lesssim 40$ au radius. The channel maps (Figures F.1, F.2, and F.3) also show no significant emission at $\lesssim 40$ au radius.

To quantitatively assess the contribution of the emission at each radius, we used a forward modeling approach to reconstruct the radial intensity profiles from the line profiles. Using the relation in Equation (4.1), the radial intensity profile (as a function of radius) can be constructed from the line profile (as a function of velocity) as demonstrated in Bosman et al. (2021b). We used an approach similar to that of Bosman et al. (2021b) to construct the radial intensity profiles of the aforementioned three bright transitions from their line profiles. Details of the modeling can be found in Appendix K. Figure 4.4 shows the reconstructed radial intensity profiles of these three transitions. All three transitions show the depression in the innermost region with a radial peak at $\sim$ 50–60 au, which is consistent with the higher-resolution Band 6 profile (Tobin et al. 2023). This suggests that the bulk of the observed Band 3 emission can be explained by emission from the 40–80 au region, and that the inner emission cavity likely exists even in the Band 3 emission as well.

4.3.3 Column Density Retrieval

To derive the disk-averaged column density of each species, we first employ a simultaneous fit of an LTE spectral model to the extracted spectra, taking into account the spectral blending and line optical depth. The same spectral model is used as for line identification (see Appendix J for details), where all (tentatively) identified species as in Section 4.3.1 are considered. We excluded the optically thick ($\tau > 0.2$) transitions from the fit (except for OCS which only have one detected transition) to minimize the optical depth effect; the selection is based on the optical depth at the line center in the best-fit model for line identification (Section 4.3.1). Specifically, we excluded the transitions of abundant species (e.g., CH_3OH, CH_3OCHO, and CH_3CHO) with a large Einstein A coefficient and a relatively low upper state energy. The excluded transitions are indicated in Table H.1 in Appendix H. The optical depth threshold of 0.2 is determined to minimize the optical depth effect while leaving a sufficient number of transitions available for the fit. When higher optical depth threshold of $\tau > 0.4$ is adopted, the resulting column densities are lower by a factor of ~ 2 or less. Although such difference does not change the conclusion of this paper, we employ the threshold value of 0.2 to discuss the result carefully.

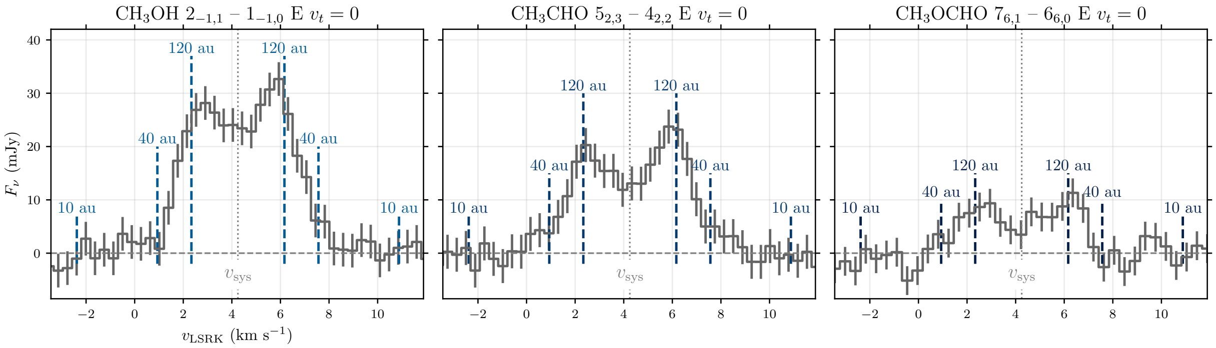

Figure 4.3. Line profiles of CH$_3$OH $2_{-1,1} - 1_{-1,0}$ E $v_t = 0$, CH$_3$CHO $5_{2,3} - 4_{2,2}$ E $v_t = 0$, and CH$_3$OCHO $7_{6,1} - 6_{6,0}$ E $v_t = 0$. The vertical gray dotted line marks the systemic velocity (4.25 km s^{-1}). The vertical blue dashed lines indicate the corresponding disk radii at each velocity channel based on the maximum velocity of Keplerian rotation in Equation (4.1). The horizontal gray dashed line indicates the zero-flux level. There are no significant emission at the velocity channels which corresponds to inside ~ 40 au radius.

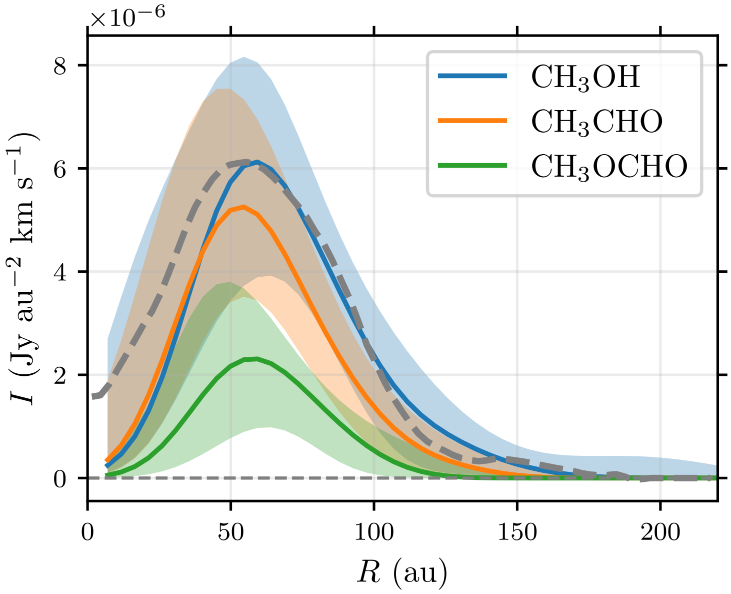

Figure 4.4. Reconstructed radial intensity profiles of CH$_3$OH (blue), CH$_3$CHO (orange), and CH$_3$OCHO (green) transitions. The horizontal gray dashed line indicates the zero-intensity level. The gray dashed curve shows the radial intensity profile of CH$_3$OH transition in Band 6 created by deprojection and azimuthal averaging on the higher-resolution ($\sim 0''.1$) velocity-integrated intensity maps (Tobin et al. 2023). The Band 6 intensity profile is normalized by its radial peak being matched to the radial peak of the Band 3 CH$_3$OH profile.

Since the emission is only marginally spatially resolved, we assumed that the emitting region in Band 3 is the same as that of CH_3OH in Band 6 (Tobin et al. 2023). The inner and outer radius of the emitting area are fixed to $0\farcs1$ and $0\farcs3$, respectively. In addition to the (tentatively) identified transitions in Section 4.3.1, we included several undetected species in the spectral fit: $^{13}CH_3CHO$, CH_2DOCHO, and CH_3OCDO. In total, we consider 24 free parameters: excitation temperature ($T_{\rm ex}$), line width ($\Delta V_{\rm FWHM}$), column density of 21 species, and an additional parameter γ for line broadening (see Appendix J). For the justification of the common excitation temperature and line width, we measured the line width of each isolated transitions with Gaussian fits, and found no systematic variations depending on the molecular species nor the upper state energies. We used the affine-invariant Markov Chain Monte Carlo (MCMC) algorithm implemented in the `emcee` Python package (Foreman-Mackey et al. 2013) to explore the parameter spaces. We run 100 walkers for 15000 steps, and the initial 12000 steps are discarded as burn-in. Figure 4.5 demonstrates the unique ability of the simultaneous spectral fit to fully exploit the transitions for column density derivation even with a severe spectral blending.

The results of the fits are summarized in Table 4.3. The derived excitation temperature is $106.7^{+4.3}_{-3.8}$ K, similar to the typical sublimation temperature of COMs ($\sim 100\,\mathrm{K}$), indicating the thermal sublimation of molecules. The column densities of COMs are $\sim 10^{15}$–10^{18} cm^{-2}, broadly in agreement with previous estimates using Band 7 data (Lee et al. 2019). The uncertainties of the derived quantities are 16th and 84th percentiles of the posterior distributions, where only the statistical uncertainty is considered. While the column density itself could have a larger uncertainty due to the absolute flux calibration uncertainty of 2.5% (1σ), the column density ratios, from which we discuss the chemistry of COMs in the following sections, are not affected by the absolute flux calibration uncertainty.

Table 4.3 Column Density of Molecules

Molecule	N (cm^{-2})
CH_3OH	$3.9^{+0.7}_{-0.6} \times 10^{18}$
CH_3CHO	$6.5^{+0.5}_{-0.5} \times 10^{17}$
CH_3OCHO	$7.4^{+0.3}_{-0.3} \times 10^{17}$
CH_3OCH_3	$5.7^{+0.5}_{-0.5} \times 10^{17}$
CH_3COCH_3	$4.4^{+0.5}_{-0.5} \times 10^{16}$
c-C_2H_4O	$3.5^{+0.5}_{-0.4} \times 10^{16}$
t-C_2H_3CHO	$5.0^{+0.3}_{-0.3} \times 10^{15}$
s-C_2H_5CHO	$1.8^{+0.3}_{-0.3} \times 10^{16}$
CH_2DOH^*	$2.2^{+0.4}_{-0.4} \times 10^{16}$
CH_3CDO^*	$5.5^{+1.3}_{-1.3} \times 10^{15}$
CH_2DCHO^*	$2.8^{+0.8}_{-0.8} \times 10^{16}$
$CH_3^{13}CHO^*$	$2.3^{+0.8}_{-0.8} \times 10^{16}$
$^{13}CH_3CHO$	$< 1.5 \times 10^{17}$
$CH_3O^{13}CHO$	$3.2^{+0.4}_{-0.3} \times 10^{16}$
$^{13}CH_3OCHO$	$3.2^{+0.3}_{-0.3} \times 10^{16}$
CH_2DOCHO	$< 1.2 \times 10^{16}$
CH_3OCDO	$< 1.4 \times 10^{16}$
$^{13}CH_3OCH_3{}^*$	$2.3^{+0.6}_{-0.6} \times 10^{16}$
SO_2	$3.0^{+0.7}_{-0.7} \times 10^{16}$
OCS	$5.5^{+2.0}_{-1.3} \times 10^{16}$
$C_2H_3CN^*$	$2.2^{+0.9}_{-0.9} \times 10^{15}$

[†] The excitation temperature and line width, which are assumed to be common for all molecules, are estimated to be $106.8^{+4.2}_{-3.9}$ K and $0.71^{+0.07}_{-0.05}$ km s^{-1}, respectively.

[‡] Uncertainties are the 16th and 84th percentile of the posterior distributions, where only the statistical uncertainty is included. The upper limits are determined based on the 99.7th percentile of the posterior distributions.

[*] Based on the tentatively detected transitions and therefore should be considered as upper limits.

4.4 Discussion

4.4.1 Comparison of the Spatial Distributions with the Sub-mm Observations

The spatial distributions of the COM emission in Band 3, where the dust continuum emission would be fainter than in the sub-mm regime, are essential information to infer the origin of the inner cavity seen in the sub-mm observations. If the central region where the emission cavity is seen in Band 6/7 is filled with COM emission in Band 3, it would be evidence that the COM emission is reduced in the sub-mm observations due to the intense dust continuum emission.

We found that the reconstructed radial intensity profiles (Figure 4.4) show the inner depression of the emission while the spatial distributions of the COM emission in Band 3 are consistently centrally-peaked in the velocity-integrated intensity maps (Figure 4.1). This indicates that the inner emission cavity is smeared out by the beam on the velocity-integrated intensity maps. We confirmed that the inner emission cavity of a CH_3OH line in Band 6[3] (Tobin et al. 2023) is smeared out when the image is smoothed to the same spatial resolution as that of the presented Band 3 data. Although the uncertainties of the reconstructed radial intensity profiles are quite large, the profiles all have radial peaks at $\sim$ 50–60 au, which is consistent with the higher-resolution Band 6 profile (Figure 4.4). Therefore, it is likely that the emission observed in Band 3 mainly traces the components outside the emission cavity ($\gtrsim 40$ au, i.e., the same component as that traced by the sub-mm observations).

We note, however, that there are some additional systematic uncertainties in the reconstructed radial intensity profiles (Figure 4.4). In reality, the molecular line emission could originate from the disk surface (or the warm molecular layer, Aikawa et al. 2002; Law et al. 2021b, 2022, 2023b; Paneque-Carreño et al. 2023), where the Keplerian velocity

---

[3] Taken from the Harvard Dataverse repository (`https://dataverse.harvard.edu/dataset.xhtml?persistentId=doi:10.7910/DVN/MDQJEU`)

is slightly smaller than that in the midplane. This invalidates the assumption made in the reconstruction of the radial intensity profiles that the emission comes entirely from the disk midplane. Therefore, while the depression of the emission in the innermost region is robust, the actual emission cavity sizes in Band 3 emission are rather uncertain. In addition, transitions with different optical depths or upper state energies, which could trace the different disk heights, may have different emission distributions.

4.4.2 The Physical and Chemical Structure of the Innermost Region of the V883 Ori Disk

Our line profile analyses suggest that the COM line emission in Band 3 also shows the inner emission cavity at $\lesssim$ 40 au radius. Here we discuss the possible origins of the emission cavity and the associated physical and chemical structures of the V883 Ori disk.

The first possible explanation for the emission cavity of the COM emission in Band 3 is that the dust continuum emission is still too intense even in Band 3 to detect the line emission in the innermost disk. In the sub-mm wavelengths, the dust continuum emission at $\lesssim$ 40 au radius has been shown to be optically thick ($\tau \gtrsim 2$) by the intra-band analysis of the ALMA Band 6 observations with a spatial resolution of $\sim 0\farcs04$ (Cieza et al. 2016). Since the dust opacity is generally smaller in lower frequencies, the dust continuum emission is expected to be more optically thin in the longer wavelengths. However, the factors that affect the line intensity are not only the dust optical depth, but also the temperature of the dust emitting layer. We consider a simple slab model for the vertical structure of a disk. If the line-emitting layer is well separated from the dust-emitting layer (near the midplane) and is closer to the observer (see e.g., Bosman et al. 2021b), the observed line intensity after the continuum subtraction is expressed as

$$\begin{aligned} I_{\mathrm{L-C}} &= B_\nu(T_{\mathrm{gas}})(1-e^{-\tau_{\mathrm{line}}}) + I_{\nu,\mathrm{dust}}e^{-\tau_{\mathrm{line}}} - I_{\nu,\mathrm{dust}} \\ &= (B_\nu(T_{\mathrm{gas}}) - I_{\nu,\mathrm{dust}})(1-e^{-\tau_{\mathrm{line}}}), \end{aligned} \tag{4.2}$$

where B_ν is the Planck function for blackbody radiation, T_{gas} is the gas temperature representing the temperature of the line emitting region, τ_{line} is the optical depth of the line emission at the line center, and $I_{\nu,\mathrm{dust}} = \chi B_\nu(T_{\mathrm{dust}})(1 - e^{-\tau_{\mathrm{dust}}})$ is the intensity of the dust continuum emission. Here χ is the intensity reduction factor due to the scattering effect (e.g., Bosman et al. 2021b), T_{dust} is the dust temperature, and τ_{dust} is the optical depth of the dust continuum emission. Equation (4.2) is an extension of the situation discussed in Bosman et al. (2021b), where the dust continuum emission is optically thick (i.e., $1 - e^{-\tau_{\mathrm{dust}}} \sim 1$) and the temperature of the line- and dust-emitting region is the same (i.e., $T_{\mathrm{gas}} = T_{\mathrm{dust}}$, vertically isothermal disk).

In archetypal disks where the temperature structure is mainly determined by the passive irradiation from the central star, the temperature in the line-emitting region (T_{gas}) is usually much higher than the temperature in the disk midplane, from which the dust emission is mostly originating (T_{dust}), allowing us to observe the line emission originating from the disk surface. However, in the case of the V883 Ori disk, where the disk temperature is expected to be elevated due to the accretion outburst, viscous heating may be efficient in the midplane, which could lead to a higher temperature in the disk midplane (T_{dust}; Alarcón et al. 2024). Indeed, Lee et al. (2019) suggest that the intensity depression of the COM emission can be reproduced by the presence of the additional heating in the midplane. Although the intensity of the dust emission also depends on the scattering effect (χ), this warmer temperature in the midplane makes it even more difficult to detect the line emission originating from its emitting layer closer to the observer, even if the optical depth of the dust continuum emission is not very high.

It is also possible that the bulk of the line emission in the innermost region ($\lesssim$ 40 au radius) is well mixed with the dust emission and originates from the disk midplane. In this case, the observed line intensity after the continuum subtraction will completely disappear if the line opacity is negligible compared to the dust opacity (see Bosman et al. 2021b, Equation (4)).

Another possible explanation for the inner emission cavity is that the molecules at $\lesssim$ 40 au radius are destroyed by the strong UV/X-ray radiation from the central protostar. The UV radiation can destroy COMs via photodissociation (e.g., Garrod & Herbst 2006; Öberg et al. 2009) in the region where the dust is optically thin. This UV effect will thus be effective only in low-density regions (e.g., disk surfaces) where the dust could be optically thin. On the other hand, X-rays can penetrate into higher-density regions than UV radiation. Recently, Notsu et al. (2021) modeled the effect of the X-ray radiation from the central protostar on the chemistry of the protostellar envelopes, and found that the gas-phase fractional abundances of CH_3OH and other COMs within their snowlines decrease as the X-ray luminosity of the central protostar increases. In the presence of the strong X-ray radiation, COMs are mainly destroyed by the X-ray-induced photodissociation (e.g., Garrod & Herbst 2006; Taquet et al. 2016; Notsu et al. 2021). In the model by Notsu et al. (2021), CH_3OH is destroyed in $\sim 10^3\,\mathrm{yr}$ when the X-ray ionization rate is $\sim 10^{-13}\,\mathrm{s}^{-1}$ in the infalling envelope. Here we use the ionization rate rather than the flux, since the former is the direct input parameter for the chemical reaction network models. While the destruction timescale may weakly depend on the gas density, which could be different between the inner $\lesssim 100\,\mathrm{au}$ radius region of the protostellar envelopes and the $\lesssim 40\,\mathrm{au}$ radius region of the V883 Ori disk, CH_3OH and other COMs could be destroyed in ~ 100 yr if the X-ray ionization rate is $\gtrsim 10^{-12}\,\mathrm{s}^{-1}$. We note that Kuhn & Hillenbrand (2019) reported that X-ray luminosities and plasma temperature of X-ray radiation in FU Ori type stars tend to be larger than in typical non-bursting YSOs, based on the comparison with a sample of low-mass stars in the Orion Nebula Cluster. In addition, cosmic-rays accelerated near the central star (in strongly magnetized shocks along the outflow or in accretion shocks near the stellar surface) could penetrate into the higher-density disk midplane and cause the destruction of COMs via cosmic-ray-induced photodissociation (e.g., Padovani et al. 2020; Cabedo et al. 2023).

In summary, the inner cavity of the COM emission in Band 3 can be explained by the absorption of the molecular line emission by the bright dust continuum emission, and/or by the chemical destruction of the molecules. Our ALMA Band 3 observations suggest that sensitive observations at longer wavelengths, where the dust continuum emission should be fainter, with ALMA Band 1, Karl G. Jansky Very Large Array (VLA), and the future next generation Vary Large Array (ngVLA), are essential to directly probe the chemistry of the innermost region of the V883 Ori disk.

4.4.3 Chemical Abundance Ratios of COMs

The V883 Ori disk is a unique and ideal target for disk chemistry since we can observe fresh sublimates and probe the chemical composition of COMs which is hidden in typical colder disks. Here we discuss the chemical composition of the COMs detected in our observations and their implications for the chemical evolution during star and planet formation. Figure 4.6 compares the column density ratios of COMs with respect to CH_3OH in the V883 Ori disk with those in different evolutionary stages, including the warm inner envelopes of the Class 0 protobinary IRAS 16293-2422 A/B (Lykke et al. 2017; Jørgensen et al. 2018; Manigand et al. 2020, 2021, see also Drozdovskaya et al. 2019), the protoplanetary disk around the Herbig Ae star Oph-IRS 48 (Brunken et al. 2022), and the solar system comet 67P/C-G (Rubin et al. 2019; Schuhmann et al. 2019, see also Drozdovskaya et al. 2019). IRAS 16293-2422 is a famous "hot corino" source, extensively studied in the ALMA Protostellar Interferometric Line Survey (PILS; Jørgensen et al. 2016), where we can observe COM-rich warm gas sublimated from ices. The Oph-IRS 48 disk is the only disk so far to show emission of multiple COM species. A localized COM emission offset from the disk center has been observed, which is interpreted to be sublimated from the icy dust mantle stirred up to the warm disk surface (van der Marel et al. 2021; Brunken et al. 2022). The comet 67P/C-G is also a well-known object whose chemical composition has recently been extensively studied by in-situ measurements in the Rosetta mission (e.g., Altwegg et al. 2019). We found higher abundance ratios of COMs in the V883 Ori disk compared to those in the warm envelopes of IRAS 16293-2422 by a factor of $\gtrsim$ 5–10, indicating that the abundance of chemically complex species is enhanced in protoplanetary disks. We note that the COM abundance ratios in protostellar envelopes also show scatter depending on the source (Belloche et al. 2020; Yang et al. 2021). The COM abundance ratios in the V883 Ori disk are similar to those in another disk Oph-IRS 48 and in comet 67P/C-G, except for one species, CH_3OCHO, which shows a lower abundance ratios in the comet compared to the disks. These results suggest that the more complex species than CH_3OH efficiently form during the evolution from the protostellar envelope to the protoplanetary disks, and that the chemical composition of disks can be inherited to comets without drastic chemical reprocessing.

In general, the formation of COMs are thought to occur mainly via reactions on dust grain surfaces (Herbst & van Dishoeck 2009, and references therein). In the cold temperature region ($\lesssim 10\,\mathrm{K}$), the CH_3OH ice forms via efficient hydrogenation of the CO ice (e.g., Tielens & Hagen 1982; Watanabe & Kouchi 2002; Watanabe et al. 2003). Therefore, the CH_3OH ice forms in cold molecular clouds and could be delivered to protoplanetary disks. On the other hand, diffusion of heavier radicals (e.g., CH_3, CH_2OH, and CH_3O), formed via the UV/X-ray/cosmic-ray-induced photolysis and hydrogen abstraction of simpler molecules including CH_3OH, are efficient on the warmer ($\sim$ 30–50 K) dust grain surfaces. More complex molecules such as CH_3CHO, CH_3OCHO, CH_3OCH_3, and CH_3COCH_3 could thus be formed via radical-radical reactions. For example, theoretical and experimental studies (e.g., Garrod & Herbst 2006; Chuang et al. 2016) have shown that CH_3CHO, CH_3OCHO, CH_3OCH_3, and CH_3COCH_3 are mainly formed via following reactions,

$$\mathrm{HCO + CH_3 \longrightarrow CH_3CHO,} \tag{4.3}$$

$$\mathrm{HCO + CH_3O \longrightarrow CH_3OCHO,} \tag{4.4}$$

$$\mathrm{CH_3 + CH_3O \longrightarrow CH_3OCH_3,} \tag{4.5}$$

$$\mathrm{CH_3 + CH_3CO \longrightarrow CH_3COCH_3.} \tag{4.6}$$

These reactions may contribute to the efficient formation of these species in protoplanetary disks (Walsh et al. 2014; Furuya & Aikawa 2014), which may be the origin of abundant complex species in the V883 Ori disk (Figure 4.6).

The present observations also detected several isomeric pairs, i.e., CH_3CHO and c-C_2H_4O pair and CH_3COCH_3 and s-C_2H_5CHO pair. The abundance ratios between isomers are key to constraining the formation pathways. We found a $CH_3CHO/c\text{-}C_2H_4O$ ratio of $9.2^{+1.2}_{-1.1}$ and a $CH_3COCH_3/s\text{-}C_2H_5CHO$ ratio of $2.2^{+0.4}_{-0.4}$ in the V883 Ori disk. These ratios are consistent with the values in IRAS 16293B (Lykke et al. 2017) within an order of magnitude, suggesting that the isomers are also similarly formed.

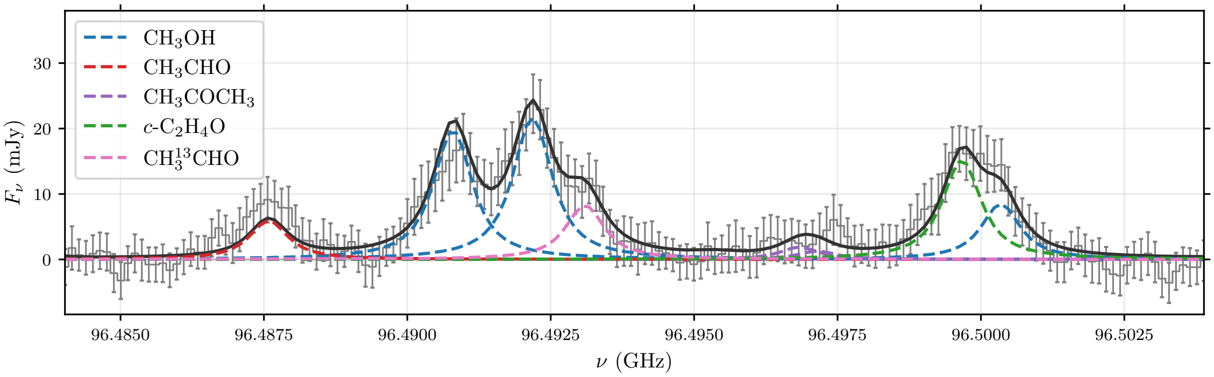

Figure 4.5. Demonstration of the simultaneous spectral fit for a selected frequency range in SPW 7. The observed spectra (gray) is well reproduced by the model (black) composed of multiple blended transitions of different species, CH_3OH, CH_3CHO, CH_3COCH_3, c-C_2H_4O, and $CH_3^{13}CHO$ (dashed colored lines).

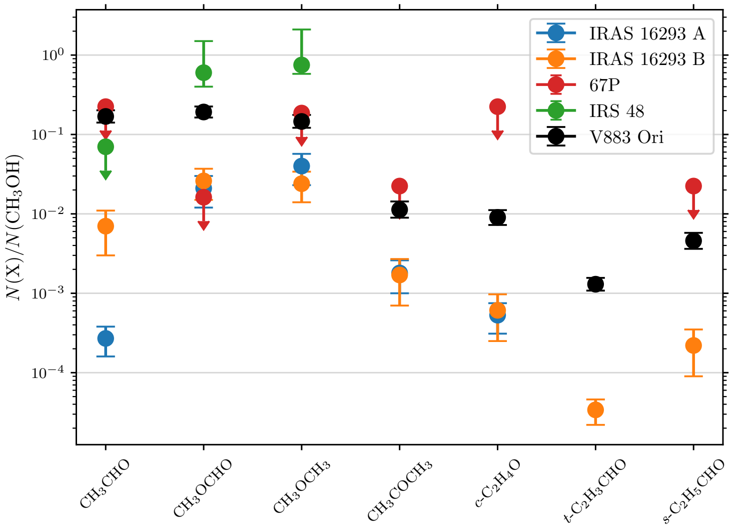

Figure 4.6. Comparison of the COM abundance ratios with respect to CH_3OH among different evolutionary stages including the V883 Ori disk measured in the present work. The data point with a down arrow indicate an upper limit. We compiled the literature values for the protostellar envelopes of IRAS 16293-2422 A/B (Lykke et al. 2017; Jørgensen et al. 2018; Manigand et al. 2020, 2021), the comet 67P/C-G (Rubin et al. 2019; Schuhmann et al. 2019), and the IRS 48 disk (Brunken et al. 2022). Note that while all the cometary values are limited to be upper limits because cometary measurement (mass spectra) cannot distinguish the isomeric molecules with the same mass (e.g., CH_3CHO and c-C_2H_4O pair and CH_3COCH_3 and s-C_2H_5CHO pair), the upper limit of CH_3CHO in the IRS 48 disk is due to non-detection.

4.4.4 Isotopic Ratios of COMs

The present observations also detected several isotopologues, including D and ^{13}C, of some abundant molecules. Here, we discuss the implications of these detections and the ^{12}C/^{13}C and D/H ratios for the isotopic chemistry in protoplanetary disks.

^{12}C/^{13}C ratio

We have identified ^{13}C-methyl formate ($^{13}CH_3OCHO$ and $CH_3O^{13}CHO$) and tentatively identified ^{13}C isotopologues of acetaldehyde and dimethyl ether. While previous observations reported the detection of $^{13}CH_3OH$ (Lee et al. 2019) and $^{13}CH_3CHO$ as a potential blended line with the HDO line (Tobin et al. 2023), measurements of ^{12}C/^{13}C ratios in COMs have not been performed. Figure 4.7 shows the probability density distributions of the ^{12}C/^{13}C ratios of CH_3CHO, CH_3OCHO, and CH_3OCH_3. The measured ^{12}C/^{13}C ratios are also summarized in Table 4.4 together with the value in the warm envelopes of IRAS 16293-2422. The measured ^{12}C/^{13}C ratios are all ∼20–30[4], which is significantly lower than the elemental abundance ratio of ^{12}C/^{13}C in the local ISM (∼ 69; Wilson 1999), although the ^{12}C/^{13}C ratios of acetaldehyde and dimethyl ether have a probability at higher values as well due to the tentative detection or non-detection. Interestingly, a similarly low ^{12}C/^{13}C ratio (21 ± 5) of CO has been reported in the 70–110 au region of the protoplanetary disk around TW Hya by Yoshida et al. (2022a) (see also Zhang et al. 2017). They suggest that the gas-phase isotope-exchange reaction,

$$^{13}\mathrm{C}^+ + ^{12}\mathrm{CO} \rightleftarrows ^{12}\mathrm{C}^+ + ^{13}\mathrm{CO} + \Delta E, \tag{4.7}$$

---

[4] We note that the statistical correction has not been applied for $^{13}CH_3OCH_3$, which apparently contains equivalent two carbon atoms in the CH_3- functional groups. However, these two carbon atoms are actually not equivalent based on the formation pathway of CH_3OCH_3 (Equation 4.5); the formation of CH_3OCH_3 (and therefore the inclusion of ^{13}C into CH_3OCH_3) happens via the reaction between non-equivalent reactants (CH_3 and CH_3O) unlike e.g., the equivalent hydrogen addition to CO which forms CH_3OH and its deuterated isotopologues. We here simply compare the ^{12}C/^{13}C of CH_3OCH_3 without statistical correction to other species, although the actual correction factor depends on the ^{12}C/^{13}C ratios of reactants (i.e., CH_3 and CH_3O), which can be varied among them.

($\Delta E \approx 35\,\mathrm{K}$; Langer et al. 1984; Furuya et al. 2011), with the help of the high gas-phase C/O ratio (> 1), would lead to such a low $^{12}CO/^{13}CO$ ratio in the warm molecular layer. The same mechanism would explain the observed low $^{12}C/^{13}C$ ratio in COMs if the ^{13}C-rich CO is incorporated into the ice on dust grains in the disk midplane via vertical mixing and freeze-out (Furuya et al. 2022), from which the COMs such as CH_3CHO and CH_3OCHO are synthesized via hydrogenation and radical-radical reactions (Equations (4.3)–(4.6)) on dust grain surfaces.

An alternative mechanism that could alter the $^{12}CO/^{13}CO$ ratio is the difference in the binding energies between the two isotopologues. Smith et al. (2015) proposed that the slightly higher binding energy of ^{13}CO than that of ^{12}CO ($840 \pm 4\,\mathrm{K}$ and $835 \pm 5\,\mathrm{K}$ on ^{12}CO ice; Smith et al. 2021) could explain the high $^{12}CO/^{13}CO$ ratios in the gas phase (~ 85–165) observed toward several low-mass young stellar objects. The difference in binding energies leads to the sublimation of ^{12}CO at a slightly lower temperature than ^{13}CO, making the gas-phase CO ^{13}C-poor (and CO ice ^{13}C-rich). However, this fractionation mechanism should work only in a very narrow temperature range. Also, the difference in binding energy between ^{12}CO and ^{13}CO is rather uncertain. It is therefore speculative that this mechanism contributes to the ^{13}C fractionation. In addition, the gas and dust dynamics in disks (e.g., vertical turbulent mixing) is a critical unknown factor for this mechanism to work for the ^{13}C fractionation of CO and consequently of COMs (e.g., Yoshida et al. 2022a).

The molecular $^{12}C/^{13}C$ ratios have been measured in different evolutionary stages (Nomura et al. 2023). In cold dense cores, single-dish observations have revealed that CO are enriched in ^{13}C (Agúndez et al. 2019), potentially indicating the isotope-exchange reaction (Equation 4.7) in the cold environment. In the warm envelope around the Class 0 protostar IRAS 16293B, similar lower values of the $^{12}C/^{13}C$ ratio (~ 30) have been observed in some COMs ($CH_2(OH)CHO$ (glycolaldehyde), CH_3OCH_3, and possibly CH_3OCHO) (see Table 4.4; Jørgensen et al. 2016, 2018), but for IRAS 16293A no evidence for ^{13}C fractionation in COMs has been observed (Table 4.4; Manigand et al. 2020). CO (and thus COMs) can be enriched in ^{13}C via the exchange reaction (Equation 4.7) only when C/O ratio is greater than unity (or more specifically, CO is not the dominant

C reservoir). In a rotationally supported disk, the C/O ratio could exceed unity due to the decoupling of the ice-coated grains from the gas. The low $^{12}C/^{13}C$ ratio of some COMs in IRAS 16293B may indicate that similar dust-gas decoupling already occurs in the protostellar envelope (e.g., Koga et al. 2022).

We note that the elemental abundance ratios of C/O and C/H in the gas phase become lower with increasing ionization rate in the disk ($\gtrsim 10^{-17}$ s^{-1}; Eistrup et al. 2016; Schwarz et al. 2018; Notsu et al. 2020), which may inhibit the increase of ^{13}CO abundance via the exchange reaction (Equation 4.7) (Woods & Willacy 2009). Alternatively, it may be possible that the destruction of carbonaceous grains enhances the C/H abundance and C/O ratio in protostellar disks and envelopes (e.g., Wei et al. 2019; van 't Hoff et al. 2020a), although it is unclear whether the destruction of carbonaceous grains efficiently occurs in the outer cold region where CO and COMs form ($\lesssim$ 100 K).

In the comet 67P/C-G, only the $CH_3OH/^{13}CH_3OH$ ratio has been measured (91 ± 10; Altwegg et al. 2020b, see Table 4.4), showing no ^{13}C fractionation from the solar value ($\sim$ 89; e.g., Mumma & Charnley 2011). The $^{12}C/^{13}C$ ratios of simpler molecular species such as CO, CO_2, and H_2CO have also been measured, but no ^{13}C fractionation has been observed (Hässig et al. 2017; Rubin et al. 2017) except for H_2CO (40 ± 14; Altwegg et al. 2020b). This trend is in contrast to the observed ^{13}C fractionation in COMs in the V883 Ori disk. Although the origin of this difference is unclear, a speculative explanation could be the formation environment of the comet 67P/C-G; it may be formed from the dust grains with non-^{13}C-rich ices, which can be produced from lower gas-phase C/O ratios ($\lesssim 1$). Yoshida et al. (2022a) reported a radial variation of the gas-phase $^{12}CO/^{13}CO$ ratio in the disk around TW Hya, where the outer region (> 130 au) shows a higher $^{12}CO/^{13}CO$ ratio (> 84) than that in the inner region (70–110 au; 21 ± 5). If a similar radial variance in the $^{12}CO/^{13}CO$ ratio existed in the proto-solar disk, the ^{13}C fractionation in comets depends on the formation location within the disk.

Table 4.4 $^{12}C/^{13}C$ Ratios of COMs

	V883 Ori[†]	IRAS 16293A[a]	IRAS 16293B[b]	67P/C-G[c]
Methanol				
$CH_3OH/^{13}CH_3OH$	—	65 ± 27	—	91 ± 10
Acetaldehyde				
$CH_3CHO/CH_3^{13}CHO$	(29^{+16}_{-8})[*]	—	67[‡]	—
$CH_3CHO/^{13}CH_3CHO$	> 4.2	—	67[‡]	—
Methyl Formate				
$CH_3OCHO/CH_3O^{13}CHO$	23^{+3}_{-3}	75 ± 32	(41)[*]	—
$CH_3OCHO/^{13}CH_3OCHO$	23^{+3}_{-2}	—	—	—
Dimethyl Ether				
$CH_3OCH_3/^{13}CH_3OCH_3$	(25^{+10}_{-6})[*]	86 ± 18	17	—
Glycolaldehyde				
$CH_2OHCHO/CH_2OH^{13}CHO$	—	—	27[‡]	—
$CH_2OHCHO/^{13}CH_2OHCHO$	—	—	27[‡]	—

[†] For the measurement in the V883 Ori disk, uncertainties are the 16th and 84th percentile of the posterior distributions. The 0.3rd percentile (corresponding to 3σ) of the posterior distributions are adopted for the lower limit of $CH_3CHO/^{13}CH_3CHO$.

[‡] Derived from the fit assuming the same column density for these isomeric pairs.

[*] Tentative measurement using tentatively detected transitions.

[a] Manigand et al. (2020).

[b] Jørgensen et al. (2016) and Jørgensen et al. (2018).

[c] Altwegg et al. (2020b)

D/H ratio

Deuterium fractionation (an enhancement of D/H ratios in molecules) is also a key to understanding the formation environment and thermal history of planetary medium (e.g., Ceccarelli et al. 2014; Nomura et al. 2023). The D/H ratios of COMs, in particular CH_3OH, has been measured in warm protostellar envelopes (e.g., Jørgensen et al. 2018; Drozdovskaya et al. 2021). Even multiply-deuterated species have been detected toward IRAS 16293-2422 protobinary (e.g., Manigand et al. 2019; Richard et al. 2021; Drozdovskaya et al. 2022), and the similarity of the D enrichment between the protostellar envelopes and the solar system comets suggests the inheritance of interstellar molecules to comets (Drozdovskaya et al. 2021). In protoplanetary disks, while the D/H ratios of several simpler molecules such as HCN, HCO^+, and N_2H^+ have been measured (e.g., Cataldi et al. 2021, see also Aikawa et al. 2022), no measurements of COM deuteration exist so far except for the CH_2DOH/CH_3OH ratio in the V883 Ori disk (Lee et al. 2019).

The deuterium fractionation is initiated by the deuteration of H_3^+ with the gas-phase ion-molecule reaction,

$$H_3^+ + HD \rightleftarrows H_2D^+ + H_2 + \Delta E. \tag{4.8}$$

This reaction is exothermic ($\Delta E \approx 230\,\mathrm{K}$; e.g., Millar et al. 1989), and therefore at the low temperature ($\lesssim 30\,\mathrm{K}$) the backward reaction is suppressed, enhancing the H_2D^+ abundance in the gas phase. In dense cold regions such as prestellar cores, a freeze-out of CO, a main reactant with H_2D^+, further enhances the fractionation (e.g., Roberts & Millar 2000). Dissociative recombination of H_2D^+ enhances the abundance of D atoms, which subsequently causes the deuteration of molecules formed on dust grain surfaces, including COMs. In the warmer conditions ($\gtrsim 30\,\mathrm{K}$), the fractionation is more moderate, since the backward reaction of Equation (4.8) is not severely suppressed. Molecular D/H ratio thus can be used to probe the formation environment of molecules including COMs. For example, some molecules showing relatively high D/H ratios ($\gtrsim$ several %) are considered to be formed in cold prestellar cores even though those are observed at warm protostellar envelopes (e.g., Jørgensen et al. 2018; Yamato et al. 2022)

We have observed multiple deuterated species of COMs, CH_3OH, CH_3CHO, and

CH_3OCHO, for the first time in protoplanetary disks, while the deuterated methanol, CH_2DOH, has also been detected in the previous Band 7 observations (Lee et al. 2019). We also tentatively identified CH_2DOH in the present observations. For deuterated CH_3CHO, two different isomers (CH_2DCHO and CH_3CDO) have been tentatively identified. Several transitions of two isomers of deuterated CH_3OCHO (CH_3OCDO and CH_2DOCHO) are covered but not detected, from which we constrain the upper limit on their column densities.

We derived a CH_2DOH/CH_3OH ratio of $0.0057^{+0.0018}_{-0.0015}$, although this value should be considered as an upper limit due to the tentative identification of CH_2DOH. In addition, the available spectroscopic data of CH_2DOH transitions in the jpl database have large uncertainties, particularly in their intensities (see Appendix L.1), making comparison and discussion more difficult. We therefore consider this measurement as a reference value. As for CH_3CHO, the CH_2DCHO/CH_3CHO and CH_3CDO/CH_3CHO ratios are measured to be $0.0084^{+0.0021}_{-0.0019}$ and $0.043^{+0.012}_{-0.012}$, respectively, but again these values should be considered as upper limits due to tentative identifications. We also constrain the upper limit on both CH_2DOCHO/CH_3OCHO and CH_3OCDO/CH_3OCHO ratios to be $\lesssim 0.02$ based on the non-detection of CH_2DOCHO and CH_3OCDO.

Figure 4.8 compare the D/H column density ratios of COMs in the V883 Ori disk with those in IRAS 16293B and 67P/C-G. The upper limit of COM D/H ratios obtained in the V883 Ori disk are lower than the ratios in IRAS 16293B. As the D/H ratios are very sensitive to the formation temperature, the lower D/H ratio of COMs in the V883 Ori disk may be explained by the formation on the lukewarm ($\sim$ 30–50 K) dust grain surfaces within the disk. On the other hand, the D/H ratio of CH_3OH (not the column density ratio, but the elemental D/H ratio after the statistical correction) in 67P/C-G has been measured to be 0.71–6.6 % (Drozdovskaya et al. 2021), which reduced to a CH_2DOH/CH_3OH ratio (0.021–0.20), consistent with the values in IRAS 16293B, pointing to the prestellar origins of CH_3OH (Drozdovskaya et al. 2021). The D/H ratios of different COMs measured in the V883 Ori disk seem to be slightly lower than the reported CH_2DOH/CH_3OH ratio in 67P/C-G. This might suggest the different origins of CH_3OH in 67P/C-G and COMs in the V883 Ori disk; while COMs in the V883 Ori disk may have been (re-)formed on the lukewarm (∼ 30–50 K) dust grain surfaces in the inner region of the disk in its quiescent phase, the comet 67P/C-G may have been formed in the cold (∼ 10 K) outer region of the proto-solar disk, where molecules are directly inherited from the natal envelope without significant chemical reset. To draw a more concrete picture on the chemical evolution of COMs, it is essential to constrain the D/H ratios of various COMs in both disks and comets with more sensitive observations of multiple transitions and accurate spectroscopic data, in particular for CH_2DOH (see Appendix L). Higher-resolution observations are also helpful to constrain the radial distributions of D/H ratios (e.g., Cataldi et al. 2021).

4.4.5 Deficiency of Nitrogen-bearing COMs

While the number of detected oxygen-bearing COMs in the V883 Ori disk is comparable to that in protostellar envelopes, nitrogen-bearing COMs seem to be deficient in the V883 Ori disk compared to those in protostellar envelopes. In the present observations, only C_2H_3CN has been tentatively detected as a nitrogen-bearing COM. Our spectral setup covers the transitions of other nitrogen-bearing COMs, such as NH_2CHO and C_2H_5CN, but they are not detected. In Band 7 observations, CH_3CN is the only nitrogen-bearing COMs that has been detected (Lee et al. 2019). Even for CH_3CN, its column density is lower than those of oxygen-bearing COMs (Lee et al. 2019). The spectral setup of the present observations did not cover intense transitions of CH_3CN, and therefore it is not detected. This apparent deficiency of nitrogen-bearing COMs may indicate that the nitrogen is locked into less volatile components, e.g., refractory carbonaceous grains (van 't Hoff et al. 2020a) and/or ammonium salt (Poch et al. 2020; Altwegg et al. 2020a). This scenario is supported by the recent observations of protostellar envelopes which report a difference in the spatial distributions between nitrogen- and oxygen-bearing COMs in protostellar envelopes (Csengeri et al. 2019; Lee et al. 2022; Nazari et al. 2023; Okoda et al. 2021, 2022). While the gaseous nitrogen-bearing COMs may exist in the inner hot regions of the V883 Ori disk, their emission may be beam-diluted and/or hidden by the intense dust continuum emission as discussed in Section 4.4.2 in the present observations. To fully reveal the nitrogen content in the V883 Ori disk, high-resolution observations

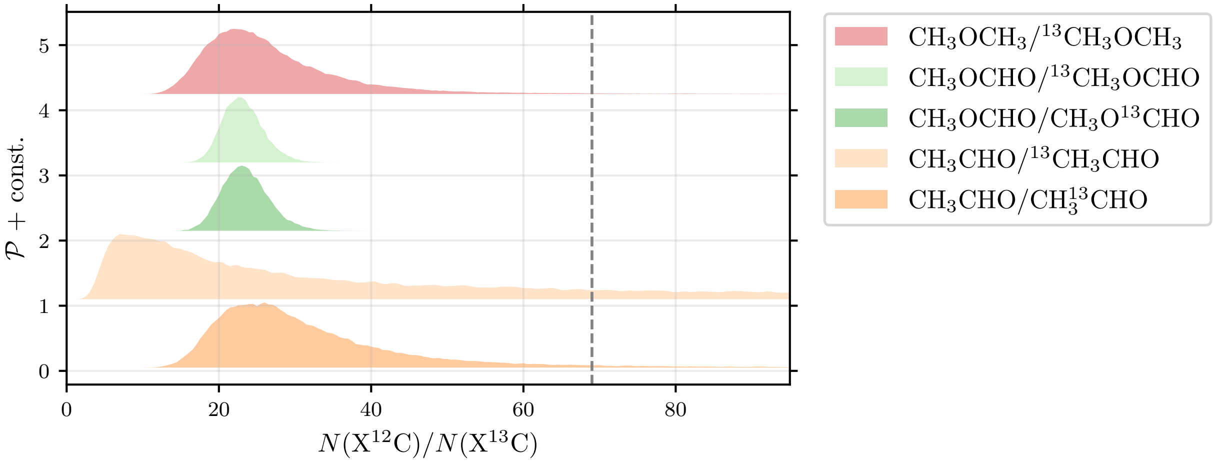

Figure 4.7. Kernel density estimate (KDE) of the posterior probability density distributions of column density ratios of ^{12}C- to ^{13}C-isotopologues for CH_3CHO, CH_3OCHO, and CH_3OCH_3. Two isomers of ^{13}C-isotopologues are observed for CH_3CHO and CH_3OCHO. The probability density is normalized by the peak being unity and offset for visual clarity. The ISM value of 69 is marked by the vertical dashed line. We note that the $^{12}C/^{13}C$ ratios of CH_3CHO and CH_3OCH_3 are based on the tentatively detected transitions of ^{13}C-isotopologues, and therefore should be considered as lower limits.

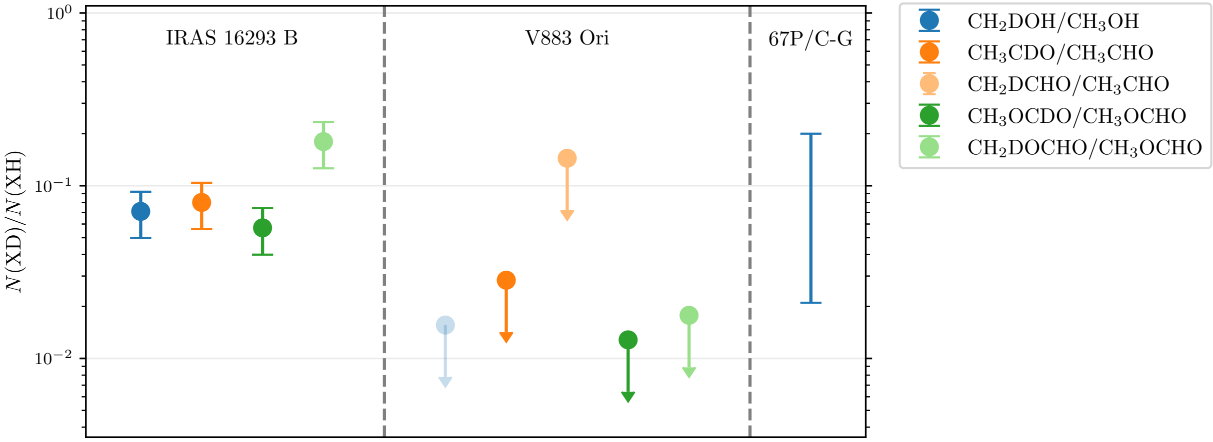

Figure 4.8. Comparison of the COM D/H ratios in the V883 Ori disk with those in IRAS 16293 B (Jørgensen et al. 2018) and 67P/C-G (Drozdovskaya et al. 2021) from literature. The different colors indicate the different molecular species of COMs as shown in the legend. Upper limits are shown by the downside arrows. The CH_2DOH/CH_3OH ratio in V883 Ori is shown by a semi-transparent circle to indicate its large uncertainty due to the large uncertainty in the spectroscopic data of CH_2DOH.

at longer wavelengths (ALMA Band 1, VLA, and ngVLA) are needed to avoid the dust absorption.

4.4.6 Implications for Sulfur Chemistry

Sulfur-bearing molecules have been routinely observed in protostellar environments and solar system comets, and their potential chemical links have been discussed (e.g., Drozdovskaya et al. 2018). On the other hand, detection of gas-phase sulfur-bearing molecules are still sparse in Class II disks except for CS and its isotopologue (Le Gal et al. 2021, and references therein). Recent observations have just began to report the (tentative) detection of sulfur-bearing molecules such as SO, SO_2, and SiS in a few warm disks, which might be originated from the thermal desorption and/or the accretion shock toward the protoplanets (Booth et al. 2021b, 2023a; Law et al. 2023a).

In the V883 Ori disk, Lee et al. (2019) reported the detection of CH_3SH and tentative detection of SO_2. The present observations have confirmed SO_2 and newly detected OCS. Since the emission distributions are similar to that of other oxygen-bearing COMs in the V883 Ori disk (see Figure 4.1 for OCS), the SO_2 and OCS detected in the present observations likely originate from the thermal sublimation as with the other molecules. The SO_2/OCS ratios are measured to be $0.56^{+0.21}_{-0.20}$ in the V883 Ori disk. In molecular clouds, SO_2 and OCS ices are ubiquitously detected by infrared observations (e.g., Boogert et al. 2015; McClure et al. 2023). These molecules are also detected in the warm envelopes of IRAS 16293-2422 (Drozdovskaya et al. 2018) and the comet 67P/C-G (Calmonte et al. 2016). The SO_2/OCS ratios are $\sim$ 0.2–0.5 in molecular cloud ice and in IRAS 16293-2422, consistent with the value in the V883 Ori disk, suggesting that the sulfur-bearing ices in the V883 Ori disk have similar origin. On the other hand, the SO_2/OCS ratio is higher in comet 67P/C-G ($\sim$ 280) than these values by three orders of magnitude, which may indicate the potential chemical evolution from the ISM.

4.5 Summary

We presented the ALMA Band 3 observations of COMs in the V883 Ori disk at an angular resolution of $0\farcs3$–$0\farcs4$. We analyzed the disk-integrated spectra in detail to obtain the spatial distribution of the COM emission and the column densities of COMs. Our major findings are summarized as follows:

1. We robustly identified eleven oxygen-bearing COMs (including isotopologues) in the disk-integrated spectra, where CH_3OCH_3, t-C_2H_3CHO, s-C_2H_5CHO, $^{13}CH_3OCHO$, and $CH_3O^{13}CHO$ are the first detection in the V883 Ori disk. We also tentatively identified five COMs (including isotopologues) and detected two sulfur-bearing molecules, OCS and SO_2. Nitrogen-bearing COMs are not detected except for a tentative detection of C_2H_3CN.

2. The detailed analyses of the line profiles revealed the inner emission cavity (~ 40 au radius), similar to the previous sub-mm observations. This indicates that the COM emissions are suppressed even in Band 3 where the dust continuum emission is fainter, possibly due to the higher dust temperature in the midplane caused by the viscous accretion heating. In addition, the destruction of COMs in the cavity region by the strong UV/X-ray/cosmic-ray radiations from the central outbursting protostar may explain the inner emission cavity of COMs. Our ALMA Band 3 observations suggest that the observations in longer wavelengths, where the dust continuum emission should be fainter, with ALMA Band 1, VLA, and future ngVLA, are essential to directly probe the chemistry of the innermost region of the V883 Ori disk.

3. We found that the column density ratios of complex molecules with respect to CH_3OH are significantly higher than those in the warm protostellar envelopes of IRAS 16293-2422, and similar to the values measured in comet 67P/C-G. This may indicate that the formation of complex molecules occurs in protoplanetary disks, which can cause the chemical evolution en route to planetary systems.

4. We characterized the ^{13}C-fractionation pattern of COMs in protoplanetary disks

for the first time. The $^{12}C/^{13}C$ ratios of CH_3CHO, CH_3OCHO, and CH_3OCH_3 consistently show a lower value ($\sim$20–30) compared to the canonical ISM ratios ($\sim$69). These COMs could be formed from CO enriched in ^{13}C due to the exchange reaction with $^{13}C^+$ in an environment characterized with a high gas-phase C/O ratios.

5. We also constrained the D/H ratios of multiple COMs in protoplanetary disks for the first time. The D/H ratios of CH_3CHO and CH_3OCHO shows lower values than those in protostellar envelopes IRAS 16293B, implying the formation of these molecules in warmer dust grain surfaces in protoplanetary disks.

Chapter 5

Detection of Dimethyl Ether in the Central Region of the MWC 480 Protoplanetary Disk

This thesis chapter originally appeared in the literature as
Yoshihide Yamato, Yuri Aikawa, Viviana V. Guzmán, Kenji Furuya, Shota Notsu, Gianni Cataldi, Karin I. Öberg, Chunhua Qi, Charles J. Law, Jane Huang, Richard Teague, & Romane Le Gal *Astrophysical Journal*, 2024, Vol. 974, id. 83. *I led the whole process of this study, including data acquisition, data reduction, analysis, and discussion.*

Abstract

Characterizing the chemistry of complex organic molecules (COMs) at the epoch of planet formation provides insights into the chemical evolution of the interstellar medium (ISM) and the origin of organic materials in our Solar System. We report a detection of dimethyl ether (CH_3OCH_3) in the disk around the Herbig Ae star MWC 480 with the sensitive Atacama Large Millimeter/submillimeter Array observations. This is the first detection of

CH_3OCH_3 in a non-transitional Class II disk. The spatially unresolved, compact ($\lesssim$25 au in radius) nature, the broad line width ($\sim$30 km s^{-1}), and the high excitation temperature ($\sim$200 K) indicate sublimation of COMs in the warm inner disk. Despite the detection of CH_3OCH_3, methanol (CH_3OH), the most abundant COM in the ISM, has not been detected, from which we constrain the column density ratio of $CH_3OCH_3/CH_3OH \gtrsim 7$. This high ratio may indicate the reprocessing of COMs during the disk phase, as well as the effect of the physical structure in the inner disk. We also find that this ratio is higher than in COM-rich transition disks recently discovered. This may indicate that, in the full disk of MWC 480, COMs have experienced substantial chemical reprocessing in the innermost region, while the COM emission in the transition disks predominantly traces the inherited ice sublimating at the dust cavity edge located at larger radii ($\gtrsim$20 au).

5.1 Introduction

Complex organic molecules (COMs), defined empirically as carbon-bearing molecules with six or more atoms, serve as precursors of prebiotic molecules and thus provide insight into the origin of organic materials and life in our solar system (e.g., Ceccarelli et al. 2023). COMs are formed initially on the cold grain surfaces in dark clouds (e.g., Herbst & van Dishoeck 2009) and will be readily observable in radio wavelengths in the warm ($\gtrsim$100 K) environment, where they are released into the gas phase by thermal desorption. Indeed, observations with the Atacama Large Millimeter/submillimeter Array (ALMA) have detected a number of COMs in the warm inner envelopes around protostars (e.g., Jørgensen et al. 2018; Belloche et al. 2020; Yang et al. 2021) and the warm protostellar disk around the FU Ori type outbursting star V883 Ori (van 't Hoff et al. 2018b; Lee et al. 2019; Yamato et al. 2024). COMs have also been detected in solar system comets, for example, 67P/Churyumov-Gerasimenko, which has been extensively studied by the Rosetta mission (Altwegg et al. 2019). While comparative studies of COM abundance ratios suggest that COMs in comets are at least partially inherited from the interstellar medium (ISM; Drozdovskaya et al. 2019), characterizing the distributions and abundances of COMs in protoplanetary disks is crucial for understanding the chemical evolution from the ISM to planetary systems.

Recent sensitive observations with ALMA have revealed the presence of thermally desorbed oxygen-bearing COMs in a few warm transition disks around Herbig Ae stars. van der Marel et al. (2021) detected warm methanol (CH_3OH) gas localized at the asymmetric dust trap in the transition disk around IRS 48, followed by additional detections in the transition disks of HD 100546 and HD 169142 (Booth et al. 2021b, 2023b). IRS 48 exhibits the highest chemical complexity among these disks, where dimethyl ether (CH_3OCH_3), methyl formate (CH_3OCHO), and ethylene oxide (c-H_2COCH_2) have been detected in addition to CH_3OH (Brunken et al. 2022; Booth et al. 2024b). Other oxygen-bearing molecules such as SO, SO_2 and NO are also detected at the dust trap, indicating the presence of oxygen-rich gas and a low C/O ratio of < 1 (Booth et al. 2021a; Leemker et al. 2023). HD 100546 also exhibits CH_3OCHO emission but no CH_3OCH_3 and c-H_2COCH_2, possibly suggesting a different reservoir of COMs compared to IRS 48 (Booth et al. 2024a). In these transition disks around Herbig Ae stars, the high luminosity of the central star and the inner dust cavity provide a warmer disk condition, which makes it possible for COMs to sublimate.

However, the current limited detections of sublimated COMs in transition disks preclude a comparison of the COM reservoir between other Herbig and T Tauri disks. Although weak, extended emission of CH_3OH has been detected in the outer cold region ($\gtrsim$30 au) of the nearest T Tauri disk TW Hya, its low abundance relative to H_2 ($\sim10^{-11}$–10^{-12}) suggests a non-thermal desorption origin (Walsh et al. 2016). Similar attempts to detect CH_3OH in the disks around Herbig Ae stars HD 163296 and MWC 480 yielded non-detections (HD 163296; Carney et al. 2019) or tentative detections (MWC 480; Loomis et al. 2018a) in the outer cold region. In this chapter, we present the first detection of CH_3OCH_3 in the MWC 480 protoplanetary disk. MWC 480 is a $\sim$7 Myr old (Montesinos et al. 2009) Class II Herbig Ae star with a stellar mass of $M_\star \approx 2.1\,M_\odot$ (Simon et al. 2019; Teague et al. 2021) in the Taurus-Auriga star-forming region ($d \approx 162$ pc; Gaia Collaboration et al. 2018). The MWC 480 disk, which has been observed in the Molecules with ALMA at Planet-forming Scales (MAPS) ALMA Large Program (Öberg et al. 2021), is one of the most extensively studied disks around Herbig Ae stars. The MWC 480 disk exhibits a prominent dust ring at ≈98 au (Long et al. 2018; Liu et al. 2019; Sierra et al. 2021), and the velocity perturbation observed in CO and its isotopologue emission suggests the presence of a planet at ≈245 au (Teague et al. 2021; Izquierdo et al. 2023). The outer disk ($\gtrsim$30 au) of MWC 480 is characterized by a gas-phase C/O > 1 (Bosman et al. 2021a; Jiang et al. 2023) and abundant hydrocarbons and cyanides (Ilee et al. 2021; Guzmán et al. 2021), while the inner disk chemistry is unknown.

We describe the ALMA Band 7 observations in Section 5.2. We present the detection of CH_3OCH_3, the tentative detection of CH_3OCHO, and the non-detection of CH_3OH, from which we constrain the excitation condition and column densities based on the spectral analysis in Section 5.3. We discuss the results in Section 5.4, and finally summarize the study in Section 5.5.

5.2 Observations

We observed the MWC 480 disk in Band 7 during ALMA Cycle 8 (project code: 2021.1.00535.S; PI: Y. Yamato). Observations were carried out in five execution blocks. Observational details including observation date, number of antennas, on-source integration time, mean precipitable water vapor (PWV), baseline coverage, angular resolution, maximum recoverable scale (MRS), and calibrator information are summarized in Table 5.1.

The pipeline calibrations were performed by ALMA staff using the standard ALMA pipeline. Subsequent self-calibration and imaging were performed using the Common Astronomy Software Applications (casa; CASA Team et al. 2022) version 6.2.1.7. The continuum visibilities were produced by averaging the line-free channels specified by visually inspecting the data cubes delivered from the observatory. The continuum emission peak on the image from each execution block was aligned to a common direction, $\alpha(\mathrm{ICRS}) = 04^{\mathrm{h}}58^{\mathrm{m}}46\overset{\mathrm{s}}{.}279, \delta(\mathrm{ICRS}) = +29^{\mathrm{d}}50^{\mathrm{m}}36\overset{\mathrm{s}}{.}40$, which was used as the disk center in the following analysis. Then, five rounds of phase-only self-calibration and one round of amplitude self-calibration were performed, resulting in a signal-to-noise ratio (S/N) increase by a factor of ≈15. The solutions were then applied to the entire dataset. The continuum emission was finally subtracted from the line visibilities by fitting a first-order polynomial to line-free channels using the casa task `uvcontsub`.

We focused on the spectral window originally dedicated for continuum acquisition, which covered a frequency range of 298.88–300.75 GHz and had a spectral resolution of 1.1 MHz (≈1.1 km s^{-1}). This spectral window contained a number of CH_3OCH_3 and CH_3OCHO transitions. We generated a single image cube for the entire frequency range by imaging the self-calibrated, continuum-subtracted visibilities with a channel spacing of 4 km s^{-1} and a Briggs robust value of 0.5 in the modified Briggs weighting scheme of `briggsbwtaper` implemented in the `tclean` task. The large channel width of 4 km s^{-1} intended to boost the S/N of detected CH_3OCH_3 emission while resolving its broad line width. The CLEANed image cube has a synthesized beam of $0.''31 \times 0.''21$ (PA = $8.^\circ2$) and a root mean square (RMS) noise level of 0.33 mJy $beam^{-1}$ at 4 km s^{-1} channel width. The RMS noise was measured on the line-free region of the image cube prior to primary beam correction. We also generated the continuum image at 1.03 mm with a Briggs robust value of −0.5 to better resolve the gap-ring structure, which is shown in the top left panel of Figure 5.1. Additionally, we report the detection of a new submillimeter source in the same field of view in Appendix P.

We also used the Band 7 data from another project (project code: 2021.1.00982.S; PI: V. V. Guzman). Observations were carried out in three execution blocks and their details are summarized in Table 5.1. The continuum spectral window of this data set, which is used in this study, covered a frequency range of 288.56–290.43 GHz with a spectral resolution of 1.1 MHz (≈1.2 km s^{-1}). This spectral window covered a cluster of CH_3OH transitions, which was used to constrain the upper limit on the CH_3OH column density. We followed the same self-calibration procedure as above, but with casa version 6.4.1. We performed three rounds of phase-only self-calibration and one round of amplitude self-calibration, which resulted in an increase in S/N by a factor of ≈5.5. We generated the image cube of the continuum spectral window in the same manner as above. The resulting beam size and the RMS noise level were $0.''31 \times 0.''22$ (P.A. = $-3.^\circ4$) and 0.67 mJy $beam^{-1}$ at 4 km s^{-1} channel width.

For both datasets, the absolute flux calibration uncertainty is expected to be $\lesssim$10%

based on the Quality Assurance (QA2) criteria described in ALMA Cycle 8 Technical Handbook. The following analyses consider only the statistical uncertainty and does not include the systematic flux calibration uncertainty.

Table 5.1 Observational Details

Date	# of Ant.	On-source Int. (min)	PWV (mm)	Baseline (m)	Ang. Res. (″)	MRS (″)	Calibrators Bandpass/Amplitude	Calibrators Phase
2021.1.00535.S (PI: Y. Yamato)								
2022 Aug. 8	42	44	0.7	15–1302	0.2	2.6	J0510+1800	J0438+3004
2022 Aug. 9	40	44	0.2	15–1246	0.2	3.0	J0510+1800	J0438+3004
2022 Aug. 9	40	44	0.1	15–1261	0.2	3.1	J0510+1800	J0438+3004
2022 Aug. 10	42	44	0.4	15–1302	0.2	2.8	J0510+1800	J0438+3004
2022 Aug. 10	41	44	0.5	15–1302	0.2	3.1	J0510+1800	J0438+3004
2021.1.00982.S (PI: V. V. Guzman)								
2022 Aug. 11	45	40	0.5	15–1302	0.2	2.9	J0510+1800	J0438+3004
2022 Aug. 11	44	40	0.5	15–1302	0.2	2.8	J0510+1800	J0438+3004
2022 Aug. 14	47	40	0.6	15–1302	0.2	2.8	J0510+1800	J0438+3004

5.3 Detection of Dimethyl Ether

5.3.1 Spectra and Spatial Distributions

We first extracted the integrated spectra by spatially integrating the image cubes in a circular aperture with $0\farcs6$ diameter toward the disk center, which securely covers the apparent emission as shown later. The middle panel of Figure 5.1 shows the resulting spectrum of the data containing detected CH_3OCH_3 transitions. We found a clear spectral feature at $\sim$299.89 GHz, whose line center spectrally coincides with the rest frequencies of CH_3OCH_3 transitions taking into account the spectral shift due to the systemic velocity (5.1 km,s^{-1}; Piétu et al. 2007; Teague et al. 2021). This feature is a blend of 12 individual CH_3OCH_3 transitions (see Table N in Appendix N for their spectroscopic properties) and shows a peak S/N of 9.4. In addition, two tentative features are seen at $\sim$299.12 GHz and $\sim$300.06 GHz, which also match with the frequencies of CH_3OCH_3 and CH_3OCHO transitions. These features show peak S/Ns of 3.4 and 4.7, respectively. Because they are lower than typical detection criteria of 5σ and the latter is blended between different species (CH_3OCH_3 and CH_3OCHO), these transitions were considered tentative detections. The zoomed-in spectra around these features are presented in the bottom panels of Figure 5.1 along with the expected spectral location of the CH_3OCH_3 and CH_3OCHO transitions. We note that an exhaustive search for other molecular lines that could be responsible for those features were performed, but only CH_3OCH_3 and CH_3OCHO can consistently explain these features among the lines of detectable species/transitions in typical disk environment.

The velocity-integrated intensity maps of these spectral features, generated using the Python package `bettermoments` (Teague & Foreman-Mackey 2018) with no flux threshold for pixel inclusion, are shown in the top panels of Figure 5.1 along with the 1.03 mm dust continuum image. These maps show the spatially-unresolved, compact emission with a peak S/N of $\sim$5–12.

Several strong transitions of CH_3OH and CH_3CHO were covered by the data from the project 2021.1.00982.S (see Table N in Appendix N for covered strong transitions), but they have not been detected in the image plane.

We also verified the (tentative) detections/non-detections of these COMs by matched filter analysis (Loomis et al. 2018b). The details and resulting response spectra are shown in Appendix M. The ∼5–17σ responses for CH_3OCH_3 and CH_3OCHO signify the detection of them, although it should be noted that the detected features are the blend of multiple transitions.

5.3.2 Spectral Analysis

To characterize the excitation temperatures and column densities of molecules, we employ a spectral fit with a simple local thermodynamic equilibrium (LTE) slab model. We basically followed the method described in Yamato et al. (2024), which is detailed in Appendix N. Briefly, the entire spectra are modeled with a total of seven free parameters: beam-averaged column densities of four molecular species ($N(CH_3OCH_3)$, $N(CH_3OCHO)$, $N(CH_3OH)$ and $N(CH_3CHO)$), excitation temperature $T_{\rm ex}$, which is assumed to be common among different species/transitions, line width ΔV (including the broadening due to disk rotation), and the systemic velocity $v_{\rm sys}$. Although CH_3OH and CH_3CHO are not detected, this simultaneous fit allows us to constrain the upper limit on their column densities. The assumption of a common excitation temperature for all COM species reflects the expectation that different COMs sublimate simultaneously with water ice.

We explored the parameter space with the affine-invariant Markov Chain Monte Carlo (MCMC) algorithm implemented in the Python package `emcee` (Foreman-Mackey et al. 2013). The details of this fitting procedure are described in Appendix N. Figure 5.1 compares the best-fit model with the observed spectra. The three observed spectral features are well reproduced by the best-fit model. While the robust feature at ∼ 299.89 GHz is explained by the cluster of CH_3OCH_3 transitions with relatively low upper state energies of 36–45 K, other two tentative features correspond to the transitions of CH_3OCH_3 and CH_3OCHO with higher upper state energies of 187–447 K (see Table N). The result of the fit is summarized in Table 5.2. The excitation temperature and line width are constrained to be $T_{\rm ex} = 200^{+50}_{-50}$ K and $\Delta V = 30^{+8}_{-6}\,{\rm km\,s^{-1}}$, where the uncertainties are 16th and 84th percentiles (corresponding to 1σ) of the posterior distributions. The resulting beam-averaged column densities of CH_3OCH_3 and CH_3OCHO are $7.4^{+4.6}_{-3.2} \times 10^{15}$ and $7.4^{+3.6}_{-4.9} \times 10^{14}$ cm^{-2}, respectively. The upper limits on the column densities of CH_3OH and CH_3CHO are also constrained to be $< 9.1 \times 10^{14}$ and $< 1.9 \times 10^{14}$ cm^{-2}, respectively. These upper limits are 99.85th percentile (corresponding to 3σ) of the posterior distributions. From these constraints on column densities, we derived a CH_3OCH_3/CH_3OH column density ratio (lower limit) of >7.

5.4 Discussion

5.4.1 Chemical Origin of the COM Emission

The spatially unresolved, compact ($\lesssim$25 au radius) CH_3OCH_3 emission with a broad line width ($\sim$30 km s^{-1}) and a high excitation temperature ($\sim$200 K; see Section 5.3.2) indicates warm CH_3OCH_3 gas in the inner disk. This is the first observational evidence of COMs sublimated in the inner warm region of the MWC 480 disk. The observed broad line width is also reproduced with the emission originating from $\lesssim$20–30 au radii, where the disk temperature is $\gtrsim$80–100 K, by a more detailed radiative transfer calculation (see Appendix O), further supporting this interpretation. Indeed, the peak brightness temperature of CO $J = 2$–1 emission already reaches $\gtrsim$70 K at $\approx$50 au (Law et al. 2021b), implying that the inner disk of MWC 480 is warm enough ($\gtrsim$100 K) for COMs to sublimate. Furthermore, super-resolution image of the Band 6 continuum emission shows a steep brightness increase inside 20 au radius (Yamaguchi et al. 2024), potentially suggesting the sublimation of water and COMs there that modify the dust optical properties. As the (sub-)mm dust continuum emission from the midplane is optically thick in the inner $\lesssim$40 au (Sierra et al. 2021), the observed CH_3OCH_3 emission likely traces the disk surface layer.

The CH_3OCH_3 detection and its icy origin lead us to expect the detection of other COMs, particularly the most abundant COM in the ISM, CH_3OH. However, the CH_3OH transitions ($E_\mathrm{u}\gtrsim$40 K) have not been detected in the present observations, resulting in

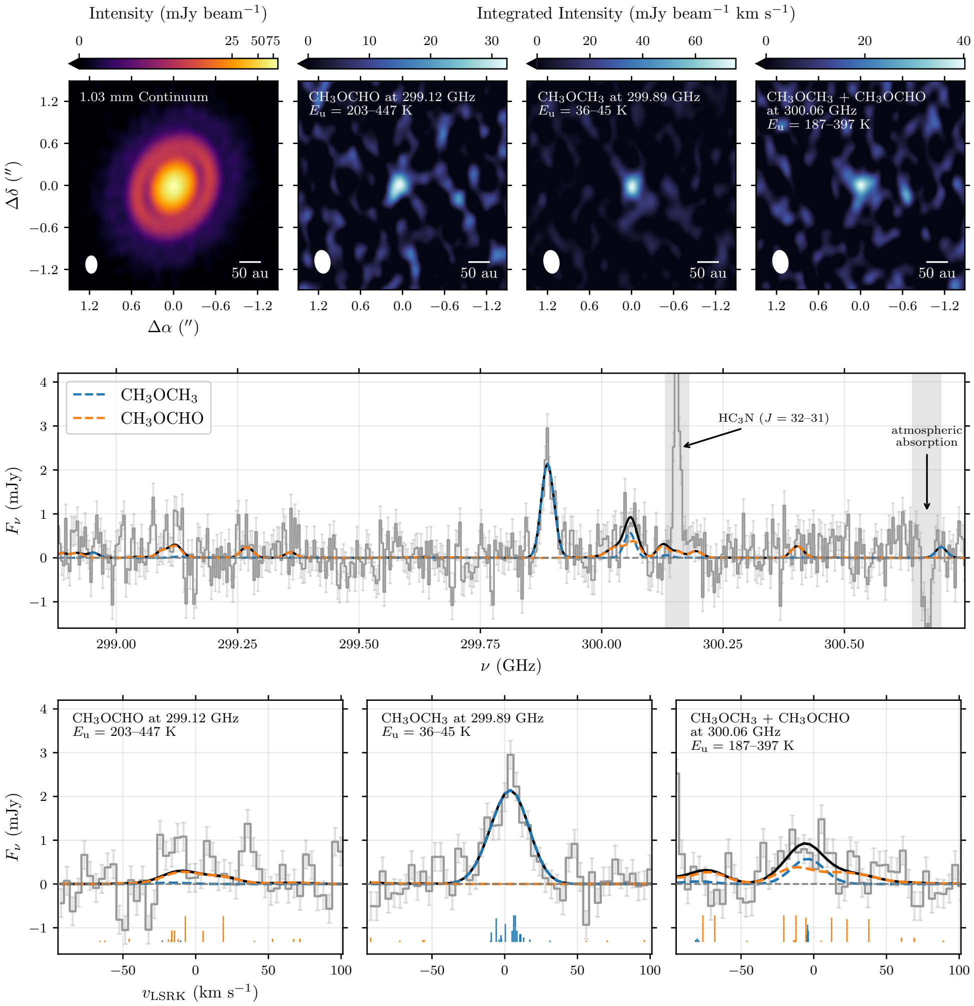

Figure 5.1. Summary of the observations toward the MWC 480 disk. Top: 1.03 mm continuum image (left) and velocity-integrated intensity maps of (tentatively) detected COMs, CH_3OCH_3 and CH_3OCHO (others). The peak S/N of the right three maps are 5.4, 12, and 6.0, respectively. The white ellipse in the lower left corner indicates the synthesized beam. A scale bar of 50 au is shown in the lower right corner. Middle: Spectra extracted in a circular aperture with 0″.6 diameter toward the disk center (gray), overlaid with the best-fit spectral model for CH_3OCH_3 (blue), CH_3OCHO (orange), and sum of both (black). The semitransparent error bars represent the associated 1σ uncertainties. The frequency ranges removed from the fit due to the atmospheric absorption or contamination from other molecular lines are shaded by gray. Bottom: Zoom-in view of the middle panel in the vicinity of the (tentatively) detected features but with the spectral axis in velocity with respect to a reference frequency of 299.11170 GHz (left), 299.89209 GHz (middle), and 300.05338 GHz (right), respectively. The vertical line segments in the bottom of the panels indicate the center and the relative strength (at 200 K) of each transition.

a high CH_3OCH_3/CH_3OH column density ratio of >7 (Section 5.3.2). This value is considerably higher than the typical values in the warm inner envelopes around protostars (e.g., Jørgensen et al. 2018; Yang et al. 2021) by more than one order of magnitude. This may indicate the efficient formation of CH_3OCH_3 during the disk phase. While it is anticipated that CH_3OH predominantly forms via hydrogenation of CO on the cold grain surfaces in the dark cloud (e.g., Watanabe & Kouchi 2002), more complex species, such as CH_3OCH_3 and CH_3OCHO, may also form on the grain surface in-situ in disks. Disk chemical models suggest that radical-radical reactions on the warm (∼30–50 K) grain surfaces may enhance the abundance of CH_3OCH_3 and CH_3OCHO (e.g., Furuya & Aikawa 2014);

$$\mathrm{CH_3 + CH_3O \longrightarrow CH_3OCH_3}, \tag{5.1}$$

$$\mathrm{HCO + CH_3O \longrightarrow CH_3OCHO}, \tag{5.2}$$

where the ingredient radicals (CH_3, CH_3O, and HCO) are the photodissociation products of CH_3OH ice (Öberg et al. 2009). These reactions, triggered by energetic processes such as UV, X-rays, and cosmic-rays, will play a pivotal role in determining the abundance of COMs during the disk phase. Additionally, gas-phase formation in the inner warm region may also be a contributing factor, as suggested by astrochemical models (Taquet et al. 2016; Garrod et al. 2022).

The derived column density ratio (CH_3OCH_3/CH_3OH >7) is still higher than the prediction of those models, which is lower than unity (e.g., Furuya & Aikawa 2014; Taquet et al. 2016). This implies that some additional effect is necessary to explain the observations. One possibility is the difference in the distributions between CH_3OCH_3 and CH_3OH. The slightly higher binding energy of CH_3OH (≈5000–6600 K; Ferrero et al. 2020; Minissale et al. 2022) than that of CH_3OCH_3 (≈4000–6500 K; Ligterink & Minissale 2023) may cause the CH_3OH ice to sublimate in warmer regions (i.e., smaller radii) and the CH_3OH emission to be more heavily beam-diluted (see Appendix O for a test of this possibility). Additionally, dust continuum emission may selectively hide the CH_3OH emission that could originate from a more inner region (e.g., Bosman et al. 2021b; Yamato et al. 2024).

Taken together, we suggest that the substantial reprocessing of COMs during the disk phase, in conjunction with an additional effect of the difference in spatial distributions could explain the detection of CH_3OCH_3 but not CH_3OH. Further observations at higher resolution and sensitivity are required to more accurately constrain the distributions and abundance ratio of COMs, thus enabling a better inference of the reprocessing of COMs during the disk phase.

5.4.2 Comparison to Other Disks

COM-rich Transition Disks

Recent deep line surveys have identified the emission from the warm gas of sublimated COMs in three transition disks: HD 100546, Oph IRS 48, and HD 169142 (Booth et al. 2023b, 2024a,b). Multiple species have been detected in Oph IRS 48 (CH_3OH, CH_3OCH_3, CH_3OCHO, and c-H_2COCH_2) and HD 100546 (CH_3OH and CH_3OCHO), while only CH_3OH has been detected in HD 169142. On the other hand, in full disks, no previous detections of sublimated COMs have been reported, and the present study provides the first evidence of icy organic sublimates. Figure 5.2 compares the abundance ratios of CH_3OCH_3 and CH_3OCHO relative to CH_3OH among HD 100546 (Booth et al. 2024a), Oph IRS 48 (Booth et al. 2024b), and MWC 480. The abundance ratios exhibit a considerable degree of variability among the sources, with particularly elevated values in the full disk of MWC 480. This suggests the potentially different chemistry and/or the effect of varying physical structures between transition and full disks. The abundance ratios in these transition disks may be determined predominantly by the sublimation of inherited ices at the dust cavity edge (or dust trap) located at larger radii ($\gtrsim$20 au; e.g., Booth et al. 2021b). In contrast, in the full disk of MWC 480, COM emission is likely to originate from more inner regions ($\lesssim$20–30 au), where COMs may have experienced more reprocessing by e.g., X-ray-driven chemistry and/or gas-phase chemistry in the disk surface layer. Indeed, the higher fractional abundance of HCO^+ relative to CO in MWC 480 compared to HD 100546 and IRS 48 may indicate the higher X-ray flux (Aikawa et al. 2021; Booth et al. 2024a,b), although the lower HCO^+ abundance in HD 100546 and IRS 48 could be attributed to the presence of gas-phase H_2O that destroys HCO^+ (e.g., Leemker et al. 2021).

It should also be noted that we obtain a tight upper limit on CH_3CHO column density, which is less than ∼3% of CH_3OCH_3 column. This is in a similar trend to the non-detection of CH_3CHO in the IRS 48 and HD 100546 disks (Booth et al. 2024b,a), while in contrast to the protostellar envelopes/disks where CH_3CHO exists in a comparable amount of CH_3OCH_3 (e.g., Jørgensen et al. 2018; Yang et al. 2021; Yamato et al. 2024). This might indicate that the specific reactions and/or branching ratios which are relevant to CH_3CHO formation/destruction may be at work in the disk phase, as suggested by the detection of $c{-}H_2COCH_2$, the isomer of CH_3CHO, in IRS 48 (Booth et al. 2024b).

Non-detection in HD 163296

It is also noteworthy that the same transitions of CH_3OCH_3 toward another well-studied full disk around the Herbig Ae star HD 163296 have not been detected with a similar sensitivity and resolution in the same project[1]. This suggests that the chemistry and/or physical structure in the inner disk may be different between MWC 480 and HD 163296. The CO snowline in MWC 480 is located at a larger radius (∼100 au) than in HD 163296 (∼65 au) as demonstrated in a comprehensive thermochemical modeling study (Zhang et al. 2021), implying a warmer inner disk of MWC 480. The higher rotation temperature of the HC_3N emission in the inner $\lesssim$10 au (∼90 K vs. ∼60 K) may also indicate that the inner region is warmer in MWC 480 (Ilee et al. 2021). Furthermore, the slightly higher mass accretion rate and bolometric luminosity of MWC 480 (Fairlamb et al. 2015; Montesinos et al. 2009; Mendigutía et al. 2013) may result in a greater quantity of organics being delivered to the inner disk (e.g., Banzatti et al. 2023).

---

[1] It should be noted that the physical scale traced by these observations are slightly different between MWC 480 and HD 163296 since the angular resolutions ($\sim0''.3$) are the same but the distances are different (162 pc vs. 101 pc).

Table 5.2 Result of the Spectral Analysis

Molecule	$T_{\rm ex}$ (K)	$\Delta V_{\rm FWHM}$ (km s^{-1})	$v_{\rm sys}$ (km s^{-1})	N (cm^{-2})	$/N(CH_3OH)$
CH_3OCH_3	200^{+50}_{-50}	30^{+8}_{-6}	$4.3^{+2.4}_{-2.5}$	$7.4^{+4.6}_{-3.2} \times 10^{15}$	> 7
CH_3OCHO				$7.4^{+3.6}_{-4.9} \times 10^{14}$	$> 0.81^{\dagger}$
CH_3OH				$< 9.1 \times 10^{14}$	—
CH_3CHO				$< 1.9 \times 10^{14}$	—

†The median value of $N(CH_3OCHO)$ divided by $N(CH_3OH)$ upper limit, which should be viewed as tentative. See Appendix N for details.

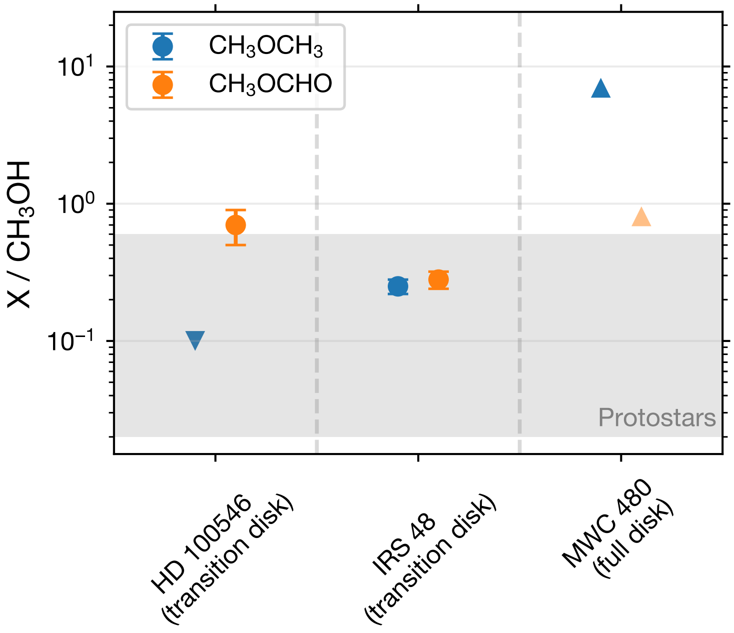

Figure 5.2. Comparison of the column density ratios of CH_3OCH_3 and CH_3OCHO relative to CH_3OH in three disks, HD 100546 (Booth et al. 2024a), Oph IRS 48 (Booth et al. 2024b), and MWC 480 (this work). The upward and downward triangles indicate lower and upper limits, respectively. Given the tentative detection (see Section 5.3.2), the value of CH_3OCHO in MWC 480 is plotted in transparent. The shaded region indicates the typical range of protostellar values measured by extensive line surveys (PILS; Jørgensen et al. 2016, CALYPSO; Belloche et al. 2020, and PEACHES; Yang et al. 2021).

5.5 Summary and Conclusion

We present ALMA Band 7 observations toward the disk around the Herbig Ae star MWC 480. We detected the line emission of CH_3OCH_3 and tentatively detected CH_3OCHO for the first time in the MWC 480 disk. This is the first detection of CH_3OCH_3 in a non-transitional Class II disk. The compact, spatially unresolved nature at a resolution of $\sim 0\farcs3$ (or $\sim$25 au radius), the broad line width ($\sim$30 $\mathrm{km\,s^{-1}}$ in FWHM), and the high excitation temperature ($\sim$200 K) indicate ice sublimation in the warm inner disk.

Furthermore, we present a non-detection of CH_3OH, which results in a high CH_3OCH_3/CH_3OH column density ratio of >7. This high ratio may be explained by the efficient formation of CH_3OCH_3 during the disk phase triggered by UV, X-ray, and cosmic rays, with a possible difference in the spatial distributions between CH_3OCH_3 and CH_3OH. We compare the column density ratios of COMs with those in COM-rich transition disks that have recently been discovered. The higher ratios in the full disk of MWC 480 may point to substantial chemical reprocessing of COMs in the innermost region, while those in transition disks may predominantly trace the sublimation of inherited ice at the dust trap located at $\gtrsim$20 au.

The detection of CH_3OCH_3 in MWC 480 provides the first evidence of icy organic sublimates in a full disk. Further observations, including the confirmation of the detection with other transitions, and detailed disk chemical modeling are necessary to better understand the inner disk chemistry. In particular, future JWST observations will provide complementary information about the COM abundances in gas and solid phases, which can be compared with the gas-phase abundances estimated from ALMA observations.

Chapter 6

Conclusion and Outlook

6.1 Thesis Summary

This thesis utilized the state-of-the-art interferometric observations with ALMA and VLA at a wide range of wavelengths spanning from (sub-)millimeters to centimeters. I specifically focused on the physical and chemical structures of a young protostellar disk, the nitrogen chemistry probed by NH_3 molecular line observations, and the complex organic chemistry in protoplanetary disks, all of which are key to understanding the detailed processes of planetary system formation and associated chemical evolution, and are only possible with the unique combination of high resolution and high sensitivity afforded by ALMA and VLA. I summarize the results of each chapter as follows.

Chapter 2 presented the high spatial resolution ($\sim 15\,\mathrm{au}$) observations of the disk around the Class I protostar L1489 IRS as part of the eDisk ALMA Large Program. Based on detailed visibility analysis, I identified a ring-gap structure in the dust continuum emission at 1.3 mm, indicating the formation of disk substructure has already started in this disk. The similar radial structure seen in the $C^{18}O$ $J = 2$–1 emission suggests that the disk gas may also have a similar ring-gap structure. This is in contrast to the younger Class 0 disks that show less substructure as revealed by the observations of a larger eDisk sample. This suggests that the formation of disk substructure and perhaps planet(s) starts during the Class I stage. In addition, I revealed the highly dynamic disk evolution during the Class I stage by characterizing the doubly warped structure of the disk. In particular, the detection of the high-velocity component of SO $J_N = 6_5$–5_4 suggests the presence of the warm inner disk misaligned with respect to the disk traced by $C^{18}O$ $J = 2$–1.

In Chapter 3–5, I focus on unveiling the chemical evolution of interstellar icy molecules by observing a "hot corino" source (Chapter 3), an FU Ori-type outbursting star (Chapter 4), and a protoplanetary disk around a Herbig Ae star (Chapter 5). These types of objects, which are in a warmer condition ($\gtrsim 100\,\mathrm{K}$) compared to typical planet-forming disks, provide unique testbeds for the chemical evolution of icy molecules. Chapter 3 uses the VLA observations of ammonia lines to constrain the formation conditions of NH_3 and its link to solar system comets. The high D/H ratio of NH_3 obtained indicates that at least part of the NH_3 ice forms on the cold grain surface during the later pre-disk evolutionary stage, namely, the dense core stage, and that NH_3 is likely to undergo a substantial chemical reprocessing during the disk stage by comparing the D/H ratios with those in comet 67P. Chapter 4 presents the ALMA observations of the outbursting star V883 Ori, which revealed the chemistry of COMs in protoplanetary disks. The elevated abundances of complex species and the anomalous isotopic ratios of COMs indicate the reformation of COMs in the disk stage. ALMA observations of the MWC 480 disk presented in Chapter 5 found an anomalously high abundance of CH_3OCH_3 relative to CH_3OH, supporting the idea of efficient reformation of COMs in protoplanetary disks.

Overall, these results suggest that planet-forming disks are unique sites of chemical evolution from the ISM to planetary systems. In other words, the chemical composition of the interstellar icy molecules can be modified and reset at the disk stage. In particular, this thesis suggests that (inter)stellar radiation, such as UV and X-rays, may be responsible for the observed anomalous abundance / isotopic ratios. In addition, these results provide important implications for the origin of solar system materials. Previous studies suggest that solar system materials are, at least partially, originated from the ISM based on the similar D/H ratio of water and methanol (Persson et al. 2013; Drozdovskaya et al. 2019). On the other hand, the significant difference in the D/H ratios of NH_3 presented in Chapter 3 indicates that something different is ongoing for NH_3. While the abundance ratios of oxygen-bearing COMs in the V883 Ori disk are similar to those in comet 67P, no significant ^{13}C fractionation is observed in solar system comets (Nomura et al. 2023) in contrast to the V883 Ori. These facts may indicate that these molecules are not the direct source of the cometary ices, i.e., the isotopic ratio depends on the formation location within the disk. Indeed, Yoshida et al. (2022a) suggest that the gas-phase ^{12}CO/^{13}CO ratio varies radially in the TW Hya disk. We need such spatially resolved measurements of the isotopic ratios of icy molecules across the whole disk, including comet-forming regions.

However, we should keep in mind that this discussion involves a number of assumptions. First, it is unclear whether the systems studied in this thesis are truly analogous to the solar system. The solar system likely formed in a clustered environment (Adams 2010), while the environmental properties of the target systems are diverse. NGC 1333, which contains IRAS 4A system (Chapter 3), is a highly clustered region, while V883 Ori (Chapter 4) and MWC 480 (Chapter 5) are located in relatively isolated environments. Indeed, the D/H ratio of water shows a dichotomy between clustered and isolated protostars (Jensen et al. 2021), suggesting some environmental effects, although the exact mechanism is still unknown. In addition, the exact mechanisms that substantially alter the composition of icy molecules remain elusive. While the observed trend is qualitatively consistent with the theoretical studies suggesting that stellar UV radiation can influence the formation and/or destruction of icy molecules (e.g., Furuya et al. 2011; Furuya & Aikawa 2014; Suzuki et al. 2024), the observed isotopic ratios / abundance ratios are still anomalous compared to the predictions of these models. This suggests that the chemical network of COMs may still be incomplete and overlook some important formation pathways. Furthermore, the chemistry in the warm ($\gtrsim 100\,\mathrm{K}$), dense ($\gtrsim 10^{10}\,\mathrm{cm}^{-3}$) region that can be reached in the inner region of the disk remains poorly understood. While I basically assume that the observed warm gas reflect the ice composition in the present work, it cannot be ruled out that the effect of gas-phase chemistry is dominant, even for V883 Ori where the timescale of the outburst duration is short. For example, HNC can be rapidly converted to HCN by gas-phase reactions during the outburst as indicated by their different emission distributions (Lee et al. 2024). Quantification of the effect of warm gas-phase chemistry has just started to be attempted by comparing the composition of ice and warm gas as observed by JWST and ALMA (e.g., Chen et al. 2024).

6.2 Future Prospect

Finally, I provide the practical future directions to tackle the remaining open questions related to each chapter. In Chapter 2, I discovered a ring-like structure in the L1489 IRS disk, and its striking contrast to the less-structured Class 0 disks as revealed by the large sample of the eDisk survey. This anchored the idea that substructure formation and thus potentially planet formation start during Class I stage (Chapter 2). The fact that only two oldest sources among 19 eDisk sample, L1489 IRS and Oph IRS63, show dust substructures and no evidence of flared dust distributions (see also Flores et al. 2023; Segura-Cox et al. 2020) supports this idea. In addition, a few evidence of the flat dust distributions in Class II disks, including an extremely settled case in the Class II Oph163131 (0.5 au dust scale height at 100 au radius; Villenave et al. 2022), has appeared in high-spatial-resolution (a few au) observations of edge-on disks, which also support the idea that older disks are in favorable condition for planet formation. Alternatively, the lack of the substructures may be due to the optically thick nature of the dust continuum emission at 1.3 mm (ALMA Band 6), which can hide the substructure in the disk midplane. Indeed, 3 mm (ALMA Band 3) observations hints a possible annular substructure in the young Class 0 disk around Oph A SM1 (Maureira et al. 2024). Observations of more samples of young disks at longer wavelengths, a few millimeter to centimeter, with ALMA Band 1, VLA, and future ngVLA, will resolve this degeneracy and are actually an ongoing follow-up project of the eDisk ALMA Large Program. Moreover, in a few large, bright Class II disks, kinematical signatures of embedded planets have recently been discovered as a perturbation from the Keplerian rotation in CO emission (e.g., Pinte et al. 2018b; Teague et al. 2019). The ongoing exoALMA Large Program will soon increase the number of kinematically-identified planets in Class II disks. Similar deep, high-resolution observations of the bulk gas tracer in Class I disks will unveil the embedded planets in young disks as well. Given its large gas disk size (~ 600 au), L1489 IRS will be one of the ideal targets for such “planet-hunting” studies.

The molecular line emission also shows a variety of interesting structures in the L1489 IRS disk (Chapter 2). In particular, SO line emission traces two distinct components: the diffuse emission originated from the accretion shock at the disk-envelope interface and the inner high-velocity component. While the spatially-resolved mapping of the SO emission at the disk-envelope interface verified the idea of accretion shock that has previously been proposed only by the velocity structure, the high-velocity component in the inner region is a completely new discovery. In Class II disks, recent observations suggest that SO and other sulfur-bearing molecules, such as SO_2 and SiS, can be a chemical tracer of embedded planets since they are efficiently produced by the accretion and/or outflow shocks onto/from the embedded planets (Booth et al. 2023a; Law et al. 2023a; Yoshida et al. 2024). Similar observations could pinpoint the embedded planets even in Class I disks in combination with the kinematical tracers, and will be key in hunting the embedded planets in these young evolutionary stages. In addition, sulfur-bearing molecules are also known to be a tracer of the elemental composition of the disk gas (Le Gal et al. 2021; Booth et al. 2023b), and are closely related to the pre-biotic chemistry. Given these wide range of utilities, sulfur-bearing molecules, including SO, SO_2, and SiS, should be a central of the planet formation studies in coming years.

In Chapter 3, I demonstrated that the VLA observations of NH_3 molecular lines are particularly useful to constrain the nitrogen chemistry, avoiding the effect of the optically thick dust continuum emission. The D/H ratio of NH_3 provided insight into the formation environment of NH_3 ices and the nitrogen reservoir in the ISM. However, the observations toward NGC 1333 IRAS 4A in Chapter 3 did not spatially resolve the NH_3 emission and thus what physical component the NH_3 emission trace is unclear, although the high excitation temperature suggests, at first order, the sublimation of NH_3 ices. I already have follow-up datasets of spatially-resolved observations of NH_3 and its isotopologues toward a nearby Class 0 protostellar system, and the analysis is ongoing. Moreover, it will be interesting to measure the $^{14}N/^{15}N$ ratio of NH_3 and compare it to the cometary $^{14}N/^{15}N$ ratio, since cometary ices consistently show a fractionation of ^{15}N ($^{14}N/^{15}N \sim 100$–140) compared to the solar system value (~ 400) and the ISM value (~ 200–300). The $^{14}N/^{15}N$ ratio of NH_3 has also been proposed to be a unique tracer of the formation location of planets within a protoplanetary disk (Barrado et al. 2023). VLA observations of NH_3 molecular lines will continue to provide fundamental insights into the nitrogen chemistry in the ISM and the origin of solar system materials. In particular, I believe that nitrogen isotopic ratio of icy molecules would be one of the most powerful indicator of the solar system's history, as nitrogen uniquely shows a clear isotopic dichotomy in the solar system while other volatile elements do not.

I also investigated the complex organic chemistry in protoplanetary disks by focusing on the warm disks around the FU Ori-type outbursting star V883 Ori and the luminous Herbig Ae star MWC 480, both of which are unique probes of disks' complex organic reservoir (Chapter 4 and 5). The overall conclusion from these studies are that the composition of COMs has likely been substantially modified along the evolution from the protostellar stage as demonstrated by the high relative abundance and anomalous isotopic ratios of COMs. Although COMs occupy a small fraction of the molecular composition, this means that some underlying fundamental mechanisms change the bulk chemical composition in disks because the formation of COMs are initiated by more abundant, simple molecules, such as CO. In particular, isotopic ratios of icy molecules are key for directly linking the interstellar medium (ISM) and large icy bodies in planetary system, such as comets, and inferring the origin of solar system materials. In addition, observations at optically thin, longer wavelengths are essential in probing the inner warm region of protoplanetary disks, the terrestrial-planet-forming zone. The ALMA Band 3 ($\sim 3\,\mathrm{mm}$) observations of V883 Ori presented in Chapter 4 revealed that the molecular line emission is still hidden from view by the optically thick continuum, meaning that the ALMA Band 1 and VLA observations are necessary. I am a co-I of an approved follow-up proposal to observe V883 Ori in Band 1 in ALMA Cycle 11, and thus the molecular content in the innermost region of the disk will soon be clarified. I am also a co-I of an approved VLA proposal to observe the NH_3 emission lines in the MWC 480 disk, which will be an interesting follow-up study. This thesis, particularly Chapter 3–5, will significantly contribute to this study in interpreting the data.

I would also emphasize that CH_3OCH_3 has been detected in the MWC 480 disk while CH_3OH, the most abundant COM in the ISM, has not. Although this might be owing to the physical structure in the innermost region of the disk as discussed in Chapter 5, this implies that CH_3OH is not necessarily the most abundant and easy-to-detect COMs in the disk setting. Moreover, I also note that the detection of CH_3OCH_3 was made serendipitously, i.e., the wide continuum spectral window happens to cover the lines. This means that it would be useful for us to (1) perform a deep line survey to observe as many molecular lines as possible, (2) be careful of covering potentially detectable lines when setting the continuum window, and (3) perform exhaustive searches for any serendipitous detections in archival data. Indeed, I already have several interesting archival detections in hand, which should be published in near future.

In summary, this thesis provided several important lessons that guide the future observations: (1) longer wavelength observations are crucial in unveiling the complete picture of planet formation, (2) centimeter wavelengths are also useful to observe the nitrogen content in planet-forming regions, and (3) deep line survey and/or exhaustive archival search would be useful for constraining the COM reservoir in disks.

While this thesis presented single-source studies and they have a significant importance as themselves, statistics are certainly required to make a more general inference. This will be mainly addressed by a number of ongoing and future ALMA Large Programs (LPs), which observe multiple sources at sufficient resolution and sensitivity. The ALMA survey of Gas Evolution in PROtoplanetary disks (AGE-PRO) LP will better constrain the disk gas mass and its evolution based on the CO isotopologues and N_2H^+ molecular lines for 30 disks. The exoALMA LP will be the first-every planet-hunting campaign with the molecular lines for $\sim$ 10 disks, and will soon publish the initial datasets. The ALMA Disk-Exoplanet C/Onnection (DECO) LP have gained the molecular line datasets for $\sim$80 disks, and statistical analysis on the elemental composition (mainly C/O ratio) of the disk gas is currently ongoing. In ALMA Cycle 11, two LPs focusing on disk are approved; A Survey of Planet-Forming Chemistry in the Precursor Environments of Giant Planets (CHEER), which will survey $\sim$ 10 disks around warm Herbig Ae stars, and The first comprehensive picture of chemical vertical structures in proto-planetary disks (DiskStrat), which will reveal the vertical structure of nine disks at high spatial resolution. Furthermore, an LP on the COMs in multiple disks is planned to be proposed in coming cycles, which I am a co-I with a significant contribution from the planning stage. This large number of LPs is a testament of a promisingly brighter future of the disk studies with ALMA.

This thesis also has significant implications for observations with the next-generation telescopes within the next decade. In particular, ALMA's Wideband Sensitivity Upgrade (WSU) and the Next Generation Very Large Array (ngVLA) will play a pivotal role in advancing the studies of planetary system formation and astrochemistry. WSU will increase the usable instantaneous bandwidth of ALMA by a factor of 2–4, which enables to observe larger numbers of spectral lines simultaneously. We will be able to conduct line surveys more efficiently with WSU to reveal the volatile reservoir in protoplanetary disks, where the content of Chapter 4 and 5 will be a critical guide for selecting the molecular species, frequency ranges, and excitation properties of lines. ngVLA will provide a significant sensitivity/resolution improvement particularly in lower frequency bands, including centimeter wavelengths, which enables to observe the innermost region of disks, the opaque region at higher frequencies. Chapter 3 (and a coming follow-up study with VLA) will be a critical benchmark for NH_3 molecular line observations with ngVLA. Overall, this thesis and follow-up studies with ALMA and VLA will play a critical role in preparing for these next-generation telescopes, while providing important scientific insights.

Appendix A

Continuum Maps with Different Robust Parameters

Figure A.1 shows the continuum emission maps at the central region imaged with different robust parameters, ranging from −2.0 (similar to uniform weighting) to 2.0 (similar to natural weighting). The central compact component is not spatially resolved even with robust = −2.0 where the beam size is $0\farcs041 \times 0\farcs023$ (or 6.9 au × 3.4 au).

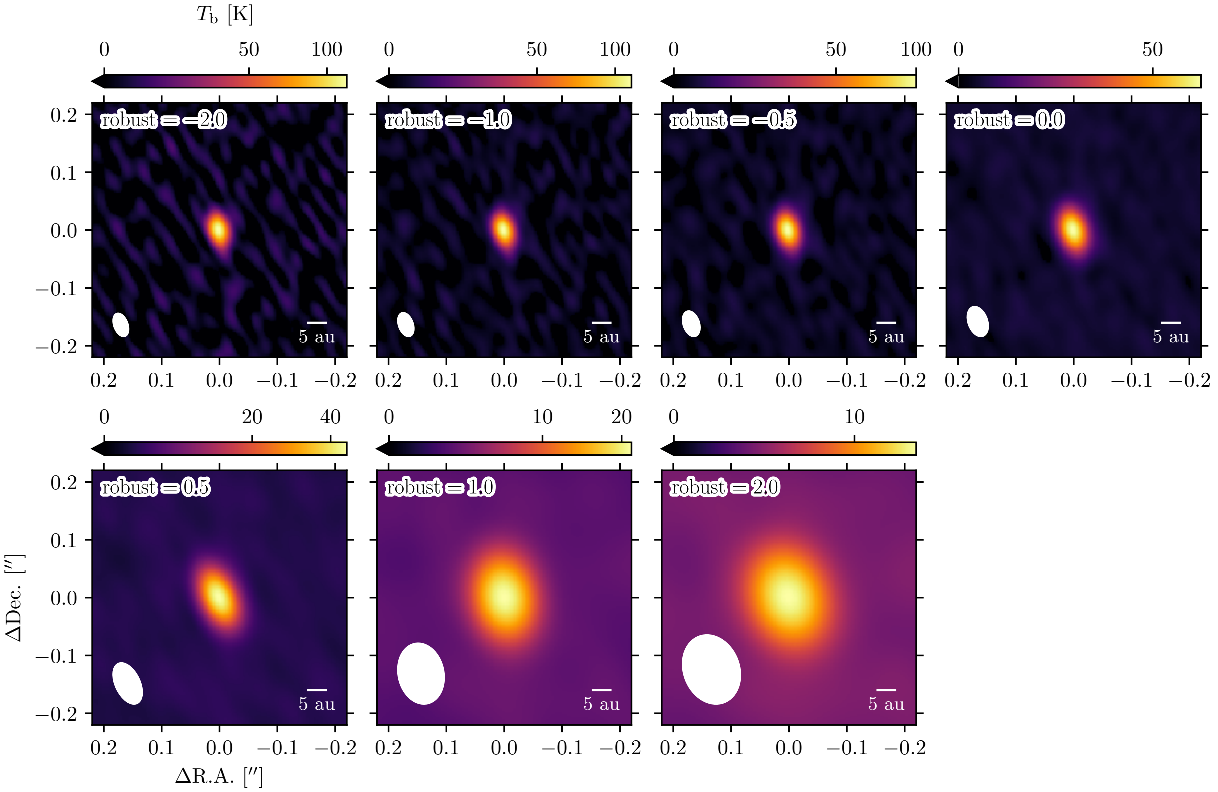

Figure A.1. Continuum emission at the central region imaged with different robust parameters (−2.0, −1.0, −0.5, 0.0, 0.5, 1.0, and 2.0). In each panel, the beam size and 5 au scale are indicated in the lower left and right, respectively.

Appendix B

Generation and Selection of Radial Intensity Profiles

We describe the detailed method to generate and select the radial intensity profiles of the continuum and line emission. We follow the methodology described in Law et al. (2021a). We generate the profiles by deprojecting the emission maps (continuum) or velocity-integrated emission maps (line). To deproject the disk coordinates, we assume the disk geometry ($i = 72^\circ$ and PA $= 67^\circ$) based on the results of the visibility analysis (Section 2.4.1) for both continuum and line profiles. The radial bin size is one-quarter of the major axis of the synthesized beam. We averaged the emission in each radial bin. The uncertainty is calculated as the standard error on the region over which the emission is averaged. We generated the continuum intensity profiles averaged over several certain azimuthal wedges ($\pm 15^\circ, \pm 30^\circ, \pm 45^\circ$ and $\pm 90^\circ$ (i.e., full azimuthal average)) with respect to the disk major axis, and compare them in Figure B.1. While the wider wedges result in low-contrast substructures due to the coarser effective resolutions in the inclined disk, narrower wedges show wavy features that are not considered actual substructures in the outer radii. We selected the profile with $\pm 45^\circ$ wedge as the representative profiles to compromise those two effects. For the line emission, we choose the same wedge ($\pm 45^\circ$) as the continuum emission to generate the radial intensity profiles at similar effective resolutions. We note that the deprojection here assumes a geometrically thin disk and does not consider the 3D structures of the disk.

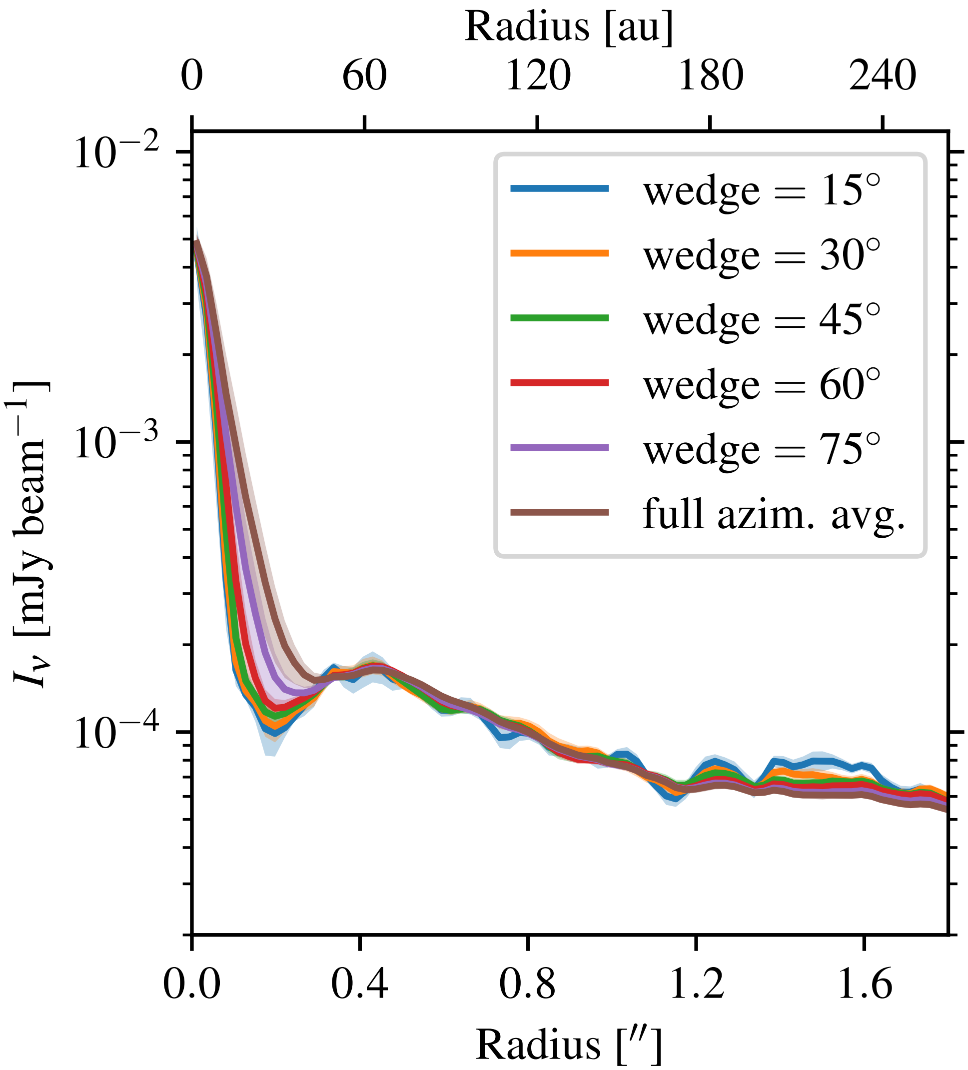

Figure B.1. Comparison of the radial continuum intensity profiles generated with different azimuthal wedges (averaged over both sides of the disk). Each color represents the radial profile extracted from ±15°, ±30°, ±45°, ±60°, ±75°, and ±90° (i.e., full azimuthal average) wedges with respect to the major axis of the disk. The color-shaded regions represent the uncertainty of the profiles.

Appendix C

Radiative Transfer Model of the L1489 IRS Disk

Figure C.1 shows the dust temperature profiles of the L1489 IRS disk at different disk scale heights ($h/r = 0.0$ (midplane), 0.15, and 0.3) calculated by the radiative transfer modeling by Sai et al. (2020). The readers are referred to the original paper for the details of modeling. In the emitting region of SO (the inset of Figure C.1), the dust temperature is higher than $\sim$40 K, comparable to the sublimation temperature of SO molecules ($\sim$50 K; see Section 2.5.5).

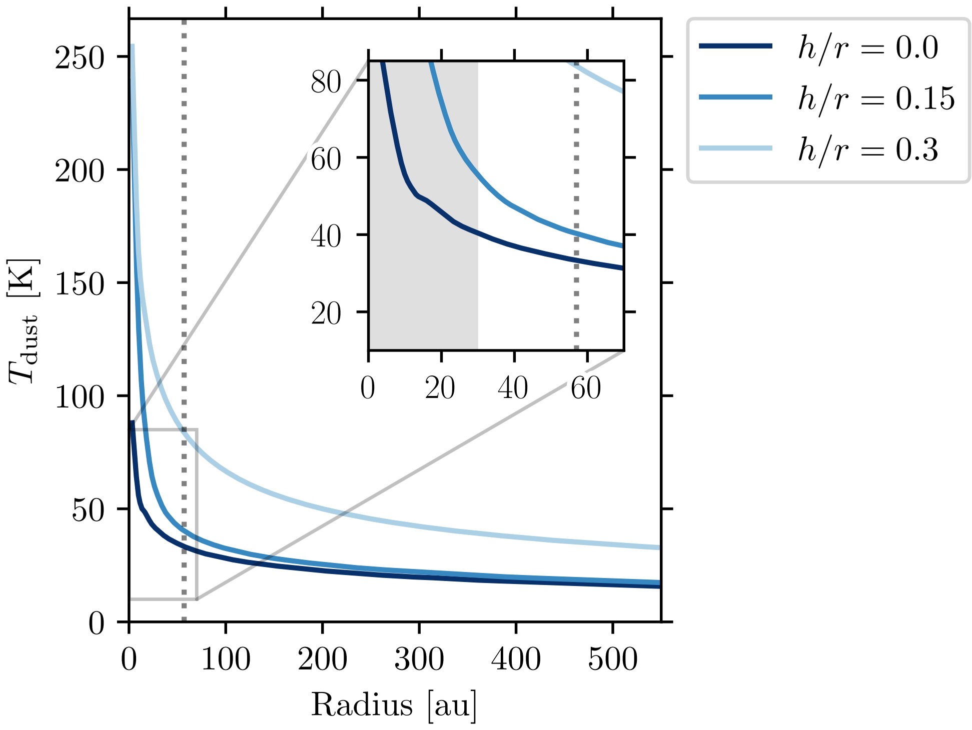

Figure C.1. Dust temperature profiles of the L1489 IRS disk at selected scale heights ($h/r = 0.0$ (midplane), 0.15, and 0.3), based on the radiative transfer calculation by Sai et al. (2020). The inset axis shows the inner region for visual clarity. The vertical dotted lines in the main and inset axes indicate the location of the dust ring. The grey-shaded region in the inset axis is an approximate SO emitting region.

Appendix D

Hyperfine Models for NH_3 and NH_2D

Here we describe the details of hyperfine models for observed NH_3 and NH_2D transitions.

D.1 NH_3 Model

We follow the methodology described in Rosolowsky et al. (2008). Observed spectra in terms of brightness temperature $T_{\rm B}(v)$ are modeled as

$$T_{\rm B}(v) = f(J_\nu(T_{\rm ex}) - J_\nu(T_{\rm bg}))(1 - e^{-\tau(v)}), \tag{D.1}$$

where f is the beam filling factor as in Equation 3.1, $T_{\rm ex}$ is the excitation temperature, $T_{\rm bg}$ is the background temperature (i.e., CMB temperature of 2.73 K here), $\tau(v)$ is the optical depth profile. For each transition of NH_3, $\tau(v)$ is given by

$$\tau(v) = \tau_0 \sum_i r_i \exp\left(-\frac{(v - \delta v_i - v_0)^2}{2\sigma_{v,i}^2}\right), \tag{D.2}$$

where τ_0 is the total optical depth of the transition, r_i, δv_i, and $\sigma_{v,i}$ are the relative strength, velocity offset, and line width of ith hyperfine component, and v_0 is the systemic velocity of the central protostar. The values of r_i, δv_i, and $\sigma_{v,i}$ are calculated as

$$r_i = \frac{g_{\mathrm{u},i} A_{\mathrm{ul},i}}{\sum_j g_{\mathrm{u},j} A_{\mathrm{u},j}}, \quad \delta v_i = \left(1 - \frac{\nu_i}{\nu_0}\right) c, \quad \sigma_{v,i} = \frac{\sigma_v}{c} \nu_i, \tag{D.3}$$

where ν_0 is the rest frequency of inversion transition listed in Table 3.1, $g_{\mathrm{u},i}$, $A_{\mathrm{ul},i}$, and ν_i are the statistical weight, Einstein A coefficient for spontaneous emission, and the rest frequency of ith hyperfine component, respectively (Table D.1, Kukolich 1967; Kukolich & Wofsy 1970). These data are retrieved from the Cologne Database for Molecular Spectroscopy (cdms, Müller et al. 2005) available at the Splatalogue database queried by `astroquery` (Ginsburg et al. 2019). We assumed that the σ_v and v_0 are common among the hyperfine components in the same inversion or rotational transition, given that they originate from the same temperature region.

The total optical depths of each transition are related back to the column density as in Friesen et al. (2009) (see also Rosolowsky et al. 2008);

$$N(J,K) = \sqrt{2\pi} \sigma_v \frac{8\pi \nu_0^3}{c^3 A_{\mathrm{ul}}} \frac{1 + \exp(-h\nu_0/k_{\mathrm{B}} T_{\mathrm{ex}})}{1 - \exp(-h\nu_0/k_{\mathrm{B}} T_{\mathrm{ex}})} \tau_0(J,K) \tag{D.4}$$

where $N(J,K)$ is the column density of NH$_3$ at the (J,K) metastable state. The column density $N(J,K)$ can be related with the total (ortho or para) NH$_3$ column density $N(\mathrm{NH_3})$ through the partition function Q as

$$N(\mathrm{NH_3}) = \frac{Q(T_{\mathrm{rot}})}{g_{\mathrm{u}}} N(J,K) \exp\left(\frac{E_{\mathrm{u}}}{T_{\mathrm{rot}}}\right) \tag{D.5}$$

where g_{u} and E_{u} are the statistical weight and energy of the upper state listed in Table 3.1. The partition function Q is calculated following Wilson et al. (2009) as

$$Q(T) = \sum_{J=0}^{\infty} \sum_{K=0}^{K=J} (2J+1) S(J,K) \exp\left[-\frac{h(BJ(J+1) + (C-B)K^2)}{k_{\mathrm{B}} T}\right], \tag{D.6}$$

where $B = 298117$ MHz and $C = 186726$ MHz are the rotational constants of NH$_3$, $S(J,K)$ is the constant factor for the nuclear spin statistics. For ortho- and para-NH$_3$ transitions, $S(J,K) = 4, 2$, respectively.

In the LTE approximation, the excitation temperature (T_{ex}) that govern the inversion transition and the rotational temperature (T_{rot}) that govern the population between the metastable levels are assumed to be the same, and these temperatures can be directly used as a proxy of the kinetic temperature ($T_{\rm kin}$). In our fit, all of these temperatures are assumed to be the same and represented by $T_{\rm ex}$.

D.2 NH_2D Model

Our NH_2D model follows the same formulation as NH_3. The spectroscopic data used for NH_2D are listed in Table D.1 (De Lucia & Helminger 1975; Cohen & Pickett 1982; Fusina et al. 1988). Since we observed only single transition for each ortho- and para-NH_2D, we directly related the optical depth to the column density assuming that $T_{\rm ex}$ is the same as that of NH_3;

$$N_{\rm u} = \sqrt{2\pi}\sigma_v \frac{8\pi\nu_0^3}{c^3 A_{\rm ul}} \left[\exp\left(\frac{h\nu_0}{k_{\rm B}T_{\rm ex}}\right) - 1\right] \tau_0 \tag{D.7}$$

where $N_{\rm u}$ is the NH_2D column density at the upper state of the transition. The total NH_2D column density is calculated as

$$N({\rm NH_2D}) = \frac{Q(T_{\rm ex})}{g_{\rm u}} N_u \exp\left(\frac{E_{\rm u}}{T_{\rm ex}}\right), \tag{D.8}$$

where Q is the full (i.e., ortho+para) partition function of NH_2D retrieved from the cdms (Müller et al. 2005).

Table D.1 Spectroscopic Data of NH_3 and NH_2D Used in Hyperfine Fits

Transition	F	ν_0 [GHz]	g_u	$\log_{10} A_\mathrm{ul}$ [s^{-1}]	$r^\dagger$	$\delta v^\ddagger$ [$\mathrm{km\,s}^{-1}$]
NH_3 $(3,3)$	2-3	23.8678062	20.0	−7.5449	0.0264	29.1753
	4-3	23.8684499	36.0	−7.794	0.0268	21.0909
	3-3	23.8701279	28.0	−6.6658	0.28	0.0163
	4-4	23.8701296	36.0	−6.6174	0.4024	−0.005
	2-2	23.8701303	20.0	−6.642	0.2112	−0.0138
	3-4	23.8718076	28.0	−7.6846	0.0268	−21.0796
	3-2	23.872452	28.0	−7.6908	0.0264	−29.1728
NH_3 $(4,4)$	3-4	24.1369314	14.0	−7.7529	0.0162	30.8605
	5-4	24.1374943	22.0	−7.9457	0.0163	23.8697
	4-4	24.139415	18.0	−6.5927	0.3007	0.0161
	5-5	24.139417	22.0	−6.5648	0.3919	−0.0087
	3-3	24.1394175	14.0	−6.5771	0.2424	−0.0149
	4-5	24.1413376	18.0	−7.8583	0.0163	−23.861
	4-3	24.1419011	18.0	−7.8617	0.0162	−30.8593
NH_3 $(5,5)$	4-5	24.5303911	18.0	−7.9088	0.0109	31.7426
	6-5	24.5308986	26.0	−8.0659	0.011	25.541
	5-5	24.532987	22.0	−6.5396	0.3113	0.0208
	6-6	24.5329892	26.0	−6.5211	0.384	−0.0061
	4-4	24.5329897	18.0	−6.529	0.261	−0.0122
	5-6	24.5350777	22.0	−7.9932	0.011	−25.5275
	5-4	24.5355856	22.0	−7.9957	0.0109	−31.734
NH_2D $3_{1,3}$–$3_{0,3}$	2-3	18.805907	15.0	−8.3826	0.0265	31.5766
	4-3	18.80649	27.0	−8.6324	0.0268	22.2837

Table D.1—*Continued*

Transition	F	ν_0 [GHz]	g_u	$\log_{10} A_\mathrm{ul}$ [$\mathrm{s^{-1}}$]	$r^\dagger$	$\delta v^\ddagger$ [$\mathrm{km\,s^{-1}}$]
	2-2	18.807831	15.0	-7.4793	0.2116	0.9086
	2-2	18.807831	27.0	-7.4562	0.4018	0.9086
	3-3	18.8080466	21.0	-7.5037	0.2801	-2.528
	3-4	18.809385	21.0	-8.523	0.0268	-23.8618
	3-2	18.8099083	21.0	-8.5284	0.0265	-32.203
NH_2D $4_{1,4}$–$4_{0,4}$	3-4	25.0216041	7.0	-8.2179	0.0162	26.2117
	5-4	25.0221167	11.0	-8.4117	0.0163	20.0706
	3-3	25.0237541	7.0	-7.0417	0.2431	0.4541
	5-5	25.0237746	11.0	-7.0314	0.3911	0.2085
	4-4	25.0238552	9.0	-7.0582	0.3008	-0.7572
	4-5	25.0255132	9.0	-8.3244	0.0163	-20.6205
	4-3	25.0260052	9.0	-8.3268	0.0162	-26.5148

† Relative strengths of hyperfine transitions. Normalized as the sum of r being one.

‡ Velocity offsets with respect to the inversion or rotation transitions listed in Table 3.1.

Appendix E

Radiative Transfer Modeling

We simulated the spectra of NH_2D transitions using the non-LTE radiative transfer code lime (Brinch & Hogerheijde 2010) to see if only the cold envelope component of NH_2D can reproduce the observed NH_2D emission. Here we will describe the simulation settings. As the density and temperature structures of the IRAS4A protostellar cores, we used the spherically symmetric envelope model presented in Persson et al. (2016). The gas density and dust temperature profiles are shown in Figure E.1 and Figure E.2. The gas density follows a single power-law profile, $n = n_{\rm in}\,(r/r_{\rm in})^{-p_{\rm env}}$, where the parameters of $n_{\rm in} = 3.1 \times 10^9\,{\rm cm}^{-3}$, $r_{\rm in} = 33.5\,{\rm au}$, and $p_{\rm env} = 1.8$ are constrained through the simultaneous fits to sub-mm dust continuum radial profiles and spectral energy distributions (SEDs) (see also Jørgensen et al. 2002; Kristensen et al. 2012). For this profile of the gas density, the dust temperature profile is self-consistently calculated (Jørgensen et al. 2002; Kristensen et al. 2012; Persson et al. 2016) assuming the observed luminosity of $9.1\,L_\odot$. We adopted this dust temperature profile as the gas temperature profile, i.e., assumed that the gas and dust are well-coupled and their temperatures are the same. The modeled dust temperature inside the observed emitting region size ($\sim$75 au) is $\gtrsim 100\,{\rm K}$, consistent with the observed excitation temperatures of $\sim 100\,{\rm K}$ and $\sim 160\,{\rm K}$ (see Section 3.4). The radial profiles are truncated at $r_{\rm in}$ and $r_{\rm out} = 33500\,{\rm au}$.

For the kinetics of the gas, we simply employed the spherically symmetric free-falling envelope with a radial velocity of $v_{\rm ff} = \sqrt{2GM_\star/r}$. We assumed the protostellar mass

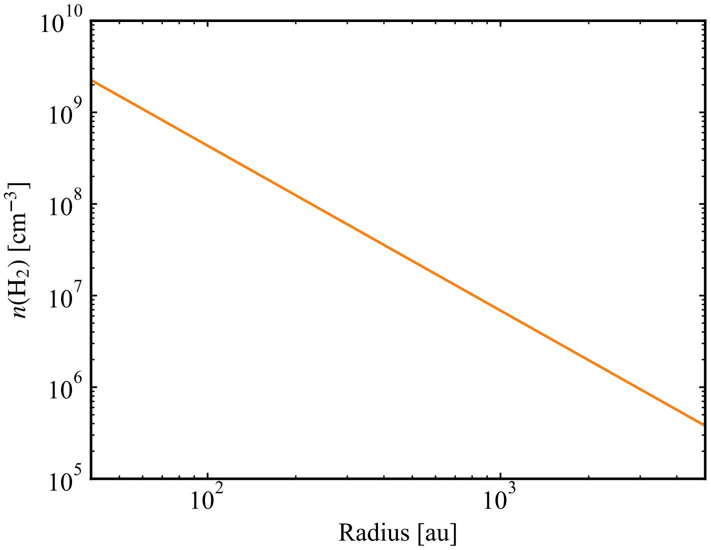

Figure E.1. Gas density profile of the IRAS4A envelope presented in Persson et al. (2016).

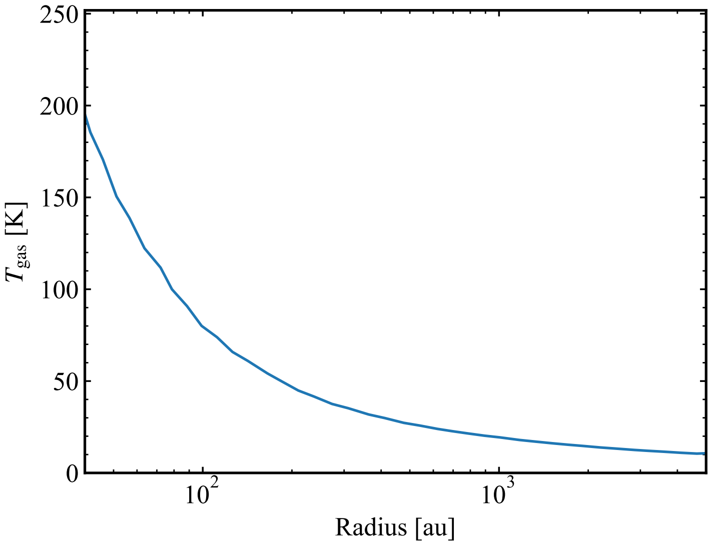

Figure E.2. Dust temperature profile of the IRAS4A envelope presented in Persson et al. (2016).

of $M_\star = 1M_\odot$ for both 4A1 and 4A2, given that there are almost no measurement of the central stellar mass. For 4A2, Choi et al. (2010) estimated it to be $0.08\,M_\odot$ from the velocity gradient analysis of NH_3 emission. Thus, we took another run with $M_\star = 0.08\,M_\odot$ to evaluate the effect of the central stellar mass to observed emission.

We calculated the NH_2D abundance in the cold envelope based on the single-dish observations and the model H_2 column density. Hatchell (2003) observed the NH_2D rotation-inversion transition with the IRAM 30 m telescope (with a beam size of ∼25″or ∼7000 au), and derived an NH_2D column density of $3.9 \times 10^{14}\,\mathrm{cm}^{-2}$. This value is divided by the model H_2 column density of $1.9 \times 10^{24}\,\mathrm{cm}^{-2}$ (see Table C.1 in Kristensen et al. 2012), resulting in an NH_2D abundance of $2.1\ \times 10^{-10}$. A constant abundance with radius is employed. The ortho-to-para ratio of NH_2D is fixed to three, as done for the observational data analysis (Section 3.3).

The collisional excitation rates of ortho-NH_2D and para-NH_2D are based on Daniel et al. (2014) and taken from the Leiden Atomic and Molecular Database (lamda, Schöier et al. 2005). Given that the collisional excitation rates for ortho-H_2 and para-H_2 are available, we employ the thermal ortho-to-para ratio of H_2 (Flower & Watt 1984, 1985);

$$\frac{n(\text{ortho-H}_2)}{n(\text{para-H}_2)} = 9\exp\left(-\frac{170.5\,\mathrm{K}}{T}\right), \tag{E.1}$$

where T is the gas temperature. This ratio is low at low temperature, e.g., ∼0.03 at 30 K.

We use the dust opacity with thin ice mantle presented in the fifth columns of Table 1 in Ossenkopf & Henning (1994) and a standard gas-to-dust mass ratio of 100. The dust opacity is the same as the one used in the modeling by Persson et al. (2016).

We run the lime code with its non-LTE mode to produce the model image cubes of NH_2D $3_{1,3} - 3_{0,3}$ and $4_{1,4} - 4_{0,4}$ transitions. To simulate the observations, first we convolved the output image cubes by the 2D Gaussian with the FWHM of the beam major and minor axis. Then, we subtracted the continuum emission by the CASA task *imcontsub* and extracted the spectra toward the continuum peak by the same manner as the case of the observations.

The simulated spectra are compared to the observed spectra in Figure E.3. The model with $0.08\,M_\odot$ stellar mass show the brighter peak intensity due to the narrower line width caused by lower free-falling velocities. For both models, the peak intensity of the model spectra are weaker compared to the observed spectra by a factor of $\gtrsim$10, except for NH_2D $3_{1,3}$–$3_{0,3}$ with a central stellar mass of $0.08\,M_\odot$. The cold component may partially contribute to NH_2D $3_{1,3}$–$3_{0,3}$ emission (∼20% in velocity-integrated intensity) if the central stellar mass is small. We note that, however, the hyperfine splitting is not considered in this modeling. If it is considered, the peak intensity can be weaker because the total emission will be distributed over the hyperfine satellites. This is particularly effective for NH_2D $3_{1,3}$–$3_{0,3}$ where it has a prominent splitting around the main component (see Table D.1 for the hyperfine spectroscopic data). Thus, this comparison between model and observed spectra suggests that the observed emission cannot be reproduced by the cold component alone. Therefore, we suggest that the observed NH_2D emission indeed traces the NH_2D sublimated from ice in the hot corino rather than the cold envelope component, and the degree of NH_3 ice deuteration is indeed high in the protostellar cores of IRAS 4A1 and 4A2. We emphasize that the purpose of the radiative transfer modeling presented here is to just evaluate the contributions of the cold component of NH_2D in the envelope to the observed emission. More detailed modeling is needed to reproduce the observed emission. Although the detailed physical structure on smaller scales can differ from the simple free-falling envelope model presented here (e.g., protostellar disk as considered by Choi et al. 2010), it is beyond the scope of the present work.

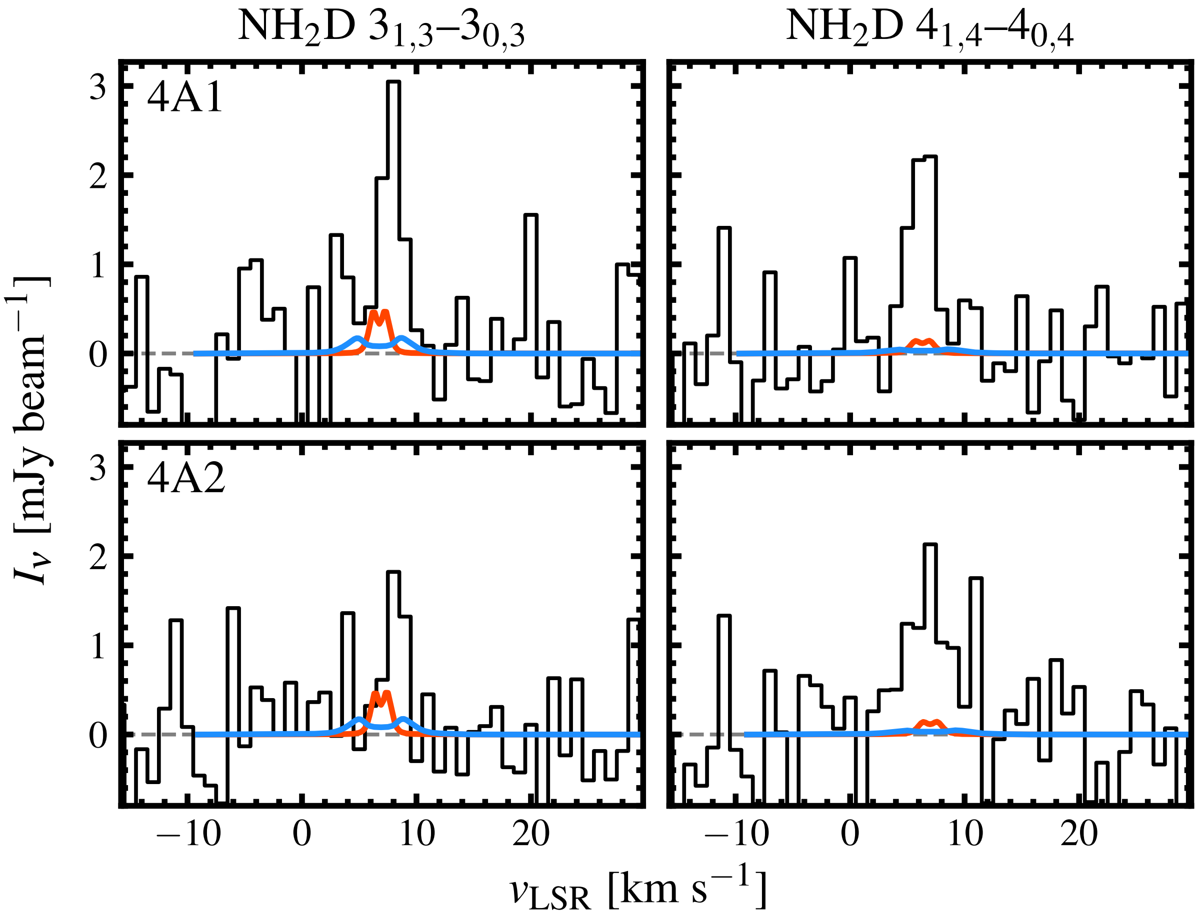

Figure E.3. Comparisom of model spectra of NH$_2$D transitions predicted by the non-LTE simulation with central stellar masses of $1.0\,M_\odot$ (blue) and $0.08\,M_\odot$ (orange) and observed spectra toward 4A1 (top) and 4A2 (bottom). The zero intensity level is indicated by the grey dashed line.

Appendix F

Channel Maps of the COM Emission

Figure F.1, F.2, and F.3 show the channel maps of the bright, unblended transitions of CH_3OH, CH_3CHO, and CH_3OCHO, respectively, which are used for the line profile analysis in Section 4.3.2. The comparison to the corresponding Keplerian radius (i.e., $r = GM_\star \sin^2 i/(v - v_{\mathrm{sys}})^2$) at each velocity channel is made.

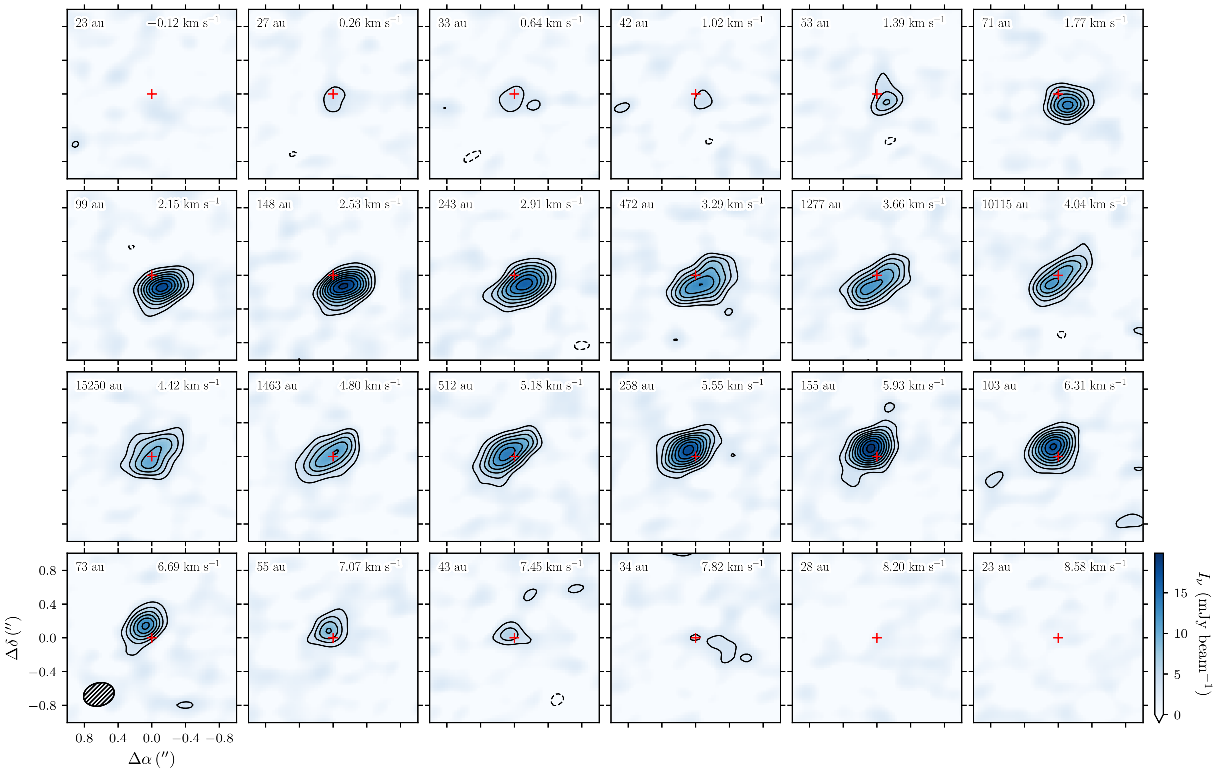

Figure F.1. Channel maps of the CH_3OH $2_{-1,1} - 1_{-1,0}$ E $v_t = 0$ transition. The black contours mark the $[-3, 3, 5, 7, ...] \times \sigma$ levels. The dashed contours indicate the negative values. The numbers in the upper-right and upper-left corners indicate the velocity of the channel and its corresponding Keplerian radius ($r = GM_\star \sin^2 i/(v - v_{\rm sys})^2$), respectively. The red cross in each panel indicate the position of the disk center. The beam is shown in the lower-left corner of the lower-left panel.

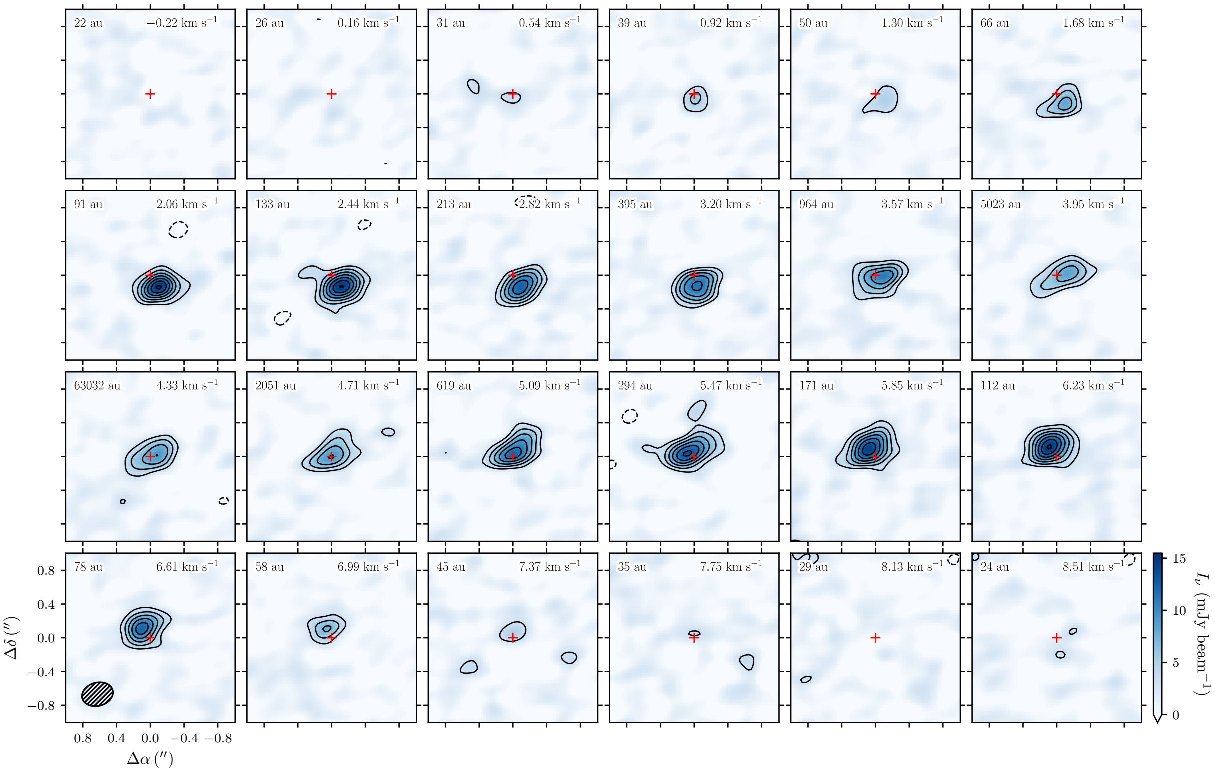

Figure F.2. Same as Figure F.1, but for CH_3CHO $5_{2,3} - 4_{2,2}$ E $v_t = 0$ transition.

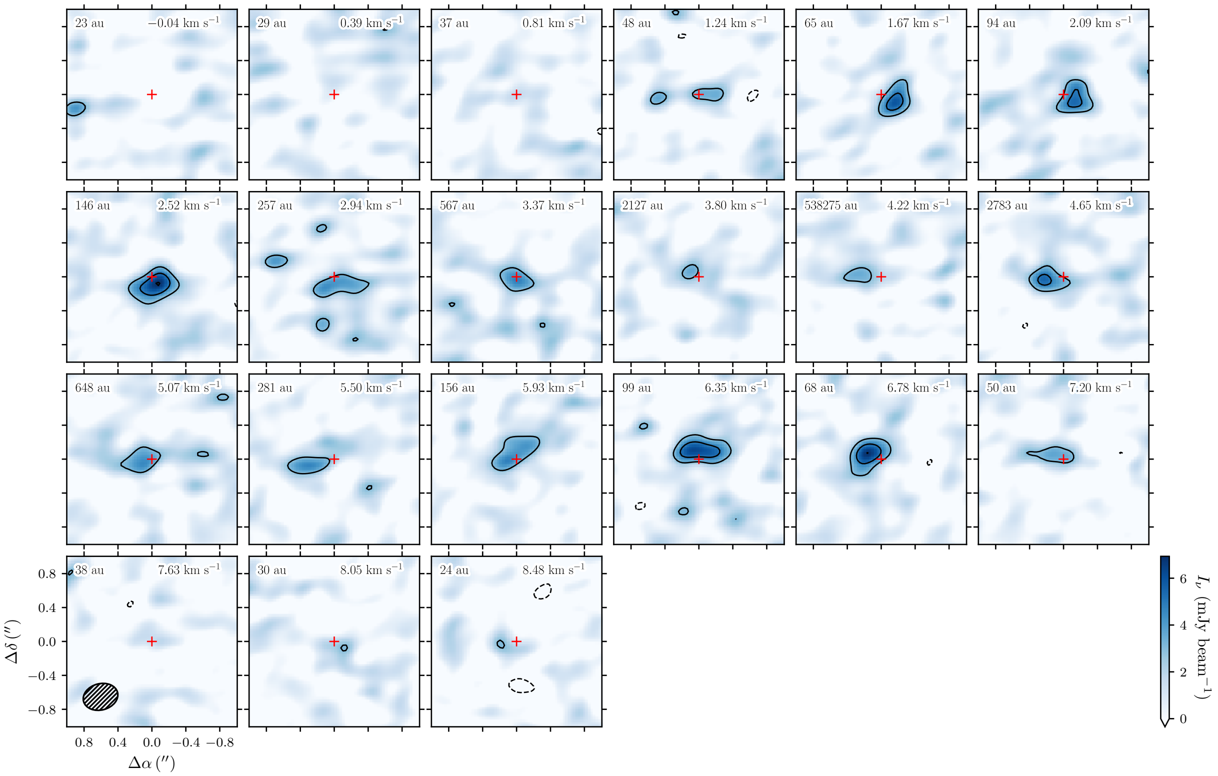

Figure F.3. Same as Figure F.1, but for CH_3OCHO $8_{5,3} - 7_{5,2}$ A $v_t = 0$ transition.

Appendix G

JvM effect and Continuum Subtraction

Here we describe a brief summary of the Jorsater & van Moorsel (JvM) effect (Jorsater & van Moorsel 1995; Czekala et al. 2021), and subsequently discuss the continuum subtraction methods, which could mitigate the JvM effect.

The JvM effect could result in incorrect measurements of the flux density on the interferometric images produced by the CLEAN deconvolution method, which was originally discussed in Jorsater & van Moorsel (1995) and extensively investigated in Czekala et al. (2021). During the imaging process, the CLEAN algorithm iteratively extracts the CLEAN components from the residual image, and this process will be terminated when the peak value of the residual image within the CLEAN mask reaches a user-defined threshold (typically 2–3 × the RMS level; see Figure 2 in Czekala et al. (2021) for a comprehensive summary of this procedure). The final image product of CLEAN is the sum of the CLEANed model image (convolved with a CLEAN beam determined by a Gaussian fit to the dirty beam) and the residual images, which have inconsistent units (Jansky per CLEAN beam and Jansky per dirty beam). Therefore, if the dirty beam significantly deviates from the CLEAN beam (Gaussian) and the faint emission below the CLEAN threshold remains on the residual image, the intensity scale in the final image can be incorrect (i.e., sum of values with two different units). The impact of this effect depends on the emission strengths, the CLEAN threshold, and the deviation of the dirty beam shape from the CLEAN beam shape: if a significant portion of the emission remains on the residual image and the deviation is large, the intensity scale in the final image will drastically modified from the correct intensity scale (Jorsater & van Moorsel 1995; Czekala et al. 2021).

To correct for this unit inconsistency, Czekala et al. (2021) applied the "JvM correction" to the line emission in protoplanetary disks, where the residual image is scaled before the addition with the CLEANed model image by the ratio of the dirty beam area to the CLEAN beam area, forcing the unit of the residual image to be Jansky per CLEAN beam. However, Casassus & Cárcamo (2022) pointed out that the JvM correction can artificially manipulate the noise levels and exaggerate the signal-to-noise ratio of the emission, as the correction will scale the residual image that contains the noise typically by a factor smaller than unity (see also Appendix A in Casassus et al. 2023). So far, no concrete solution for this problem has been drawn.

We applied the JvM correction to our data following Czekala et al. (2021), which obtained a JvM ϵ (the ratio of dirty beam area to the CLEAN beam area) of ~ 0.28, indicating that the effect is severe. This could result in a drastic underestimation of the uncertainties of physical quantities derived from the fits described in Section 4.3. Another possible solution is CLEANing deeper (e.g., down to 0.5–1 × the RMS level) so that all the emission components are recovered, but this would be unrealistic as too deep CLEANing will not converge and it is practically unfeasible to CLEAN down to such deep levels particularly for the line image cubes with a lot of channels. Alternatively, we mitigate the JvM effect and recover correct flux scale as much as possible by employing the continuum subtraction on the image plane (with the CASA task `imcontsub`) rather than on the visibility plane (with the CASA task `uvcontsub`). The line emission in our data is almost co-spatial to the strong continuum emission, and therefore imaging without continuum subtraction can almost completely include the line emission into the CLEAN model, thanks to the strong line plus continuum intensity well above the CLEAN threshold. While the continuum component is still affected by the JvM effect, the line emission can be safely recovered by subsequent continuum subtraction on the image plane. Figure G.1

shows an example demonstrating that almost no spectral line component remain in the residual spectrum and the line emission is almost fully recovered in the CLEANed image. We note that this method is only applicable to the spectral line data associated with a strong continuum emission. If the continuum emission is faint in the emitting region of the spectral line, the spectral line component will still remain in the residual even with the continuum subtraction on the image plane.

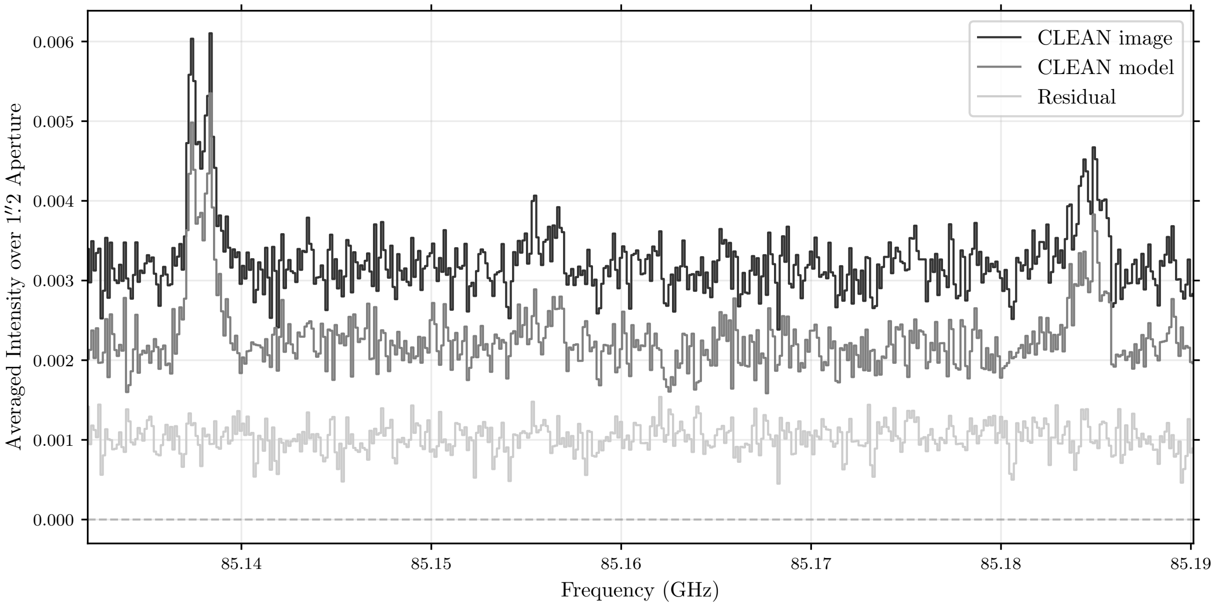

Figure G.1. Line plus continuum spectra of SPW 2 averaged over 1."2 aperture for the CLEAN image (dark gray), the CLEAN model (gray), and the residual (light gray). The CLEAN model spectrum (in unit of Jy pixel^{-1} by default) is scaled up by a ratio of the CLEAN beam area to the pixel area for visual clarity. The spectral line emission is almost fully recovered into the CLEAN model and none of that remains in the residual spectrum. The horizontal dashed line indicates the zero-flux level.

Appendix H

Detected Transitions

Table H.1 lists the transitions detected in our observations for each molecular species, including the blended ones.

Table H.1 Detected Transitions for Each Species

Species	Transition	ν_0 (GHz)	$\log_{10}A_{\rm ul}$ (s^{-1})	$g_{\rm u}$	$E_{\rm u}$ (K)	SPW
Methanol (CH_3OH)						
$CH_3OH^{\ddagger*}$	$2_{-1,2} - 1_{-1,1}$ E $v_t = 1$	96.492163	-5.5963	20.0	298	7
$CH_3OH^{\ddagger*}$	$2_{0,2} - 1_{0,1}$ E $v_t = 1$	96.493551	-5.4706	20.0	307	7
$CH_3OH^{\ddagger}$	$2_{1,1} - 1_{1,0}$ E $v_t = 1$	96.501713	-5.5967	20.0	420	7
CH_3OH	$2_{0,2} - 1_{0,1}$ A $v_t = 1$	96.513686	-5.4709	20.0	430	7
$CH_3OH^{\dagger*}$	$2_{1,2} - 1_{1,1}$ E $v_t = 0$	96.739358	-5.5923	20.0	12	9
$CH_3OH^{\dagger*}$	$2_{0,2} - 1_{0,1}$ A $v_t = 0$	96.741371	-5.4676	20.0	6	9
CH_3OH^{*}	$2_{0,2} - 1_{0,1}$ E $v_t = 0$	96.744545	-5.4676	20.0	20	9
CH_3OH^{*}	$2_{-1,1} - 1_{-1,0}$ E $v_t = 0$	96.755501	-5.581	20.0	28	9
CH_3OH^{*}	$2_{1,1} - 1_{1,0}$ A $v_t = 0$	97.582798	-5.5807	20.0	21	10
$CH_3OH^{\dagger}$	$21_{6,16} - 22_{5,17}$ A $v_t = 0$	97.677684	-5.8404	172.0	729	10
$CH_3OH^{\dagger}$	$21_{6,15} - 22_{5,18}$ A $v_t = 0$	97.678803	-5.8403	172.0	729	10
Methanol (CH_2DOH)						
$CH_2DOH^{\ddagger}$	$2_{1,1} - 2_{0,2}$ e0	86.668751	-5.3322	5.0	10	4
$CH_2DOH^{\ddagger}$	$4_{1,3} - 4_{0,4}$ o1	97.870192	-5.3363	9.0	44	10
CH_2DOH	$4_{0,4} - 3_{1,3}$ e0	98.031213	-5.616	9.0	21	10
Methyl Formate (CH_3OCHO)						
CH_3OCHO	$7_{6,1} - 6_{6,0}$ E $v_t = 1$	85.157135	-5.6248	30.0	228	3
$CH_3OCHO^{\dagger}$	$7_{5,3} - 6_{5,2}$ A $v_t = 1$	85.185466	-5.3602	30.0	220	3
$CH_3OCHO^{\dagger}$	$7_{5,2} - 6_{5,1}$ A $v_t = 1$	85.186063	-5.3602	30.0	220	3
CH_3OCHO	$7_{4,3} - 6_{4,2}$ E $v_t = 1$	85.506219	-5.2142	30.0	214	1
CH_3OCHO	$7_{5,3} - 6_{5,2}$ E $v_t = 1$	85.55338	-5.3527	30.0	220	1
CH_3OCHO	$7_{6,1} - 6_{6,0}$ E $v_t = 0$	85.919209	-5.6138	30.0	40	2
$CH_3OCHO^{\dagger*}$	$7_{6,2} - 6_{6,1}$ E $v_t = 0$	85.926553	-5.6137	30.0	40	2
$CH_3OCHO^{\dagger*}$	$7_{6,2} - 6_{6,1}$ A $v_t = 0$	85.927227	-5.6136	30.0	40	2
$CH_3OCHO^{\dagger*}$	$7_{6,1} - 6_{6,0}$ A $v_t = 0$	85.927227	-5.6136	30.0	40	2

Table H.1—*Continued*

Species	Transition	ν_0 (GHz)	$\log_{10}A_{\rm ul}$ (s^{-1})	$g_{\rm u}$	$E_{\rm u}$ (K)	SPW
CH_3OCHO	$7_{4,4} - 7_{3,5}$ E $v_t = 0$	96.507882	-6.1542	30.0	27	7
CH_3OCHO	$8_{4,5} - 8_{3,6}$ A $v_t = 0$	96.709259	-5.9454	34.0	31	9
CH_3OCHO	$7_{4,3} - 7_{3,5}$ E $v_t = 0$	96.776715	-6.4523	30.0	27	9
CH_3OCHO	$5_{4,2} - 5_{3,3}$ A $v_t = 0$	96.794121	-6.1026	22.0	19	9
CH_3OCHO	$8_{5,3} - 7_{5,2}$ E $v_t = 1$	97.577303	-5.0823	34.0	225	10
CH_3OCHO	$8_{3,6} - 7_{3,5}$ A $v_t = 1$	97.597161	-4.9359	34.0	214	10
$CH_3OCHO^\dagger$	$8_{7,2} - 7_{7,1}$ E $v_t = 1$	97.65127	-5.4962	34.0	240	10
$CH_3OCHO^\dagger$	$10_{4,7} - 10_{3,8}$ E $v_t = 0$	97.65127	-5.9015	42.0	43	10
CH_3OCHO	$8_{4,5} - 7_{4,4}$ A $v_t = 1$	97.661401	-4.9937	34.0	219	10
$CH_3OCHO^\ddagger$	$10_{4,7} - 10_{3,8}$ A $v_t = 0$	97.69426	-5.8957	42.0	43	10
$CH_3OCHO^\ddagger$	$12_{1,11} - 12_{0,12}$ A $v_t = 1$	97.727054	-6.2029	50.0	234	10
CH_3OCHO	$8_{6,3} - 7_{6,2}$ E $v_t = 1$	97.738738	-5.2243	34.0	232	10
CH_3OCHO	$8_{4,4} - 7_{4,3}$ A $v_t = 1$	97.752885	-4.9924	34.0	219	10
$CH_3OCHO^\ddagger$	$8_{4,4} - 8_{3,5}$ E $v_t = 1$	97.871147	-5.967	34.0	219	10
$CH_3OCHO^\ddagger$	$10_{4,7} - 10_{3,8}$ A $v_t = 1$	97.878933	-5.8854	42.0	230	10
CH_3OCHO	$8_{5,4} - 7_{5,3}$ E $v_t = 1$	97.885663	-5.0787	34.0	224	10
CH_3OCHO	$8_{4,4} - 7_{4,3}$ E $v_t = 1$	97.897118	-4.9875	34.0	219	10
$CH_3OCHO^\ddagger$	$21_{4,17} - 21_{3,18}$ A $v_t = 1$	98.066305	-5.7833	86.0	337	10
$CH_3OCHO^\ddagger$	$8_{4,5} - 7_{4,4}$ E $v_t = 1$	98.176293	-4.9853	34.0	218	10
CH_3OCHO	$8_{7,1} - 7_{7,0}$ E $v_t = 0$	98.182336	-5.4902	34.0	53	10
$CH_3OCHO^{\dagger *}$	$8_{7,2} - 7_{7,1}$ A $v_t = 0$	98.190658	-5.4899	34.0	53	10
$CH_3OCHO^{\dagger *}$	$8_{7,1} - 7_{7,0}$ A $v_t = 0$	98.190658	-5.4899	34.0	53	10
$CH_3OCHO^{\dagger *}$	$8_{7,2} - 7_{7,1}$ E $v_t = 0$	98.19146	-5.49	34.0	53	10
CH_3OCHO*	$8_{6,2} - 7_{6,1}$ E $v_t = 0$	98.270501	-5.218	34.0	45	10
$CH_3OCHO^{\dagger *}$	$8_{6,3} - 7_{6,2}$ E $v_t = 0$	98.278921	-5.2178	34.0	45	10
$CH_3OCHO^{\dagger *}$	$8_{6,3} - 7_{6,2}$ A $v_t = 0$	98.279762	-5.2178	34.0	45	10

Table H.1—*Continued*

Species	Transition	ν_0 (GHz)	$\log_{10}A_{\rm ul}$ (s^{-1})	$g_{\rm u}$	$E_{\rm u}$ (K)	SPW
$CH_3OCHO^{\dagger *}$	$8_{6,2} - 7_{6,1}$ A $v_t = 0$	98.279762	-5.2178	34.0	45	10
$CH_3OCHO^{\dagger *}$	$9_{0,9} - 8_{1,8}$ A $v_t = 1$	98.423165	-5.701	38.0	212	10
$CH_3OCHO^{\dagger *}$	$8_{5,3} - 7_{5,2}$ E $v_t = 0$	98.424207	-5.0722	34.0	37	10
$CH_3OCHO^{\dagger *}$	$8_{5,4} - 7_{5,3}$ E $v_t = 0$	98.431803	-5.072	34.0	37	10
$CH_3OCHO^{\dagger *}$	$8_{5,4} - 7_{5,3}$ A $v_t = 0$	98.43276	-5.0719	34.0	37	10
CH_3OCHO	$8_{5,3} - 7_{5,2}$ A $v_t = 0$	98.435802	-5.0719	34.0	37	10
CH_3OCHO	$8_{4,5} - 7_{4,3}$ E $v_t = 0$	98.443186	-6.4657	34.0	31	10
		Methyl Formate ($CH_3O^{13}CHO$)				
$CH_3O^{13}CHO^{\dagger}$	$8_{-6,3} - 7_{-6,2}$ E $v_t = 0$	97.549352	-5.2185	34.0	44	10
$CH_3O^{13}CHO^{\dagger}$	$8_{6,3} - 7_{6,2}$ A $v_t = 0$	97.55014	-5.2185	34.0	44	10
$CH_3O^{13}CHO^{\dagger}$	$8_{6,2} - 7_{6,1}$ A $v_t = 0$	97.550183	-5.2185	34.0	44	10
$CH_3O^{13}CHO^{\ddagger}$	$8_{-5,4} - 7_{-5,3}$ E $v_t = 0$	97.702479	-5.0727	34.0	37	10
$CH_3O^{13}CHO^{\ddagger}$	$8_{5,4} - 7_{5,3}$ A $v_t = 0$	97.703323	-5.0726	34.0	37	10
$CH_3O^{13}CHO$	$8_{-3,6} - 7_{-3,5}$ E $v_t = 0$	97.874331	-4.9221	34.0	27	10
$CH_3O^{13}CHO^{\ddagger}$	$8_{3,6} - 7_{3,5}$ A $v_t = 0$	97.878443	-4.9215	34.0	27	10
$CH_3O^{13}CHO^{\ddagger}$	$8_{4,4} - 7_{4,3}$ E $v_t = 0$	98.019644	-4.9931	34.0	31	10
		Methyl Formate ($^{13}CH_3OCHO$)				
$^{13}CH_3OCHO^{\ddagger}$	$8_{3,5} - 7_{3,4}$ E $v_t = 0$	97.816488	-5.2344	34.0	22	10
$^{13}CH_3OCHO^{\ddagger}$	$8_{-3,5} - 7_{-3,4}$ E $v_t = 0$	97.816489	-5.2237	34.0	26	10
$^{13}CH_3OCHO^{\ddagger}$	$8_{3,5} - 7_{3,4}$ A $v_t = 0$	97.829563	-5.2228	34.0	26	10
$^{13}CH_3OCHO^{\ddagger}$	$9_{1,9} - 8_{1,8}$ E $v_t = 0$	97.871736	-5.1613	38.0	24	10
$^{13}CH_3OCHO^{\ddagger}$	$9_{1,9} - 8_{1,8}$ A $v_t = 0$	97.873563	-5.1612	38.0	24	10
$^{13}CH_3OCHO^{\dagger}$	$8_{-1,7} - 7_{-1,6}$ E $v_t = 0$	98.207248	-5.1648	34.0	22	10
$^{13}CH_3OCHO^{\dagger}$	$8_{1,7} - 7_{1,6}$ E $v_t = 0$	98.207251	-5.1756	34.0	17	10
$^{13}CH_3OCHO^{\dagger}$	$8_{1,7} - 7_{1,6}$ A $v_t = 0$	98.215266	-5.1647	34.0	22	10
		Acetaldehyde (CH_3CHO)				

Table H.1—*Continued*

Species	Transition	ν_0 (GHz)	$\log_{10}A_{\mathrm{ul}}$ (s^{-1})	g_{u}	E_{u} (K)	SPW
$\mathrm{CH_3CHO}$	$9_{1,8} - 9_{0,9}$ E $v_t = 1$	85.947624	-5.559	38.0	249	2
$\mathrm{CH_3CHO}^{\dagger}$	$12_{2,11} - 12_{1,11}$ E $v_t = 1$	87.303557	-6.1944	50.0	285	6
$\mathrm{CH_3CHO}^{\dagger}$	$11_{4,7} - 12_{3,9}$ E $v_t = 1$	87.303714	-6.2602	46.0	303	6
$\mathrm{CH_3CHO}*$	$5_{2,3} - 4_{2,2}$ E $v_t = 0$	96.475524	-4.6168	22.0	23	7
$\mathrm{CH_3CHO}$	$11_{4,8} - 12_{3,10}$ E $v_t = 0$	96.48895	-6.1541	46.0	97	7
$\mathrm{CH_3CHO}^{\dagger*}$	$5_{3,3} - 4_{3,2}$ A $v_t = 2$	96.716114	-4.7374	22.0	420	9
$\mathrm{CH_3CHO}^{\dagger*}$	$5_{3,2} - 4_{3,1}$ A $v_t = 2$	96.717473	-4.7374	22.0	420	9
$\mathrm{CH_3CHO}^{\dagger*}$	$5_{2,3} - 4_{2,2}$ A $v_t = 1$	96.718409	-4.6093	22.0	228	9
$\mathrm{CH_3CHO}^{*}$	$7_{0,7} - 6_{1,6}$ A $v_t = 0$	96.765371	-5.5556	30.0	25	9
$\mathrm{CH_3CHO}^{*}$	$5_{2,4} - 4_{2,3}$ E $v_t = 1$	96.800291	-4.613	22.0	226	9
$\mathrm{CH_3CHO}$	$5_{3,2} - 4_{3,1}$ E $v_t = 2$	97.612131	-4.9808	22.0	419	10
$\mathrm{CH_3CHO}$	$19_{2,18} - 18_{3,15}$ E $v_t = 0$	97.796104	-6.1248	78.0	183	10
$\mathrm{CH_3CHO}$	$10_{4,7} - 11_{3,8}$ A $v_t = 1$	97.941422	-6.1583	42.0	290	10
$\mathrm{CH_3CHO}$	$21_{3,18} - 20_{4,17}$ A $v_t = 0$	98.20169	-6.01	86.0	235	10
$\mathrm{CH_3CHO}$	$6_{3,3} - 7_{2,5}$ E $v_t = 0$	98.368631	-6.245	26.0	39	10
Acetaldehyde ($\mathrm{CH_3^{13}CHO}$)						
$\mathrm{CH_3^{13}CHO}^{\ddagger*}$	$5_{2,3} - 4_{2,2}$ A $v_t = 0$	96.494465	-4.5971	11.0	22	7
Acetaldehyde ($\mathrm{CH_3CDO}$)						
$\mathrm{CH_3CDO}$	$5_{1,4} - 4_{1,3}$ E $v_t = 0$	97.81231	-4.5235	11.0	15	10
$\mathrm{CH_3CDO}$	$5_{1,4} - 4_{1,3}$ A $v_t = 0$	97.828514	-4.5234	11.0	15	10
Acetaldehyde ($\mathrm{CH_2DCHO}$)						
$\mathrm{CH_2DCHO}$	$11_{2,9}i - 11_{1,10}i$	98.412832	-5.2329	23.0	66	10
Dimethyl Ether ($\mathrm{CH_3OCH_3}$)						
$\mathrm{CH_3OCH_3}^{\dagger}$	$16_{3,14} - 15_{4,11}$ AA	97.990629	-5.8984	330.0	136	10
$\mathrm{CH_3OCH_3}^{\dagger}$	$16_{3,14} - 15_{4,11}$ EE	97.993382	-5.8983	528.0	136	10
$\mathrm{CH_3OCH_3}^{\dagger}$	$16_{3,14} - 15_{4,11}$ EA	97.996098	-5.8984	132.0	136	10

Table H.1—*Continued*

Species	Transition	ν_0 (GHz)	$\log_{10}A_{\mathrm{ul}}$ (s^{-1})	g_{u}	E_{u} (K)	SPW
CH_3OCH_3†	$16_{3,14} - 15_{4,11}$ AE	97.996174	-5.8984	198.0	136	10
			Acetone (CH_3COCH_3)			
CH_3COCH_3†	$17_{6,11} - 17_{5,12}$ AE	97.929123	-4.7694	210.0	110	10
CH_3COCH_3†	$17_{6,11} - 17_{5,12}$	97.929247	-4.7694	140.0	110	10
CH_3COCH_3†	$17_{7,11} - 17_{6,12}$ AE	97.930235	-4.7694	70.0	110	10
CH_3COCH_3†	$17_{7,11} - 17_{6,12}$	97.930344	-4.7693	140.0	110	10
CH_3COCH_3†	$17_{6,11} - 17_{5,12}$ EE	98.052399	-4.7674	560.0	110	10
CH_3COCH_3†	$17_{7,11} - 17_{6,12}$ EE	98.053535	-4.7674	560.0	110	10
			Ethylene Oxide (c-C_2H_4O)			
c-C_2H_4O‡	$11_{9,3} - 11_{8,4}$	96.501033	-5.0737	115.0	146	7
c-C_2H_4O‡	$12_{9,4} - 12_{8,5}$	97.728742	-4.9909	75.0	169	10
			Propenal (t-C_2H_3CHO)			
t-C_2H_3CHO‡	$11_{2,10} - 10_{2,9}$	97.815592	-4.3286	23.0	36	10
t-C_2H_3CHO‡	$11_{8,3} - 10_{8,2}$	97.947054	-4.6391	23.0	159	10
t-C_2H_3CHO‡	$11_{8,4} - 10_{8,3}$	97.947054	-4.6391	23.0	159	10
t-C_2H_3CHO‡	$11_{7,5} - 10_{7,4}$	97.947549	-4.5377	23.0	129	10
t-C_2H_3CHO‡	$11_{7,4} - 10_{7,3}$	97.94755	-4.5377	23.0	129	10
t-C_2H_3CHO‡	$11_{9,2} - 10_{9,1}$	97.948051	-4.793	23.0	194	10
t-C_2H_3CHO‡	$11_{9,3} - 10_{9,2}$	97.948051	-4.793	23.0	194	10
t-C_2H_3CHO‡	$11_{10,1} - 10_{10,0}$	97.950017	-5.0727	23.0	233	10
t-C_2H_3CHO‡	$11_{10,2} - 10_{10,1}$	97.950017	-5.0727	23.0	233	10
t-C_2H_3CHO‡	$11_{6,5} - 10_{6,4}$	97.950286	-4.4656	23.0	102	10
t-C_2H_3CHO‡	$11_{6,6} - 10_{6,5}$	97.950286	-4.4656	23.0	102	10
t-C_2H_3CHO‡	$11_{5,7} - 10_{5,6}$	97.957003	-4.4126	23.0	79	10
t-C_2H_3CHO‡	$11_{5,6} - 10_{5,5}$	97.957003	-4.4126	23.0	79	10
t-C_2H_3CHO†	$11_{4,8} - 10_{4,7}$	97.972119	-4.3735	23.0	61	10

Table H.1—*Continued*

Species	Transition	ν_0 (GHz)	$\log_{10} A_{\rm ul}$ (s^{-1})	$g_{\rm u}$	$E_{\rm u}$ (K)	SPW
t-$C_2H_3CHO^\dagger$	$11_{4,7} - 10_{4,6}$	97.972119	-4.3735	23.0	61	10
t-C_2H_3CHO	$11_{3,9} - 10_{3,8}$	98.001321	-4.3451	23.0	46	10
t-$C_2H_3CHO^\ddagger$	$11_{3,8} - 10_{3,7}$	98.019044	-4.3448	23.0	46	10
			Propanal (s-C_2H_5CHO)			
s-$C_2H_5CHO^\ddagger$	$14_{4,11} - 14_{3,12}$ E	87.307042	-5.1587	29.0	62	6
s-$C_2H_5CHO^\ddagger$	$14_{4,11} - 14_{3,12}$ A	87.307594	-5.1587	29.0	62	6
s-$C_2H_5CHO^\ddagger$	$29_{6,23} - 29_{5,24}$ E	96.793208	-4.8841	59.0	245	9
s-$C_2H_5CHO^\ddagger$	$29_{6,23} - 29_{5,24}$ A	96.794186	-4.8841	59.0	245	9
s-$C_2H_5CHO^\dagger$	$12_{5,7} - 12_{4,8}$ E	98.378025	-5.0192	25.0	53	10
s-$C_2H_5CHO^\dagger$	$12_{5,7} - 12_{4,8}$ A	98.378025	-5.0191	25.0	53	10
s-$C_2H_5CHO^\dagger$	$29_{7,22} - 29_{6,23}$ A	98.39443	-4.847	59.0	250	10
s-$C_2H_5CHO^\dagger$	$29_{7,22} - 29_{6,23}$ E	98.394692	-4.847	59.0	250	10
			Others			
C_2H_3CN	$9_{1,8} - 8_{1,7}$	87.312812	-4.2778	57.0	23	6
$SO_2^\ddagger$	$7_{3,5} - 8_{2,6}$	97.702334	-5.7413	15.0	47	10
OCS	7 – 6	85.139103	-5.7658	15.0	16	3

†Blended with the other transitions of the same species.

‡Blended with transitions of other species.

*Transitions excluded from the fit.

Appendix I

Disk-integrated Spectra

Figure I.1–I.4 show the disk-integrated spectra for all SPWs. The line profile of each transition exhibits the double-peaked feature, which is typical for Keplerian rotation, with some spectral blending. Figure I.5–I.8 shows the disk-integrated spectra with spectral alignment, overlaid by the best-fit model of the spectral fit (Section 4.3.3). The double-peaked profiles are aligned and appeared to be single-peaked, which are well reproduced with the best-fit model including spectral blending.

We additionally present the zoom-in spectra of $CH_3O^{13}CHO$ and $^{13}CH_3OCHO$ transitions detected with no blending from other molecular species in Figure I.9 to confirm the detection of these species, which is critical for the robust measurement of $^{12}C/^{13}C$ ratios in CH_3OCHO (Section 4.4.4).

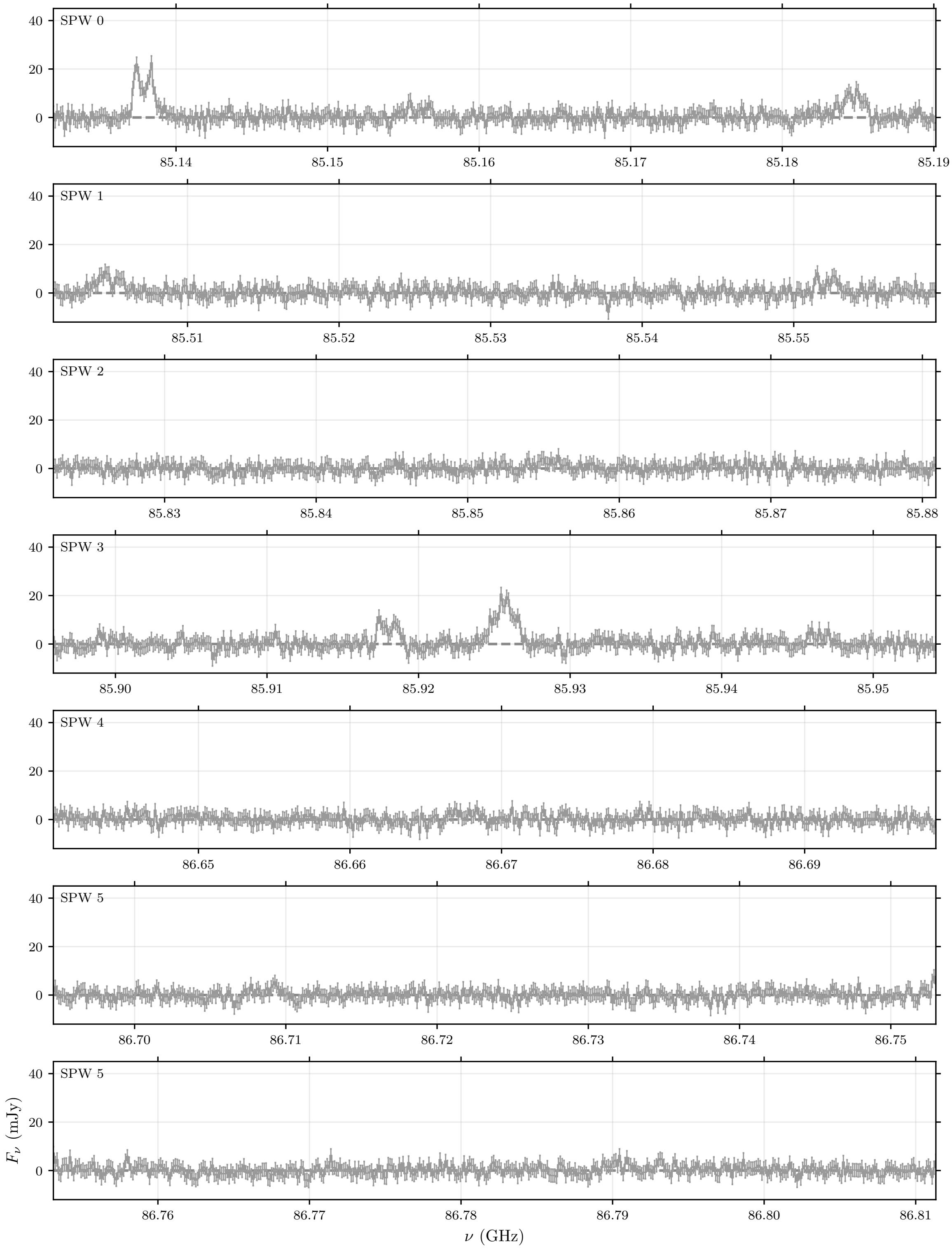

Figure I.1. Disk-integrated spectra toward V883 Ori without spectral alignment. The emission is integrated over the deprojected disk region with the outer radius of $0''.6$ (or 240 au).

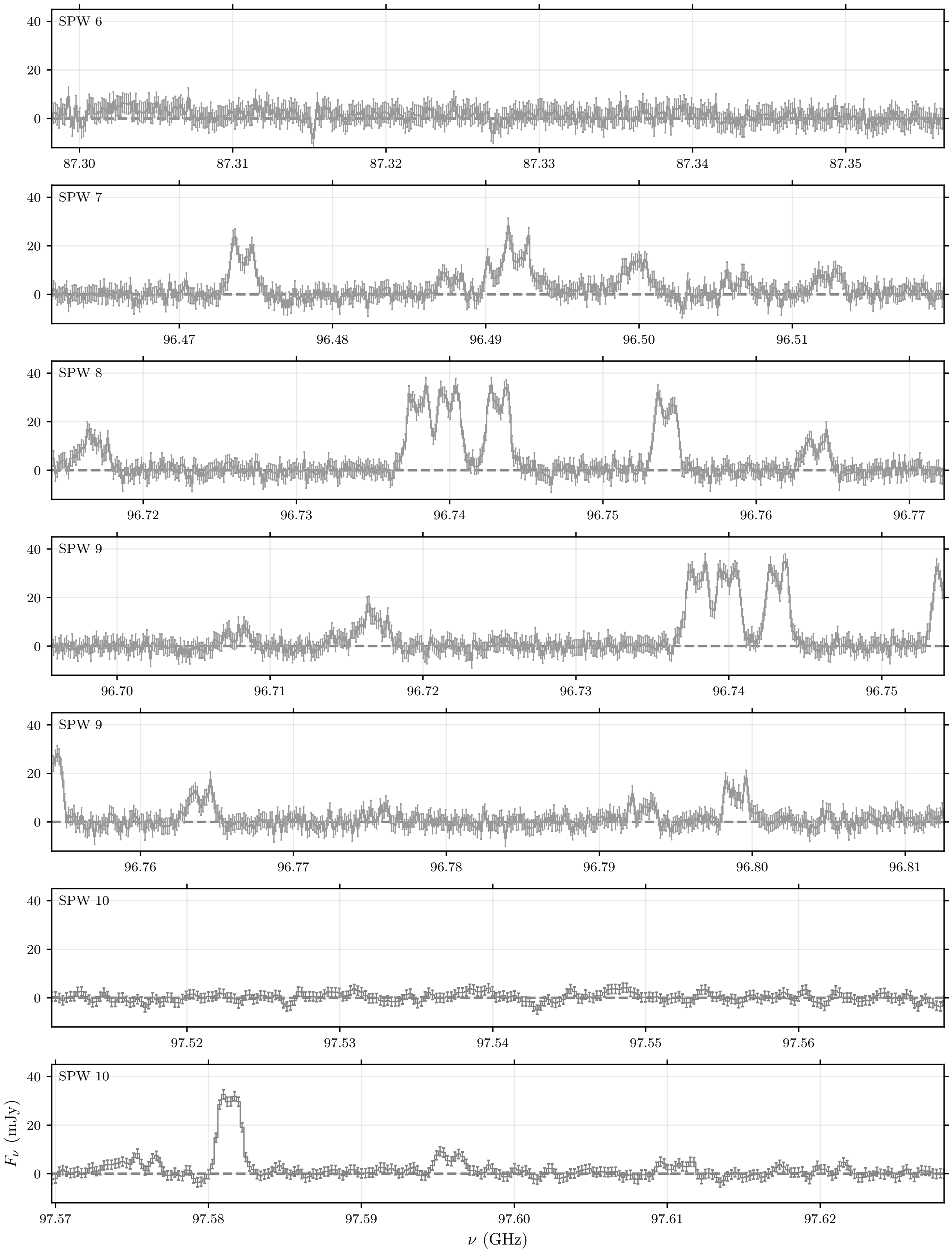

Figure I.2. Continuation of Figure I.1.

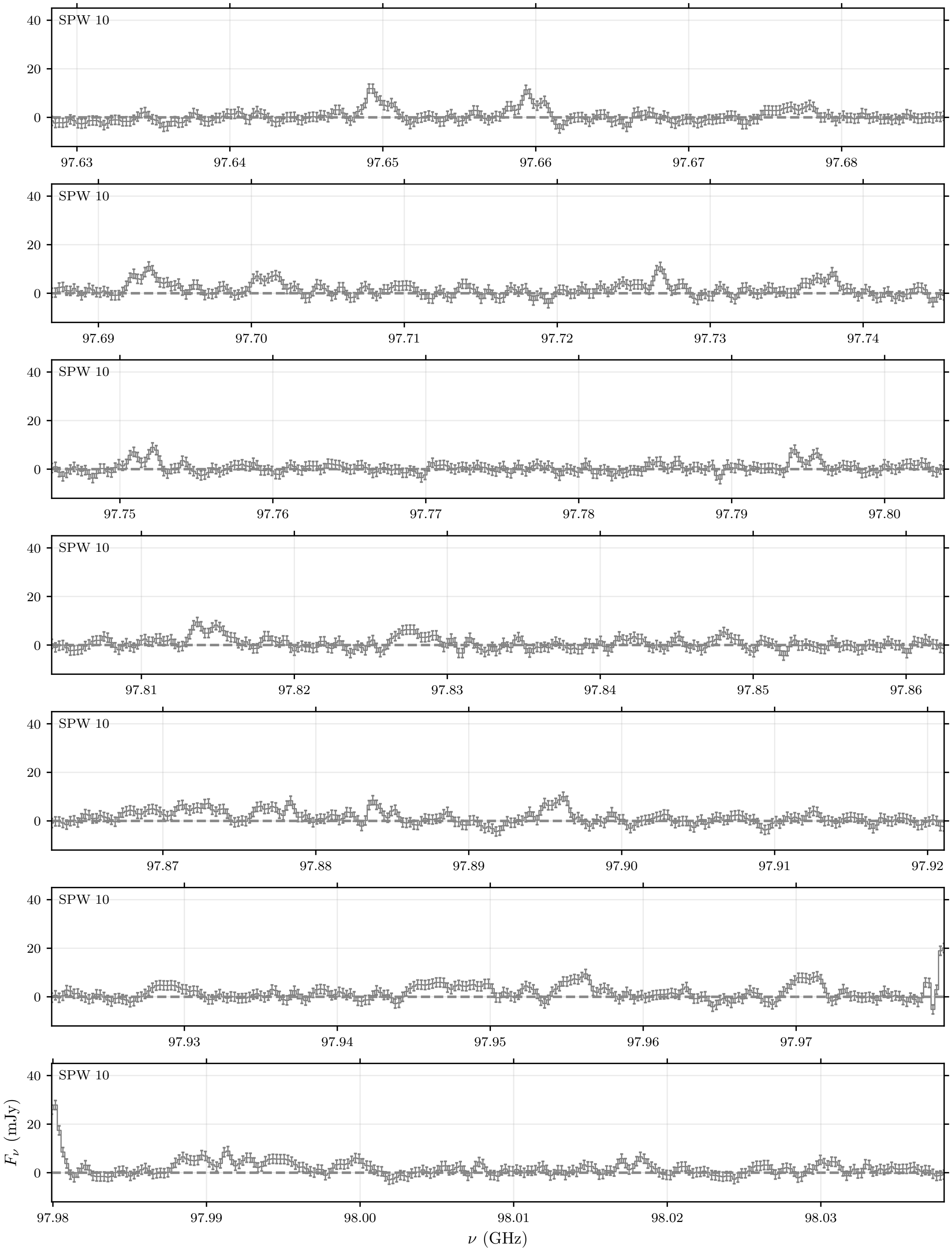

Figure I.3. Continuation of Figure I.2.

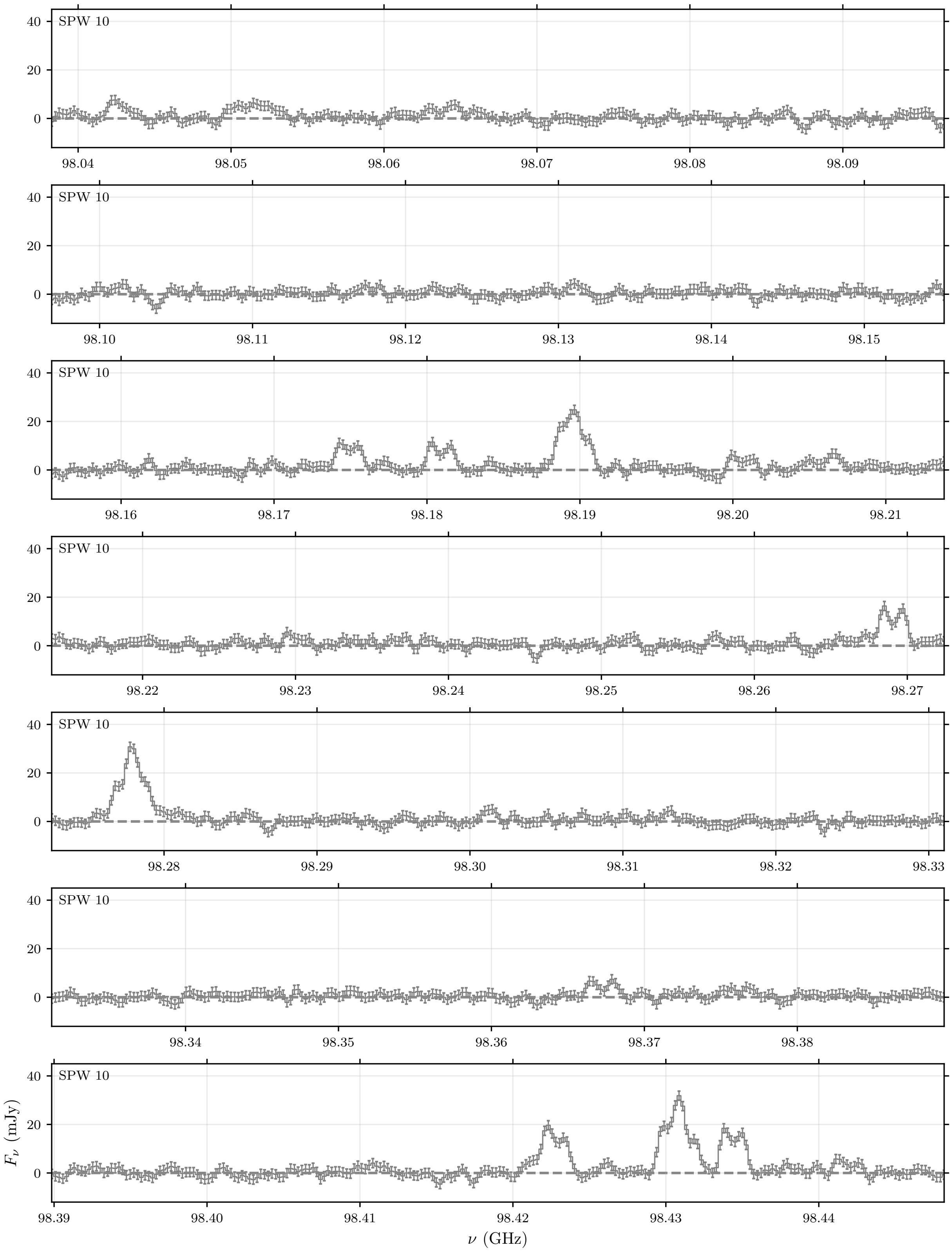

Figure I.4. Continuation of Figure I.3.

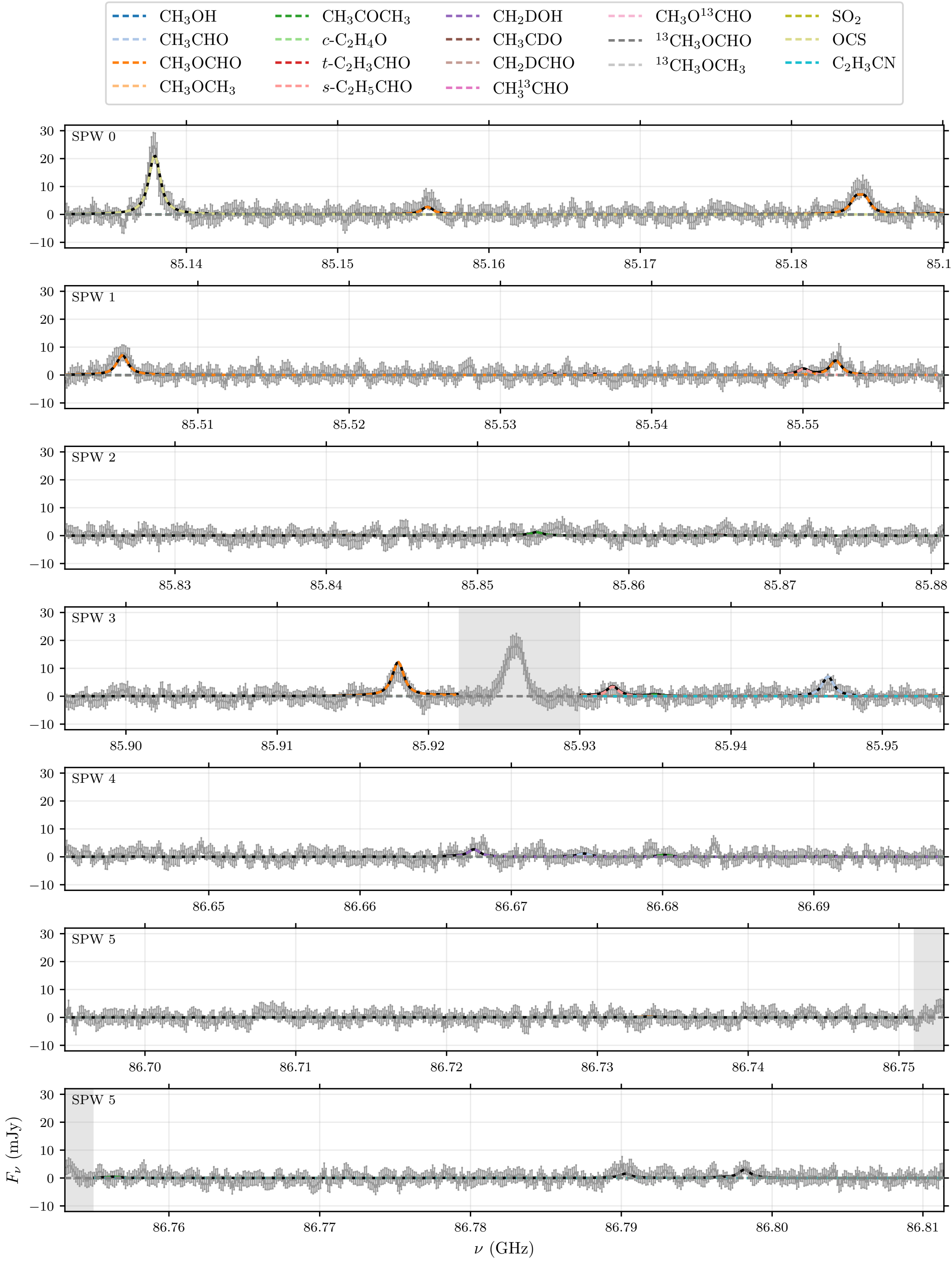

Figure I.5. Disk-integrated spectra toward V883 Ori after the spectral alignment, overlaid with the best-fit model. The black solid lines indicate the full model composed of all detected species, while dashed colored lines are the model for each species shown in the legend. The gray-shaded region are removed from the fit (see Section 4.3.3 for details.)

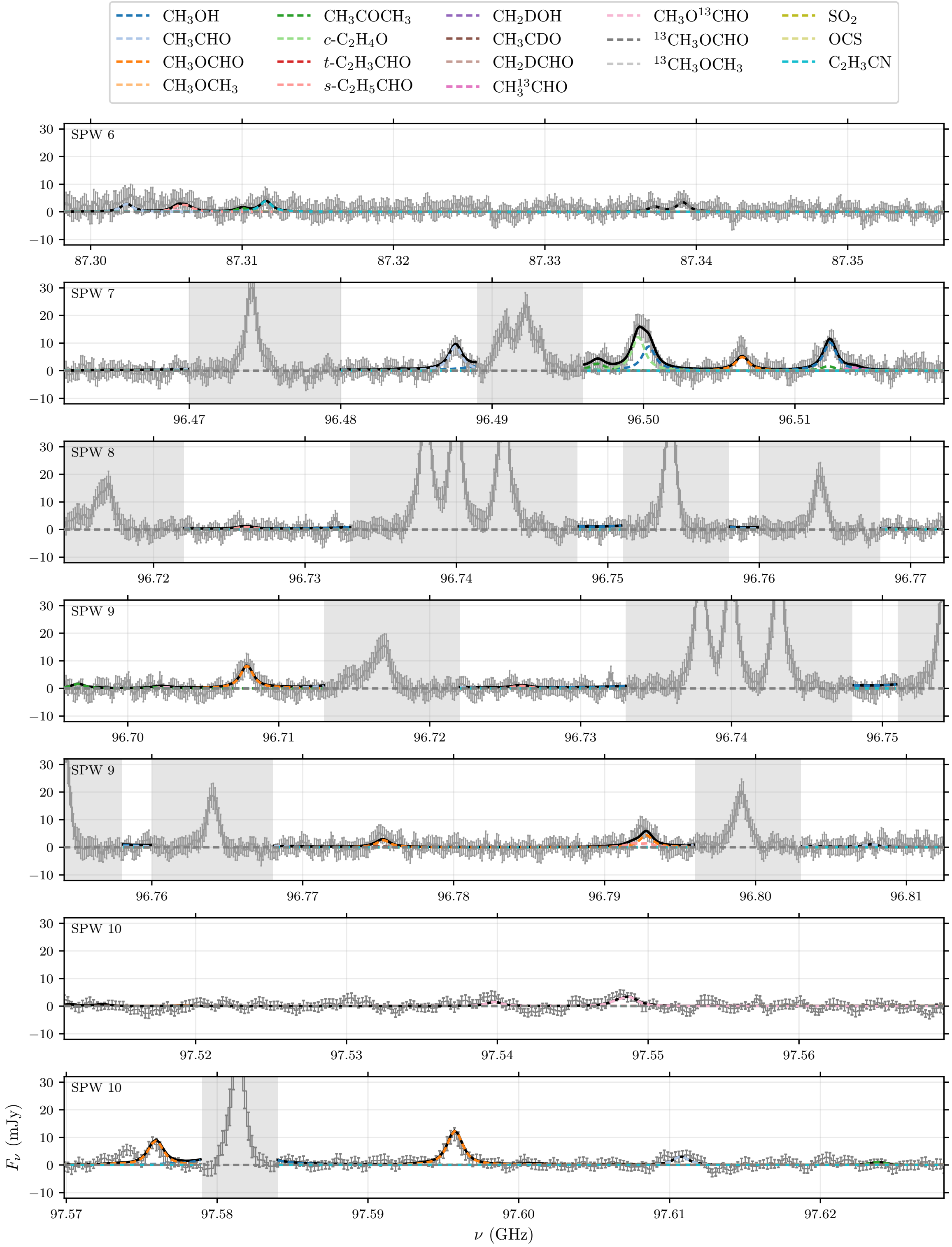

Figure I.6. Continuation of Figure I.5.

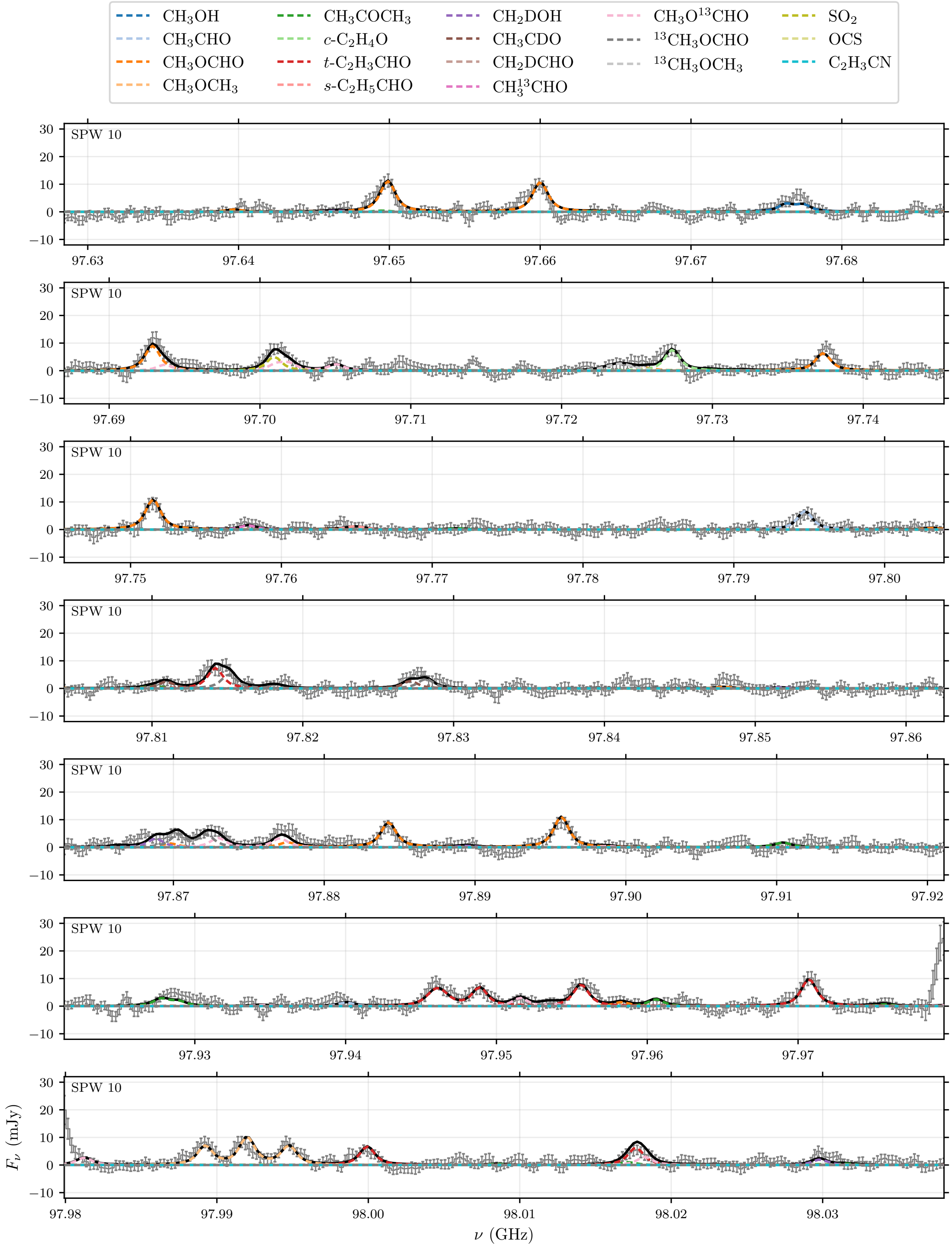

Figure I.7. Continuation of Figure I.6.

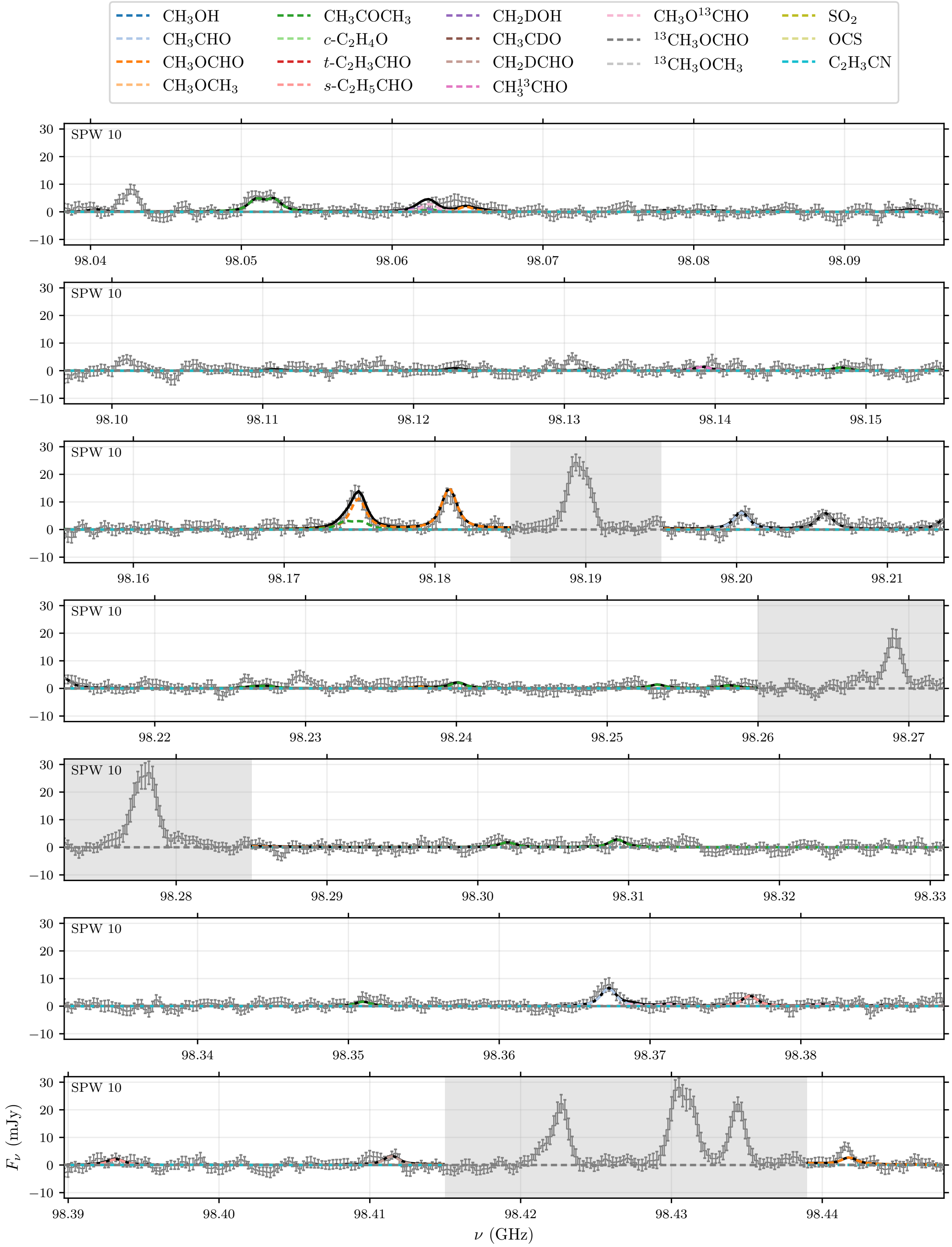

Figure I.8. Continuation of Figure I.7.

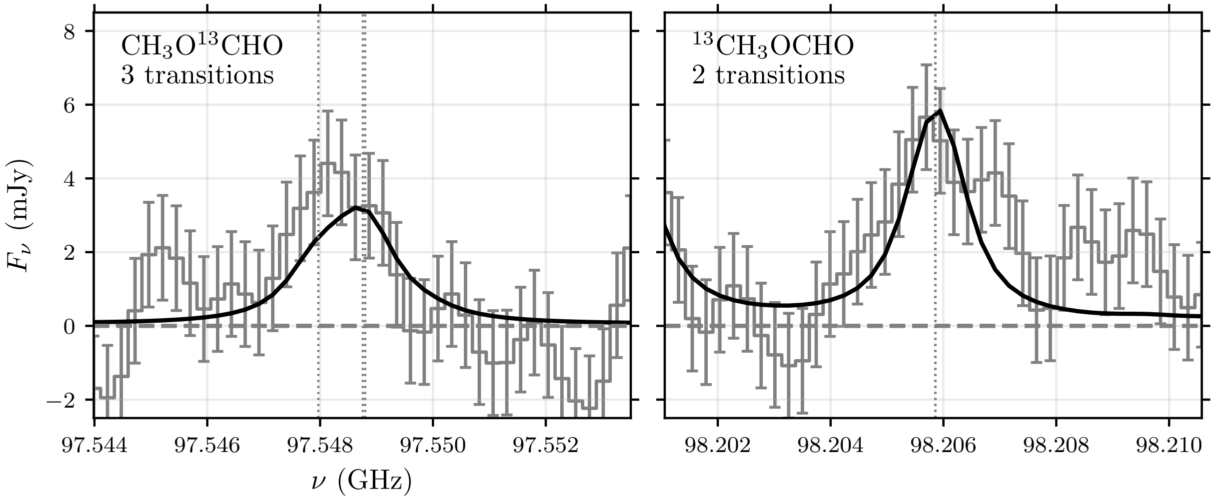

Figure I.9. Zoom-in spectra of CH$_3$O^{13}CHO (left) and ^{13}CH$_3$OCHO (right) transitions detected with no blending from other molecular species. The gray lines with error bars are the observed spectra, and the black solid lines indicate the best-fit model (see Section 4.3.3). The central frequency of transitions are marked by the vertical dotted lines.

Appendix J

LTE Spectral Model

Here we describe the details of the spectral model which is fitted to the spectra corrected for Keplerian rotation for column density derivation. We assume that the excitation condition of observed COM emission is well approximated by local thermodynamic equilibrium (LTE), where the gas temperature is equal to the excitation temperature ($T_{\rm ex}$) of the emitting molecules. This assumption should be reasonable as the typical gas density in protoplanetary disks ($\gtrsim 10^8\ \rm cm^{-3}$) is high enough to thermalize the excitation condition. We further assume that different species are sufficiently cospatial to share the same emitting region size and excitation temperature. This assumption is also broadly supported by the similar emission extent of different COMs shown in Figure 4.1.

The model intensity I_ν are computed based on a solution of the basic radiative transfer equations for an isothermal, uniform slab:

$$I_\nu = (B_\nu(T_{\rm ex}) - B_\nu(T_{\rm CMB}))(1 - e^{-\tau_\nu}), \tag{J.1}$$

where B_ν is the Planck function for a blackbody radiation, $T_{\rm CMB} = 2.73$ K is the temperature of the cosmic microwave background, and τ_ν is the optical depth of the line emission at a frequency ν. Following the formulation described in Appendix A of Yamato et al. (2022), the line optical depth τ_ν is computed considering different transitions from various species as

$$\tau_\nu = \sum_i \tau_{0,i} \exp\left(- \frac{(\nu - \nu_{\rm c})^2}{2\sigma_\nu^2}\right), \tag{J.2}$$

where i is the indices for different transitions, $\tau_{0,i}$ is the optical depth at the line center of ith transition, $\nu_{\rm c}$ is the central frequency of the transition, and σ_ν is the line width in terms of frequency. The central frequency $\nu_{\rm c}$ is calculated as $\nu_{\rm c} = \nu_0(1 - v_{\rm sys}/c)$, where c is the speed of light and $v_{\rm sys}$ is the systemic velocity of the source, assumed to be 4.25 km s^{-1} for V883 Ori (Tobin et al. 2023). The frequency line width σ_ν is converted from the velocity line width σ_v as $\sigma_\nu = \nu_0\sigma_v/c$, where ν_0 is the rest frequency of each transition listed in Table H.1. In practice, the full width of half maximum (FWHM) of the velocity $\Delta V_{\rm FWHM}$ is used as a parameter instead of σ_ν or σ_v. The optical depth at the line center ($\tau_{\rm 0,i}$) is calculated as

$$\tau_{0,i} = \frac{c^2 A_{\rm u} N_{\rm u}}{8\pi\nu_0^2\sqrt{2\pi}\sigma_\nu}\left(\exp\left(\frac{h\nu_0}{k_{\rm B}T_{\rm ex}}\right) - 1\right), \tag{J.3}$$

$$\frac{N_{\rm u}}{N} = \frac{g_{\rm u}}{Q(T_{\rm ex})}\exp\left(-\frac{E_{\rm u}}{k_{\rm B}T_{\rm ex}}\right), \tag{J.4}$$

where $A_{\rm ul}$ is the Einstein A coefficient for spontaneous emission, $g_{\rm u}$ is the upper state degeneracy, N is the molecular column density, Q is the partition function of the molecule, and $E_{\rm u}$ is the upper state energy of the transition. While this suit of formulation is similar to that of the eXtended CASA Line Analysis Software Suite (XCLASS; Möller et al. 2017), which is used in a previous work on the V883 Ori disk (Lee et al. 2019), we used an independent implementation by ourselves for technical flexibility.

The model intensity I_ν (in unit of Jy sr^{-1}) is then integrated over a solid angle of the emitting region Ω, which is common for all transitions and species, to obtain the spectra of flux density (in unit of Jy). Finally, the model flux density spectra are convolved with a Lorentz function $f(\nu)$ with a width of γ,

$$f(\nu) = \frac{1}{\pi\gamma}\frac{\gamma^2}{\gamma^2 + \nu^2}, \tag{J.5}$$

to take line broadening in the spectra corrected for Keplerian rotation. As shown in Figure J.1, the spectra corrected for Keplerian rotation still deviates from a simple Gaussian due to (1) the finite spatial resolution or beam smearing, which cannot fully resolve the highest velocity component of Keplerian rotation and (2) potential emission from the elevated disk surface of the back side and front side of the disk, which have different projected velocities. In our data, both (1) and (2) could be dominant causes of the deviation, since the spatial resolution is not so high to fully resolve the disk emission and the COM emission could originate from the warm disk surface in addition to the midplane. Figure J.1 demonstrates that the convolution with the Lorentz function well approximates the deviation from Gaussian while conserving the velocity-integrated flux density, which is relevant for column density derivation. Furthermore, to account for the finite spectral resolution, the model spectra is additionally convolved with a Gaussian function with a FWHM of the spectral resolution. This process also accounts for the different spectral resolutions (per channel width) between SPW 10 and others (see Table 4.2). A similar approach has been employed in the spectral line analysis in protoplanetary disks (Cataldi et al. 2021), where they used only a Gaussian convolution to take the line broadening into account (see also Bergner et al. 2021; Guzmán et al. 2021).

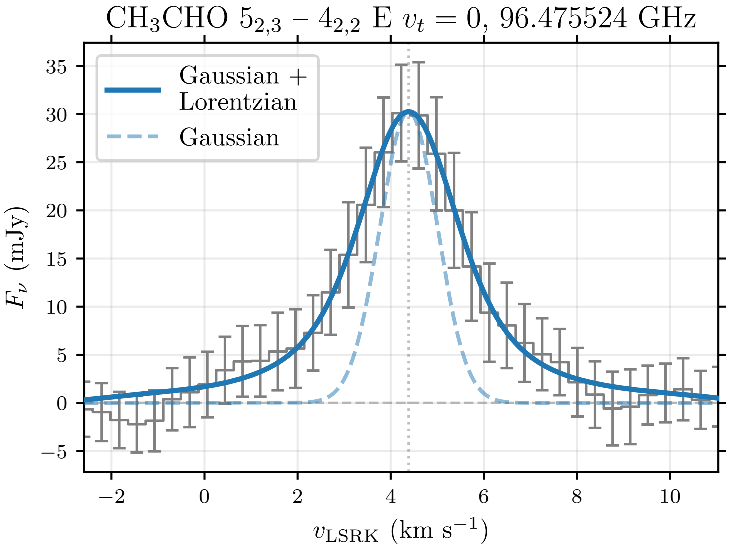

Figure J.1. Fit of a Gaussian + Lorentzian model (i.e., Voigt profile; solid blue) to the observed spectra of a CH$_3$CHO transition at 96.476 GHz (gray). The original Gaussian before the convolution with Lorentzian is indicated by the dashed line. The Gaussian + Lorentzian model well reproduces the wing of the spectra. The horizontal dashed line and vertical dotted line marks the zero-flux level and the systemic velocity ($v_{\rm sys}$ = 4.25 km s^{-1}), respectively.

Appendix K

Reconstruction of Radial Intensity Profile

Here we describe details of the forward modeling approach to reconstruct the radial intensity profiles from the line profiles (Section 4.3.2). The method we employed is similar to the way described in Bosman et al. (2021b) but slightly different. First we create the model emission component originating from an annulus at a given radius of the inclined disk. We made a grid of cubes and calculated the line shape of the spatially integrated emission as a function of velocity assuming that the emission is completely originating from the midplane of the Keplerian-rotating disk, i.e.,

$$F_{r_i}(v) \propto \int_{\Omega_{\rm annulus}} I_{r_i} \exp\left[-\frac{(v - v_{\rm kep}(r,\theta) - v_{\rm sys})^2}{2\sigma_v^2}\right] d\Omega, \tag{K.1}$$

where $\Omega_{\rm annulus}$ is the solid angle of the annulus, I_{r_i} is the surface brightness (in Jy au^{-2} km s^{-1}) at the radius of r_i, $v_{\rm kep}(r,\theta) = \sqrt{GM_\star/r}\cos\theta\sin i$ is the Keplerian velocity at the deprojected polar disk coordinate (r,θ), $v_{\rm sys}$ is the systemic velocity of the source (fixed to 4.25 km s^{-1}), and σ_v is the local line width at each position within the disk. We assumed that the local line width is narrower than the spectral resolution (0.5 km s^{-1}), where 0.05 km s^{-1} was used practically. The normalization of Equation (K.1) is taken as the integration of $F_{r_i}(v)$ along the velocity axis being the spatial integration of I_{r_i}. The emission component at each radius r_i is summed over i to construct the disk-integrated spectra, i.e.,

$$F(v) = \sum_i F_{r_i}(v), \tag{K.2}$$

which is fitted to the observed disk-integrated spectra by varying each I_{r_i} as free parameters. We used a regularly spaced grid in velocity space, which result in the unevenly spaced radial grid due to the non-linear relationship between Keplerian velocity and disk radius (see Equation 4.1). The spacing of the grid is regulated by the spectral resolution: we used one grid point (r_i) per two velocity resolution components to obtain reasonable constraints on each I_{r_i}. This treatment resulted in a very sparse radial grid r_i in larger radii, which makes it difficult to infer the radial distribution there. To mitigate this effect, we employed four fits with different radial grid created with different starting radii ($r_0 = 3, 5, 7, 9\,\mathrm{au}$) and composed these four fits at the end to construct the final radial intensity profile. The actual fits were conducted by the MCMC algorithm implemented in the `emcee` package (Foreman-Mackey et al. 2013). The reconstructed intensity profiles are further convolved with the 1D Gaussian function with a $0''.1$ FWHM to emulate the beam smearing effect and presented in Figure 4.4.

Appendix L

Spectroscopic Data for Molecules

To employ the astronomical modeling of the observed spectra and estimate column density, spectroscopic data such as transition frequencies, intrinsic line strengths, and partition functions are essential information. They are basically retrieved from the Cologne Database of Molecular Spectroscopy (CDMS; Müller et al. 2001, 2005; Endres et al. 2016) or the Jet Propulsion Laboratory (jpl) database (Pickett et al. 1998). We describe the origin of these data and molecule-specific issues for each species below, with a particular care on the vibratinonal contributions to the partition functions.

L.1 Methanol

Spectroscopic data for CH_3OH are taken from the CDMS, which are largely based on the theoretical calculation for the ground state ($v_t = 0$) and the first three torsional states ($v_t = 1, 2, 3$) by Xu et al. (2008). The partition function of CH_3OH which considers the contributions from these states is also available in the CDMS.

The data for the deuterated isotopologues, CH_2DOH, are taken from the jpl database, which is based on the laboratory experiment for the ground torsional state (Pearson et al. 2012). The partition function available in the jpl database only considers the ground torsional state. However, since the spectroscopic calculation of CH_2DOH is challenging, the data have a large uncertainty, in particular for the line intensities of *b*-type and *c*-type transitions (Pearson et al. 2012; Oyama et al. 2023). The tentatively detected transitions with the present observations are all *b*-type transitions, which could have a factor of ~ 3 uncertainties at maximum judging from the intensity difference found between the jpl database and the new experiment in ALMA Band 6 frequencies by Oyama et al. (2023). The derived column density and CH_2DOH/CH_3OH ratios could thus have a similar level uncertainty, which should be viewed with strong caution.

L.2 Acetaldehyde

The data for CH_3CHO are taken from the jpl database. This is based on the data listed in Kleiner et al. (1996) for the ground state ($v_t = 0$) and the first two torsional states ($v_t = 1, 2$). The partition function of CH_3CHO available in the jpl database also considers these three torsional states.

There are two isomers of ^{13}C-acetaldehyde: $^{13}CH_3CHO$ and $CH_3^{13}CHO$. The data of both isomers for the ground state ($v_t = 0$) and the first torsional state ($v_t = 1$) are available at the CDMS based on the laboratory measurement by (Margulès et al. 2015). The partition function which considers the contributions from torsional states up to $v_t = 8$ is also available at the CDMS.

There are also two isomers of deuterated acetaldehyde: CH_2DCHO and CH_3CDO. While the data of the ground states ($v_t = 0$) and the first torsional states ($v_t = 1$) are available for CH_3CDO at the CDMS, only the data of the ground states ($v_t = 0$) exists for CH_2DCHO. These data are based on the laboratory experiments by Coudert et al. (2019). The partition functions of these molecules are available at the CDMS. The partition function of CH_2CDO are calculated considering the contributions from the first three torsional modes and the approximate contributions from the lowest vibrational mode. The partition function for CH_2DCHO are, on the other hand, calculated considering the approximate contributions from the lowest torsional mode and the lowest vibrational mode.

L.3 Methyl Formate

We used the spectroscopic data for CH_3OCHO taken from the jpl database. This data is based on the laboratory experiment for the ground states ($v_t = 0$) and the first torsional state ($v_t = 1$) by Ilyushin et al. (2009). Similar to acetaldehyde, there are two ^{13}C-isotopologues of methyl formate: $^{13}CH_3OCHO$ and $CH_3O^{13}CHO$. While the data of the ground states ($v_t = 0$) and the first torsional state ($v_t = 1$) for $CH_3O^{13}CHO$ are available at the CDMS, which is based on the laboratory measurements (Carvajal et al. 2010, and references therein), no CDMS entry for $^{13}CH_3OCHO$ are found. Instead, we compiled the experimental data and theoretical predictions for $^{13}CH_3OCHO$ transitions from literature (Carvajal et al. 2009; Haykal et al. 2014; Favre et al. 2014).

For the partition function of these three molecules, we used the one calculated by Favre et al. (2014), who fully considered the contributions from torsional (up to $v_t = 6$) and vibrational populations. The partition function data exist in the jpl database as well for the normal isotopologues (CH_3OCHO), but only the contributions from $v_t = 0, 1$ states are considered. This resulted in a difference between the one by Favre et al. (2014) and the one in the jpl database by a factor of 1.2 at 150 K and 2.5 at 300 K (Favre et al. 2014). We note that there are difference in the treatment of the degeneracy, where Favre et al. (2014) ignore the nuclear spin degeneracy (i.e., $g_I = 1$) while the CDMS and jpl entries take $g_I = 2$. To take this difference into account, we multiply the partition function listed in Favre et al. (2014) by two in practice.

We also examined the data for deuterated methyl formate. Similarly, there are two isomers: CH_2DOCHO and CH_3OCDO. Spectroscopic data for both molecules are taken from the CDMS, which is based on the experimental measurement by Coudert et al. (2013) and Margulès et al. (2009) for CH_2DOCHO, and Margulès et al. (2010) and Duan et al. (2015) for CH_3OCDO. The partition functions of these molecules available in the CDMS only take the ground vibrational state into account. Manigand et al. (2019) uses the vibrational correction factor of 1.31 and 1.11 at 115 K for CH_2OCHO and CH_3OCDO, respectively, assuming that the correction factor is the same as ^{13}C-isotopologues. We applied these factors to the partition functions of these molecules.

L.4 Dimethyl Ether

The data for CH_3OCH_3 are taken from the CDMS, which is based on the experimental measurement by Endres et al. (2009) for the ground vibrational states ($v = 0$) with four substates (AA, AE, EA, and EE). The partition function is calculated considering the torsionally excited states ($v_{11} = 1$ and $v_{15} = 1$), C-O-C bending states ($v_7 = 1$), and $v_{11} + v_{15} = 2$, and available at the CDMS.

The spectroscopic data for ^{13}C isotopologue ($^{13}CH_3OCH_3$) are also available at the CDMS and based on the laboratory experiments by Koerber et al. (2013). The partition function in the CDMS is calculated only taking the ground vibrational states into account, and the vibrational correction factor is not yet available.

L.5 Acetone

The data for CH_3COCH_3 are taken from the jpl. The jpl entry compiled the data from Peter & Dreizler (1965), Vacherand et al. (1986), Oldag & Sutter (1992), and Groner et al. (2002). The partition function which takes into account the torsional and vibrational state are available at the jpl and used for the spectral fit.

L.6 Ethylene Oxide

The data for c-C_2H_4O are taken from the CDMS. This CDMS entry is based on the experimental data in Creswell & Schwendeman (1974) and Müller et al. (2022). The partition function available at the CDMS takes into account the ground vibrational state only, and the vibrational correction factor is not available.

L.7 Propenal

The data for t-C_2H_3CHO are taken from the CDMS, which are largely based on the experimental data in Daly et al. (2015) with additional data from Winnewisser et al. (1975) and Cherniak & Costain (1966). The partition function is calculated by considering no vibrational states nor other conformers, and the vibrational and conformational correction factors are not yet available. We thus do not apply any correction factors to the partition function.

L.8 Propanal

The data for s-C_2H_5CHO are taken from the CDMS, which are largely based on the experimental measurements by Zingsheim et al. (2017) with additional data from Hardy et al. (1982) and Demaison et al. (1987). The partition function is calculated by considering no vibrational states nor other conformers, and the vibrational and conformational correction factors are not yet available. We thus do not apply any correction factors to the partition function.

Appendix M

Matched Filter Analysis

We performed the matched filter analysis (Loomis et al. 2018b), which is commonly used to extract weak molecular line emission in protoplanetary disks, to verify the detections/non-detections of COMs. As a filter kernel, we used a simple Keplerian-rotating disk model generated with the Python script `keplerian_mask` (Teague 2020) assuming a disk inclination angle of $37\overset{\circ}{.}0$, position angle of $148\overset{\circ}{.}0$ and central stellar mass of $2.1\,M_{\odot}$ (Öberg et al. 2021; Teague et al. 2021). The outer radius of the disk was set as $0\overset{\prime\prime}{.}15$ based on the extent of the emission in the velocity-integrated intensity maps. The Python package `VISIBLE` (Loomis et al. 2018b) was used to compute the cross-correlation between observed visibilities and the filter kernel. The resultant response spectra are shown in Figure M.1. The brightest cluster of CH_3OCH_3 lines at $\sim$299.89 GHz shows a $\sim17\sigma$ filter response, while the two tentative features at $\sim$299.12 GHz and $\sim$300.06 GHz exhibit $\sim$5–6σ filter responses. The response spectra do not exhibit any $\geq5\sigma$ responses of CH_3OH and CH_3CHO transitions.

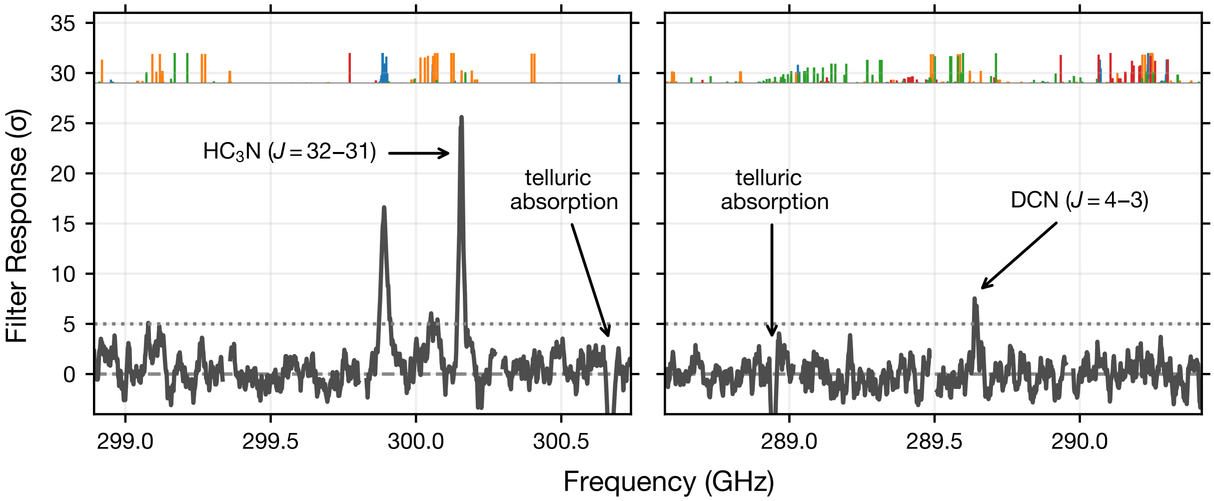

Figure M.1. Matched filter responses. The horizontal dotted line marks 5σ. The relative intensities of covered lines at 200 K are shown by vertical segments for CH_3OCH_3 (blue), CH_3OCHO (orange), CH_3OH (red), and CH_3CHO (green). A cluster of CH_3OCH_3 lines at ∼299.89 GHz exhibits a ∼17σ response, while tentative features at ∼299.12 GHz and ∼300.06 GHz shows ∼5–6σ responses.

Appendix N

Details of Spectral Analysis

Here, we describe the details of the spectral analysis (Section 5.3.2) to derive the excitation temperature and column density of COMs. We fit the entire spectra by an LTE slab model based on the basic radiative transfer equations (e.g., Yamato et al. 2024). The emergent intensity of the line emission I_ν at each frequency is modeled as

$$I_\nu = (B_\nu(T_{\rm ex}) - B_\nu(T_{\rm CMB}))(1 - e^{-\tau_\nu}), \tag{N.1}$$

where B_ν is the Planck function of the blackbody radiation, $T_{\rm ex}$ is the excitation temperature, $T_{\rm CMB} = 2.73\,{\rm K}$ is the temperature of cosmic microwave background, and τ_ν is the optcial depth profile. We assume that $T_{\rm ex}$ is shared by different species of COMs, i.e., the emitting regions are common among different COMs, given that COMs are expected to sublimate at a similar temperature. The optical depth profile τ_ν is computed as

$$\tau_\nu = \sum_i \frac{c^2 A_{{\rm ul},i} N_{{\rm u},i}}{8\pi\nu^2} \left[\exp\left(\frac{h\nu}{k_{\rm B}T_{\rm ex}}\right) - 1\right] \phi_{\nu,i}, \tag{N.2}$$

where c is the speed of light, $A_{{\rm ul},i}$ is the Einstein A coefficient of ith transition, $N_{{\rm u},i}$ is the upper state column density of ith transition, h is the Planck constant, $k_{\rm B}$ is the Boltzmann constant, and $\phi_{\nu,i}$ is the line profile function of ith transition. The summation i goes over different transitions of all molecular species. The upper state column density $N_{{\rm u},i}$ is related to the total column density N as

$$N_{{\rm u},i} = \frac{N}{Q(T_{\rm ex})} g_{{\rm u},i} \exp\left(-\frac{E_{{\rm u},i}}{k_{\rm B}T_{\rm ex}}\right), \tag{N.3}$$

where Q is the partition function, g_u is the upper state degeneracy, and E_u is the upper state energy. The line profile function $\phi_{\nu,i}$ in Equation N.2 is defined as

$$\phi_{\nu,i} = \frac{1}{\sqrt{2\pi}\sigma_{\nu,i}} \exp\left[-\frac{(\nu - \nu_{0,i} - \delta\nu_i)^2}{2\sigma_{\nu,i}^2}\right], \tag{N.4}$$

where $\sigma_{\nu,i}$ is the frequency line width, $\nu_{0,i}$ is the rest frequency of ith transition, and $\delta\nu_i$ is the frequency shift due to the systemic velocity v_sys. The frequency line width $\sigma_{\nu,i}$ is related to the velocity line width in Full Width Half Maximum (FWHM) ΔV_FWHM as $\sigma_{\nu,i} = \frac{\nu_{0,i}}{c}\frac{\Delta V_\mathrm{FWHM}}{\sqrt{8\ln 2}}$[1].

Within this model, we consider > 600 transitions of four molecular species, CH_3OCH_3, CH_3OCHO, CH_3OH and CH_3CHO, whose Einstein A coefficient is larger than $10^{-8}\,\mathrm{s}^{-1}$ and upper state energy is lower than 1000 K. Table N lists the strong transitions and their spectroscopic properties that effectively constrain the column density (and its upper limit). The spectroscopic data of these transitions, including partition functions, are taken from the Cologne Database for Molecular Spectroscopy (CDMS; Müller et al. 2001, 2005; Endres et al. 2016) for CH_3OCH_3 and CH_3OH and the Jet Propulsion Laboratory (jpl) database (Pickett et al. 1998) for CH_3OCHO and CH_3CHO. In total, we include seven free parameters into the fit: the excitation temperature T_ex, the velocity line width ΔV_FWHM, the systemic velocity v_sys, and the logarithm of column densities of these four species. We note that here we assume a Gaussian line shape (Equation N.4) and the line width is the one after including the broadening due to Keplerian rotation rather than the intrinsic one. This predominantly reflects the underlying assumption that the emission is optically thin, where only the velocity-integrated intensity matters for column density derivation. The actual line shape may be different from Gaussian as usually seen in the spectra of rotating disks, but given the unresolved emission, the low S/N, and the low spectral resolution, we do not perform a detailed line shape modeling here and it is partly addressed in the radiative transfer modeling (Appendix O).

We explore the parameter space with the affine-invariant Markov Chain Monte Carlo (MCMC) algorithm implemented in the Python package `emcee` (Foreman-Mackey et al.

---

[1] This sort of column density retrieval, including the functions of querying molecular spectroscopic data, is packaged into a public Python code `specfit` (`https://github.com/yyamato-as/specfit`).

2013) using uniform prior distributions:

$$\begin{aligned}
T_{\mathrm{ex}}\,(\mathrm{K}) &= \mathcal{U}(5, 1000), \\
\Delta V_{\mathrm{FWHM}}\,(\mathrm{km\,s^{-1}}) &= \mathcal{U}(0.0, 100.0), \\
v_{\mathrm{sys}}\,(\mathrm{km\,s^{-1}}) &= \mathcal{U}(-5.0, 15.0), \\
\log_{10} N(\mathrm{X})\,(\mathrm{cm^{-2}}) &= \mathcal{U}(10.0, 20.0),
\end{aligned}$$

where $\mathcal{U}(a, b)$ denotes the uniform distributions between a and b, and X represents the four molecular species. We exclude the following frequency ranges from the fit due to the contamination from other molecular lines and telluric absorption lines: [288.85, 289.00], [289.62, 289.66], [300.13, 300.18], and [300.64, 300.70] in GHz. We run 50 walkers for 10000 steps to sample the posterior distributions and the initial 2000 steps are discarded as burn-in. Figure N.1 shows the parameter covariances and marginalized posterior distributions. Only the upper limits on CH_3OH and CH_3CHO column density are constrained due to the non-detection. The median value of the systemic velocity (≈4.3 km s^{-1}) is slightly shifted from the literature value (≈5.1 km s^{-1}; Piétu et al. 2007; Teague et al. 2021) due to the coarse channel width (≈4 km s^{-1}), and these are consistent within the uncertainty. From these posterior samples, we compute the column density ratios relative to CH_3OH, where $N(CH_3OCH_3)/N(CH_3OH)$ is constrained to be >7 (0.15th percentile, corresponding to 3σ for a Gaussian distribution). For CH_3OCHO, while the 0.15th percentile of $N(CH_3OCH_3)/N(CH_3OH)$ is very small due to the long tail in the posterior distributions of $N(CH_3OCHO)$ (see Figure N.1), the median value of $N(CH_3OCHO)$ divided by the upper limit of $N(CH_3OH)$ are listed in Table 5.2 and added in Figure 5.2 as a reference. For CH_3CHO, we do not obtain meaningful constrains due to the non-detection.

Table N.1 Spectroscopic Properties of Major Molecular Lines

Transition	ν_0 (GHz)	$\log_{10} A_{\rm ul}$ (s^{-1})	$g_{\rm u}$	$E_{\rm u}$ (K)
Dimethyl Ether (CH_3OCH_3)				
$5_{4,2}$–$4_{3,1}$ AE	299.884130	−3.763	22	36.1
$5_{4,2}$–$4_{3,2}$ EA	299.886128	−3.769	44	36.2
$5_{4,1}$–$4_{3,1}$ EA	299.886804	−3.769	44	36.1
$5_{4,1}$–$4_{3,2}$ AE	299.888802	−3.763	66	36.1
$5_{4,1}$–$4_{3,1}$ EE	299.889910	−3.784	176	36.1
$5_{4,2}$–$4_{3,2}$ EE	299.890981	−3.784	176	36.1
$5_{4,2}$–$4_{3,1}$ AA	299.892089	−3.763	66	36.1
$5_{4,1}$–$4_{3,2}$ AA	299.896762	−3.763	110	36.1
$8_{3,5}$–$7_{2,6}$ AE	299.899470	−4.007	34	45.4
$8_{3,5}$–$7_{2,6}$ EA	299.899781	−4.008	68	45.4
$8_{3,5}$–$7_{2,6}$ EE	299.903025	−4.008	272	45.4
$8_{3,5}$–$7_{2,6}$ AA	299.906424	−4.007	102	45.4
$29_{6,23}$–$29_{5,24}$ AA	300.062299	−3.825	590	447.5
$29_{6,23}$–$29_{5,24}$ EE	300.062707	−3.825	944	447.5
$29_{6,23}$–$29_{5,24}$ AE	300.063115	−3.825	354	447.5
$29_{6,23}$–$29_{5,24}$ EA	300.063116	−3.825	236	447.5
Methyl Formate (CH_3OCHO)				
$23_{5,18}$–$22_{5,17}$ E, $v_t = 0$	299.097870	−3.410	94	183.9
$25_{3,22}$–$24_{3,21}$ E, $v_t = 1$	299.111695	−3.406	102	387.6
$23_{5,18}$–$22_{5,17}$ A, $v_t = 0$	299.123858	−3.410	94	183.9
$27_{1,26}$–$26_{2,25}$ A, $v_t = 1$	299.128806	−4.243	110	397.2
$27_{2,26}$–$26_{2,25}$ A, $v_t = 1$	299.131294	−3.397	110	397.2
$24_{8,16}$–$23_{8,16}$ E, $v_t = 0$	299.131361	−4.932	98	220.4

Table N.1—*Continued*

Transition	ν_0 (GHz)	$\log_{10} A_{\mathrm{ul}}$ (s^{-1})	g_{u}	E_{u} (K)
$27_{1,26}$–$26_{1,25}$ A, $v_t = 1$	299.133165	−3.397	110	397.2
$27_{2,26}$–$26_{1,25}$ A, $v_t = 1$	299.135510	−4.243	110	397.2
$12_{6,6}$–$11_{5,7}$ A, $v_t = 0$	299.162434	−4.481	50	70.0
$24_{7,18}$–$23_{7,17}$ E, $v_t = 0$	300.020579	−3.426	98	210.9
$24_{7,18}$–$23_{7,17}$ A, $v_t = 0$	300.035621	−3.425	98	210.9
$24_{6,19}$–$23_{6,18}$ E, $v_t = 0$	300.046229	−3.415	98	202.7
$24_{6,19}$–$23_{6,18}$ A, $v_t = 0$	300.063893	−3.415	98	202.7
$26_{3,24}$–$25_{3,23}$ E, $v_t = 0$	300.070744	−3.398	106	206.8
$34_{2,32}$–$34_{1,33}$ A, $v_t = 0$	300.071349	−4.903	138	340.3
$34_{3,32}$–$34_{2,33}$ A, $v_t = 0$	300.072325	−4.903	138	340.3
$26_{3,24}$–$25_{3,23}$ A, $v_t = 0$	300.079079	−3.398	106	206.8
Methanol (CH_3OH)				
$4_{-3,2}$–$5_{-2,4}$ E, $v_t = 0$	288.705624	−4.734	36	70.9
$6_{0,6}$–$5_{0,5}$ E, $v_t = 0$	289.939377	−3.976	52	61.8
$6_{1,6}$–$5_{1,5}$ E, $v_t = 0$	290.069747	−3.987	52	54.3
$6_{0,6}$–$5_{0,5}$ A, $v_t = 0$	290.110637	−3.975	52	48.7
$6_{5,2}$–$5_{5,1}$ E, $v_t = 0$	290.117786	−4.489	52	172.8
$6_{-5,1}$–$5_{-5,0}$ E, $v_t = 0$	290.138889	−4.489	52	184.8
$6_{5,2}$–$5_{5,0}$ A, $v_t = 0$	290.145085	−4.487	52	186.6
$6_{5,1}$–$5_{5,1}$ A, $v_t = 0$	290.145085	−4.487	52	186.6
$6_{4,3}$–$5_{4,2}$ A, $v_t = 0$	290.161348	−4.229	52	129.1
$6_{4,2}$–$5_{4,1}$ A, $v_t = 0$	290.161352	−4.229	52	129.1
$6_{4,3}$–$5_{4,2}$ E, $v_t = 0$	290.162356	−4.230	52	136.6
$6_{-4,2}$–$5_{-4,1}$ E, $v_t = 0$	290.183289	−4.227	52	144.7

Table N.1—*Continued*

Transition	ν_0 (GHz)	$\log_{10} A_{\mathrm{ul}}$ (s^{-1})	g_{u}	E_{u} (K)
$6_{2,5}$–$5_{2,4}$ A, $v_t = 0$	290.184674	−4.023	52	86.5
$6_{3,4}$–$5_{3,3}$ A, $v_t = 0$	290.189515	−4.100	52	98.5
$6_{3,3}$–$5_{3,2}$ A, $v_t = 0$	290.190549	−4.100	52	98.5
$6_{3,3}$–$5_{3,2}$ E, $v_t = 0$	290.209695	−4.097	52	111.5
$6_{-3,4}$–$5_{-3,3}$ E, $v_t = 0$	290.213180	−4.098	52	96.5
$6_{-1,5}$–$5_{-1,4}$ E, $v_t = 0$	290.248685	−3.975	52	69.8
$6_{2,4}$–$5_{2,3}$ A, $v_t = 0$	290.264068	−4.022	52	86.5
$6_{2,4}$–$5_{2,3}$ E, $v_t = 0$	290.307281	−4.024	52	74.7
$6_{-2,5}$–$5_{-2,4}$ E, $v_t = 0$	290.307738	−4.029	52	71.0
Acetaldehyde (CH_3CHO)				
$16_{0,16}$–$15_{0,15}$ E, $v_t = 0$	299.174780	−3.038	66	123.6
$16_{0,16}$–$15_{0,15}$ A, $v_t = 0$	299.218175	−3.038	66	123.5
$15_{6,10}$–$14_{6,9}$ A, $v_t = 0$	289.149836	−3.157	62	192.2
$15_{6,9}$–$14_{6,8}$ A, $v_t = 0$	289.149853	−3.157	62	192.2
$15_{6,9}$–$14_{6,8}$ E, $v_t = 0$	289.163254	−3.157	62	192.2
$15_{6,10}$–$14_{6,9}$ E, $v_t = 0$	289.200782	−3.157	62	192.1
$7_{2,5}$–$6_{1,6}$ E, $v_t = 0$	289.238518	−4.459	30	35.1
$15_{5,11}$–$14_{5,10}$ A, $v_t = 0$	289.272555	−3.132	62	167.5
$15_{5,10}$–$14_{5,9}$ A, $v_t = 0$	289.273794	−3.132	62	167.5
$15_{5,10}$–$14_{5,9}$ E, $v_t = 0$	289.316721	−3.132	62	167.4
$15_{5,11}$–$14_{5,10}$ E, $v_t = 0$	289.322537	−3.132	62	167.4
$15_{4,12}$–$14_{4,11}$ A, $v_t = 0$	289.506111	−3.112	62	147.2
$15_{4,11}$–$14_{4,10}$ A, $v_t = 0$	289.558746	−3.112	62	147.3
$15_{4,11}$–$14_{4,10}$ E, $v_t = 0$	289.562297	−3.112	62	147.2

Table N.1—*Continued*

Transition	ν_0 (GHz)	$\log_{10} A_{\rm ul}$ (s^{-1})	$g_{\rm u}$	$E_{\rm u}$ (K)
$15_{4,12}$–$14_{4,11}$ E, $v_t = 0$	289.585326	−3.112	62	147.2
$15_{3,13}$–$14_{3,12}$ A, $v_t = 0$	289.602928	−3.097	62	131.5
$15_{3,13}$–$14_{3,12}$ E, $v_t = 0$	289.716267	−3.101	62	131.4
$7_{2,5}$–$6_{1,6}$ A, $v_t = 0$	289.942040	−4.371	30	35.0

Note. — For (tentatively) detected species (CH_3OCH_3 and CH_3OCHO), all transitions which could be responsible for the observed signals are listed. For non-detected species (CH_3OH and CH_3CHO), only strong transitions ($\log_{10} A_{\rm ul}\,({\rm s}^{-1}) \geq -5$ and $E_{\rm u} \leq 200\,{\rm K}$) that effectively constrain the column upper limits are listed.

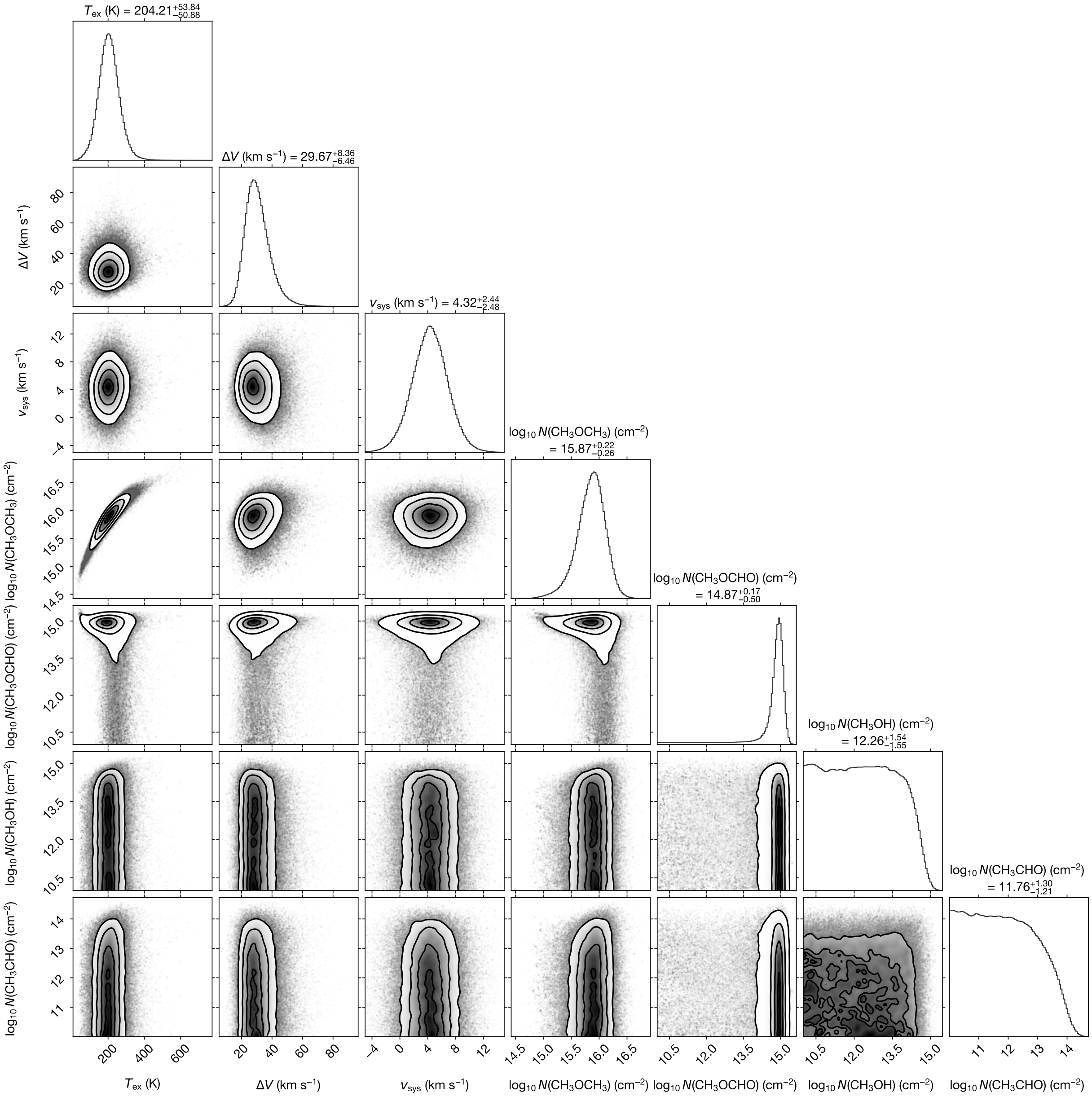

Figure N.1. Parameter covariances and marginalized posterior distributions for the MCMC spectral fit. The values and errors in the top of each panel indicate 16th, 50th (median), and 84th percentiles of posterior distributions.

Appendix O

Parametric Disk Model

Here, we demonstrate a detailed radiative transfer calculation of a disk model that aims to constrain what spatial distributions of COMs in the inner disk can explain the observed CH_3OCH_3 emission with a more realistic disk physical structure. Additionally, we examine if the difference in the spatial distributions of CH_3OCH_3 and CH_3OH can explain the non-detection of CH_3OH, as discussed in Section 5.4.1.

As the disk density and temperature structures, we used the disk model tailored to MWC 480 in Zhang et al. (2021). The details of the model are referred to the original paper. Briefly, the model assumed two populations (small and large) of dust grains, and the distributions of large dust grains are constrained from the high-resolution ALMA observations. The small dust grains are assumed to be completely coupled with the gas. While in the original model the gas temperature structure is computed by the thermochemical modeling, given the uncertainty of the modeling in the inner region, here we simply assumed that the gas temperature is the same as the dust temperature (surface-area-weighted over both populations) computed with thermal Monte Carlo simulations using the RADMC-3D package (Dullemond et al. 2012). The gas density and temperature distributions used for the present calculations are shown in Figure O.1.

The distributions of the warm CH_3OCH_3 and CH_3OH gas are assumed based on the dust temperature, which controls the ice sublimation. Since in general the sublimation temperature of a specific molecule is proportional to the binding energy of the molecule (e.g., Furuya & Aikawa 2014), the sublimation temperature ratio between CH_3OCH_3 and CH_3OH should be the same as the binding energy ratio. Although the absolute values of binding energy for CH_3OCH_3 and CH_3OH shows some scatter depending on the experimental methods and the composition of the surface, there are a trend that CH_3OCH_3 have a lower binding energy than CH_3OH. The experimental estimates of the binding energies of CH_3OCH_3 ($\approx$4000 K; Lattelais et al. 2011) and CH_3OH ($\approx$5000–5500 K; Ferrero et al. 2020; Minissale et al. 2022) thus lead to the sublimation temperature ratio of $T_{\rm sub}(CH_3OH)/T_{\rm sub}(CH_3OCH_3) \approx 1.2$–$1.4$. Based on this ratio and the gas density of the inner disk, we constructed a series of models, in which CH_3OCH_3 and CH_3OH distribute with a constant abundance x (relative to H_2 molecule) in the regions where the dust temperature is higher than 80 and 100 K for CH_3OCH_3, and 100, 120, and 140 K for CH_3OH. This emulates the drastic gas-phase abundance increases due to the thermal desorption. We additionally set an upper boundary of $z/r \lesssim 0.3$, reflecting the expectation that molecules can be destroyed in the irradiated surface of the disk (e.g., Walsh et al. 2014). Outside these boundaries, the abundances of CH_3OH and CH_3OCH_3 are set to zero, which is a suitable first-order approximation given the steep (exponential) dependence of gaseous molecular abundances on visual extinction and dust temperature around its sublimation temperature. The dependence of COM abundances on other parameters such as gas density is weaker (e.g., Hasegawa et al. 1992; Furuya & Aikawa 2014). This resulted in the distributions of warm CH_3OCH_3 and CH_3OH gas all within $\lesssim$20–30 au (the middle panel of Figure O.1). The velocity structure of the warm gas is assumed to be in Keplerian rotation with a known stellar mass of $2.1M_\odot$ (e.g., Teague et al. 2021).

For the models with different combinations of boundary temperatures as listed in Table O, which have at maximum a sublimation temperature ratio of 1.5 as the most extreme case, we compute the image cubes covering the frequency ranges of the robustly detected CH_3OCH_3 transitions at $\sim$299.89 GHz and the undetected CH_3OH transitions at 290.0–290.4 GHz using the RADMC-3D package (Dullemond et al. 2012). The resulting image cubes are convolved with the observing beam, continuum-subtracted, and spatially integrated to create the disk-integrated spectra, which is then compared to the observed spectra. The abundance $x(\mathrm{CH_3OCH_3})$ and $x(\mathrm{CH_3OH})$ are adjusted to fit the observed spectra.

The right panel of Figure O.1 compares the best-fit model with the observed spectrum of $\mathrm{CH_3OCH_3}$ at ∼299.89 GHz. Both models with boundary temperatures of 80 and 100 K reproduce the spectrum well, particularly the broad line width. Furthermore, the non-detection of $\mathrm{CH_3OH}$ places constraints on the abundance ratio $x(\mathrm{CH_3OCH_3})/x(\mathrm{CH_3OH})$ of the warm gas, as listed in Table O. The constrained lower limits of the abundance ratios span ∼0.3–2, depending on the combination of the boundary temperatures. These values are lower than the column density ratio derived in the spectral analysis in Section 5.3.2 (where the same distributions are implicitly assumed) by a factor of ∼3–20. This indicates that the spatial distribution is a critical factor in measuring the correct abundance ratio. Further spatially-resolved observations are necessary. It should be noted that the disk physical structure used in this modeling is an extrapolation of the outer disk structure. The actual structure can vary due, for example, to the accretion heating that could modify the temperature structure of the inner disk. Constraining the inner disk structure is also essential to infer the inner disk chemistry.

Table O.1 Disk Modeling Results

r_{in} (au)	r_{out} (au)	$(z/r)_{\mathrm{min}}$	$(z/r)_{\mathrm{max}}$	$T_{\mathrm{sub}}(\mathrm{CH_3OCH_3})$ (K)	$T_{\mathrm{sub}}(\mathrm{CH_3OH})$ (K)	$x(\mathrm{CH_3OCH_3})$	$x(\mathrm{CH_3OH})$	$x(\mathrm{CH_3OCH_3})/x(\mathrm{CH_3OH})$
0.5	30	0.0	0.3	80	100	3.0×10^{-8}	$< 3.1 \times 10^{-8}$	> 0.97
0.5	30	0.0	0.3	80	120	3.0×10^{-8}	$< 1.2 \times 10^{-7}$	> 0.25
0.5	30	0.0	0.3	100	120	1.8×10^{-7}	$< 1.0 \times 10^{-7}$	> 1.8
0.5	30	0.0	0.3	100	140	1.8×10^{-7}	$< 5.8 \times 10^{-7}$	> 0.31

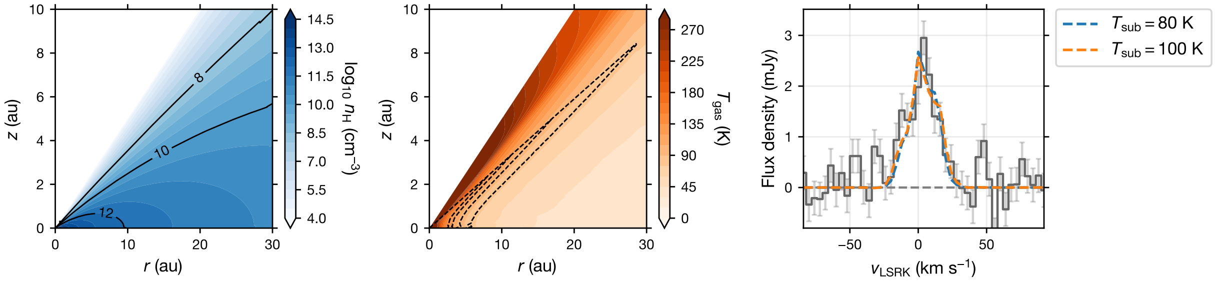

Figure O.1. Left and middle: Gas density (left) and temperature (middle) structure of the disk model. The dashed lines in the middle panel enclose the region where molecules distribute for each boundary temperature in the models (80, 100, 120, and 140 K from outside). The upper boundary of the regions is $z/r = 0.3$, which is also depicted by the dashed lines. Right: Comparison of the observed and modeled spectra of the CH_3OCH_3 transitions at ~ 299.89 GHz for the models with different boundary temperatures of CH_3OCH_3 (blue for 80 K model and orange for 100 K model). The spectra of these models are nearly identical and overlap.

Appendix P

Detection of a New Submillimeter Source

We report the detection of a new submillimeter source at a separation of $\approx 5''\!.2$ from the central star with a position angle of $212^{\circ}\!.5$ (Figure P.1). The emission is compact and reaches a peak S/N of ≈ 7 on the image made with a Briggs robust value of 0.5. The coordinate of the continuum peak is $\alpha(\mathrm{J2000}) = 4^{\mathrm{h}}58^{\mathrm{m}}46^{\mathrm{s}}\!.066$; $\delta(\mathrm{J2000}) = 29^{\mathrm{d}}50^{\mathrm{m}}32^{\mathrm{s}}\!.04$. To characterize the emission, we performed a Gaussian fit to this component with the CASA task `imfit`, which obtained a deconvolved size of $0''\!.33 \times 0''\!.13$ (P.A. $= 179^{\circ}$) and a flux density of 0.32 mJy. Although the origin of this emission is unclear, this component is located at outside the ^{12}CO gas disk analysed in Teague et al. (2021), and thus it is unlikely that the emission is attributed to the circumplanetary disk around a forming planet in the MWC 480 disk. It is possible that this originates from the disk or envelope around a field star, or a background galaxy.

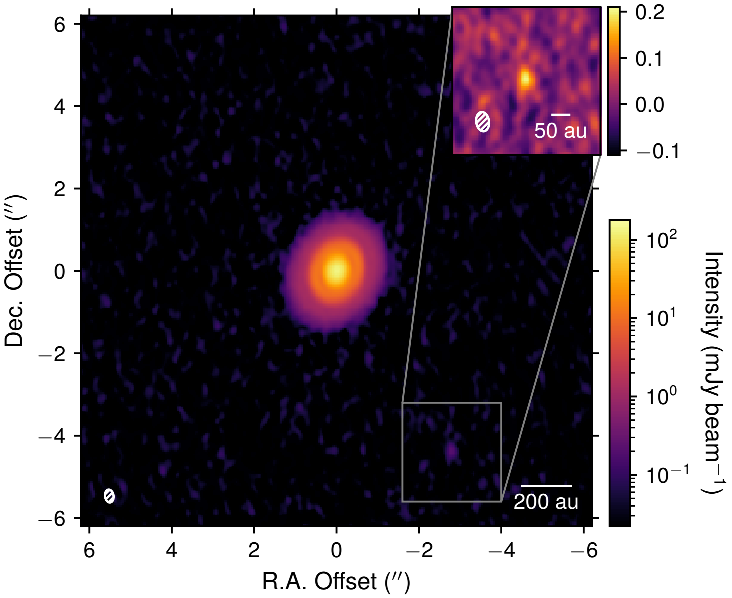

Figure P.1. 1.03 mm continuum image made with a Briggs robust value of 0.5. The inset panel presents the zoomed-in view of the vicinity of the new submillimeter source. The beam size of $0\farcs31 \times 0\farcs21$ (P.A. = $8\fdg2$) is shown in the lower left corner of each panel. A scale bar is shown in the lower right corner of each panel.

References

Adams, F. C. 2010, ARA&A, 48, 47

Agúndez, M., Marcelino, N., Cernicharo, J., Roueff, E., & Tafalla, M. 2019, A&A, 625, A147

Aikawa, Y., Herbst, E., Roberts, H., & Caselli, P. 2005, ApJ, 620, 330

Aikawa, Y., Okuzumi, S., & Pontoppidan, K. 2022, arXiv e-prints, arXiv:2212.14529

Aikawa, Y., van Zadelhoff, G. J., van Dishoeck, E. F., & Herbst, E. 2002, A&A, 386, 622

Aikawa, Y., Wakelam, V., Hersant, F., Garrod, R. T., & Herbst, E. 2012, ApJ, 760, 40

Aikawa, Y., Cataldi, G., Yamato, Y., et al. 2021, ApJS, 257, 13

Alarcón, F., Casassus, S., Lyra, W., Pérez, S., & Cieza, L. 2024, MNRAS, 527, 9655

Ali-Dib, M. 2017, MNRAS, 467, 2845

ALMA Partnership, Brogan, C. L., Pérez, L. M., et al. 2015, ApJ, 808, L3

Altwegg, K., Balsiger, H., & Fuselier, S. A. 2019, ARA&A, 57, 113

Altwegg, K., Balsiger, H., Berthelier, J. J., et al. 2017, Philosophical Transactions of the Royal Society of London Series A, 375, 20160253

Altwegg, K., Balsiger, H., Hänni, N., et al. 2020a, Nature Astronomy, 4, 533

Altwegg, K., Balsiger, H., Combi, M., et al. 2020b, MNRAS, 498, 5855

Alves, F. O., Girart, J. M., Caselli, P., et al. 2017, A&A, 603, L3

Andre, P., Ward-Thompson, D., & Barsony, M. 1993, ApJ, 406, 122

Andrews, S. M., Terrell, M., Tripathi, A., et al. 2018a, ApJ, 865, 157

Andrews, S. M., & Williams, J. P. 2005, ApJ, 631, 1134

Andrews, S. M., Wilner, D. J., Hughes, A. M., et al. 2012, ApJ, 744, 162

Andrews, S. M., Huang, J., Pérez, L. M., et al. 2018b, ApJ, 869, L41

Ansdell, M., Williams, J. P., van der Marel, N., et al. 2016, ApJ, 828, 46

Ansdell, M., Williams, J. P., Trapman, L., et al. 2018, ApJ, 859, 21

Aota, T., Inoue, T., & Aikawa, Y. 2015, ApJ, 799, 141

Aso, Y., & Machida, M. N. 2020, ApJ, 905, 174

Aso, Y., & Sai, J. 2023, jinshisai/SLAM: First Release of SLAM, doi:10.5281/zenodo.7783868

Aso, Y., Ohashi, N., Saigo, K., et al. 2015, ApJ, 812, 27

Aso, Y., Ohashi, N., Aikawa, Y., et al. 2017, ApJ, 849, 56

Bae, J., Teague, R., Andrews, S. M., et al. 2022, ApJ, 934, L20

Banzatti, A., Pontoppidan, K. M., Pére Chávez, J., et al. 2023, AJ, 165, 72

Barrado, D., Mollière, P., Patapis, P., et al. 2023, Nature, 624, 263

Beckwith, S. V. W., Sargent, A. I., Chini, R. S., & Guesten, R. 1990, AJ, 99, 924

Belloche, A., Maury, A. J., Maret, S., et al. 2020, A&A, 635, A198

Beltrán, M. T., & de Wit, W. J. 2016, A&A Rev., 24, 6

Benisty, M., Bae, J., Facchini, S., et al. 2021, ApJ, 916, L2

Bergin, E. A., Du, F., Cleeves, L. I., et al. 2016, ApJ, 831, 101

Bergin, E. A., Cleeves, L. I., Gorti, U., et al. 2013, Nature, 493, 644

Bergner, J. B., Guzmán, V. G., Öberg, K. I., Loomis, R. A., & Pegues, J. 2018, ApJ, 857, 69

Bergner, J. B., Öberg, K. I., Guzmán, V. V., et al. 2021, ApJS, 257, 11

Bi, J., van der Marel, N., Dong, R., et al. 2020, ApJ, 895, L18

Bianchi, E., Codella, C., Ceccarelli, C., et al. 2019, MNRAS, 483, 1850

Birnstiel, T., Dullemond, C. P., Zhu, Z., et al. 2018, ApJ, 869, L45

Bohlin, R. C., Savage, B. D., & Drake, J. F. 1978, ApJ, 224, 132

Boley, A. C. 2009, ApJ, 695, L53

Boogert, A. C. A., Gerakines, P. A., & Whittet, D. C. B. 2015, ARA&A, 53, 541

Booth, A. S., Ilee, J. D., Walsh, C., et al. 2023a, A&A, 669, A53

Booth, A. S., Law, C. J., Temmink, M., Leemker, M., & Macias, E. 2023b, arXiv e-prints, arXiv:2308.07910

Booth, A. S., van der Marel, N., Leemker, M., van Dishoeck, E. F., & Ohashi, S. 2021a, A&A, 651, L6

Booth, A. S., Walsh, C., Terwisscha van Scheltinga, J., et al. 2021b, Nature Astronomy, 5, 684

Booth, A. S., Leemker, M., van Dishoeck, E. F., et al. 2024a, AJ, 167, 164

Booth, A. S., Temmink, M., van Dishoeck, E. F., et al. 2024b, AJ, 167, 165

Bosman, A. D., Alarcón, F., Bergin, E. A., et al. 2021a, ApJS, 257, 7

Bosman, A. D., Bergin, E. A., Loomis, R. A., et al. 2021b, ApJS, 257, 15

Boss, A. P. 1997, Science, 276, 1836

Bottinelli, S., Boogert, A. C. A., Bouwman, J., et al. 2010, ApJ, 718, 1100

Brinch, C., Crapsi, A., Jørgensen, J. K., Hogerheijde, M. R., & Hill, T. 2007, A&A, 475, 915

Brinch, C., & Hogerheijde, M. R. 2010, A&A, 523, A25

Brunken, N. G. C., Booth, A. S., Leemker, M., et al. 2022, A&A, 659, A29

Cabedo, V., Maury, A., Girart, J. M., et al. 2023, A&A, 669, A90

Calahan, J. K., Bergin, E. A., van't Hoff, M., et al. 2024, ApJ, 967, 158

Calmonte, U., Altwegg, K., Balsiger, H., et al. 2016, MNRAS, 462, S253

Cami, J., Bernard-Salas, J., Peeters, E., & Malek, S. E. 2010, Science, 329, 1180

Carney, M. T., Hogerheijde, M. R., Guzmán, V. V., et al. 2019, A&A, 623, A124

REFERENCES

Carvajal, M., Kleiner, I., & Demaison, J. 2010, ApJS, 190, 315

Carvajal, M., Margulès, L., Tercero, B., et al. 2009, A&A, 500, 1109

CASA Team, Bean, B., Bhatnagar, S., et al. 2022, PASP, 134, 114501

Casassus, S., & Cárcamo, M. 2022, MNRAS, 513, 5790

Casassus, S., Cieza, L., Cárcamo, M., et al. 2023, MNRAS, 526, 1545

Caselli, P., Pineda, J. E., Sipilä, O., et al. 2022, ApJ, 929, 13

Cassen, P., & Moosman, A. 1981, Icarus, 48, 353

Cataldi, G., Yamato, Y., Aikawa, Y., et al. 2021, ApJS, 257, 10

Cazaux, S., Tielens, A. G. G. M., Ceccarelli, C., et al. 2003, ApJ, 593, L51

Ceccarelli, C., Caselli, P., Bockelée-Morvan, D., et al. 2014, in Protostars and Planets VI, ed. H. Beuther, R. S. Klessen, C. P. Dullemond, & T. Henning, 859–882

Ceccarelli, C., Codella, C., Balucani, N., et al. 2023, in Astronomical Society of the Pacific Conference Series, Vol. 534, Astronomical Society of the Pacific Conference Series, ed. S. Inutsuka, Y. Aikawa, T. Muto, K. Tomida, & M. Tamura, 379

Chen, Y., Rocha, W. R. M., van Dishoeck, E. F., et al. 2024, A&A, 690, A205

Cherniak, E. A., & Costain, C. C. 1966, J. Chem. Phys., 45, 104

Chiang, E. I., & Goldreich, P. 1997, ApJ, 490, 368

Choi, M., Kang, M., Tatematsu, K., Lee, J.-E., & Park, G. 2011, PASJ, 63, 1281

Choi, M., Tatematsu, K., & Kang, M. 2010, ApJ, 723, L34

Choi, M., Tatematsu, K., Park, G., & Kang, M. 2007, ApJ, 667, L183

Chuang, K. J., Fedoseev, G., Ioppolo, S., van Dishoeck, E. F., & Linnartz, H. 2016, MNRAS, 455, 1702

Cieza, L. A., Casassus, S., Tobin, J., et al. 2016, Nature, 535, 258

Cieza, L. A., Ruíz-Rodríguez, D., Perez, S., et al. 2018, MNRAS, 474, 4347

Cieza, L. A., Ruíz-Rodríguez, D., Hales, A., et al. 2019, MNRAS, 482, 698

Cohen, E. A., & Pickett, H. M. 1982, Journal of Molecular Spectroscopy, 93, 83

REFERENCES

Coudert, L. H., Drouin, B. J., Tercero, B., et al. 2013, ApJ, 779, 119

Coudert, L. H., Margulès, L., Vastel, C., et al. 2019, A&A, 624, A70

Coutens, A., Jørgensen, J. K., Persson, M. V., et al. 2014, ApJ, 792, L5

Crapsi, A., Caselli, P., Walmsley, C. M., et al. 2005, ApJ, 619, 379

Crapsi, A., van Dishoeck, E. F., Hogerheijde, M. R., Pontoppidan, K. M., & Dullemond, C. P. 2008, A&A, 486, 245

Creswell, R. A., & Schwendeman, R. H. 1974, Chemical Physics Letters, 27, 521

Cridland, A. J., Eistrup, C., & van Dishoeck, E. F. 2019, A&A, 627, A127

Csengeri, T., Belloche, A., Bontemps, S., et al. 2019, A&A, 632, A57

Czekala, I., Loomis, R. A., Teague, R., et al. 2021, ApJS, 257, 2

D'Alessio, P., Cantö, J., Calvet, N., & Lizano, S. 1998, ApJ, 500, 411

Daly, A. M., Bermúdez, C., Kolesniková, L., & Alonso, J. L. 2015, ApJS, 218, 30

Daniel, F., Faure, A., Wiesenfeld, L., et al. 2014, MNRAS, 444, 2544

de Gregorio-Monsalvo, I., Ménard, F., Dent, W., et al. 2013, A&A, 557, A133

De Lucia, F. C., & Helminger, P. 1975, Journal of Molecular Spectroscopy, 54, 200

De Simone, M., Ceccarelli, C., Codella, C., et al. 2020, ApJ, 896, L3

—. 2022, ApJ, 935, L14

Demaison, J., Maes, H., Van Eijck, B. P., Wlodarczak, G., & Lasne, M. C. 1987, Journal of Molecular Spectroscopy, 125, 214

Di Francesco, J., Myers, P. C., Wilner, D. J., Ohashi, N., & Mardones, D. 2001, ApJ, 562, 770

Doi, K., & Kataoka, A. 2021, ApJ, 912, 164

Drozdovskaya, M. N., Coudert, L. H., Margulès, L., et al. 2022, A&A, 659, A69

Drozdovskaya, M. N., van Dishoeck, E. F., Rubin, M., Jørgensen, J. K., & Altwegg, K. 2019, MNRAS, 490, 50

Drozdovskaya, M. N., van Dishoeck, E. F., Jørgensen, J. K., et al. 2018, MNRAS, 476, 4949

Drozdovskaya, M. N., Schroeder I, I. R. H. G., Rubin, M., et al. 2021, MNRAS, 500, 4901

Duan, C., Carvajal, M., Yu, S., et al. 2015, A&A, 576, A39

Dullemond, C. P., Juhasz, A., Pohl, A., et al. 2012, RADMC-3D: A multi-purpose radiative transfer tool, Astrophysics Source Code Library, record ascl:1202.015, ascl:1202.015

Dutrey, A., Guilloteau, S., Piétu, V., et al. 2017, A&A, 607, A130

Eistrup, C., Walsh, C., & van Dishoeck, E. F. 2016, A&A, 595, A83

Endres, C. P., Drouin, B. J., Pearson, J. C., et al. 2009, A&A, 504, 635

Endres, C. P., Schlemmer, S., Schilke, P., Stutzki, J., & Müller, H. S. P. 2016, Journal of Molecular Spectroscopy, 327, 95

Enoch, M. L., Evans, Neal J., I., Sargent, A. I., & Glenn, J. 2009, ApJ, 692, 973

Evans, II, N. J., Dunham, M. M., Jørgensen, J. K., et al. 2009, ApJS, 181, 321

Facchini, S., Birnstiel, T., Bruderer, S., & van Dishoeck, E. F. 2017, A&A, 605, A16

Facchini, S., Juhász, A., & Lodato, G. 2018, MNRAS, 473, 4459

Fairlamb, J. R., Oudmaijer, R. D., Mendigutía, I., Ilee, J. D., & van den Ancker, M. E. 2015, MNRAS, 453, 976

Favre, C., Carvajal, M., Field, D., et al. 2014, ApJS, 215, 25

Favre, C., Fedele, D., Semenov, D., et al. 2018, ApJ, 862, L2

Fedoseev, G., Ioppolo, S., Zhao, D., Lamberts, T., & Linnartz, H. 2015, MNRAS, 446, 439

Ferrero, S., Zamirri, L., Ceccarelli, C., et al. 2020, ApJ, 904, 11

Fischer, W. J., Hillenbrand, L. A., Herczeg, G. J., et al. 2023, in Astronomical Society of the Pacific Conference Series, Vol. 534, Protostars and Planets VII, ed. S. Inutsuka, Y. Aikawa, T. Muto, K. Tomida, & M. Tamura, 355

Flores, C., Duchêne, G., Wolff, S., et al. 2021, AJ, 161, 239

Flores, C., Ohashi, N., Tobin, J. J., et al. 2023, ApJ, 958, 98

Flower, D. R., & Watt, G. D. 1984, MNRAS, 209, 25

—. 1985, MNRAS, 213, 991

Foreman-Mackey, D., Hogg, D. W., Lang, D., & Goodman, J. 2013, PASP, 125, 306

Friesen, R. K., Di Francesco, J., Shirley, Y. L., & Myers, P. C. 2009, ApJ, 697, 1457

Furlan, E., Fischer, W. J., Ali, B., et al. 2016, ApJS, 224, 5

Furuya, K. 2024, ApJ, 974, 115

Furuya, K., & Aikawa, Y. 2014, ApJ, 790, 97

Furuya, K., Aikawa, Y., Sakai, N., & Yamamoto, S. 2011, ApJ, 731, 38

Furuya, K., Drozdovskaya, M. N., Visser, R., et al. 2017, A&A, 599, A40

Furuya, K., Lee, S., & Nomura, H. 2022, ApJ, 938, 29

Furuya, K., & Persson, M. V. 2018, MNRAS, 476, 4994

Furuya, K., van Dishoeck, E. F., & Aikawa, Y. 2016, A&A, 586, A127

Furuya, K., Watanabe, Y., Sakai, T., Aikawa, Y., & Yamamoto, S. 2018, A&A, 615, L16

Fusina, L., Di Lonardo, G., Johns, J. W. C., & Halonen, L. 1988, Journal of Molecular Spectroscopy, 127, 240

Gaia Collaboration, Brown, A. G. A., Vallenari, A., et al. 2018, A&A, 616, A1

Garrod, R. T., & Herbst, E. 2006, A&A, 457, 927

Garrod, R. T., Jin, M., Matis, K. A., et al. 2022, ApJS, 259, 1

Garufi, A., Podio, L., Codella, C., et al. 2022, A&A, 658, A104

Gibb, E. L., Whittet, D. C. B., Schutte, W. A., et al. 2000, ApJ, 536, 347

Ginsburg, A., Sipőcz, B. M., Brasseur, C. E., et al. 2019, AJ, 157, 98

Greene, T. P., Wilking, B. A., Andre, P., Young, E. T., & Lada, C. J. 1994, ApJ, 434, 614

Groner, P., Albert, S., Herbst, E., et al. 2002, ApJS, 142, 145

Guzmán, V. V., Bergner, J. B., Law, C. J., et al. 2021, ApJS, 257, 6

Hama, T., & Watanabe, N. 2013, Chemical Reviews, 113, 8783

Hardy, J. A., Cox, A. P., Fliege, E., & Dreizler, H. 1982, Zeitschrift Naturforschung Teil A, 37, 1035

Harsono, D., Bjerkeli, P., van der Wiel, M. H. D., et al. 2018, Nature Astronomy, 2, 646

Hasegawa, T. I., Herbst, E., & Leung, C. M. 1992, ApJS, 82, 167

Hässig, M., Altwegg, K., Balsiger, H., et al. 2017, A&A, 605, A50

Hatchell, J. 2003, A&A, 403, L25

Haykal, I., Carvajal, M., Tercero, B., et al. 2014, A&A, 568, A58

Herbst, E., & van Dishoeck, E. F. 2009, ARA&A, 47, 427

Herczeg, G. J., Johnstone, D., Mairs, S., et al. 2017, ApJ, 849, 43

Hidaka, H., Watanabe, M., Kouchi, A., & Watanabe, N. 2011, Physical Chemistry Chemical Physics (Incorporating Faraday Transactions), 13, 15798

Hirano, S., & Machida, M. N. 2019, MNRAS, 485, 4667

Hirano, S., Tsukamoto, Y., Basu, S., & Machida, M. N. 2020, ApJ, 898, 118

Högbom, J. A. 1974, A&AS, 15, 417

Hogerheijde, M. R., & Sandell, G. 2000, ApJ, 534, 880

Hogerheijde, M. R., van Dishoeck, E. F., Blake, G. A., & van Langevelde, H. J. 1998, ApJ, 502, 315

Hollenbach, D. J., & Tielens, A. G. G. M. 1999, Reviews of Modern Physics, 71, 173

Huang, J., Ansdell, M., Birnstiel, T., et al. 2024, ApJ, 976, 132

Ilee, J. D., Walsh, C., Booth, A. S., et al. 2021, ApJS, 257, 9

Ilyushin, V., Kryvda, A., & Alekseev, E. 2009, Journal of Molecular Spectroscopy, 255, 32

Izquierdo, A. F., Testi, L., Facchini, S., et al. 2023, A&A, 674, A113

Jensen, S. S., Jørgensen, J. K., Kristensen, L. E., et al. 2021, A&A, 650, A172

—. 2019, A&A, 631, A25

Jeong, J.-H., Lee, J.-E., Lee, S., et al. 2025, ApJS, 276, 49

Jiang, H., Wang, Y., Ormel, C. W., Krijt, S., & Dong, R. 2023, A&A, 678, A33

Jonusas, M., Leroux, K., & Krim, L. 2020, Journal of Molecular Structure, 1220, 128736

Jørgensen, J. K., Belloche, A., & Garrod, R. T. 2020, ARA&A, 58, 727

Jørgensen, J. K., Favre, C., Bisschop, S. E., et al. 2012, ApJ, 757, L4

Jørgensen, J. K., Schöier, F. L., & van Dishoeck, E. F. 2002, A&A, 389, 908

Jørgensen, J. K., van der Wiel, M. H. D., Coutens, A., et al. 2016, A&A, 595, A117

Jørgensen, J. K., Müller, H. S. P., Calcutt, H., et al. 2018, A&A, 620, A170

Jorsater, S., & van Moorsel, G. A. 1995, AJ, 110, 2037

Kanagawa, K. D., Muto, T., Tanaka, H., et al. 2015, ApJ, 806, L15

Keppler, M., Benisty, M., Müller, A., et al. 2018, A&A, 617, A44

Kido, M., Takakuwa, S., Saigo, K., et al. 2023, ApJ, 953, 190

Kleiner, I., Lovas, F. J., & Godefroid, M. 1996, Journal of Physical and Chemical Reference Data, 25, 1113

Koerber, M., Bisschop, S. E., Endres, C. P., et al. 2013, A&A, 558, A112

Koga, S., Kawasaki, Y., & Machida, M. N. 2022, MNRAS, 515, 6073

Kratter, K., & Lodato, G. 2016, ARA&A, 54, 271

Kraus, S., Kreplin, A., Young, A. K., et al. 2020, Science, 369, 1233

Kristensen, L. E., van Dishoeck, E. F., Bergin, E. A., et al. 2012, A&A, 542, A8

Kuhn, M. A., & Hillenbrand, L. A. 2019, ApJ, 883, 117

Kukolich, S. G. 1967, Physical Review, 156, 83

Kukolich, S. G., & Wofsy, S. C. 1970, J. Chem. Phys., 52, 5477

Kwon, W., Looney, L. W., & Mundy, L. G. 2011, ApJ, 741, 3

Lacy, J. H., Faraji, H., Sandford, S. A., & Allamandola, L. J. 1998, ApJ, 501, L105

Lada, C. J. 1987, in IAU Symposium, Vol. 115, Star Forming Regions, ed. M. Peimbert & J. Jugaku, 1

REFERENCES

Lada, C. J., & Wilking, B. A. 1984, ApJ, 287, 610

Lambrechts, M., & Johansen, A. 2014, A&A, 572, A107

Langer, W. D., Graedel, T. E., Frerking, M. A., & Armentrout, P. B. 1984, ApJ, 277, 581

Larson, R. B. 1969, MNRAS, 145, 271

Lattelais, M., Bertin, M., Mokrane, H., et al. 2011, A&A, 532, A12

Law, C. J., Booth, A. S., & Öberg, K. I. 2023a, ApJ, 952, L19

Law, C. J., Loomis, R. A., Teague, R., et al. 2021a, ApJS, 257, 3

Law, C. J., Teague, R., Loomis, R. A., et al. 2021b, ApJS, 257, 4

Law, C. J., Crystian, S., Teague, R., et al. 2022, ApJ, 932, 114

Law, C. J., Teague, R., Öberg, K. I., et al. 2023b, ApJ, 948, 60

Lay, O. P., Carlstrom, J. E., & Hills, R. E. 1995, ApJ, 452, L73

Le Gal, R., Hily-Blant, P., Faure, A., et al. 2014, A&A, 562, A83

Le Gal, R., Öberg, K. I., Teague, R., et al. 2021, ApJS, 257, 12

Lee, C.-F., Codella, C., Ceccarelli, C., & López-Sepulcre, A. 2022, ApJ, 937, 10

Lee, C.-F., Li, Z.-Y., Ho, P. T. P., et al. 2017, Science Advances, 3, e1602935

Lee, C. W., Kim, G., Myers, P. C., et al. 2018, ApJ, 865, 131

Lee, J.-E., Lee, S., Baek, G., et al. 2019, Nature Astronomy, 3, 314

Lee, S., Lee, J.-E., & Lee, S. 2024, Journal of Korean Astronomical Society, 57, 163

Leemker, M., Booth, A. S., van Dishoeck, E. F., et al. 2023, A&A, 673, A7

Leemker, M., van't Hoff, M. L. R., Trapman, L., et al. 2021, A&A, 646, A3

Ligterink, N. F. W., & Minissale, M. 2023, A&A, 676, A80

Lin, Z.-Y. D., Li, Z.-Y., Tobin, J. J., et al. 2023, ApJ, 951, 9

Linsky, J. L., Draine, B. T., Moos, H. W., et al. 2006, ApJ, 647, 1106

Liu, Y., Dipierro, G., Ragusa, E., et al. 2019, A&A, 622, A75

Loinard, L., Castets, A., Ceccarelli, C., Caux, E., & Tielens, A. G. G. M. 2001, ApJ, 552, L163

Long, F., Pinilla, P., Herczeg, G. J., et al. 2018, ApJ, 869, 17

Long, F., Andrews, S. M., Rosotti, G., et al. 2022, ApJ, 931, 6

Loomis, R. A., Cleeves, L. I., Öberg, K. I., et al. 2018a, ApJ, 859, 131

Loomis, R. A., Öberg, K. I., Andrews, S. M., et al. 2018b, AJ, 155, 182

Looney, L. W., Mundy, L. G., & Welch, W. J. 2000, ApJ, 529, 477

López-Sepulcre, A., Sakai, N., Neri, R., et al. 2017, A&A, 606, A121

Lykke, J. M., Coutens, A., Jørgensen, J. K., et al. 2017, A&A, 597, A53

Machida, M. N., Inutsuka, S.-I., & Matsumoto, T. 2011, PASJ, 63, 555

Manara, C. F., Morbidelli, A., & Guillot, T. 2018, A&A, 618, L3

Manigand, S., Calcutt, H., Jørgensen, J. K., et al. 2019, A&A, 623, A69

Manigand, S., Jørgensen, J. K., Calcutt, H., et al. 2020, A&A, 635, A48

Manigand, S., Coutens, A., Loison, J. C., et al. 2021, A&A, 645, A53

Maret, S., Bergin, E. A., & Lada, C. J. 2006, Nature, 442, 425

Maret, S., Maury, A. J., Belloche, A., et al. 2020, A&A, 635, A15

Margulès, L., Coudert, L. H., Møllendal, H., et al. 2009, Journal of Molecular Spectroscopy, 254, 55

Margulès, L., Motiyenko, R. A., Ilyushin, V. V., & Guillemin, J. C. 2015, A&A, 579, A46

Margulès, L., Huet, T. R., Demaison, J., et al. 2010, ApJ, 714, 1120

Martín-Doménech, R., Muñoz Caro, G. M., Bueno, J., & Goesmann, F. 2014, A&A, 564, A8

Mathis, J. S., Rumpl, W., & Nordsieck, K. H. 1977, ApJ, 217, 425

Matsumoto, T., Machida, M. N., & Inutsuka, S.-i. 2017, ApJ, 839, 69

Maureira, M. J., Pineda, J. E., Liu, H. B., et al. 2024, A&A, 689, L5

McClure, M. K., Bergin, E. A., Cleeves, L. I., et al. 2016, ApJ, 831, 167

McClure, M. K., Rocha, W. R. M., Pontoppidan, K. M., et al. 2023, Nature Astronomy, 7, 431

McGuire, B. A. 2022, ApJS, 259, 30

McGuire, B. A., Burkhardt, A. M., Kalenskii, S., et al. 2018, Science, 359, 202

Mendigutía, I., Brittain, S., Eiroa, C., et al. 2013, ApJ, 776, 44

Mercimek, S., Codella, C., Podio, L., et al. 2022, A&A, 659, A67

Milam, S. N., Savage, C., Brewster, M. A., Ziurys, L. M., & Wyckoff, S. 2005, ApJ, 634, 1126

Millar, T. J., Bennett, A., & Herbst, E. 1989, ApJ, 340, 906

Minissale, M., Aikawa, Y., Bergin, E., et al. 2022, ACS Earth and Space Chemistry, 6, 597

Miotello, A., Kamp, I., Birnstiel, T., Cleeves, L. C., & Kataoka, A. 2023, in Astronomical Society of the Pacific Conference Series, Vol. 534, Protostars and Planets VII, ed. S. Inutsuka, Y. Aikawa, T. Muto, K. Tomida, & M. Tamura, 501

Miura, H., Yamamoto, T., Nomura, H., et al. 2017, ApJ, 839, 47

Möller, T., Endres, C., & Schilke, P. 2017, A&A, 598, A7

Montesinos, B., Eiroa, C., Mora, A., & Merín, B. 2009, A&A, 495, 901

Mori, S., Aikawa, Y., Oya, Y., Yamamoto, S., & Sakai, N. 2024, ApJ, 961, 31

Motte, F., & André, P. 2001, A&A, 365, 440

Mottram, J. C., van Dishoeck, E. F., Schmalzl, M., et al. 2013, A&A, 558, A126

Müller, H. S. P., Guillemin, J.-C., Lewen, F., & Schlemmer, S. 2022, Journal of Molecular Spectroscopy, 384, 111584

Müller, H. S. P., Schlöder, F., Stutzki, J., & Winnewisser, G. 2005, Journal of Molecular Structure, 742, 215

Müller, H. S. P., Thorwirth, S., Roth, D. A., & Winnewisser, G. 2001, A&A, 370, L49

Mumma, M. J., & Charnley, S. B. 2011, ARA&A, 49, 471

Nazari, P., Tabone, B., van't Hoff, M. L. R., Jørgensen, J. K., & van Dishoeck, E. F. 2023, ApJ, 951, L38

Nealon, R., Dipierro, G., Alexander, R., Martin, R. G., & Nixon, C. 2018, MNRAS, 481, 20

Nixon, C., King, A., & Price, D. 2013, MNRAS, 434, 1946

Nomura, H., Aikawa, Y., Nakagawa, Y., & Millar, T. J. 2009, A&A, 495, 183

Nomura, H., & Millar, T. J. 2004, A&A, 414, 409

Nomura, H., Furuya, K., Cordiner, M. A., et al. 2023, in Astronomical Society of the Pacific Conference Series, Vol. 534, Astronomical Society of the Pacific Conference Series, ed. S. Inutsuka, Y. Aikawa, T. Muto, K. Tomida, & M. Tamura, 1075

Notsu, S., Eistrup, C., Walsh, C., & Nomura, H. 2020, MNRAS, 499, 2229

Notsu, S., Nomura, H., Ishimoto, D., et al. 2016, ApJ, 827, 113

—. 2017, ApJ, 836, 118

Notsu, S., van Dishoeck, E. F., Walsh, C., Bosman, A. D., & Nomura, H. 2021, A&A, 650, A180

Öberg, K. I., & Bergin, E. A. 2021, Phys. Rep., 893, 1

Öberg, K. I., Boogert, A. C. A., Pontoppidan, K. M., et al. 2011, ApJ, 740, 109

Öberg, K. I., Garrod, R. T., van Dishoeck, E. F., & Linnartz, H. 2009, A&A, 504, 891

Öberg, K. I., Guzmán, V. V., Furuya, K., et al. 2015, Nature, 520, 198

Öberg, K. I., & Wordsworth, R. 2019, AJ, 158, 194

Öberg, K. I., Guzmán, V. V., Walsh, C., et al. 2021, ApJS, 257, 1

Ohashi, N., Saigo, K., Aso, Y., et al. 2014, ApJ, 796, 131

Ohashi, N., Tobin, J. J., Jørgensen, J. K., et al. 2023, ApJ, 951, 8

Ohashi, S., Kobayashi, H., Sai, J., & Sakai, N. 2022a, ApJ, 933, 23

Ohashi, S., Nakatani, R., Liu, H. B., et al. 2022b, ApJ, 934, 163

Ohashi, S., Kobayashi, H., Nakatani, R., et al. 2021, ApJ, 907, 80

Okoda, Y., Oya, Y., Abe, S., et al. 2021, ApJ, 923, 168

Okoda, Y., Oya, Y., Imai, M., et al. 2022, ApJ, 935, 136

Okuzumi, S., Momose, M., Sirono, S.-i., Kobayashi, H., & Tanaka, H. 2016, ApJ, 821, 82

Oldag, F., & Sutter, D. H. 1992, Zeitschrift Naturforschung Teil A, 47, 527

Ortiz-León, G. N., Loinard, L., Dzib, S. A., et al. 2018, ApJ, 865, 73

Ossenkopf, V., & Henning, T. 1994, A&A, 291, 943

Oya, Y., Sakai, N., López-Sepulcre, A., et al. 2016, ApJ, 824, 88

Oya, Y., Moriwaki, K., Onishi, S., et al. 2018, ApJ, 854, 96

Oyama, T., Ohno, Y., Tamanai, A., et al. 2023, ApJ, 957, 4

Padgett, D. L., Brandner, W., Stapelfeldt, K. R., et al. 1999, AJ, 117, 1490

Padovani, M., Ivlev, A. V., Galli, D., et al. 2020, Space Sci. Rev., 216, 29

Paneque-Carreño, T., Miotello, A., van Dishoeck, E. F., et al. 2023, A&A, 669, A126

Panić, O., Hogerheijde, M. R., Wilner, D., & Qi, C. 2009, A&A, 501, 269

Pearson, J. C., Yu, S., & Drouin, B. J. 2012, Journal of Molecular Spectroscopy, 280, 119

Penston, M. V. 1969, MNRAS, 144, 425

Persson, M. V., Harsono, D., Tobin, J. J., et al. 2016, A&A, 590, A33

Persson, M. V., Jørgensen, J. K., & van Dishoeck, E. F. 2013, A&A, 549, L3

Persson, M. V., Jørgensen, J. K., van Dishoeck, E. F., & Harsono, D. 2014, A&A, 563, A74

Peter, R., & Dreizler, H. 1965, Zeitschrift Naturforschung Teil A, 20, 301

Pickett, H. M., Poynter, R. L., Cohen, E. A., et al. 1998, J. Quant. Spec. Radiat. Transf., 60, 883

Piétu, V., Dutrey, A., & Guilloteau, S. 2007, A&A, 467, 163

Pineda, J. E., Harju, J., Caselli, P., et al. 2022, AJ, 163, 294

Pinte, C., Dent, W. R. F., Ménard, F., et al. 2016, ApJ, 816, 25

Pinte, C., Ménard, F., Duchêne, G., et al. 2018a, 609, A47

Pinte, C., Price, D. J., Ménard, F., et al. 2018b, ApJ, 860, L13

Poch, O., Istiqomah, I., Quirico, E., et al. 2020, Science, 367, aaw7462

Przybilla, N., Nieva, M.-F., & Butler, K. 2008, ApJ, 688, L103

Qi, C., Öberg, K. I., Wilner, D. J., et al. 2013, Science, 341, 630

Richard, C., Jørgensen, J. K., Margulès, L., et al. 2021, A&A, 651, A120

Roberts, H., & Millar, T. J. 2000, A&A, 361, 388

Robitaille, T. P., Whitney, B. A., Indebetouw, R., Wood, K., & Denzmore, P. 2006, ApJS, 167, 256

Roccatagliata, V., Franciosini, E., Sacco, G. G., Randich, S., & Sicilia-Aguilar, A. 2020, A&A, 638, A85

Rosenfeld, K. A., Andrews, S. M., Hughes, A. M., Wilner, D. J., & Qi, C. 2013, ApJ, 774, 16

Rosolowsky, E. W., Pineda, J. E., Foster, J. B., et al. 2008, ApJS, 175, 509

Rubin, M., Altwegg, K., Balsiger, H., et al. 2015, Science, 348, 232

—. 2017, A&A, 601, A123

—. 2019, MNRAS, 489, 594

Ruíz-Rodríguez, D., Cieza, L. A., Williams, J. P., et al. 2017, MNRAS, 468, 3266

Sahu, D., Liu, S.-Y., Su, Y.-N., et al. 2019, ApJ, 872, 196

Sai, J., Ohashi, N., Maury, A. J., et al. 2022, ApJ, 925, 12

Sai, J., Ohashi, N., Saigo, K., et al. 2020, ApJ, 893, 51

Sakai, N., Hanawa, T., Zhang, Y., et al. 2018, Nature, 565, 206

Sakai, N., & Yamamoto, S. 2013, Chemical Reviews, 113, 8981

Sakai, N., Sakai, T., Hirota, T., et al. 2014, Nature, 507, 78

Sakai, N., Oya, Y., Higuchi, A. E., et al. 2017, MNRAS, 467, L76

REFERENCES

Santamaría-Miranda, A., de Gregorio-Monsalvo, I., Ohashi, N., et al. 2024, A&A, 690, A46

Schöier, F. L., van der Tak, F. F. S., van Dishoeck, E. F., & Black, J. H. 2005, A&A, 432, 369

Schuhmann, M., Altwegg, K., Balsiger, H., et al. 2019, ACS Earth and Space Chemistry, 3, 1854

Schwarz, K. R., & Bergin, E. A. 2014, ApJ, 797, 113

Schwarz, K. R., Bergin, E. A., Cleeves, L. I., et al. 2018, ApJ, 856, 85

Segura-Cox, D. M., Schmiedeke, A., Pineda, J. E., et al. 2020, Nature, 586, 228

Seifried, D., Sánchez-Monge, Á., Walch, S., & Banerjee, R. 2016, MNRAS, 459, 1892

Shah, R. Y., & Wootten, A. 2001, ApJ, 554, 933

Sheehan, P. D., & Eisner, J. A. 2017, ApJ, 851, 45

—. 2018, ApJ, 857, 18

Sheehan, P. D., Tobin, J. J., Federman, S., Megeath, S. T., & Looney, L. W. 2020, ApJ, 902, 141

Shirley, Y. L. 2015, PASP, 127, 299

Shu, F. H. 1977, ApJ, 214, 488

Sierra, A., Pérez, L. M., Zhang, K., et al. 2021, ApJS, 257, 14

Simon, M., Guilloteau, S., Beck, T. L., et al. 2019, ApJ, 884, 42

Smith, L. R., Gudipati, M. S., Smith, R. L., & Lewis, R. D. 2021, A&A, 656, A82

Smith, R. L., Pontoppidan, K. M., Young, E. D., & Morris, M. R. 2015, ApJ, 813, 120

Strom, K. M., & Strom, S. E. 1993, ApJ, 412, L63

Sturm, J. A., McClure, M. K., Beck, T. L., et al. 2023, A&A, 679, A138

Suzuki, T., Furuya, K., Aikawa, Y., Shibata, T., & Majumdar, L. 2024, MNRAS, 532, 1796

Tachibana, S., & Sakai, N. 2024, Elements, 20, 31

Takahashi, S. Z., & Muto, T. 2018, ApJ, 865, 102

Takakuwa, S., Saigo, K., Kido, M., et al. 2024, ApJ, 964, 24

Tamura, M., Gatley, I., Waller, W., & Werner, M. W. 1991, ApJ, 374, L25

Taquet, V., Charnley, S. B., & Sipilä, O. 2014, ApJ, 791, 1

Taquet, V., López-Sepulcre, A., Ceccarelli, C., et al. 2013, ApJ, 768, L29

Taquet, V., Wirström, E. S., & Charnley, S. B. 2016, ApJ, 821, 46

Taquet, V., Bianchi, E., Codella, C., et al. 2019, A&A, 632, A19

Tazzari, M., Beaujean, F., & Testi, L. 2018, MNRAS, 476, 4527

Teague, R. 2019, 4, 1632

Teague, R. 2020, richteague/keplerian_mask: Initial Release, doi:10.5281/zenodo.4321137

Teague, R., Bae, J., & Bergin, E. A. 2019, Nature, 574, 378

Teague, R., & Foreman-Mackey, D. 2018, Research Notes of the American Astronomical Society, 2, 173

Teague, R., Law, C. J., Huang, J., & Meng, F. 2021, 6, 3827

Teague, R., & Loomis, R. 2020, ApJ, 899, 157

Teague, R., Bae, J., Aikawa, Y., et al. 2021, ApJS, 257, 18

Terebey, S., Shu, F. H., & Cassen, P. 1984, ApJ, 286, 529

Tielens, A. G. G. M., & Hagen, W. 1982, A&A, 114, 245

Tinacci, L., Germain, A., Pantaleone, S., et al. 2022, ACS Earth and Space Chemistry, 6, 1514

Tobin, J. J., Hartmann, L., Chiang, H.-F., et al. 2012, Nature, 492, 83

Tobin, J. J., Sheehan, P. D., Megeath, S. T., et al. 2020, ApJ, 890, 130

Tobin, J. J., van't Hoff, M. L. R., Leemker, M., et al. 2023, Nature, 615, 227

Trapman, L., Facchini, S., Hogerheijde, M. R., van Dishoeck, E. F., & Bruderer, S. 2019, A&A, 629, A79

Trapman, L., Zhang, K., van't Hoff, M. L. R., Hogerheijde, M. R., & Bergin, E. A. 2022, ApJ, 926, L2

Tripathi, A., Andrews, S. M., Birnstiel, T., & Wilner, D. J. 2017, ApJ, 845, 44

Turner, B. E. 2001, ApJS, 136, 579

Tychoniec, Ł., Tobin, J. J., Karska, A., et al. 2018, ApJS, 238, 19

Tychoniec, Ł., Manara, C. F., Rosotti, G. P., et al. 2020, A&A, 640, A19

Tychoniec, Ł., van Dishoeck, E. F., van't Hoff, M. L. R., et al. 2021, A&A, 655, A65

Ulrich, R. K. 1976, ApJ, 210, 377

Vacherand, J. M., Van Eijck, B. P., Burie, J., & Demaison, J. 1986, Journal of Molecular Spectroscopy, 118, 355

van der Marel, N., Booth, A. S., Leemker, M., van Dishoeck, E. F., & Ohashi, S. 2021, A&A, 651, L5

van der Marel, N., van Dishoeck, E. F., Bruderer, S., et al. 2013, Science, 340, 1199

van der Tak, F. F. S., Schilke, P., Müller, H. S. P., et al. 2002, A&A, 388, L53

van Dishoeck, E. F., Blake, G. A., Draine, B. T., & Lunine, J. I. 1993, in Protostars and Planets III, ed. E. H. Levy & J. I. Lunine, 163

van Gelder, M. L., Tabone, B., van Dishoeck, E. F., & Godard, B. 2021, A&A, 653, A159

van 't Hoff, M. L. R., Bergin, E. A., Jørgensen, J. K., & Blake, G. A. 2020a, ApJ, 897, L38

van 't Hoff, M. L. R., Persson, M. V., Harsono, D., et al. 2018a, A&A, 613, A29

van 't Hoff, M. L. R., Tobin, J. J., Trapman, L., et al. 2018b, ApJ, 864, L23

van 't Hoff, M. L. R., van Dishoeck, E. F., Jørgensen, J. K., & Calcutt, H. 2020b, A&A, 633, A7

van't Hoff, M. L. R., Tobin, J. J., Li, Z.-Y., et al. 2023, ApJ, 951, 10

Villenave, M., Ménard, F., Dent, W. R. F., et al. 2020, A&A, 642, A164

Villenave, M., Stapelfeldt, K. R., Duchêne, G., et al. 2022, ApJ, 930, 11

Vorobyov, E. I. 2009, ApJ, 704, 715

Walsh, C., Millar, T. J., Nomura, H., et al. 2014, A&A, 563, A33

REFERENCES

Walsh, C., Loomis, R. A., Öberg, K. I., et al. 2016, ApJ, 823, L10

Ward-Thompson, D., Motte, F., & Andre, P. 1999, MNRAS, 305, 143

Watanabe, N., & Kouchi, A. 2002, ApJ, 571, L173

Watanabe, N., Shiraki, T., & Kouchi, A. 2003, ApJ, 588, L121

Weaver, E., Isella, A., & Boehler, Y. 2018, ApJ, 853, 113

Wei, C.-E., Nomura, H., Lee, J.-E., et al. 2019, ApJ, 870, 129

Wenzel, G., Cooke, I. R., Changala, P. B., et al. 2024, Science, 386, 810

Wilson, T. L. 1999, Reports on Progress in Physics, 62, 143

Wilson, T. L., Rohlfs, K., & Hüttemeister, S. 2009, Tools of Radio Astronomy, doi:10.1007/978-3-540-85122-6

Winnewisser, M., Winnewisser, G., Honda, T., & Hirota, E. 1975, Zeitschrift Naturforschung Teil A, 30, 1001

Woods, P. M., & Willacy, K. 2009, ApJ, 693, 1360

Xu, L.-H., Fisher, J., Lees, R. M., et al. 2008, Journal of Molecular Spectroscopy, 251, 305

Yamaguchi, M., Muto, T., Tsukagoshi, T., et al. 2024, PASJ, 76, 437

Yamato, Y., Furuya, K., Aikawa, Y., et al. 2022, ApJ, 941, 75

Yamato, Y., Notsu, S., Aikawa, Y., et al. 2024, AJ, 167, 66

Yang, Y.-L., Sakai, N., Zhang, Y., et al. 2021, ApJ, 910, 20

Yen, H.-W., Koch, P. M., Liu, H. B., et al. 2016, ApJ, 832, 204

Yen, H.-W., Takakuwa, S., Ohashi, N., & Ho, P. T. P. 2013, ApJ, 772, 22

Yen, H.-W., Takakuwa, S., Ohashi, N., et al. 2014, ApJ, 793, 1

Yen, H.-W., Takakuwa, S., Chu, Y.-H., et al. 2017, A&A, 608, A134

Yoshida, T. C., Nomura, H., Furuya, K., Tsukagoshi, T., & Lee, S. 2022a, ApJ, 932, 126

Yoshida, T. C., Nomura, H., Law, C. J., et al. 2024, ApJ, 971, L15

Yoshida, T. C., Nomura, H., Tsukagoshi, T., Furuya, K., & Ueda, T. 2022b, ApJ, 937, L14

Young, A. K., Alexander, R., Walsh, C., et al. 2021, MNRAS, 505, 4821

Yu, S., Pearson, J. C., Drouin, B. J., et al. 2010, J. Chem. Phys., 133, 174317

Zhang, K., Bergin, E. A., Blake, G. A., Cleeves, L. I., & Schwarz, K. R. 2017, Nature Astronomy, 1, 0130

Zhang, K., Blake, G. A., & Bergin, E. A. 2015, ApJ, 806, L7

Zhang, K., Booth, A. S., Law, C. J., et al. 2021, ApJS, 257, 5

Zhang, S., Zhu, Z., Huang, J., et al. 2018, ApJ, 869, L47

Zhu, Z. 2019, MNRAS, 483, 4221

Zingsheim, O., Müller, H. S. P., Lewen, F., Jørgensen, J. K., & Schlemmer, S. 2017, Journal of Molecular Spectroscopy, 342, 125

Zucker, C., Speagle, J. S., Schlafly, E. F., et al. 2020, A&A, 633, A51

—. 2019, ApJ, 879, 125